Technische Universität München
Max-Planck-Institut für Quantenoptik

Quantum and classical simulation of High Energy Physics

Stefan Kühn

Vollständiger Abdruck der von der Fakultät für Physik
der Technischen Universität München
zur Erlangung des akademischen Grades eines

Doktors der Naturwissenschaften (Dr. rer. nat.)

genehmigten Dissertation.

Vorsitzender:	Prof. Dr. Alexander Holleitner
Prüfer der Dissertation:	1. Hon.-Prof. Ignacio Cirac, Ph.D.
	2. Prof. Dr. Nora Brambilla

Die Dissertation wurde am 02.10.2017
bei der Technischen Universität München eingereicht
und durch die Fakultät für Physik am 09.11.2017 angenommen.

Abstract

In this thesis, we demonstrate some of the first necessary steps towards an application of tensor networks to lattice gauge theories. Using matrix product states, a particular kind of one-dimensional tensor network, we numerically investigate certain 1+1 dimensional lattice gauge models in the Hamiltonian formulation. The models we study encompass all the fundamental features appearing in relevant 3+1 dimensional scenarios, such as quantum chromodynamics, in particular matter fields coupled to a gauge field, and, the Abelian and non-Abelian cases we address also suffer from the sign problem in certain parameter regimes. Our analysis demonstrates the suitability of matrix product states to study statical as well as dynamical properties of gauge models, especially in regimes which cannot be accessed with Monte Carlo methods. Furthermore we employ matrix product states to assess some crucial questions regarding the quantum simulation of lattice gauge theories.

First, we study two models suitable for the quantum simulation of 1+1 dimensional quantum electrodynamics, also known as the Schwinger model. We explore the effect of representing the gauge degrees of freedom with finite-dimensional systems and show that the results converge quickly with increasing dimensions. Moreover, we also investigate a possible adiabatic preparation protocol for the interacting vacuum of the theory and demonstrate that the resources needed are essentially independent of the system size and the dimension of the systems representing the gauge degrees of freedom in the studied parameter regime. Furthermore, we asses the effect of gauge-invariance-breaking noise terms during the preparation protocol and quantify up to which noise level the ground-state energy is still reasonably close to the noise free case.

Second, we address the phase structure of the multiflavor Schwinger model with nonzero chemical potential for a fixed physical volume, a regime where the conventional Monte Carlo approach suffers from the sign problem. We reproduce known analytic results for the two-flavor case at zero temperature and vanishing mass and extend the computation to the massive case, where no analytical prediction is available. Our calculations allow us to map out the phase diagram of the model in the mass – chemical potential plane, thus providing an example of overcoming the sign problem with tensor networks in a lattice gauge theory calculation. Moreover, we also study the spatially resolved chiral condensate within the different phases for the massless case. We recover the theoretically predicted oscillatory behavior and quantify the volume depen-

dence of the oscillation amplitude and frequency for the different phases.

Third, we investigate the phenomenon of string breaking in a non-Abelian SU(2) lattice gauge model. We compute the static potential between heavy external charges, similar to conventional Monte Carlo simulations, and also explore the real-time dynamics of a string imposed on top of the interacting vacuum of the theory between heavy external and fully dynamical charges. Furthermore, we propose a number of (local) observables that can be used for detecting string breaking and apply them to characterize the phenomenon in the statical and dynamical cases.

Finally, we develop a basis for the physical subspace of a SU(2) lattice gauge theory, where the gauge degrees of freedom are integrated out. Our formulation is completely general and might have potential applications for the design of future quantum simulators. Moreover, it is suitable for addressing the theory with tensor networks. Using our formulation together with matrix product states, we study the low-lying spectrum and determine the scaling exponent of the vector mass gap for a family of SU(2) gauge models where the gauge degrees of freedom are truncated to a finite dimension. In addition, we also investigate the entanglement in the ground state and explore the scaling of the entanglement entropy while approaching the continuum limit.

Zusammenfassung

In der vorliegenden Arbeit zeigen wir einige der ersten notwendigen Schritte hin zu einer Anwendung von Tensornetzwerken auf Gittereichtheorien. Unter Verwendung von Matrixproduktzuständen, einer speziellen Form von eindimensionalen Tensornetzwerken, untersuchen wir numerisch verschiedene 1+1 dimensionale Gittereichmodelle in der Hamiltonschen Formulierung. Die Modellsysteme, die wir behandeln, beinhalten alle grundlegenden Eigenschaften von wichtigen 3+1 dimensionalen Szenarien, wie beispielsweise Quantenchromodynamik, insbesondere Matriefelder die an Eichfelder koppeln, und die Abelschen und nicht-Abelschen Fälle mit denen wir uns beschäftigen unterliegen in bestimmten Parameterbereichen auch dem negativen Vorzeichenproblem. Unsere Analyse zeigt die Eignung von Matrixproduktzuständen für die Untersuchung von statischen und dynamischen Eigenschaften von Eichtheorien, insbesondere in Bereichen in denen ein Zugang mit Monte Carlo Methoden nicht möglich ist. Weiterhin verwenden wir Matrixproduktzustände um entscheidenden Fragen bezüglich der Quantensimulation von Gittereichtheorien zu behandeln.

Zuerst untersuchen wir zwei Modelle, die sich für die Quantensimulation von Quantenelektrodynamik in 1+1 Dimensionen, auch bekannt als das Schwingermodell, eignen. Wir analysieren die Auswirkung, die durch die Darstellung der Eichfreiheitsgrade mit endlichdimensionalen Systemen entsteht und zeigen die schnelle Konvergenz der Ergebnisse mit zunehmender Dimension. Weiterhin erforschen wir ein mögliches Protokoll für die adiabatische Herstellung des wechselwirkenden Vakuums der Theorie und legen dar, dass die benötigten Ressourcen im untersuchten Parameterbereich im Wesentlichen unabhängig von der Systemgröße und der Dimension der Systeme, die die Eichfreiheitsgrade darstellen, sind. Außerdem behandeln wir die Frage nach dem Einfluss von nicht eichinvarianten Störtermen während des Protokolls zur adiabatischen Herstellung des Grundzustandes und quantifizieren, bis zu welcher Stärke der Störung die Grundzustandsenergie noch in vernünftigem Maße mit der des störungsfreien Falls übereinstimmt.

Als Zweites behandeln wir die Phasensruktur des mehrflavor Schwinger Modells mit nicht verschwindendem chemischen Potential in einem festen physikalischem Volumen, einem Parameterbereich in dem der herkömmliche Monte Carlo Zugang dem negativen Vorzeichenproblem unterliegt. Wir reproduzieren bekannte analytische Ergebnisse für den masselosen Fall und dehnen die Berechnung auf den massiven Fall aus, für den keine analytische Vorhersa-

ge existiert. Unsere Berechnungen ermöglichen uns das Phasendiagramm des Modells in der Masse – chemisches Potential – Ebene zu bestimmen und stellen ein Beispiel für das Überwinden des negativen Vorzeichenproblems mit Hilfe von Tensornetzwerken in einer Gittereichtheorieberechnung dar. Weiterhin analysieren wir das ortsaufgelöste chirale Kondensat innerhalb der verschiedenen Phasen für den masselosen Fall. Wir beobachten das theoretisch vorhergesagte oszillierende Verhalten und bestimmen die Volumenabhängigkeit von Oszillationsamplitude und Frequenz für die einzelnen Phasen.

Als Drittes untersuchen wir das Phänomen des "String breakings" in einem nicht-abelschen SU(2) Gittereichmodell. Wir berechnen das statische Potential zwischen schweren externen Ladungen, vergleichbar mit konventionellen Monte Carlo Simulationen, und erforschen die Zeitentwicklung eines Strings sowohl zwischen schweren externen und komplett dynamischen Ladungen, der im wechselwirkenden Vakuum der Theorie generiert wurde. Weiterhin schlagen wir eine Reihe von (lokalen) Observablen vor, die es erlauben String breaking zu detektieren und verwenden diese um die statischen und dynamischen Fälle zu charakterisieren.

Zuletzt entwickeln wir eine Basis für den physikalischen Unterraum einer SU(2) Gittereichtheorie, bei der die Eichfreiheitsgrade ausintegriert sind. Unsere Formulierung ist nicht auf eine spezielle Methode beschränkt und könnte möglicherweise Anwendung beim Entwurf von zukünftigen Quantensimulatoren finden. Außerdem ist sie geeignet um die Theorie mit Tensornetzwerken zu behandeln. Wir verwenden unsere Formulierung in Kombination mit Matrixproduktzuständen um das niederenergetische Spektrum und den kritischen Exponent der Vektormasse für eine Familie von SU(2) Eichmodellen zu bestimmen, bei denen die Eichfreiheitsgrade auf eine endliche Dimension beschnitten sind. Zusätzlich untersuchen wir auch die Verschränkung im Grundzustand und das Skalierungsverhalten der Verschränkungsentropie bei Annäherung ans Kontinuum.

Publications

Publications covered in this thesis

1. **Quantum simulation of the Schwinger model: A study of feasibility**
   Stefan Kühn, J. Ignacio Cirac, Mari Carmen Bañuls
   Physical Review A **90**, 042305 (2014), Chapter 4

2. **Non-Abelian string breaking phenomena with matrix product states**
   Stefan Kühn, Erez Zohar, J. Ignacio Cirac, Mari Carmen Bañuls
   Journal of High Energy Physics **2015**, 130 (2015), Chapter 6

3. **The multi-flavor Schwinger model – Overcoming the sign problem with matrix product states**
   Mari Carmen Bañuls, Krzysztof Cichy, J. Ignacio Cirac, Karl Jansen, Stefan Kühn, Hana Saito
   PoS(LATTICE 2016)316 (2016), Chapter 5

4. **Density Induced Phase Transitions in the Schwinger model: A Study with Matrix Product States**
   Mari Carmen Bañuls, Krzysztof Cichy, J. Ignacio Cirac, Karl Jansen, Stefan Kühn
   Physical Review Letters **118**, 071601 (2017), Chapter 5

5. **Towards overcoming the Monte Carlo sign problem with tensor networks**
   Mari Carmen Bañuls, Krzysztof Cichy, J. Ignacio Cirac, Karl Jansen, Stefan Kühn, Hana Saito
   EPJ Web of Conferences **137**, 04001 (2017), Chapter 5

6. **Efficient basis formulation for 1+1 dimensional SU(2) lattice gauge theory: Spectral calculations with matrix product states**
   Mari Carmen Bañuls, Krzysztof Cichy, J. Ignacio Cirac, Karl Jansen, Stefan Kühn
   arXiv:1707.06434 (2017), Chapter 7

Publications not covered in this thesis

1. **Transport of dipolar Bose-Einstein condensates in a one-dimensional optical lattice**
   Stefan Kühn, Thomas E. Judd
   Physical Review A **87**, 023608 (2013)

Contents

Chapter 1

Introduction

The Standard Model is the basis of our understanding of modern high energy physics. Providing a full classification of all known elementary particles and describing all the fundamental forces among them, except for gravity, it shaped our picture of the subatomic structure of matter and led to major experimental breakthroughs, with the most recent one being the discovery of the Higgs boson [1, 2]. At the theoretical level, it is described by non-Abelian gauge theories. Since Weyl introduced the notion of a gauge theory in his early attempts to unify electromagnetism and gravity [3], the generalization to non-Abelian symmetry groups by C. Yang and R. Mills [4] has become the foundation of our theoretical description of high energy physics. In case of the Standard Model the underlying Yang-Mills theories are given by quantum chromodynamics (QCD), a SU(3) gauge theory describing the strong interactions, and the Glashow-Weinberg-Salam model for the electroweak interactions corresponding to a gauge theory with a $U(1) \times SU(2)$ symmetry.

Despite their great importance for the theoretical description of high energy physics, the analytical investigation of Yang-Mills theories is inherently challenging and a full solution seems elusive in most cases. A further complication arises from the fact that a perturbative approach to many relevant problems, such as QCD at low energies, is impossible. Due to asymptotic freedom [5, 6], QCD is strongly coupled at low energy scales, which leads to a breakdown of the perturbative methods in that regime and leaves a lot of theoretical questions unanswered. For example, the mechanism leading to confinement in QCD, meaning that at low energies only bound states of quarks are observed, is not yet fully understood. More generally, it is still an open question if Yang-Mills theories have a finite energy gap between the ground state and the first excited state,[1] which in the context of QCD is responsible for the interaction potential between the quarks being strong but short ranged.

A standard tool for exploring gauge theories in the nonperturbative limit is *lattice gauge theory* (LGT). Discretizing the action [8] or the Hamiltonian [9] of

[1] Proving that Yang-Mills theories with a simple, compact symmetry group in four space-time dimensions are gapped is in fact one of the Millennium Problems stated by the Clay Mathematics Institute [7].

the theory on a lattice while simultaneously preserving the gauge symmetry, allows for a numerical treatment. In particular, the discretized Lagrangian formulation enables the application of sophisticated Markov chain based Monte Carlo (MC) methods that have been highly successful for studying mass spectra [10], phase diagrams [11] and many other (static) properties. However, despite this great success, the MC approach faces a major obstacle in the sign problem [12], as the onset of negative or even complex probability amplitudes in certain parameter regimes prevents an efficient MC sampling. As a consequence, there are many relevant problems which cannot be addressed with it as for example real-time dynamics, or large parts of the QCD phase diagram at nonzero temperature and baryon density. Hence, there is an ongoing search for alternative approaches overcoming these limitations, among them MC on Lefshetz thimbles [13–16], complex Langevin methods [15], density of states techniques [17, 18], dualization [17, 19–22] and new integration methods [23, 24].

During recent years, approaches originating from quantum information theory have proven themselves as promising alternatives. For one, numerical methods based on *tensor networks* (TN) have been successfully applied to lattice gauge models. Being free from the sign problem, they can access parameter regimes and questions which are unamenable to the MC approach. Although TN can be used to address the Lagrangian formulation [25–34], they are particularly suited for the Hamiltonian formulation, for which powerful algorithms for the computation of low-lying spectra as well as for simulating time evolution exist. Moreover, contrary to the MC approach, these methods explicitly yield the wave function at the end of the computation, thus allowing for easy access to all kinds of (local) observables, and also the entanglement structure of the state, which opens up new perspectives to characterize LGT problems. The power of those techniques for spectral calculations and simulating dynamical problems for both Abelian and non-Abelian theories, as well as for addressing finite temperature has already been successfully demonstrated in the last few years [35–53], and the work reported in this thesis has been part of this effort. Furthermore, there is a lot of progress in developing gauge invariant TN suitable for LGT [37, 54–63].

A different quantum information based approach is *quantum simulation* of (lattice) gauge theories. This approach, originally envisioned by Feynman [64], uses an experimentally controllable quantum system to simulate another while exploiting its quantum nature, and thus does not suffer from purely numerical limitations as opposed to the simulations on a classical computer discussed previously. Quantum simulators have already been discussed and demonstrated for many condensed matter problems in a variety of experimental platforms ranging from ultracold atoms [65–68], trapped ions [69–71], and Rydberg atoms [72] over superconducting circuits [73], photons [74], to nuclear spins [75] and many others, and in some cases already outperformed the clas-

sical simulations [76]. This great success also motives the application of the method to LGT problems, and lately there has been a variety of proposals to quantum simulate gauge theories [55, 57, 60, 77–100]. Recently, the first quantum simulator for quantum electrodynamics (QED) in 1+1 dimensions, also known as the Schwinger model [101], has been realized experimentally in a small system of trapped ions [102]. Hence, this route is particularly promising for the future.

Here we address questions related to quantum simulation of gauge theories and the TN approach to LGT for certain gauge models in 1+1 dimensions. Although these two approaches are seemingly unrelated, they have much in common. One the one hand, the TN approach can help to explore the feasibility of quantum simulation proposals. Since a majority of these also adopts the Hamiltonian lattice formulation, numerical methods based on TN can be used to investigate relevant questions for the practical implementation, as for example possible protocols for the preparation of ground states and the influence of noise terms. In particular, TN also allow for the analysis of the effects of approximations that might be necessary for an experimental realization and how those can affect the performance of future quantum simulators. On the other hand, the TN approach to LGT enables to explore parameter regimes and problems intractable with MC methods and to access all kinds of local observables. Hence, the results obtained from applying TN methods to LGT problems can also help to find observables and setups that might be more accessible in future quantum simulation experiments than the ones typically used in MC simulations.

The rest of this thesis is structured as follows: Chapters 2 and 3 give a brief introduction to the theoretical background. In Chapter 2, we present the basics of LGT with a particular focus on the Hamiltonian formulation, as this is the more natural framework for TN and quantum simulation. Starting from the continuum Lagrangian, we derive the Hamiltonian and show the lattice discretization with Kogut-Susskind staggered fermions which we adopt for our numerical simulations throughout this thesis. The particular kind of one-dimensional TN, the matrix product states (MPS), which we use in our numerical computations, are introduced in Chapter 3. After a short summary of the theoretical foundations, we present the numerical algorithms we apply to compute low-lying spectra and time evolution for the various gauge models we examine.

Chapters 4 and 5 are devoted to the Abelian case of lattice Schwinger model. In Chapter 4 we study two proposals for quantum simulation of the Schwinger model where the gauge degrees of freedom are truncated to a finite dimension. First, using variational methods based on MPS, we investigate the spectral properties of these proposals and systematically explore the effect of the truncation on ground-state energy density. Second, taking advantage of the fact that TN allow us to simulate real-time dynamics, we analyze a possible

adiabatic preparation protocol for the interacting vacuum of the theory and the physical resources needed therefor. We give evidence that the initial part of the adiabatic evolution is decisive for its success and that the total time needed for a successful preparation is essentially independent of the system size in the parameter regime we study. Finally, we also assess the effect of gauge invariance breaking noise during the procedure and quantify the noise level for which the final state is still reasonably close to the ground state.

Afterwards, we turn to the multiflavor case at nonzero chemical potential, a situation where the conventional MC approach suffers from the sign problem, in Chapter 5. Using a formulation where the gauge degrees of freedom are integrated out, we determine the phase structure for two flavors at a fixed physical volume. Going through the full extrapolation procedure to recover the continuum limit, we reproduce known analytical results for the massless case with great precision and extend the study to the massive case, where no analytical predictions are available. Our observations show that the phase structure for the massive case changes significantly and we map out the phase diagram of the theory in the mass – chemical potential plane. Moreover, with the MPS approach we can also access the spatially resolved chiral condensate within the different phases. Studying the chiral condensate for vanishing mass, we observe the theoretically predicted spatial oscillations and quantify their frequency as well as their amplitude.

Chapters 6 and 7 are devoted to the non-Abelian case. First, we study the statical and dynamical aspects of string breaking in a SU(2) lattice gauge model with a finite-dimensional representation for the gauge degrees of freedom in Chapter 6. Using MPS simulations in imaginary time, we determine the static potential of a color-flux string between two heavy external charges, similar to the conventional MC approach. This allows us to identify the parameter regimes for which string breaking occurs and to show that the signatures of string breaking are clearly visible in certain (local) observables. These observables can also be used to characterize the dynamical case and we analyze the real-time evolution of a string between two heavy external charges imposed on top of the interacting vacuum of the theory. With our observables, we can clearly identify the breaking case and observe the screening of the external charges after the color-flux string breaks and particles are created. Finally, we also investigate a scenario closer to more realistic out-of-equilibrium situations, where the charges added to the vacuum are themselves fully dynamical. In that case, we again observe string breaking for small enough fermions masses and characterize the phenomenon using our observables.

Furthermore, in Chapter 7, we develop a basis for the physical subspace of a SU(2) lattice gauge theory, where the gauge degrees of freedom are integrated out. The resulting formulation, which is similar to the one we use for the multiflavor Schwinger case, is completely general and lends itself to any numerical or analytical method. Due to the vastly reduced degrees of free-

dom and its similarity to the one recently realized experimentally in trapped ions for the Schwinger model [102], it might also be potentially suited for the design of future quantum simulators. Moreover, our formulation also allows for an efficient truncation of the color-electric flux at an arbitrary maximum value while simultaneously preserving the gauge invariance. These truncated models can be addressed with TN, and combining our basis with variational methods based on MPS, we investigate the low-lying spectrum for a family of truncated SU(2) models. Thanks to the great reduction of basis states in our formulation, we can access much larger values for the color-electric flux than amenable in previous numerical studies with TN [43, 52] and we analyze the effects of the truncation in a systematic way. In particular, we explore the effect on the closing of the vector mass gap and its scaling exponent as we approach criticality and the scaling of the entanglement entropy in the ground state towards the continuum limit.

Finally, we give a brief summary of our main results and point out possible future directions and perspectives in Chapter 8.

In the Appendices A to C we elaborate on the numerical simulation techniques and the data analysis procedure, and we proof certain relations used in the main text. These Appendices are not necessary for the understanding of the rest of this thesis and we refer the reader interested in the technical details to those.

Chapter 2

Lattice gauge theory

In this Chapter, we briefly review the basic elements of (lattice) gauge theory we use throughout the rest of this work. After introducing the continuum formulation in Sec. 2.1, we focus on the Hamiltonian lattice formulation with Kogut-Susskind staggered fermions in Sec. 2.2. Moreover, we illustrate the discussion with two particular models in Sec. 2.3, the (Abelian) Schwinger model, which is presumably the simplest nontrivial gauge theory with matter, and a 1+1 dimensional SU(2) LGT as a paradigmatic example for the non-Abelian case. After establishing the theoretical background of gauge theories and their lattice formulation, we comment on the prospects and challenges of potential future quantum simulators for gauge theories in Sec. 2.4.

2.1 Yang-Mills theory in the continuum

Before we turn to the Hamiltonian lattice formulation, let us briefly summarize the main aspects of the continuum theory. To this end, we start with the *classical Lagrangian density* for noninteracting, relativistic fermions in 4 space-time dimensions, given by[1] [103, 104]

$$\mathcal{L} = \overline{\psi}(x)\left(i\gamma^\mu \partial_\mu - m\right)\psi(x). \tag{2.1}$$

Here $\psi(x)$ is a spinor of some group $\mathcal{G}$, $x = (t, \mathbf{x})$ a four vector in Minkowski space, m the bare fermion mass, γ^μ are the Dirac matrices fulfilling the anti-commutation relation $\{\gamma^\mu, \gamma^\nu\} = 2\eta^{\mu\nu}$ with $\eta = \mathrm{diag}(1,-1,-1,-1)$ the metric tensor, and $\overline{\psi} = \psi^\dagger \gamma^0$. Throughout the Chapter Greek indices refer to Lorentz indices ranging from 0 to 3, and, unless stated otherwise, the Einstein summation convention is implied. Looking at the Lagrangian above, it is easy to see that it is invariant under *global symmetry transformations*

$$\psi(x) \to V\psi(x), \qquad \overline{\psi}(x) \to \overline{\psi}(x)V^\dagger,$$

where $V \in \mathcal{G}$ is some group element in the same representation as $\psi(x)$. For all the rest, we restrict ourselves to the compact (matrix) Lie groups SU(N_c) and

[1] Throughout this thesis we use natural units $\hbar = c = 1$.

U(1), hence, the group elements can be written as the exponential of a finite set of traceless hermitian generators, t^a, forming a Lie algebra. The Lie bracket is then simply the usual commutator fulfilling

$$[t^a, t^b] = i f^{abc} t^c,$$

where f^{abc} are the (totally antisymmetric) structure constants of the group. Similar to the Lorentz indices, we label all indices associated to the group and the algebra with Latin letters and, again, the Einstein summation convention applies unless stated otherwise. For the rest of this Chapter, we assume that the generators fulfill the normalization condition

$$\mathrm{tr}\left(t^a t^b\right) = \frac{1}{2}\delta^{ab}. \tag{2.2}$$

Since different space-time points are independent, there is a priori no reason to allow for global symmetry transformations only, and we can also consider *local symmetry transformations*

$$\psi(x) \to V(x)\psi(x), \qquad \overline{\psi}(x) \to \overline{\psi}(x)V^\dagger(x).$$

While this transformation leaves the mass term of the Lagrangian in Eq. (2.1) invariant, one can immediately see that the kinetic term changes due to the derivative. The definition of the derivate along the direction n^μ

$$n^\mu \partial_\mu \psi(x) = \lim_{h\to 0} \frac{\psi(x+hn) - \psi(x)}{h}$$

shows that the problem arises because it involves two different space-time points and hence $\partial_\mu\psi(x)$ does not have a simple transformation behavior. To compensate for the different transformation at different space-time points, we introduce the *comparator*, $U(x', x)$, a unitary matrix which we require to transform as

$$U(x', x) \to V(x')U(x', x)V^\dagger(x) \tag{2.3}$$

and $U(x, x) = \mathbb{1}$ [104]. Hence, the *covariant derivative*

$$n^\mu D_\mu \psi(x) = \lim_{h\to 0} \frac{\psi(x+hn) - U(x+hn, x)\psi(x)}{h} \tag{2.4}$$

has a simple transformation behavior under local symmetry transformations. To find the explicit form of the comparator and the covariant derivative, we can make use of the fact that we consider compact Lie groups, and expand $U(x+hn, x)$ for infinitesimal h around the identity:

$$U(x+hn, x) = \mathbb{1} + igh n^\mu A^a_\mu(x) t^a + \mathcal{O}(h^2). \tag{2.5}$$

The infinitesimal form of the expansion suggests that the comparator along a path $\mathcal{C}$ between two points y and z is given by [104–106]

$$U(z,y) = \mathcal{P}\exp\left(ig\int_{\mathcal{C}} \mathrm{d}x^\mu\, A^a_\mu(x)t^a\right), \tag{2.6}$$

where $\mathcal{P}$ indicates path ordering. Here we have introduced the *connection* $A^a_\mu(x)$ and the (matrix valued) *gauge field* $A^a_\mu(x)t^a$ which transforms according to

$$A^a_\mu(x)t^a \to V(x)\left(A^a_\mu(x)t^a + \frac{i}{g}\partial_\mu\right)V^\dagger(x). \tag{2.7}$$

Using this relation, one can indeed show that the explicit forms of the comparator we found in Eqs. (2.5) and (2.6) fulfill the transformation behavior from Eq. (2.3). Substituting the expansion for the comparator in Eq. (2.4), we find the explicit form for covariant derivative

$$D_\mu = \partial_\mu - igA^a_\mu t^a.$$

Consequently, if we replace the derivative in the kinetic term of Eq. (2.1) with the covariant derivative D_μ, the resulting Lagrangian is invariant under local symmetry transformations.

Up to now, $A^a_\mu(x)$ is not a dynamical variable. In order to introduce dynamics, we have to add an invariant term to the Lagrangian containing the connection and its derivatives. In analogy to the Abelian case, one finds for the *non-Abelian field strength tensor* the expression [4, 104]

$$F^a_{\mu\nu} = \partial_\mu A^a_\nu - \partial_\nu A^a_\mu + g f^{abc} A^b_\mu A^c_\nu. \tag{2.8}$$

This quantity is, however, not gauge invariant, as it carries an index of the Lie algebra, and, contrary to the Abelian case, it contains a self-interaction term between the gauge fields. To obtain a kinetic term for the gauge field from this quantity, one has to form a gauge invariant combination. The simplest one is given by the *classical Yang-Mills Lagrangian density* [4, 104]

$$\mathcal{L}_{\mathrm{YM}} = -\frac{1}{2}\mathrm{tr}\left(\left(F^{a,\mu\nu}t^a\right)\left(F^b_{\mu\nu}t^b\right)\right) = -\frac{1}{4}F^{a,\mu\nu}F^a_{\mu\nu}, \tag{2.9}$$

where the trace is understood in group space. The classical Lagrangian density including the fermions and the gauge part hence reads [104, 107]

$$\mathcal{L} = \overline{\psi}(x)\left(i\gamma^\mu D_\mu - m\right)\psi(x) + \mathcal{L}_{\mathrm{YM}}. \tag{2.10}$$

Notice that there is no mass term for the gauge field present as due to the transformation behavior of $A^a_\mu(x)t^a$ from Eq. (2.7) such a term would not be

gauge invariant and, thus, cannot appear in the Lagrangian density. Hence, the Lagrangian from Eq. (2.10) describes the interaction of massive fermions mediated by massless gauge bosons.

Before we consider the equations of motion and continue to present the Hamiltonian formulation let us make a few remarks:

1. The derivation above shows the geometrical origin of the (matrix-valued) gauge field $A^a_\mu(x)t^a$ which arises due to the local symmetry and the necessity to introduce the comparator to obtain a sensible derivative.

2. The structure constants of the group appear in Eq. (2.8) and, hence, determine the form of the self interaction. In particular, one can see that for Abelian groups the self interaction is absent. Moreover, the interaction term for the gauge field and the fermion field contains the covariant derivative which depends on the (adjoint) representation of the Lie algebra. Thus, it is also affected by the structure of the gauge group. As a consequence, the symmetry group has a decisive influence on the form of the interactions in the theory.

The Euler-Lagrange equations for Eq. (2.10) are given by [104]:

$$\begin{aligned} \left(i\gamma^\mu D_\mu - m\right)\psi(x) &= 0, \\ \partial^\mu F^a_{\mu\nu}(x) + g f^{abc} A^{b,\mu}(x) F^c_{\mu\nu}(x) &= -g\overline{\psi}(x)\gamma_\nu t^a \psi(x). \end{aligned} \tag{2.11}$$

The first equation for the fermion field is simply the Dirac equation in an external field. The second set of equations contain the non-Abelian generalization of Gauss' law (temporal component) and Ampère's law (spatial components).

In the context of quantum simulation and TN, which we are exploring in the later part of the thesis, it is more convenient to work with the Hamiltonian formulation. The Hamiltonian can be obtained from Eq. (2.10) by computing the Legendre transformation. The canonical momenta are given by the following functional derivatives of the classical Lagrangian density [103, 108–110]

$$\pi^\ell_F = \frac{\delta\mathcal{L}}{\delta(\partial_0\psi^\ell(x))} = i\psi^{\dagger\ell}(x),\ \pi^{a,0} = \frac{\delta\mathcal{L}}{\delta(\partial_0 A^a_0(x))} = 0,\ \pi^{a,k} = \frac{\delta\mathcal{L}}{\delta(\partial_0 A^a_k(x))} = F^{a,k0}(x), \tag{2.12}$$

where $k = 1, 2, 3$ refers to the spatial indices of the gauge field. Hence, we find

for the *classical Hamiltonian* [103, 108]

$$\begin{aligned} H &= \int \mathrm{d}^3\mathbf{x}\,\left(\pi_F^\ell(\mathbf{x})\partial_0\psi^\ell(\mathbf{x}) + \pi^{a,k}(\mathbf{x})\partial_0 A_k^a(\mathbf{x}) - \mathcal{L}\right) \\ &= \int \mathrm{d}^3\mathbf{x}\,\psi^\dagger(\mathbf{x})\Big(-i\boldsymbol{\alpha}\boldsymbol{\nabla} + g\boldsymbol{\alpha}\mathbf{A}(\mathbf{x}) + \gamma^0 m\Big)\psi(\mathbf{x}) \\ &\quad + \int \mathrm{d}^3\mathbf{x}\,\left(-\frac{1}{2}\pi^{a,k}(\mathbf{x})\pi_k^a(\mathbf{x}) + \frac{1}{4}F^{a,kj}(\mathbf{x})F_{kj}^a(\mathbf{x})\right) \\ &\quad - \int \mathrm{d}^3\mathbf{x}\,A_0^a(\mathbf{x})\Big(\partial^k F_{k0}^a(\mathbf{x}) + gf^{abc}A^{b,k}(\mathbf{x})F_{k0}^c(\mathbf{x}) + g\psi^\dagger(\mathbf{x})t^a\psi(\mathbf{x})\Big). \end{aligned}$$

Since the Hamiltonian formulation is no longer Lorentz invariant, we distinguish explicitly between the temporal and spatial components (labeled by k, j), and we omit the time arguments for all fields. Moreover, we have introduced the vectors $\boldsymbol{\alpha}$ and $\mathbf{A}(\mathbf{x})$ consisting of the components $\gamma^0\gamma^k$ and $A^{a,k}(\mathbf{x})t^a$. From the Hamiltonian, we can again find the equations of motion by taking the functional derivatives with respect to the generalized positions and momenta.

Up to know, we have considered a purely classical theory. To quantize it, we can impose the canonical equal-time (anti) commutation relations between the fields and the conjugate momenta. Equation (2.12) reveals, however, that $\pi^{a,0} = 0$ and hence the commutation relation with the conjugate temporal component of the gauge field cannot be nontrivial. One way of avoiding this problem is making use of gauge freedom and setting the temporal components of the gauge field to zero, $A_0^a = 0$, which is known as *temporal* or *Weyl gauge* [108, 109, 111]. Thus, imposing

$$\begin{gathered} \{\psi^a(\mathbf{x}), \psi^{\dagger b}(\mathbf{y})\} = \delta(\mathbf{x}-\mathbf{y})\delta_{ab}, \qquad \{\psi^a(\mathbf{x}), \psi^b(\mathbf{y})\} = 0, \\ [A_k^a(\mathbf{x}), \pi_j^b(\mathbf{y})] = i\delta_{ab}\delta_{kj}\delta(\mathbf{x}-\mathbf{y}), \qquad [A_k^a(\mathbf{x}), A_j^b(\mathbf{y})] = 0, \qquad [\pi_k^a(\mathbf{x}), \pi_j^b(\mathbf{y})] = 0, \end{gathered} \tag{2.13}$$

yields the *quantized Hamiltonian*

$$\begin{aligned} H &= \int \mathrm{d}^3\mathbf{x}\,\psi^\dagger(\mathbf{x})\Big(-i\boldsymbol{\alpha}\boldsymbol{\nabla} + g\boldsymbol{\alpha}\boldsymbol{A}(x) + \gamma^0 m\Big)\psi(\mathbf{x}) \\ &\quad + \int \mathrm{d}^3\mathbf{x}\,\left(-\frac{1}{2}\pi^{a,k}(\mathbf{x})\pi_k^a(\mathbf{x}) + \frac{1}{4}F^{a,kj}(\mathbf{x})F_{kj}^a(\mathbf{x})\right). \end{aligned} \tag{2.14}$$

As a result of the choice of gauge, we cannot take the functional derivative with respect to the temporal component of the gauge field anymore. Thus, we do not recover the quantized version of Gauss' law from the Hamiltonian and it has to be added as an additional constraint imposed on the physical states, $|\Psi\rangle$, of the Hamiltonian

$$G^a(\mathbf{x})|\Psi\rangle = q^a(\mathbf{x})|\Psi\rangle, \qquad G^a(\mathbf{x}) = \partial^k F_{k0}^a(\mathbf{x}) + gf^{abc}A^{b,k}(\mathbf{x})F_{k0}^c(\mathbf{x}) + \rho^a(\mathbf{x}).$$

In the expression above $\rho^a(\mathbf{x}) = g\psi^\dagger(\mathbf{x})t^a\psi(\mathbf{x})$ are the (non-Abelian) charge density components and $q^a(\mathbf{x})$ can be interpreted as the components of an external, static charge density distribution. It is easy to see that for non-Abelian groups the Gauss law components fulfill the commutation relation [108, 111]

$$\left[G^a(\mathbf{x}), G^b(\mathbf{y})\right] = igf^{abc}G^c(\mathbf{x})\delta(\mathbf{x}-\mathbf{y})$$

and hence cannot be diagonalized simultaneously. However, they all commute with the Hamiltonian from Eq. (2.14) and, thus, are conserved. The choice $A_0^a = 0$ does not fix the gauge completely and we can still apply time-independent gauge transformations. As one can show, the Gauss Law components are the *generators* for such *time-independent gauge transformations*.

The pure gauge part of the Hamiltonian in the second line of Eq. (2.14) can be cast to a more familiar form. If we interpret the spatial components $A^{a,k}(\mathbf{x})$ of the gauge field for a fixed color index as the components of a vector potential, $\mathbf{A}^a(\mathbf{x})$, we can define the color-electric and color-magnetic field as [108, 111]

$$\mathbf{E}^a(\mathbf{x}) = -\partial_t\mathbf{A}^a(\mathbf{x}), \qquad \mathbf{B}^a(\mathbf{x}) = \nabla\times\mathbf{A}^a(\mathbf{x}) - \frac{1}{2}gf^{abc}\mathbf{A}^b(\mathbf{x})\times\mathbf{A}^c(\mathbf{x}).$$

With this definition, we can rewrite the Yang-Mills part of the Hamiltonian as $H_{\text{el}} + H_{\text{mag}}$ with

$$H_{\text{el}} = \frac{1}{2}\int \mathrm{d}^3\mathbf{x}\ \mathbf{E}^a(\mathbf{x})\mathbf{E}^a(\mathbf{x}), \tag{2.15}$$

$$H_{\text{mag}} = \frac{1}{2}\int \mathrm{d}^3\mathbf{x}\ \mathbf{B}^a(\mathbf{x})\mathbf{B}^a(\mathbf{x}), \tag{2.16}$$

the color-electric and color-magnetic energy contributions.

Let us briefly mention that it is also possible to quantize the theory using functional integrals. In this approach the quantum theory is obtained by superposing all field configurations weighted with the classical action of the corresponding path, $\exp(iS)$, $S = \int \mathrm{d}^4x\,\mathcal{L}$. Ground state expectation values for an observable O can then be formally obtained from the functional integral expression [104, 112]

$$\langle O\rangle = \frac{1}{\mathcal{Z}}\int \mathcal{D}A\mathcal{D}\psi\mathcal{D}\overline{\psi}\,O\exp(iS) \tag{2.17}$$

with $\mathcal{Z} = \int \mathcal{D}A\mathcal{D}\psi\mathcal{D}\overline{\psi}\exp(iS)$ the "partition function" of the system. In particular, if one applies a Wick rotation, $t\to -i\tau$, to Eq. (2.17) and looks at its formulation in Euclidean space-time, one can see that the expression is formally analogous to the one obtained for expectation values in statistical mechanics. This analogy is one of the key ingredients which have led to the great success of LGT, as it allows us to apply sophisticated Monte Carlo methods after discretizing the theory on a space-time lattice [112]. The discretization procedure is discussed in the following Section.

2.2 Lattice formulation

From the continuum theory, reviewed in the previous Section, we would now like to go to a discretized lattice formulation. Originally pioneered by Wilson starting from the path integral formulation [8], the theory is formulated on a discretized space-time lattice in such a way that the gauge symmetry is preserved and the continuum model is recovered in the limit of vanishing lattice spacing. Shortly after Wilson's proposal, Kogut and Susskind showed how to obtain a discretized version of the Hamiltonian formulation [9]. In this Section we introduce the basics of the lattice Hamiltonian formulation, as this is the framework better suited for quantum simulation and TN.

2.2.1 The doubling problem

Looking at Eq. (2.14) a discretized formulation for the Hamiltonian might seem straightforward: one could simply introduce a spatial lattice, discretize the fields and approximate the derivatives with finite differences. However, this naive discretization fails to reproduce the correct continuum limit even in the simplest case of free, massless fermions in 1+1 dimensions, as we illustrate in the following.

The Hamiltonian for free massless fermions in 1+1 dimensions is given by

$$H = \int \mathrm{d}x\, \psi^\dagger(x)\left(-i\gamma^0\gamma^1\partial_x\right)\psi(x) \tag{2.18}$$

and the equation of motion obtained via $i\partial_t\psi(x) = [\psi(x), H]$ is simply the Dirac equation

$$\partial_t\psi(x) = -\gamma^0\gamma^1\partial_x\psi(x). \tag{2.19}$$

It can be easily solved using the plain wave ansatz $\psi(x) = \exp(i(Et - px))\,u(p,E)$ where $u(p,E)$ is a two component spinor. If we choose the Weyl representation for the Dirac matrices [113],

$$\gamma^0 = \begin{pmatrix} 0 & 1 \\ 1 & 0 \end{pmatrix}, \qquad \gamma^1 = \begin{pmatrix} 0 & -1 \\ 1 & 0 \end{pmatrix}, \qquad \gamma^5 = \gamma^0\gamma^1 = \begin{pmatrix} 1 & 0 \\ 0 & -1 \end{pmatrix},$$

the equations for the different components of the spinor decouple and we obtain the trivial eigenvalue problem

$$\begin{pmatrix} p & 0 \\ 0 & -p \end{pmatrix} u(p,E) = E\,u(p,E)$$

from which we find the usual dispersion relation for relativistic particles, $E = \pm p$, with the corresponding eigenvectors $u_\pm(p,E)$. Due to our choice of the

Dirac matrices, it is apparent that the two solutions are eigenstates of γ^5, $\gamma^5 u_\pm(p,E) = \pm u_\pm(p,E)$, thus they have a well defined chirality of ± 1. Moreover, the group velocity for the two solutions is simply $\partial E/\partial p = \pm 1$. As a consequence, the eigenstates with positive chirality correspond to right moving fermions and antifermions, whereas the eigenstates with negative chirality correspond to left moving ones [114, 115].

Let us now look at the same problem after discretizing space on a lattice with spacing a and replacing the continuous position by na, $n \in \mathbb{Z}$. To obtain a proper discretization which approaches the continuum formulation in the naive continuum limit,[2] $a \to 0$, we make the replacements

$$\psi(x) \to \hat{\psi}_n/\sqrt{a}, \qquad \partial_x \psi(x) \to \frac{1}{2a^{3/2}}\left(\hat{\psi}_{n+1} - \hat{\psi}_{n-1}\right), \qquad \int \mathrm{d}x \to a\sum_n,$$

where we have chosen the symmetric finite difference for approximating the derivative to obtain a hermitian lattice version of the Dirac operator. The resulting lattice Hamiltonian reads

$$\hat{H} = \sum_n \hat{\psi}_n^\dagger \left(-i\gamma^0\gamma^1 \frac{1}{2a}\left(\delta_{k,n+1} - \delta_{k,n-1}\right)\right)\hat{\psi}_k$$

from which we can again get the equation of motion for the discretized spinor via $i\partial_t \hat{\psi}_n = [\hat{\psi}_n, \hat{H}]$, yielding

$$\partial_t \hat{\psi}_n = -\gamma^0\gamma^1 \frac{1}{2a}\left(\hat{\psi}_{n+1} - \hat{\psi}_{n-1}\right).$$

To solve the equation, we use the lattice version of the ansatz before, $\hat{\psi}_n = \exp\left(i(Et - pna)\right)\hat{u}(p,E)$, again resulting in the trivial eigenvalue equation

$$\begin{pmatrix} \sin(pa)/a & 0 \\ 0 & -\sin(pa)/a \end{pmatrix}\hat{u}(p,E) = E\hat{u}(p,E),$$

with the momentum restricted to the first Brillouin zone $-\pi/a \le p \le \pi/a$, as the lattice provides a cutoff and $\exp(-i(p + 2\pi/a)na) = \exp(-ipna)$. The two solutions $\hat{u}_\pm(p,E)$, which in turn are eigenstates of the chirality operator γ^5, have different to the continuous case the dispersion $E = \pm\bar{p}$ with $\bar{p} = \sin(pa)/a$ (cf. Fig. 2.1). Comparing the lattice dispersion to the continuum one, we observe that for $p = \pm\pi/a$ additional low energy states appear in the spectrum.

[2] We call the continuum limit, $a \to 0$, for the lattice Hamiltonian the naive continuum limit. As we are going to see, the fact that we recover the continuum Hamiltonian from the discretized one in the limit of vanishing lattice spacing does not necessarily mean that the physics of the lattice theory approaches the one of the continuum model one tried to discretize.

Expanding the lattice dispersion around the low-energy regions and looking at the corresponding group velocity, we find

$$E \approx \begin{cases} \pm p & \text{for } p \text{ close to } 0 \\ \mp p \pm \frac{\pi}{a} & \text{for } p \text{ close to } \pm\pi/a \end{cases} \quad \Rightarrow \quad \frac{\partial E}{\partial p} \approx \begin{cases} \pm 1 & \text{for } p \text{ close to } 0 \\ \mp 1 & \text{for } p \text{ close to } \pm\pi/a. \end{cases} \tag{2.20}$$

Consequently, for a given energy we find two solutions for each chirality, a left moving one and a right moving one [114, 115], as it is illustrated in Fig. 2.1. These additional contributions, caused by the zeros of the dispersion at edges of the Brillouin zone, do not vanish in the continuum limit $a \to 0$. Hence, our naive lattice discretization corresponds to two flavors of Dirac fermions in the continuum theory. In general, if we discretize the Dirac theory in d spatial dimensions following the same scheme, there occur 2^d zeros in the region of nonegative momenta of the first Brillouin zone, of which $2^d - 1$ yield unwanted contributions. Since the number of contributions doubles with each dimension, this is called the *doubling problem*.

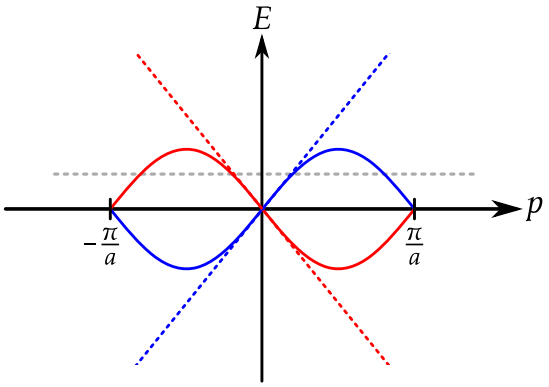

Figure 2.1: Dispersion relation obtained from the continuum Dirac equation (dashed blue and red lines) and the lattice discretization (solid blue and red lines) in the first Brillouin zone. The red lines correspond to the solution with chirality +1, the blue ones to the solution with chirality −1. The dashed horizontal line shows that for a given energy smaller then the maximum one allowed by the cutoff, the lattice formulation yields two solutions for each chirality. One of these solutions corresponds to right moving particles (intersection in the region of positive slope) and one to left moving particles (intersection in the region with negative slope).

Obviously this poses the question if the doubling problem is an artifact of the lattice discretization we have chosen and can be avoided. It was shown in series of works by Nielsen and Ninomiya [116–119] that any local, translationally invariant, hermitian lattice formulation of a chiral fermion gives rise to an

equal number of left and right movers. Thus, one cannot find a local, translational invariant, hermitian lattice formulation of Eq. (2.14) preserving the chiral symmetry for the case of massless fermions which avoids the doubling problem.

To circumvent the doubling problem, one has to violate one of the prerequisites of the Nielsen-Ninomiya theorem. One solution, presented by Wilson, is to break the chiral symmetry explicitly by adding a term to the action which prevents the zeros at the boundary of the Brillouin zone and vanishes in the continuum limit. The same mechanism of avoiding the doublers is used when introducing *Wilson twisted mass fermions* which have certain other interesting feature with respect to the standard Wilson fermions [120]. A different (partial) solution are the *staggered fermions* [9, 114, 121, 122], where the fermionic degrees of freedom are "thinned out" to avoid the doubling problem. A solution, which preserves at least a lattice version of the chiral symmetry are the *Ginsparg-Wilson fermions* [123, 124]. *Minimally doubled fermions* [125], originally introduced by Karsten and Wilczek [126, 127] and in a different variant suggested by Boriçi and Creutz [128, 129], also preserve the chiral symmetry while reducing the doublers to two degenerate flavors in the continuum. The doubling problem can also be avoided at the expense of locality which is for example the case for *SLAC fermions* [130] or *perfect lattice fermions* [131, 132]. *Domain wall fermions* [133–135] circumvent the doubler solutions by introducing an additional dimension which separates solutions of different chirality. Here we focus on staggered fermions which we are going to discuss in the next Section.

2.2.2 The Kogut-Susskind Hamiltonian formulation

Staggered fermions

One possible way of (partially) removing the doubler solutions, which turns out to be convenient in the context of quantum simulation and TN, are the *Kogut-Susskind staggered fermions* [9, 114, 121, 122]. To illustrate the method, let us again start with the 1+1 dimensional case. The lattice Hamiltonian we consider is [114, 121]

$$\hat{H} = -\frac{i}{2a}\sum_n \left(\hat{\phi}_n^\dagger \hat{\phi}_{n+1} - \hat{\phi}_{n+1}^\dagger \hat{\phi}_n\right), \tag{2.21}$$

where, contrary to our naive discretization approach, on every site n there is only a *single component fermionic field*, $\hat{\phi}_n$, which fulfills the usual anticommutation relations, $\{\hat{\phi}_n, \hat{\phi}_m\} = 0$, $\{\hat{\phi}_n^\dagger, \hat{\phi}_m\} = \delta_{mn}$. The equation of motion for this case is given by

$$\partial_t \hat{\phi}_n = \frac{1}{2a}\left(\hat{\phi}_{n+1} - \hat{\phi}_{n-1}\right),$$

which is exactly the equation we have found for the lower component of the spinor in our naive discretization approach. Hence, the solution corresponds to the red branch of the dispersion shown in Fig. 2.1 and we obtain a single left and a single right moving solution. Looking at the equation of motion, it is apparent that the time derivative for the even sites is determined by the odd sites, and vice versa. To make this more apparent, we relabel the field $\hat{\phi}_n$ as $\hat{\psi}_{\mathrm{u},n}$ for even n and $\hat{\psi}_{\mathrm{l},n}$ for odd n, and the equation of motion can be written as

$$\partial_t \hat{\psi}_{\mathrm{u},n} = \frac{1}{2a}\left(\hat{\psi}_{\mathrm{l},n+1} - \hat{\psi}_{\mathrm{l},n-1}\right), \qquad \partial_t \hat{\psi}_{\mathrm{l},n} = \frac{1}{2a}\left(\hat{\psi}_{\mathrm{u},n+1} - \hat{\psi}_{\mathrm{u},n-1}\right).$$

Taking the naive continuum limit, $a \to 0$, of these equations, we recover the Dirac equation (2.19) if we choose the representation

$$\gamma^0 = \begin{pmatrix} 1 & 0 \\ 0 & -1 \end{pmatrix}, \qquad \gamma^1 = \begin{pmatrix} 0 & 1 \\ -1 & 0 \end{pmatrix}, \qquad \gamma^0\gamma^1 = \begin{pmatrix} 0 & 1 \\ 1 & 0 \end{pmatrix},$$

for the Dirac matrices and identify the continuum limit of $\hat{\psi}_{\mathrm{u},n}$ ($\hat{\psi}_{\mathrm{l},n}$) with the upper (lower) component of the Dirac spinor [114, 121]:

$$\lim_{a\to 0} \begin{pmatrix} \hat{\psi}_{\mathrm{u},n}/\sqrt{a} \\ \hat{\psi}_{\mathrm{l},n}/\sqrt{a} \end{pmatrix} \to \begin{pmatrix} \psi_1(x) \\ \psi_2(x) \end{pmatrix} = \psi(x).$$

Moreover, it is straightforward to see that with this identification, we recover the Dirac Hamiltonian from our lattice formulation. Using the relabeling of $\hat{\phi}_n$, the lattice Hamiltonian reads

$$\begin{aligned} \hat{H} &= -\frac{i}{2a} \sum_{n \text{ even}} \left(\hat{\psi}^\dagger_{\mathrm{u},n}\left(\hat{\psi}_{\mathrm{l},n+1} - \hat{\psi}_{\mathrm{l},n-1}\right) + \hat{\psi}^\dagger_{\mathrm{l},n+1}\left(\hat{\psi}_{\mathrm{u},n+2} - \hat{\psi}_{\mathrm{u},n}\right)\right) \\ &= -ia \sum_{n \text{ even}} \left(\frac{\hat{\psi}^\dagger_{\mathrm{u},n}}{\sqrt{a}} \frac{1}{2a}\left(\frac{\hat{\psi}_{\mathrm{l},n+1}}{\sqrt{a}} - \frac{\hat{\psi}_{\mathrm{l},n-1}}{\sqrt{a}}\right) + \frac{\hat{\psi}^\dagger_{\mathrm{l},n+1}}{\sqrt{a}} \frac{1}{2a}\left(\frac{\hat{\psi}_{\mathrm{u},n+2}}{\sqrt{a}} - \frac{\hat{\psi}_{\mathrm{u},n}}{\sqrt{a}}\right)\right). \end{aligned}$$

From the rewriting in the last line it is easy to see that in the naive continuum limit this reduces to Eq. (2.18):

$$\begin{aligned} \hat{H} \to H &= -i \int \mathrm{d}x \left(\psi_1^\dagger(x)\partial_x\psi_2(x) + \psi_2^\dagger(x)\partial_x\psi_1(x)\right) \\ &= \int \mathrm{d}x\, \psi^\dagger(x)(-i\gamma^0\gamma^1\partial_x)\psi(x). \end{aligned}$$

The considerations above show that the staggered discretization corresponds to separating the two components of the Dirac spinor to different lattice sites, the upper ones to even sites and the lower ones to odd sites. The resulting lattice fields for the even sites, $\hat{\psi}_{\mathrm{u},n}$, and the odd sites, $\hat{\psi}_{\mathrm{l},n}$, have an effective

lattice spacing of $2a$. As a result, the doubling contributions are removed and one recovers the correct continuum limit.

So far, we have only considered the massless case. To add a mass term, we have to include the lattice analog of

$$\int \mathrm{d}x\, m\overline{\psi}(x)\psi(x) = \int \mathrm{d}x\, m\left(\psi_1^\dagger(x)\psi_1(x) - \psi_2^\dagger(x)\psi_2(x)\right)$$

in Eq. (2.21) which is given by [114]

$$m\left(\sum_{n\ \text{even}} \hat{\psi}_{\mathrm{u},n}^\dagger \hat{\psi}_{\mathrm{u},n} - \sum_{n\ \text{odd}} \hat{\psi}_{\mathrm{l},n}^\dagger \hat{\psi}_{\mathrm{l},n}\right) = m\sum_n (-1)^n \hat{\phi}_n^\dagger \hat{\phi}_n.$$

The staggered formulation can also be generalized to higher dimensions, where again the components of the Dirac spinors are distributed in different sublattices. The Hamiltonian for d spatial dimensions is of the form [9, 114]

$$\hat{H} = \epsilon_d \sum_{\mathbf{n}} \sum_{k=1}^{d} \left(\hat{\phi}_{\mathbf{n}}^\dagger \hat{\phi}_{\mathbf{n}+\mathbf{e}_k} e^{i\theta_k} + \text{h.c.}\right) + m\sum_{\mathbf{n}} (-1)^{\sum_{k=1}^d n_k} \hat{\phi}_{\mathbf{n}}^\dagger \hat{\phi}_{\mathbf{n}} \tag{2.22}$$

where $\mathbf{n} \in \mathbb{Z}^d$ is a lattice vector with components n_k, $\mathbf{e}_k$ is a lattice unit vector pointing in direction k, ϵ_d a dimension dependent prefactor and $\exp(i\theta_k)$ are direction dependent phase factors. In higher dimensions the staggered formulation only leads to a reduction of the doubling solutions and does not remove them completely, for example, in three dimensions one recovers two flavors of Dirac fermions after taking the continuum limit instead of 8 in the naive approach [114].

Up to now we have only considered Dirac spinors with no additional internal degrees of freedom such as color. The staggered formulation also works the same way in that case. Since we are only distributing the Dirac components, the color degrees of freedom stay unaffected and the single component fermionic field at each site, $\hat{\phi}_{\mathbf{n}}$, is simply replaced by a color spinor.

Throughout the rest of this thesis, it will be clear from the context if we refer to lattice quantities or the continuum ones, hence, we drop for all the following the hat we used in this Section to distinguish between both. Moreover, since we are only working with the Kogut-Susskind staggered formulation we call all lattice fermionic fields from now on again $\psi_{\mathbf{n}}$.

Inclusion of the gauge field

Now that we know how to treat fermion fields on the lattice, we would like to find the lattice version of Eq. (2.14). Starting from the staggered Hamiltonian

in Eq. (2.22), it is easy to see that it is again invariant under global symmetry transformations

$$\psi_{\mathbf{n}} \to V\psi_{\mathbf{n}}, \qquad \psi_{\mathbf{n}}^\dagger \to \psi_{\mathbf{n}}^\dagger V^\dagger,$$

where V is some group element. Looking at the lattice version of local symmetry transformations,

$$\psi_{\mathbf{n}} \to V_{\mathbf{n}}\psi_{\mathbf{n}}, \qquad \psi_{\mathbf{n}}^\dagger \to \psi_{\mathbf{n}}^\dagger V_{\mathbf{n}}^\dagger, \tag{2.23}$$

we discover the same problem as already for the continuum theory: the hopping term involves two different lattice sites and hence cannot be invariant under such transformations. In the continuum case, the invariance under local transformations was ensured by introducing the comparator. Looking at Eq. (2.6) we can see that for a directed path between two space-time points it is nothing but a group element. Hence, in the lattice case, we are led to put a group element $U_{\mathbf{n},k}$ on the link going from site $\mathbf{n}$ to $\mathbf{n}+\mathbf{e}_k$ which under gauge transformations transforms as [8]

$$U_{\mathbf{n},k} \to V_{\mathbf{n}} U_{\mathbf{n},k} V_{\mathbf{n}+\mathbf{e}_k}^\dagger \tag{2.24}$$

and $U_{\mathbf{n}+\mathbf{e}_k,-k} = U_{\mathbf{n},k}^\dagger$. In particular, due to the last property, the links are directed objects, as it is illustrated in Fig. 2.2. Since we restricted ourselves to the compact (matrix) Lie groups U(1) and SU(N_c), we can again write $U_{\mathbf{n},k}$ as the exponential of the generators

$$U_{\mathbf{n},k} = \exp\left(i\Lambda_{\mathbf{n},k}^a t^a\right)$$

with $\Lambda_{\mathbf{n},k}^a$ parameters in the group space.[3] For small lattice spacings, we can expand the expression around the identity which yields [8]

$$U_{\mathbf{n},k} = \mathbb{1} + i\Lambda_{\mathbf{n},k}^a t^a + \mathcal{O}\left(\left(\Lambda_{\mathbf{n},k}^a\right)^2\right). \tag{2.25}$$

Comparing this equation to the continuum case in Eq. (2.5), we find the relation

$$\frac{1}{ag}\Lambda_{\mathbf{n},k}^a \to A_k^a(\mathbf{x}) \tag{2.26}$$

between the lattice quantity and the continuum gauge field in the limit of vanishing lattice spacing.

[3] Notice that the $\Lambda_{\mathbf{n},k}^a$ are (hermitian) operators on the physical Hilbert space for the link between sites $\mathbf{n}$ and $\mathbf{n}+\mathbf{e}_k$. Hence, after choosing a representation, $U_{\mathbf{n},k}$ can be interpreted as a matrix whose entries are operators acting on the physical Hilbert space.

Up to now the lattice gauge field is not a dynamical quantity. To generate dynamics we have to add a term corresponding to the canonical momentum of the gauge field to the Hamiltonian which in the continuum case was simply given by its time derivative. To find the corresponding lattice version, let us first consider the Abelian case of U(1) for which the operators $U_{\mathbf{n},k}$ are simply phases on group space, $\exp(i\Lambda_{\mathbf{n},k})$. The conjugate momentum $L_{\mathbf{n},k}$ for the gauge field should, analogously to the continuum case, fulfill

$$[\Lambda_{\mathbf{n},k}, L_{\mathbf{n}',k'}] = i\delta_{kk'}\delta_{\mathbf{n}\mathbf{n}'} \tag{2.27}$$

which implies for its differential representation $L_{\mathbf{n},k} = -i\partial/\partial\Lambda_{\mathbf{n},k}$ [136]. Moreover, from the canonical commutation relation, we find for the commutator between $U_{\mathbf{n},k}$ and $L_{\mathbf{n},k}$

$$[L_{\mathbf{n},k}, U_{\mathbf{n},k}] = U_{\mathbf{n},k}. \tag{2.28}$$

In particular, the expression above shows that $L_{\mathbf{n},k}$ is the *generator of transformations* for the link variables

$$U_{\mathbf{n},k} \to V_{\mathbf{n}} U_{\mathbf{n},k} = U_{\mathbf{n},k} V_{\mathbf{n}},$$

where $V_{\mathbf{n}}$ commutes with $U_{\mathbf{n},k}$ since we are working with the Abelian group U(1). Hence, a suitable candidate for the lattice version of the electric energy is given by

$$H_{\mathrm{el}} = c_{\mathrm{el}} \sum_{\mathbf{n},k} L_{\mathbf{n},k}^2.$$

The constant c_{el} can be determined by requiring that H_{el} reduces to the continuum expression from Eq. (2.15) for vanishing lattice spacing. To this end let us first relate the lattice electric field to the continuum one, $c_L L_{\mathbf{n},k} \to E_k(\mathbf{x})$ with some constant c_L, as we have already done for the gauge field in Eq. (2.26). In order to recover the canonical commutation relation from Eq. (2.13) for $a \to 0$, the lattice analogs of the electric field and the gauge field should fulfill

$$\frac{i}{a^d} = \left[c_L L_{\mathbf{n},k}, \frac{\Lambda_{\mathbf{n},k}}{ag}\right] = \frac{c_L}{ag}[L_{\mathbf{n},k}, \Lambda_{\mathbf{n},k}] = i\frac{c_L}{ag}.$$

Here we have used Eq. (2.27) and that on a regular lattice in d spatial dimensions with spacing a the delta distribution can be discretized as a rectangular function of height $1/a^d$. Thus we find

$$g a^{1-d} L_{\mathbf{n},k} \to E_k(\mathbf{x})$$

and together with the correspondence that for d dimensions $a^d \sum_{\mathbf{n}} \to \int \mathrm{d}^d\mathbf{x}$ in the limit of vanishing lattice spacing, we obtain $c_{\mathrm{el}} = a^{2-d} g^2/2$. For the

Abelian case $L_{\mathbf{n},k}$ can also be rewritten using its differential representation and Eq. (2.28) as [136]

$$L_{\mathbf{n},k} = -i\,(\partial_t U_{\mathbf{n},k})\,U^\dagger_{\mathbf{n},k} = -i\,U^\dagger_{\mathbf{n},k}\,(\partial_t U_{\mathbf{n},k}). \tag{2.29}$$

Let us now turn to the case of SU(N_c). Due to the non-Abelian nature of the group, Eq. (2.29) does not hold anymore, and we have to distinguish between left and right transformations of $U_{\mathbf{n},k}$. To this end, let us define two sets of operators [136]

$$L_{\mathbf{n},k} = -i\,(\partial_t U_{\mathbf{n},k})\,U^\dagger_{\mathbf{n},k}, \qquad R_{\mathbf{n},k} = -i\,U^\dagger_{\mathbf{n},k}\,(\partial_t U_{\mathbf{n},k}).$$

Since we are working with a compact Lie group, we can expand $L_{\mathbf{n},k}$ and $R_{\mathbf{n},k}$ in terms of the generators of the group

$$L_{\mathbf{n},k} = L^a_{\mathbf{n},k} t^a, \qquad R_{\mathbf{n},k} = R^a_{\mathbf{n},k} t^a$$

where $L^a_{\mathbf{n},k}$, $R^a_{\mathbf{n},k}$ are operators on the physical Hilbert space. Using this expansion, one finds for the commutation relations with the entries of $U_{\mathbf{n},k}$ [136]

$$\begin{aligned} \left[L^a_{\mathbf{n},k}, (U_{\mathbf{n}',k'})_{jl}\right] &= \delta_{\mathbf{n}\mathbf{n}'}\delta_{kk'}(t^a)_{ji}(U_{\mathbf{n},k})_{il}, \\ \left[R^a_{\mathbf{n},k}, (U_{\mathbf{n}',k'})_{jl}\right] &= \delta_{\mathbf{n}\mathbf{n}'}\delta_{kk'}(U_{\mathbf{n},k})_{ji}(t^a)_{il}, \end{aligned} \tag{2.30}$$

indeed showing that the set of operators $\{L^a_{\mathbf{n},k}\}$ ($\{R^a_{\mathbf{n},k}\}$) are nothing but the generators of left (right) transformations for $U_{\mathbf{n},k}$. Moreover, they fulfill the algebra of the group [57, 96]

$$\begin{gathered} \left[L^a_{\mathbf{n},k}, L^b_{\mathbf{n}',k'}\right] = -i\delta_{\mathbf{n}\mathbf{n}'}\delta_{kk'}f^{abc}L^c_{\mathbf{n},k}, \quad \left[R^a_{\mathbf{n},k}, R^b_{\mathbf{n}',k'}\right] = i\delta_{\mathbf{n}\mathbf{n}'}\delta_{kk'}f^{abc}R^c_{\mathbf{n},k}, \\ \left[L^a_{\mathbf{n},k}, R^b_{\mathbf{n}',j}\right] = 0. \end{gathered} \tag{2.31}$$

From the definition of $L_{\mathbf{n},k}$ and $R_{\mathbf{n},k}$ it is apparent that

$$L_{\mathbf{n},k} = U_{\mathbf{n},k}R_{\mathbf{n},k}U^\dagger_{\mathbf{n},k}, \qquad R_{\mathbf{n},k} = U^\dagger_{\mathbf{n},k}L_{\mathbf{n},k}U_{\mathbf{n},k}, \tag{2.32}$$

and, thus, $\mathrm{tr}(L^2_{\mathbf{n},k}) = \mathrm{tr}(R^2_{\mathbf{n},k})$ where the trace is understood in group space. Hence, a suitable candidate for the lattice analog to the color-electric energy from Eq. (2.15) is given by

$$H_{\mathrm{el}} = \frac{a^{2-d}g^2}{2}\sum_{\mathbf{n},k}\mathrm{tr}(L^2_{\mathbf{n},k}) = \frac{a^{2-d}g^2}{2}\sum_{\mathbf{n},k}\sum_a L^a_{\mathbf{n},k}L^a_{\mathbf{n},k} = \frac{a^{2-d}g^2}{2}\sum_{\mathbf{n},k}\mathbf{J}^2_{\mathbf{n},k},$$

where we have used the expansion in terms of the generators of the group and defined the Casimir operator $\mathbf{J}^2_{\mathbf{n},k} = \sum_a L^a_{\mathbf{n},k}L^a_{\mathbf{n},k} = \sum_a R^a_{\mathbf{n},k}R^a_{\mathbf{n},k}$. The operators

$L^a_{\mathbf{n},k}$ and $R^a_{\mathbf{n},k}$ can be interpreted as the components of the left and right color-electric field on a gauge link (see Fig. 2.2).

Besides the color-electric contribution, we also would like to add the lattice analog to the color-magnetic field to the Hamiltonian. Hence, we are looking for a pure gauge term that reduces in the limit of vanishing lattice spacing to Eq. (2.16). A possible term we can add to the Hamiltonian is the trace of a product of the matrices $U_{\mathbf{n},k}$ around a closed loop. Locality leads us to take the smallest loops possible, which are plaquettes on the lattice (see Fig. 2.2). Thus a suitable candidate for the lattice analog of the magnetic part is [112]

$$H_{\text{mag}} = c_{\text{mag}} \sum_{\square_p} \left(1 - \frac{1}{2}\left(\text{tr}\left(U_p\right) + \text{h.c.}\right)\right),$$

with a constant c_{mag}. The $\sum_{\square_p}$ indicates a sum over all possible plaquette terms given by

$$U_p = U_{\mathbf{n},k} U_{\mathbf{n}+\mathbf{e}_k,j} U_{\mathbf{n}+\mathbf{e}_k+\mathbf{e}_j,-k} U_{\mathbf{n}+\mathbf{e}_j,-j} = U_{\mathbf{n},k} U_{\mathbf{n}+\mathbf{e}_k,j} U^\dagger_{\mathbf{n}+\mathbf{e}_j,k} U^\dagger_{\mathbf{n},j}.$$

To see that the naive continuum limit of this expression reduces to the color-magnetic energy contribution let us expand the group parameters for small lattice spacing [115]

$$\begin{aligned}
\Lambda^a_{\mathbf{n}+\mathbf{e}_k,j} &= \Lambda^a_{\mathbf{n},j} + a\partial_k \Lambda^a_{\mathbf{n},j} + \mathcal{O}(a^2) \\
\Lambda^a_{\mathbf{n}+\mathbf{e}_j,k} &= \Lambda^a_{\mathbf{n},k} + a\partial_j \Lambda^a_{\mathbf{n},k} + \mathcal{O}(a^2).
\end{aligned}$$

Plugging this back into the expression for the plaquette terms, using the Baker-Campbell-Hausdorff identity and the algebra of the group generators we find [115]

$$\begin{aligned}
U_p &\approx \text{tr}\left(e^{ia\left(\partial_j \Lambda^a_{\mathbf{n},k} - \partial_k \Lambda^a_{\mathbf{n},j}\right) t^a + i f^{abc} \Lambda^b_{\mathbf{n},k} \Lambda^c_{\mathbf{n},j} t^a}\right) \\
&\approx 1 + \frac{1}{4}\left(ia\left(\partial_j \Lambda^a_{\mathbf{n},k} - \partial_k \Lambda^a_{\mathbf{n},j}\right) + i f^{abc} \Lambda^b_{\mathbf{n},k} \Lambda^c_{\mathbf{n},j}\right)^2 \\
&= 1 - \frac{1}{4} a^4 g^2 \left(\partial_j \frac{\Lambda^a_{\mathbf{n},k}}{ag} - \partial_k \frac{\Lambda^a_{\mathbf{n},j}}{ag} + g f^{abc} \frac{\Lambda^b_{\mathbf{n},k}}{ag} \frac{\Lambda^c_{\mathbf{n},j}}{ag}\right)^2,
\end{aligned}$$

where we have expanded the exponential up to second order and used that the generators are traceless and normalized according to Eq. (2.2) in the second line and merely rewritten the expression in the third line. Looking at the correspondence between $\Lambda^a_{\mathbf{n},k}$ and the continuum gauge field in Eq. (2.26), we see that the expression in brackets reduces to $F^{a,kj} F^a_{kj}$. Thus, if we choose $c_{\text{mag}} = a^{d-4}/g^2$, H_{mag} approaches the continuum expression for the magnetic contribution to Hamiltonian in the limit of vanishing lattice spacing.

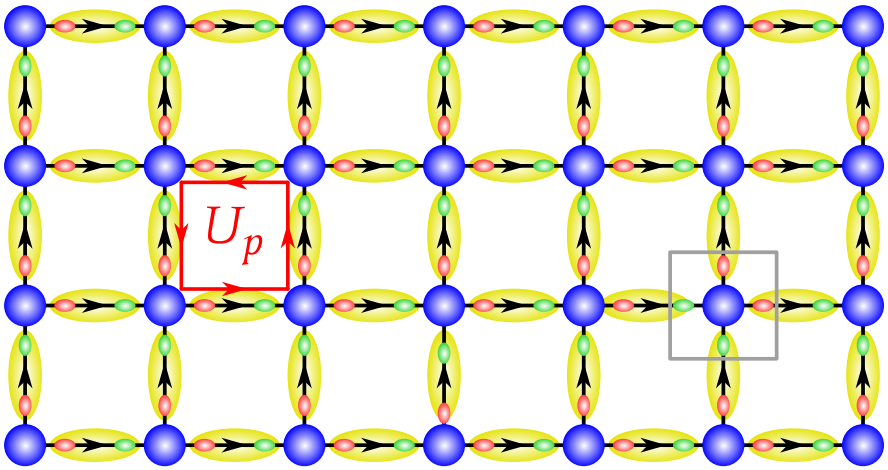

Figure 2.2: Illustration of a two dimensional lattice. The fermionic fields are located at the vertices of the lattice indicated by blue circles. The black lines are the gauge links connecting two vertices, where the arrows indicate the orientation. The yellow ovals indicate where the entries of the matrices U_n act. The light red (green) oval corresponds to the left (right) electric field on a link. The red square illustrates a plaquette term, where the arrows indicate along which direction the links are traversed. The gray square shows an example of a vertex and the associated left and right electric fields where the generators for gauge transformations act.

Taking all the different contributions together, we obtain the final form of the *gauge invariant lattice Hamiltonian* which reads

$$\begin{aligned} H =& \epsilon_d \sum_{\mathbf{n},k} \left(\psi^\dagger_{\mathbf{n}} U_{\mathbf{n},k} \psi_{\mathbf{n}+\mathbf{e}_k} e^{i\theta_k} + \text{h.c.} \right) + m \sum_{\mathbf{n}} (-1)^{\sum_k n_k} \psi^\dagger_{\mathbf{n}} \psi_{\mathbf{n}} \\ &+ \frac{a^{d-4}}{g^2} \sum_{\square_p} \left(1 - \frac{1}{2} \left(\text{tr}\left(U_p \right) + \text{h.c.} \right) \right) + \frac{a^{2-d} g^2}{2} \sum_{\mathbf{n},k} \mathbf{J}_{\mathbf{n},k}. \end{aligned} \tag{2.33}$$

Besides the Hamiltonian we still need to find the discretized form of the generators for gauge transformations. In the derivation above we have already seen that due to Eq. (2.30) the operators $L^a_{\mathbf{n}}$ and $R^a_{\mathbf{n}}$ are the generators of left and right transformations for $U_{\mathbf{n},k}$. Similarly, since we are working with compact Lie groups, we can also define generators $Q^a_{\mathbf{n}}$ for the transformation of the fermion fields from Eq. (2.23) which can be interpreted as dynamical charges [57]. Consequently, the generators for time-independent gauge transformations, and thus components of the *lattice version of Gauss' law*, are given by

$$G^a_{\mathbf{n}} = \sum_{\mathbf{e}_k \text{ outgoing from site } \mathbf{n}} L^a_{\mathbf{n},k} - \sum_{\mathbf{e}_k \text{ ingoing to site } \mathbf{n}} R^a_{\mathbf{n}-\mathbf{e}_k,k} - Q^a_{\mathbf{n}}, \tag{2.34}$$

where $Q^a_{\mathbf{n}}$ acts on the vertex $\mathbf{n}$ and the operators $L^a_{\mathbf{n},k}$ and $R^a_{\mathbf{n}-\mathbf{e}_k,k}$ on the left and right electric field on the links surrounding the vertex (see also Fig. 2.2). Since the Hamiltonian is by construction gauge invariant, it commutes with the generators of gauge transformations, $[H, G^a_{\mathbf{n}}] = 0\ \forall \mathbf{n}, a$. Thus, the physical states, $|\Psi\rangle$, of the lattice Hamiltonian from Eq. (2.33) are eigenstates of the generators for gauge transformations

$$G^a_{\mathbf{n}}|\Psi\rangle = q^a_{\mathbf{n}}|\Psi\rangle \qquad \forall a, \mathbf{n}$$

where $\{q^a_{\mathbf{n}}\}$ can be interpreted as a static, external charge distribution.[4] As a result, the physical Hilbert space of the theory decomposes into the direct sum of sectors with different static charge configuration $\{q^a_{\mathbf{n}}\}$.

Notice that in the derivation above we argued how the gauge invariant lattice formulation should look like on the basis of recovering the continuum Hamiltonian from Eq. (2.14) in the limit of vanishing lattice spacing. However, there is a great amount of freedom involved and one could in principle add more or different terms to the Hamiltonian without changing the naive continuum limit. This freedom can be exploited to obtain improved Hamiltonians for which the discretization errors decay faster [137, 138].

Our presentation of the lattice formulation focused on the Hamiltonian framework, as it is the more natural one to work with in the context of TN and quantum simulation. However, it is of course possible to obtain a lattice formulation for the Lagrangian from Eq. (2.10) in a similar fashion, where the temporal direction is usually discretized, too, as spatial and temporal components are not treated differently in the continuum Lagrangian [8, 105, 112, 115, 139, 140]. Moreover, similar to the continuum case it is also possible to recover the discretized Hamiltonian from the Lagrangian lattice formulation: after taking the continuum limit of the temporal direction and choosing Weyl gauge, a Legendre transformation yields the discretized lattice Hamiltonian [105, 115].

2.3 Examples in 1+1 dimensions

In order to illustrate the discussion above, let us consider some examples with one spatial and one temporal dimension. For that case, there are no transversal directions, hence, there is no magnetic field, which means that there are no plaquette terms in the lattice Hamiltonian.

[4] These external charges are not explicitly considered in the Hamiltonian. Since they are static, they only contribute a constant mass term which leads to an overall shift of the energy scale and thus can be dropped.

2.3.1 The lattice Schwinger model

Let us first look at the lattice formulation of the Schwinger model [101], or QED in 1+1 dimensions, as an example for the Abelian case. Due to the Abelian nature of the group U(1) the structure constants vanish and we only have a single generator which is trivial:

$$f^{abc} = 0, \qquad t^a = 1.$$

Hence, the group elements U_k are simply phases $e^{i\Lambda_k}$, and we choose to work with a compact formulation where Λ_k is restricted to $[0, 2\pi]$. The Kogut-Susskind Hamiltonian for the Schwinger model with F flavors of fermions is given by [121]

$$\begin{aligned} H = &- \frac{i}{2a} \sum_k \sum_{f=1}^{F} \left(\psi_{k,f}^\dagger e^{i\Lambda_k} \psi_{k+1,f} - \text{h.c.} \right) + \sum_k \sum_{f=1}^{F} \left((-1)^k m_f + \kappa_f \right) \psi_{k,f}^\dagger \psi_{k,f} \\ &+ \frac{ag^2}{2} \sum_k L_k^2, \end{aligned} \tag{2.35}$$

where m_f and κ_f are the mass and the chemical potential for flavor f.[5] As we have seen above, for the Abelian case we do not have to distinguish between left and right electric field and the operators L_k and Λ_j fulfill the commutation relation $[\Lambda_j, L_k] = i\delta_{kj}$. Hence, the operator L_k is nothing but the z-component of an angular momentum operator for a quantum rotor with integer eigenvalues and $\exp(i\Lambda_k)$ acts as a rising operator for the electric flux. A suitable basis for the Hamiltonian is thus given by $|n_{1,1}, \ldots, n_{1,F}\rangle \otimes |\ell_1\rangle \otimes |n_{2,1}, \ldots, n_{2,F}\rangle \otimes |\ell_2\rangle \ldots$, where $n_{k,f}$ corresponds to the fermionic occupation for flavor f on site k, and $|\ell_k\rangle$ to an eigenstate of the angular momentum operator acting on link k:

$$L_k|\ell_k\rangle = \ell_k|\ell_k\rangle, \qquad e^{i\Lambda_k}|\ell_k\rangle = |\ell_k + 1\rangle, \qquad \ell_k \in \mathbb{Z}.$$

Notice that the spectrum of the operators L_k is unbounded and given by the entire range of the integers. As a result, the Hilbert space of a single link is already infinite dimensional. The Gauss law from Eq. (2.34) for the Abelian case reads

$$G_k = L_k - L_{k-1} - Q_k, \tag{2.36}$$

where $Q_k = \sum_{f=1}^{F} \left(\psi_{k,f}^\dagger \psi_{k,f} - \frac{1}{2}(\mathbb{1} - (-\mathbb{1})^k) \right)$ is the staggered Abelian charge [57]. The physical states, $|\Psi\rangle$, of the Hamiltonian (2.35) are given by $G_k|\Psi\rangle = q_k|\Psi\rangle$ $\forall k$ where $\{q_k\}$ is an external, static charge distribution.

[5] Notice that for the single-flavor case the density term corresponding to the chemical potential is just a constant energy offset, since due to the global U(1) symmetry of the model the total particle number is conserved. Hence, for the single-flavor case it can be dropped.

In the strong-coupling limit, $g \gg 1$, the electric field term dominates and the hopping can be neglected, hence allowing for an analytical solution of the Hamiltonian. The Gauss law fulfilling ground state in the sector of vanishing external charges is then given by the lattice analog of the Dirac sea with occupied odd sites, empty even sites and the links carrying no flux [121, 141]

$$|\Psi_{\text{sc}}\rangle = |\mathbf{1},\dots,\mathbf{1}\rangle \otimes |0\rangle \otimes |\mathbf{0},\dots,\mathbf{0}\rangle \otimes |0\rangle \otimes \dots \,. \tag{2.37}$$

In the expression above, the numbers in bold face represent the fermionic occupation.

For the case of finite systems it is also possible to integrate out the gauge field and to obtain a lattice Hamiltonian directly restricted to the physical subspace of the theory. Assuming open boundary conditions (OBC) and an electric field value of l_0 on the left boundary, the Gauss law can be solved explicitly yielding

$$L_k = l_0 + \sum_{l=1}^{k} (Q_l + q_l).$$

Plugging this back into the Hamiltonian (2.35) for the case of N sites, and applying a residual gauge transformation [141], we obtain

$$\begin{aligned} H = &-\frac{i}{2a} \sum_{k=1}^{N-1} \sum_{f=1}^{F} \left(\psi_{k,f}^{\dagger} \psi_{k+1,f} - \text{h.c.} \right) + \sum_{k=1}^{N} \sum_{f=1}^{F} \left(m_f (-1)^k + \kappa_f \right) \psi_{k,f}^{\dagger} \psi_{k,f} \\ &+ \frac{a g^2}{2} \sum_{k=1}^{N-1} \left(l_0 + \sum_{l=1}^{k} (Q_l + q_l) \right)^2 . \end{aligned} \tag{2.38}$$

Notice that the charge Q_k only depends on the fermionic content of the sites, hence, the gauge field is removed completely in the formulation above. Compared to the original Hamiltonian, the formulation after integrating out the gauge fields is nonlocal.

2.3.2 SU(2) lattice gauge theory

As a second example, let us look at a non-Abelian SU(2) LGT. For this case, we have two "colors" of fermions, hence, at each vertex k there is a two component spinor $\psi_k^{\dagger} = \begin{pmatrix} \psi_{-1/2,k}^{\dagger} & \psi_{1/2,k}^{\dagger} \end{pmatrix}$ taking into account the two different colors.[6] The structure constants are the Levi-Civita symbols ε^{abc}, and the three generators

[6] Here we label the color components $\psi_{l,k}$ of the spinor at vertex k with $l = \pm 1/2$ to make the related z-component of the angular momentum explicit. For simplicity, we sometimes also refer to the different color components as "red" ($l = -1/2$) and "green" ($l = 1/2$) whenever the explicit angular momentum value is not relevant.

for the fundamental representation are essentially given by the Pauli matrices σ^a,

$$f^{abc} = \varepsilon^{abc}, \qquad t^a = \frac{1}{2}\sigma^a, \qquad a \in \{x, y, z\},$$

where the prefactor 1/2 is due to our choice of normalization condition from Eq. (2.2). Thus, the operators U_k are SU(2) matrices whose entries, $(U_k)_{ll'}$, act on the link between the fermionic sites k and $k+1$ and change the corresponding color-electric flux. The Kogut-Susskind Hamiltonian for the SU(2) case reads

$$\begin{aligned} H &= -\frac{i}{2a}\sum_k \left(\psi_k^\dagger U_k \psi_{k+1} - \text{h.c.}\right) + m\sum_k (-1)^k \psi_k^\dagger \psi_k + \frac{ag^2}{2}\sum_k \mathbf{J}_k^2, \\ &= -\frac{i}{2a}\sum_k \sum_{l,l'=-1/2}^{1/2} \left(\psi_{l,k}^\dagger (U_k)_{ll'} \psi_{l',k+1} - \text{h.c.}\right) + m\sum_k \sum_{l=-1/2}^{1/2} (-1)^k \psi_{l,k}^\dagger \psi_{l,k} \\ &\quad + \frac{ag^2}{2}\sum_k \mathbf{J}_k^2, \end{aligned} \tag{2.39}$$

where in the second line we have made the color degrees of freedom explicit. For the SU(2) case, the commutation relations from Eq. (2.31) for the left and right electric field from Eq. (2.31) are nothing but an angular momentum algebra, hence the operators L_k^a and R_k^a correspond to the components of two angular momentum operators. Moreover, the operators U_k can be interpreted as rotation matrices as they are nothing but SU(2) matrices in the fundamental representation. Hence, Eq. (2.32) shows that the two angular momentum operators are related to each other by a rotation and the total angular momentum $\mathbf{J}^2 = \sum_a L^a L^a = \sum_a R^a R^a$ is the same. Consequently, the Hilbert spaces for the gauge links can be described by those of a spherical symmetric quantum rigid rotor with total angular momentum j [9] with the corresponding angular momentum operators for the body-fixed frame (L^a) and the space-fixed inertial frame of reference (R^a). The basis states can be labeled by the total angular momentum, j, and the two z-components ℓ, ℓ' for both frames

$$\mathbf{J}^2|j\ell\ell'\rangle = j(j+1)|j\ell\ell'\rangle, \qquad L^z|j\ell\ell'\rangle = \ell|j\ell\ell'\rangle, \qquad R^z|j\ell\ell'\rangle = \ell'|j\ell\ell'\rangle.$$

The entries of the matrix U then change the angular momentum according to the proper composition rules for angular momenta [9, 142, 143]

$$\begin{aligned} (U)_{ll'}|j\ell\ell'\rangle = \; & C^{\frac{1}{2}\ j\ j-\frac{1}{2}}_{l\ \ell\ l+\ell} C^{\frac{1}{2}\ j\ j-\frac{1}{2}}_{l'\ \ell'\ l'+\ell'} |j-1/2, \ell+l, \ell'+l'\rangle \\ & + C^{\frac{1}{2}\ j\ j+\frac{1}{2}}_{l\ \ell\ l+\ell} C^{\frac{1}{2}\ j\ j+\frac{1}{2}}_{l'\ \ell'\ l'+\ell'} |j+1/2, \ell+l, \ell'+l'\rangle, \end{aligned}$$

where $C^{j_1\ j_2\ J}_{\ell_1\ \ell_2\ M} = \langle J, M | j_1 \ell_1; j_2, \ell_2 \rangle$ are the usual Clebsch-Gordan coefficients for coupling two angular momenta j_1, j_2 to a total angular momentum J. Thus, a suitable basis for addressing the Hamiltonian is $|n_1^{-\frac{1}{2}}, n_1^{\frac{1}{2}}\rangle \otimes |j_1 \ell_1 \ell_1'\rangle \otimes |n_2^{-\frac{1}{2}}, n_2^{\frac{1}{2}}\rangle \ldots$, where n_k^l is the fermionic occupation number for color l at vertex k. The generators for gauge transformations for the SU(2) case are given by

$$G_k^a = L_k^a - R_k^a - Q_k^a, \qquad a \in \{x, y, z\} \tag{2.40}$$

with the non-Abelian charge components $Q_k^a = \sum_{l,l'=-1/2}^{1/2} \frac{1}{2} \psi_{l,k}^\dagger (\sigma^a)_{ll'} \psi_{l',k}$. Again, the physical states, $|\Psi\rangle$, of the Hamiltonian have to be eigenstates of the Gauss law, $G_k^a |\Psi\rangle = q_k^a |\Psi\rangle \ \forall k, a$.

Similar to the Schwinger case, the strong-coupling limit of the Hamiltonian can be solved analytically, as the hopping term can be neglected. The gauge invariant ground state for vanishing external charges is then again given by the lattice analog of the Dirac sea corresponding to odd sites occupied by a fermion of each color, empty even sites and vanishing color flux on the links [144]:

$$|\Psi_{\text{sc}}\rangle = |\mathbf{1}, \mathbf{1}\rangle \otimes |000\rangle \otimes |\mathbf{0}, \mathbf{0}\rangle \otimes |000\rangle \ldots . \tag{2.41}$$

In the formula above the numbers in bold face represent the fermionic occupation numbers while $|000\rangle$ represents a link carrying no flux.

Notice that for the SU(2) case it is not straightforward to integrate out the gauge degrees of freedom for the case of finite systems with OBC and to obtain a formulation restricted to the physical subspace. This problem is addressed in detail in Chapter 7.

2.4 Quantum simulation of lattice gauge theories

In spite of the great success of LGT, there are also some limitations. The conventional MC approach to LGT in the Lagrangian formulation suffers from the sign problem in certain parameter regimes which limits its applicability. In particular, many problems at at finite fermion density as well as real-time dynamics are intractable with the method (although recently techniques have been developed that enable the simulation of dynamics in restricted regimes [145–147]). Methods originating from quantum information theory, might offer an alternative route to overcome these limitations and, on the basis of the Hamiltonian lattice formulation which we presented above, there have been several of those approaches to LGT during recent years. On the one hand it can be addressed with TN methods, as we will discuss further in Chapter 3. On the other hand the Hamiltonian lattice formulation is the starting point for a vast majority of proposals to quantum simulate gauge theories [55, 57, 60,

78–90, 92–98, 100, 148, 149] (albeit there also exist proposals directly addressing quantum field theories in the continuum [77, 150, 151]). Here we briefly review the prospects and challenges of such quantum simulators.

In general, the problem we would like to solve is the following: given the Hamiltonian, H, of the system and some initial state, $|\Psi(0)\rangle$, we want to obtain some of the physical properties from $|\Psi(t)\rangle$ at a certain time t. Quantum simulators [64, 152–155] are controllable quantum systems that can emulate the evolution of $|\Psi(0)\rangle$ while exploiting quantum effects of the simulation platform. Hence, for a system to be a viable candidate for a quantum simulator, one has to be able to initialize it in a suitable initial state at the beginning of the simulation, evolve the prepared state in time and finally extract the desired information via a measurement at the end of the simulation. There are two basic types of such simulators, *digital quantum simulators* and *analog quantum simulators* [152, 154]. In the analog approach, the Hamiltonian of the system is directly mapped to an experimentally controllable system (see Fig. 2.3(a)). In contrast, the digital approach is based on the circuit model of quantum computation [156]. The unitary evolution is generated by decomposing the evolution operator in a quantum circuit and applying it to the desired initial wave function encoded in the computational basis (see Fig. 2.3(b)).

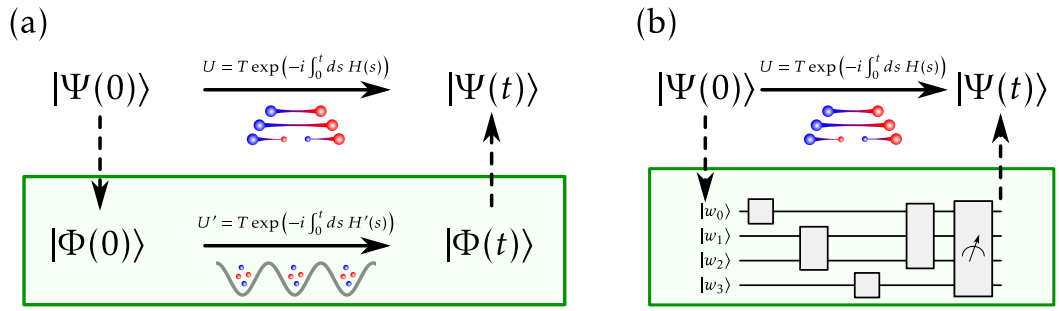

Figure 2.3: (a) Illustration of an analog quantum simulator. The Hamiltonian of the system, H, is mapped to an experimentally controllable system which allows to emulate the unitary time evolution. At the end of the evolution a measurement reveals the desired properties. (b) Sketch of a digital quantum simulator. The initial wave function of the system is encoded in the computational basis $\otimes_i |w_i\rangle$, $w_i \in \{0,1\}$, and the evolution is simulated by applying a sequence of quantum gates. At the end of the computation a measurement yields the desired information.

Quantum simulation is a particularly promising approach for the future, as it is free from the purely numerical limitations faced in simulations on classical computers, and there has been a variety of proposals for analog [78–82, 85–87, 89, 90, 92, 100, 148, 149, 157–160] and digital quantum simulators [60, 84, 93, 99, 161] for LGT problems and even combinations of both techniques [97, 98]. Recently, the first digital quantum simulator for the Schwinger model has

been realized in a small system of trapped ions [102], showing that the first experimental implementations are coming into reach with nowadays remarkable level of experimental control.

Despite these promising prospects, quantum simulation of LGT also poses a number of particular challenges. As the examples in the previous Section illustrate, continuous gauge symmetries lead to infinite-dimensional Hilbert spaces for the gauge degrees of freedom. In contrast, the systems that can be controlled experimentally are typically finite dimensional. Hence, many proposals for quantum simulation of LGT correspond to truncated versions of the original theory [78, 80–82, 99, 100, 149, 157] or quantum link models [162–164], where the link variables are replaced by finite-dimensional spins [60, 79, 84–87, 89, 90, 93, 148]. Since the original theory is only recovered in the limit of infinite-dimensional links, it is an important question how such a truncation might affect the predictive power of future experimental realizations.

Furthermore, the gauge symmetry of the model to be simulated is typically not a fundamental symmetry of the simulation platform. In many proposals it is ensured via an energy penalty on the noninvariant states and the desired gauge Hamiltonian arises as an effective theory in the low-energy limit [78, 79, 82, 85, 92, 157]. Even if the gauge symmetry can be mapped to a more fundamental conservation law of the simulation platform [80, 81, 86, 87, 149] or protected by other means [89], it is likely that experimental imperfections nevertheless lead to noninvariant terms in a practical realization. Hence, a further crucial question is how the nonfundamental character of the gauge symmetry affects the expected performance of future quantum simulators.

Additionally, to asses the practical feasibility of quantum simulation schemes, it is essential to analyze the physical requirements, too. This concerns the minimal system sizes for observing interesting phenomena, the time scales required for preparing relevant states of the theory and the necessary level of noise control to obtain credible results. In particular, quantum simulation is only advantageous over a simulation on a classical computer, if those resources do not scale exponentially with the size of the system to be simulated.

As we are going to see in the following Chapter, numerical techniques based on TN are not only a promising alternative to approach LGT problems, but they also allow for investigating some of these questions relevant for quantum simulation of LGT.

Chapter 3

Matrix product states

In the previous Chapter we introduced the lattice formulation of gauge theories and discussed the perspectives and limitations of potential quantum simulators for gauge models. In order to examine certain gauge models and proposals for potential quantum simulators numerically, we use a particular kind of one-dimensional TN, the MPS. In the following we summarize the basic concepts of MPS with a particular focus on the numerical techniques we employ in the later part of the thesis. In Sec. 3.1 we introduce the ansatz and show why it is suitable to approximate the physically relevant states for many Hamiltonians before we review the numerical methods we employ for our simulations in Sec. 3.2. Finally, we discuss the application of TN to LGT in Sec. 3.3.

3.1 The matrix product state ansatz

Let us consider a quantum lattice system composed of N individual systems (e.g. spins), with local Hilbert space dimension $d < \infty$.[1] Any pure state of the system can then be written as

$$|\Psi\rangle = \sum_{i_1,i_2,\ldots,i_N=1}^{d} c_{i_1,\ldots i_N} |i_1\rangle \otimes \cdots \otimes |i_N\rangle, \tag{3.1}$$

with a tensor $c_{i_1,\ldots i_N}$ having d^N complex entries. From this consideration the "curse of dimensionality" for numerical calculations taking into account the full Hilbert space is already apparent: after choosing a basis, the state is fully characterized by d^N complex numbers and storing those would require an exponential amount of memory. Consequently, even if one is only interested in the low-lying spectrum and makes clever use of symmetries, one is in general limited to small N [165, 166].

[1] For simplicity we assume that all systems have the same physical dimension. This does not necessarily have to be the case and the arguments presented here would also apply if each system has a different dimension, d_k, $k = 1,\ldots,N$.

An efficient ansatz for the many-body wave function is given by the *matrix product states* with OBC which are given by

$$|\Psi\rangle = \sum_{i_1,i_2,\ldots i_N=1}^{d} A_1^{i_1} A_2^{i_2} \ldots A_N^{i_N} |i_1\rangle \otimes \cdots \otimes |i_N\rangle. \tag{3.2}$$

In the expression above the $A_k^{i_k}$ are complex $D \times D$ matrices for $k = 2,\ldots,N-1$ and $A_1^{i_1}$ ($A_N^{i_N}$) is a D dimensional row (column) vector. Hence, we have a family of states for which, instead of a single tensor $c_{i_1,\ldots i_N}$ with d^N entries, the coefficients are parametrized by a product of matrices for every combination of indices $i_1,\ldots,i_N$. The number of parameters in the ansatz is given $\mathcal{O}((N-2)dD^2 + 2Dd) = \mathcal{O}(ND^2d)$, where D is called the *bond dimension* of the MPS.[2] Obviously, the scaling of the number parameters for a fixed bond dimension is only polynomial in system size.

Before we continue our discussion, it is convenient to introduce a graphical notation, in which each tensor is represented as a box and each index as a leg sticking out of the box. Connected legs between two tensors indicate a contraction of the corresponding index meaning that it is summed. Hence, the tensor $c_{i_1,\ldots i_N}$ and the MPS from Eq. (3.2) can be represented graphically as shown in Fig. 3.1.

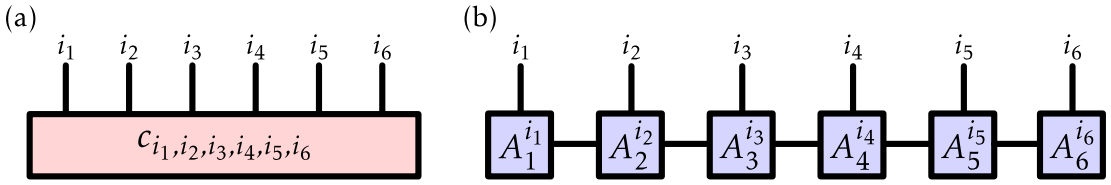

Figure 3.1: Illustration of the graphical notation described in the text for a system with 6 sites. (a) The tensor $c_{i_1,\ldots,i_6}$, each of the legs corresponds to a single index. (b) Graphical notation for the MPS from Eq. (3.2), the connected legs correspond to contracted indices.

From Eq. (3.2) it also apparent that the MPS representation is not unique, one can always insert a pair of invertible $D \times D$ matrices $Y_k Y_k^{-1} = \mathbb{1}$ at each bond and obtain an equivalent MPS representation with tensors $B_k^{i_k} = Y_{k-1}^{-1} A_k^{i_k} Y_k$ and $B_1^{i_1} = A_1^{i_1} Y_1$ ($B_N^{i_N} = Y_{N-1}^{-1} A_k^{i_N}$) on the left (right) boundary, as shown in Fig. 3.2(a). This *gauge freedom* can be used to obtain the *left canonical form* of a MPS in

[2] It is also possible to allow for a varying bond dimension between different sites. In that case $A_k^{i_k} \in \mathbb{C}^{D_{k-1} \times D_k}$ for $k = 2,\ldots,N-1$ and $A_1^{i_1}$ ($A_N^{i_N}$) is a D_1 dimensional row vector (D_N dimensional column vector. The bond dimension is then defined as $D = \max_k D_k$. Here we consider for simplicity a homogeneous D.

which the matrices fulfill the condition [167]

$$\sum_{i_k=1}^{d} \left(B_k^{i_k}\right)^\dagger B_k^{i_k} = \mathbb{1}, \qquad \sum_{i_k=1}^{d} B_k^{i_k} \Lambda_k \left(B_k^{i_k}\right)^\dagger = \Lambda_{k-1}, \tag{3.3}$$

where Λ_k is a diagonal matrix with positive entries fulfilling $\mathrm{tr}(\Lambda_k) = 1$ and $\Lambda_0 = 1 = \Lambda_N$. In the graphical notation this corresponds to the conditions shown in Fig. 3.2(b)-(c). Similar to the left canonical form, we can also use the gauge freedom to obtain the *right canonical form*, where the tensors fulfill

$$\sum_{i_k=1}^{d} B_k^{i_k} \left(B_k^{i_k}\right)^\dagger = \mathbb{1}, \qquad \sum_{i_k=1}^{d} \left(B_k^{i_k}\right)^\dagger \Lambda_{k-1} B_k^{i_k} = \Lambda_k. \tag{3.4}$$

Especially the possibility to achieve an identity in the partial contraction of two tensors turns out to be crucial for the efficiency and the stability of the numerical algorithms, as we are going to discuss later.

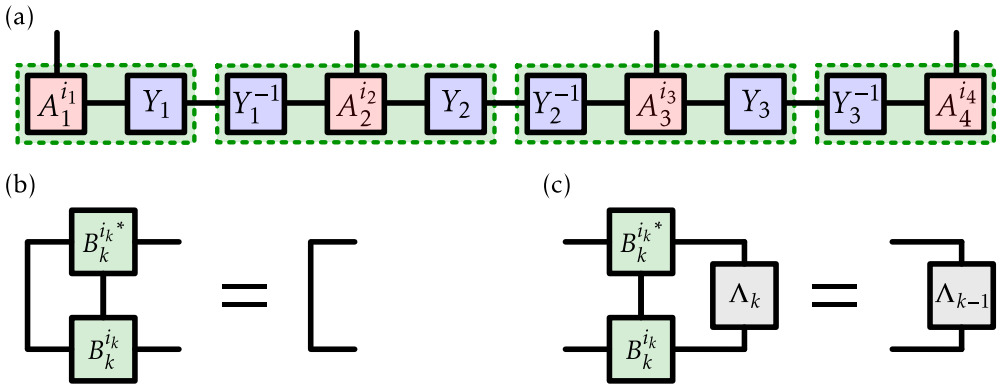

Figure 3.2: (a) Equivalent MPS representation after inserting a pair of invertible matrices at each bond. The green dashed boxes indicate the new tensors $B_k^{i_k}$. Panels (b) and (c) illustrate the conditions for the left canonical gauge from Eq. (3.3). (b) The first condition ensures that the partial contraction of two tensors yields the identity. (c) The second condition ensures a contraction with the diagonal matrix Λ_{k-1} yields another diagonal matrix Λ_k.

So far we have introduced MPS as an ansatz for the many-body wave function and it is not yet clear which states they parametrize. To get more insight into the set of states corresponding to MPS with fixed bond dimension, let us bipartition the system into a subsystem $\mathcal{A}$ containing the sites $1,\ldots,r$ and its complement $\bar{\mathcal{A}}$ containing the rest of the sites from $r+1,\ldots,N$. Using this bipartition, we can rewrite Eq. (3.1) as

$$|\Psi\rangle = \sum_{i_\mathcal{A}, i_{\bar{\mathcal{A}}}=1}^{d} c_{i_\mathcal{A}, i_{\bar{\mathcal{A}}}} |i_\mathcal{A}\rangle \otimes |i_{\bar{\mathcal{A}}}\rangle,$$

where $i_{\mathcal{A}}$ ($i_{\bar{\mathcal{A}}}$) is a multi-index referring to all i_k for $k \in \mathcal{A}$ ($k \in \bar{\mathcal{A}}$). We can now interpret $c_{i_{\mathcal{A}},i_{\bar{\mathcal{A}}}}$ as the entries of a $d^r \times d^{N-r}$ dimensional complex matrix and compute its *singular value decomposition*[3] which yields

$$|\Psi\rangle = \sum_{i_{\mathcal{A}},i_{\bar{\mathcal{A}}}=1}^{d} \sum_{\alpha=1}^{D_r} U_{i_{\mathcal{A}},\alpha} S_{\alpha,\alpha} V^{\dagger}_{\alpha,i_{\bar{\mathcal{A}}}} |i_{\mathcal{A}}\rangle \otimes |i_{\bar{\mathcal{A}}}\rangle. \tag{3.5}$$

In the expression above $U_{i_{\mathcal{A}},\alpha}$, $V^{\dagger}_{\alpha,i_{\bar{\mathcal{A}}}}$ are the entries of two unitary matrices U, $V^{\dagger}$ and $S = \mathrm{diag}(s_1, s_2, \ldots, s_{D_r})$ is a diagonal matrix of rank $D_r \leq \min(d^r, d^{N-r})$, with the real, positive singular values in decreasing oder, $s_i \geq s_{i+1} > 0$. Due to the unitarity of the matrices U and $V^{\dagger}$, the vectors $|r_\alpha\rangle = \sum_{i_{\mathcal{A}}=1}^{d} U_{i_{\mathcal{A}},\alpha} |i_{\mathcal{A}}\rangle$ ($|\bar{r}_\alpha\rangle = \sum_{i_{\bar{\mathcal{A}}}=1}^{d} V^{\dagger}_{\alpha,i_{\bar{\mathcal{A}}}} |i_{\bar{\mathcal{A}}}\rangle$) are pairwise orthonormal and this form is known as *Schmidt decomposition* of the state. The singular values are called the Schmidt values and D_r is the Schmidt rank. Since the Schmidt vectors are orthonormal, it is particularly easy to compute the reduced density matrix (RDM) of the subsystem $\mathcal{A}$ which yields

$$\rho_{\mathcal{A}} = \mathrm{tr}_{\bar{\mathcal{A}}}\Big(|\Psi\rangle\langle\Psi|\Big) = \sum_{\alpha=1}^{D_r} s_\alpha^2 |r_\alpha\rangle\langle r_\alpha|$$

where $\mathrm{tr}_{\bar{\mathcal{A}}}$ refers to the partial trace over the subsystem $\bar{\mathcal{A}}$. Moreover, as the reduced density matrix is diagonal in the Schmidt vectors, we can directly compute the *entanglement entropy* for the bipartition $\mathcal{A}$, $\bar{\mathcal{A}}$ which is given by the *von Neumann entropy of the reduced density matrix*

$$S(\rho_{\mathcal{A}}) = -\mathrm{tr}\Big(\rho_{\mathcal{A}} \log_2(\rho_{\mathcal{A}})\Big) = -\sum_{\alpha=1}^{D_r} s_\alpha^2 \log_2(s_\alpha^2). \tag{3.6}$$

As one can show, the entanglement entropy is maximized if the reduced density matrix for the subsystem has a flat spectrum, meaning that $s_\alpha^2 = 1/D_r$, $\alpha = 1, \ldots, D_r$, resulting in $S(\rho_{\mathcal{A}}) = \log_2(D_r)$ [168]. Hence, we see that the entanglement entropy between the two subsystems is upper bounded by the logarithm of the Schmidt rank.

Instead of just taking a single bipartition, we can use the decomposition from above sequentially starting from the left and iteratively applying it to the resulting tensors $V^{\dagger}$. In a first step, we decompose the tensor according to Eq. (3.5) where we bipartition the system into the first site and the rest (see also

[3] We use the compact singular value decomposition and only keep the columns of U and the rows of $V^{\dagger}$ corresponding to nonzero entries of S.

Fig. 3.3(a)-(b))

$$c_{i_1,\ldots,i_N} = c_{i_1,(i_2,\ldots,i_N)} = \sum_{\alpha_1=1}^{D_1} U^{(1)}_{i_1,\alpha_1} S^{(1)}_{\alpha_1,\alpha_1} V^{(1)\dagger}_{\alpha_1,(i_2,\ldots,i_N)}.$$

In a second step, we interpret $V^{(1)\dagger}_{\alpha_1,(i_2,\ldots,i_N)}$ as a tensor $\bar{c}_{(\alpha_1 i_2),(i_3\ldots,i_N)}$ and decompose it again, hence yielding (see Fig. 3.3(c))

$$c_{i_1,\ldots,i_N} = \sum_{\alpha_1=1}^{D_1} \sum_{\alpha_2=1}^{D_2} U^{(1)}_{i_1,\alpha_1} S^{(1)}_{\alpha_1,\alpha_1} U^{(2)}_{(i_2,\alpha_1),\alpha_2} S^{(2)}_{\alpha_2,\alpha_2} V^{(2)\dagger}_{\alpha_2,(i_3,\ldots,i_N)}.$$

Iterating the procedure until we arrive at the right boundary, we obtain a decomposition of the form

$$c_{i_1,\ldots,i_N} = \sum_{\alpha_1=1}^{D_1} \sum_{\alpha_2=1}^{D_2} \cdots \sum_{\alpha_{N-1}=1}^{D_{N-1}} U^{(1)}_{i_1,\alpha_1} S^{(1)}_{\alpha_1,\alpha_1} U^{(2)}_{(i_2,\alpha_1),\alpha_2} S^{(2)}_{\alpha_2,\alpha_2} \ldots S^{(N-1)}_{\alpha_{N-1},\alpha_{N-1}} U^{(N)}_{i_N,\alpha_{N-1}}.$$

where $S^{(k)}_{\alpha_k,\alpha_k}$ are the entries of the diagonal matrices S_k arising from the singular value decompositions. This can be cast into a simple form, if we interpret the rank three tensors $U^{(k)}_{(i_k,\alpha_{k-1}),\alpha_k}$ for a fixed i_k, $k = 2,\ldots,N-1$, as the entries of matrices $U^{i_k}_k$ in $\mathbb{C}^{D_{k-1}\times D_k}$, too. Correspondingly, the rank two tensors at boundary $U^{(1)}_{i_1,\alpha_1}$ ($U^{(N)}_{i_N,\alpha_{N-1}}$) can be seen as the entries of a D_1-dimensional row vector $U^{i_1}_1$ (D_N-dimensional column vector $U^{i_N}_N$). As a result, we arrive at a state of the form [169]

$$|\Psi\rangle = \sum_{i_1,i_2,\ldots,i_N=1}^{d} U^{i_1}_1 S_1 U^{i_2}_2 S_2 \ldots S_{N-1} U^{i_N}_N |i_1\rangle \otimes \cdots \otimes |i_N\rangle, \tag{3.7}$$

where instead of a single tensor $c_{i_1,\ldots i_N}$, we have now a product of matrices for every combination of indices $i_1,\ldots,i_N$ (see Fig. 3.3(d) for the graphical notation). The diagonal matrices S_k contain the Schmidt values for the corresponding bipartition of the system, hence, one can immediately read of the entanglement properties for any subsystem of contiguous sites. Alternatively, if we contract the tensors carrying the Schmidt values into the matrices to the right and set $A^{i_1}_1 = U^{i_1}_1$, $A^{i_k}_k = S_{k-1} U^{i_k}_k$, $k = 2\ldots,N$, we obtain a MPS in right canonical form[4] (see Eq. (3.4)) and the matrices Λ_k are given by S^2_k. Our considerations above show the following:

[4] Correspondingly, one can also contract the matrices to left and obtain a MPS in left canonical form.

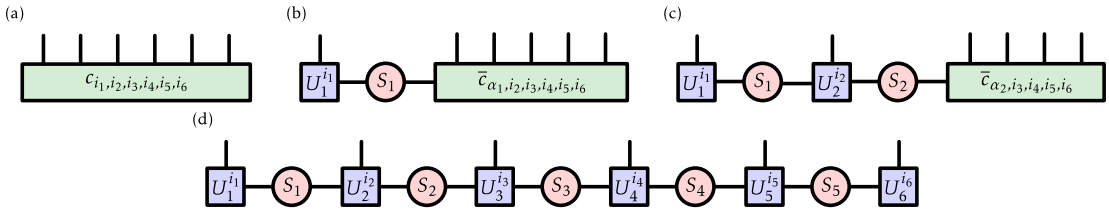

Figure 3.3: (a) The original tensor $c_{i_1,\ldots,i_6}$. (b) We apply a singular value decomposition and obtain the first tensor $U_1^{i_1}$ carrying a physical index and the matrix S_1. (c) After reshaping and decomposing $\bar{c}_{\alpha_1,i_2,i_3,i_4,i_5,i_6}$, we obtain the second tensor $U_2^{i_2}$ carrying another physical index and S_2. (d) The result after iterating the decomposition procedure until reaching the right boundary.

1. Since we have merely rewritten Eq. (3.1) to arrive at Eq. (3.7), every state can be a cast to a MPS form. However, the resulting bond dimension necessary to do so scales in general exponentially in the system size, as the maximum Schmidt rank for a system of N sites can reach up to $d^{\llcorner N/2 \lrcorner}$.

2. The MPS ansatz from Eq. (3.2) represents states with Schmidt rank at most D for any bipartition and, hence, as we have seen in the derivation above, the entanglement entropy for a subsystem is upper bounded by $\log_2(D)$. Thus, MPS correspond to a subset of states of the full Hilbert space having limited entanglement, and by increasing the maximally allowed bond dimension, one obtains a strictly larger set which contains all MPS of smaller bond dimension (see Fig. 3.4).

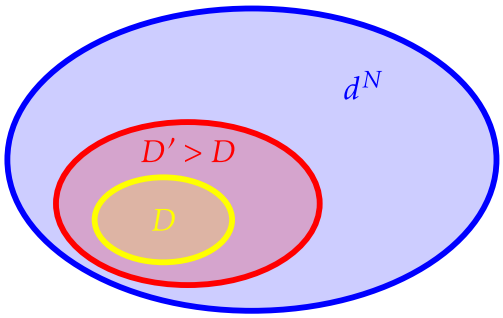

Figure 3.4: Full Hilbert space of the system (blue outer oval) and the set of states parametrized by MPS with fixed bond dimension (red and yellow inner ovals). The set of states parametrized grows with increasing bond dimension and strictly includes all states with smaller bond dimension.

The MPS from Eq. (3.2) can also be derived in a different way using the *valence bond picture* [170, 171]. To this end, we introduce for every site a virtual system consisting of two D-dimensional qudits such that two neighboring qudits on different sites form a maximally entangled pair (see also Fig. 3.5). The

resulting state of the virtual system is then

$$|\Psi_{\mathrm{VB}}\rangle = |\omega_1\rangle \otimes |\omega_2\rangle \otimes \cdots \otimes |\omega_{N-1}\rangle$$

with the maximally entangled pairs $|\omega_k\rangle = \frac{1}{\sqrt{D}} \sum_{l=1}^{D} |b_k = l, a_{k+1} = l\rangle$. If we now

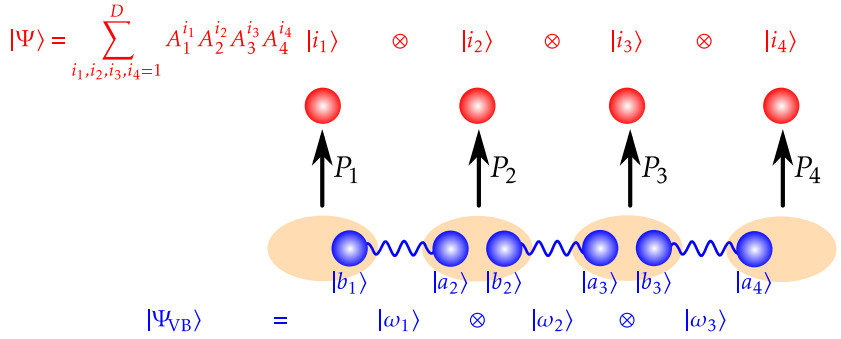

Figure 3.5: Illustration of the valence bond picture. The blue circles correspond to the virtual qudits sitting on a site indicated by the orange ovals. The wiggly line indicates two qudits forming a maximally entangled pair. After applying the linear map P_i on each site, we obtain the physical system indicated by a red sphere.

apply locally the linear map

$$P_k = \sum_{i_k=1}^{d} \sum_{a_k,b_k=1}^{D} A^{(k)}_{i_k,a_k,b_k} |i_k\rangle\langle a_k, b_k|$$

at each of the middle sites and

$$P_1 = \sum_{i_1=1}^{d} \sum_{b_1=1}^{D} A^{(1)}_{i_1,b_1} |i_1\rangle\langle b_1|, \qquad P_N = \sum_{i_N=1}^{d} \sum_{a_N=1}^{D} A^{(N)}_{i_N,a_N} |i_N\rangle\langle a_N|$$

at the left and right boundary, we obtain a state

$$\begin{aligned} |\Psi\rangle &= P_1 \otimes P_2 \otimes \cdots \otimes P_N |\Psi_{\mathrm{VB}}\rangle \\ &= \sum_{i_1,i_2,\ldots i_N=1}^{d} A_1^{i_1} A_2^{i_2} \ldots A_N^{i_N} |i_1\rangle \otimes \cdots \otimes |i_N\rangle. \end{aligned}$$

which is exactly the MPS we have already found previously, if we again consider the $A^{(k)}_{i_k,a_k,b_k}$ as the entries of a complex matrix $A_k^{i_k}$ for each value of i_k, $k = 2,\ldots,N-1$, and $A^{(1)}_{i_1,b_1}$ ($A^{(N)}_{i_N,a_N}$) as the entries of a row vector $A_1^{i_1}$ (column vector $A_N^{i_N}$).

The valence bond picture again shows that MPS with a fixed D carry limited entanglement. For every bipartition in a left and a right part of the system, there is exactly one maximally entangled pair of D-dimensional qudits shared by the two subsystems. Hence, the entanglement entropy is upper bounded by the entropy of this pair. Moreover, the valence bond picture presented here can be immediately generalized to two and higher spatial dimensions yielding the *projected entangled pair states* (PEPS) [172].

Historically, this construction has been adopted to describe the exact ground state of an extension of the spin-1 Heisenberg model introduced by Affleck, Kennedy, Lieb and Tasaki [173] which can be obtained by projecting two virtual spin-1/2 particles onto the spin-1 subspace. The construction was generalized in Ref. [170] which formally introduced translational invariant MPS under the name of finitely correlated states.

In our considerations we focused on systems with OBC, however, it is easy to generalize the MPS ansatz to periodic boundary conditions. In the valence bond picture this corresponds to putting another virtual particle in the first and last site which form a maximally entangled state, too [171]. The resulting state after projecting then reads

$$|\Psi\rangle = \sum_{i_1,i_2,\dots i_N=1}^{d} \mathrm{tr}(A_1^{i_1} A_2^{i_2} \dots A_N^{i_N}) |i_1\rangle \otimes \dots \otimes |i_N\rangle,$$

where contrary to the OBC case $A_1^{i_1}$ and $A_N^{i_N}$ are now matrices as well. Furthermore, there exist generalizations for continuous systems [174] as well as a class of states which can be considered as MPS with infinite bond dimension [175].

3.1.1 Efficient approximation with matrix product states

So far, we have introduced MPS as a theoretical concept and it is not yet clear if they can be used to efficiently approximate physically relevant states. A key concept for assessing if a state can be efficiently approximated with a MPS, is the *area law* [176]. A state is said to fulfill the area law, if the entropy for a subsystem $\mathcal{A}$ described by the reduced density matrix $\rho_{\mathcal{A}}$ scales as the surface area of the boundary $\partial\mathcal{A}$ of the subsystem:

$$S(\rho_{\mathcal{A}}) \propto |\partial\mathcal{A}|.$$

For the one-dimensional case, the surface area of the boundary is simply a constant, independent of the subsystem size. As we have seen before, the entanglement entropy for a MPS with a fixed bond dimension D is upper bounded by $\log_2(D)$, independent of the subsystem size, thus, MPS fulfill the area law by construction.

States fulfilling the area law are very nongeneric. A random state drawn from the Hilbert space is typically expected to have a volume law behavior, meaning that the entanglement entropy of a subsystem is extensive in its volume [177–179]. Nevertheless, it turns out that ground states of a large class of physically relevant one-dimensional systems fall into this category. For Hamiltonians with local interactions of finite strength, unique ground state and a finite energy gap to the first excited state, it can be shown that the ground state fulfills the area law [180]. In particular, for these systems one can show that the area law also implies that the Schmidt values decay fast and, thus, *ground states of local, gapped Hamiltonians* can be efficiently approximated with MPS [180].

In a more general setting, it was shown that MPS allow for efficiently approximating any state, for which all *Rényi entropies*

$$S_\alpha(\rho_\mathcal{A}) = \frac{1}{1-\alpha}\log_2\left(\mathrm{tr}\left(\rho_\mathcal{A}^\alpha\right)\right) \tag{3.8}$$

for $0 < \alpha < 1$ fulfill the area law up to logarithmic corrections [181, 182]. More specifically, if there exist constants c, c' such that $S_\alpha(\rho_\mathcal{A}) \leq c\log_2(L_\mathcal{A}) + c'$ for $\alpha \in (0,1)$ for arbitrary contiguous regions $\mathcal{A}$ with corresponding length $L_\mathcal{A}$, the state can be efficiently approximated with MPS. Efficiently approximated means that given a fixed error, the bond dimension necessary to obtain an approximation with at most this error scales at most polynomially with the system size N. Notice that this does not generalize to higher dimensions: for two and more spatial dimensions there exist states for which all Rényi entropies fulfill an area law, nevertheless they cannot be efficiently approximated by PEPS. These states are, however, not the ground states of local Hamiltonians [183].

In particular, in one dimension the states that can be efficiently approximated also encompass ground states of critical systems, for which arguments from conformal field theory suggest a logarithmic scaling of the Rényi entropies with respect to the subsystem size [184]. In that case, the bond dimension required to obtain a MPS approximation for a given state with a fixed error scales polynomially in the system size [181]. Moreover, there exist TN which have the logarithmic corrections to the area law built in such as *tree tensor networks* [185] and the *multi-scale entanglement renormalization ansatz* [186], hence, having a more efficient scaling in bond dimension for critical systems. Similar to MPS, these can also be generalized to higher dimensions [187, 188] and continuous systems [189].

3.1.2 Matrix product operators

Up to now we have only considered states. For the numerical calculations we also need the form corresponding to Eq. (3.2) for operators such as the Hamil-

tonian describing the system. Similar to a quantum state, any operator

$$O = \sum_{i_1,\ldots,i_N=1}^{d} \sum_{j_1,\ldots,j_N=1}^{d} c_{i_1,\ldots,i_N}^{j_1,\ldots,j_N} |i_1\rangle\langle j_1| \otimes \cdots \otimes |i_N\rangle\langle j_N| \tag{3.9}$$

can be written as *matrix product operator* (MPO) [190–193]

$$O = \sum_{i_1,\ldots,i_N=1}^{d} \sum_{j_1,\ldots,j_N=1}^{d} M_1^{i_1,j_1} \ldots M_N^{i_N,j_N} |i_1\rangle\langle j_1| \otimes \cdots \otimes |i_N\rangle\langle j_N|, \tag{3.10}$$

where $M_k^{i_k,j_k}$ are again complex matrices for $k = 2,\ldots,N-1$ and $M_1^{i_1,j_1}$ ($M_N^{i_N,j_N}$) is a row (column) vector. In the graphical notation, a MPO is a MPS in an operator basis and, hence, has an additional physical leg (see Fig. 3.6(a)). Again, any operator can be cast into MPO form, if one allows for matrices of exponential size in N. Provided the Hamiltonian of a system is local, one can always find

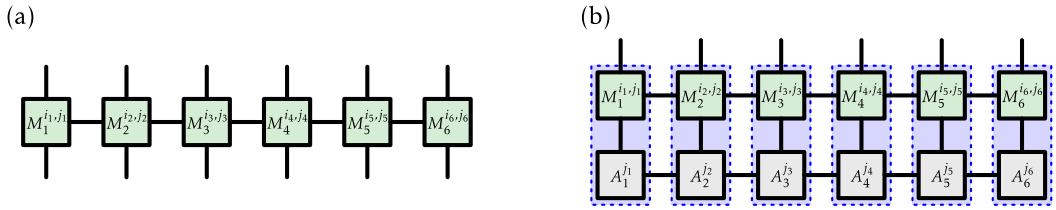

Figure 3.6: (a) Example of a MPO for a system with 6 sites. (b) Application of a MPO to an MPS results again in a MPS with the tensors indicated by the blue dashed boxes.

an efficient MPO representation for it [192, 194]. Moreover, also for certain types of long-range interactions it is possible to find an efficient MPO representation [193]. In general, it can be shown that every operator of the form of Eq. (3.9) corresponds to a complex weighted finite automaton and the finite automaton allows for finding a MPO representation with a bond dimension related to the number of states of the automaton [194].[5]

From the graphical notation it is apparent that applying a MPO to a MPS yields again a MPS (see Fig. 3.6(b)). The bond dimension of the resulting MPS is in general the product of the bond dimension of the initial MPS and the MPO, as the new matrices $B_k^{i_k}$ have entries of the form

$$B^{(k)}_{i_k,(\alpha_{k-1},\beta_{k-1}),(\alpha_k\beta_k)} = \sum_{j_k=1}^{d} M^{(k)}_{i_k,j_k,\beta_{k-1},\beta_k} A^{(k)}_{j_k,\alpha_{k-1},\alpha_k},$$

[5] Notice, since operators can be interpreted as states in an operator basis, this is also true for states. Hence, every quantum state can be expressed as finite automaton which allows for finding an MPS representation with a bond dimension proportional to the number of internal states of the automaton.

and the vectors $B_1^{i_1}$ and $B_N^{i_N}$ at the boundaries are given by

$$B^{(1)}_{i_1,(\alpha_1,\beta_1)} = \sum_{j_1=1}^{d} M^{(1)}_{i_1,j_1,\beta_1} A^{(1)}_{j_1,\alpha_1}, \qquad B^{(N)}_{i_N,(\alpha_{N-1},\beta_{N-1})} = \sum_{j_N=1}^{d} M^{(N)}_{i_N,j_N,\beta_{N-1}} A^{(N)}_{j_N,\alpha_{N-1}}.$$

3.2 Numerical algorithms

Besides being a viable theoretical tool, the MPS formalism allows the efficient computation of ground-state approximations [195, 196] and time evolution [190, 197–200]. In particular, MPS are the underlying variational ansatz of the highly successful *density matrix renormalization group* (DMRG) [201, 202]. Here we briefly review the two main algorithms we use throughout the rest of the thesis to examine different gauge models and proposals for quantum simulating those. Detailed reviews explaining the computational techniques in depth can be found in Refs. [168, 198, 203, 204].

3.2.1 Variational ground-state search

Given the Hamiltonian of the system in MPO form, we can use the family of MPS with fixed bond dimension D, $\mathcal{M}_D$, as variational ansatz to efficiently determine an approximation for the ground state of the system. To this end, we would like to find the MPS which minimizes the energy $E = \langle\Psi|H|\Psi\rangle/\langle\Psi|\Psi\rangle$ which according to the Rayleigh-Ritz variational principle is given by [204]

$$\min_{|\Psi\rangle\in\mathcal{M}_D} \frac{\langle\Psi|H|\Psi\rangle}{\langle\Psi|\Psi\rangle}. \tag{3.11}$$

If we plug the MPS ansatz from Eq. (3.2) into this expression and directly try to find the set of tensors $A_k^{i_k}$ minimizing it, this would in general turn into a complicated high-dimensional nonlinear optimization problem which is numerically hardly tractable. Instead, we choose a different approach and minimize the expression iteratively by updating the tensors one by one while keeping the others fixed [171]. The optimal tensor for a site k while keeping the others fixed is then found by extremizing Eq. (3.11) with respect to this tensor:

$$\min_{A_k^{i_k}} \frac{\left\langle \Psi\left[A_k^{i_k}\right] \middle| H \middle| \Psi\left[A_k^{i_k}\right]\right\rangle}{\left\langle \Psi\left[A_k^{i_k}\right] \middle| \Psi\left[A_k^{i_k}\right]\right\rangle} = \min_{\vec{A}_k} \frac{\vec{A}_k^\dagger H_{\text{eff},k} \vec{A}_k}{\vec{A}_k^\dagger N_k \vec{A}_k}. \tag{3.12}$$

Here $\Psi\left[A_k^{i_k}\right]$ refers to a MPS with all tensors fixed except for the tensor at site k, $A_k^{i_k}$. In the second step, we have used that with Eqs. (3.2) and (3.10) one

can explicitly compute this expression and cast it to a matrix form, where $\vec{A}_k$ is the dD^2-dimensional vectorization of the tensor components of $A_k^{i_k}$, $H_{\text{eff},k}$ is a $dD^2 \times dD^2$ effective Hamiltonian matrix describing the interaction of site k with its environment and N_k a $dD^2 \times dD^2$ matrix obtained by partially contracting $\langle\Psi|\Psi\rangle$ up to site k. Thus, the new tensor at every step can found by solving the generalized eigenvalue problem [171]

$$H_{\text{eff},k}\vec{A}_k = \lambda N_k \vec{A}_k,$$

and is given by the eigenvector corresponding to the smallest eigenvalue. The smallest eigenvalue is in turn the energy of the state at the current step [168, 171]. In the graphical language this can be expressed as shown in Fig. 3.7.

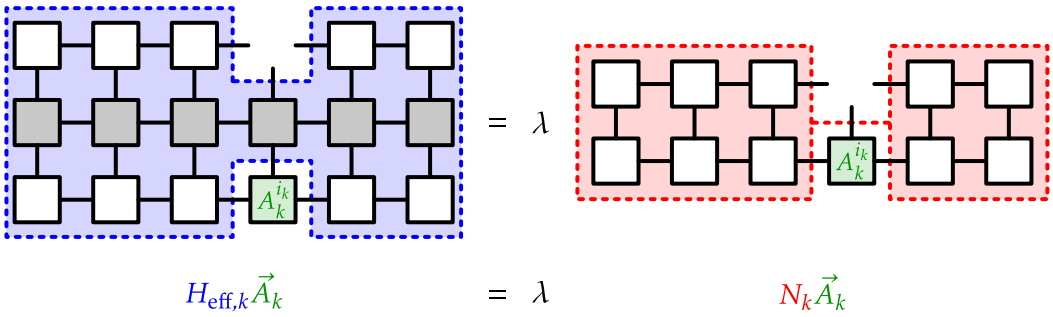

Figure 3.7: Illustration of the eigenvalue problem for updating a single site. The dark boxes correspond the MPO tensors of H, the white boxes to the tensors of the state $|\Psi\rangle$. The left part represents $H_{\text{eff},k}\vec{A}_k$, where the effective Hamiltonian (indicated in blue) is obtained by contracting the tensor network corresponding to $\langle\Psi|H|\Psi\rangle$ up to site k. The right part represents $N_k\vec{A}_k$ where the matrix N_k (indicated in red) corresponds to the partial contraction of the TN representing $\langle\Psi|\Psi\rangle$ up to site k. The green box indicates the tensor $A_k^{i_k}$ which is determined after proper vectorization and solving the generalized eigenvalue problem $H_{\text{eff},k}\vec{A}_k = \lambda N_k \vec{A}_k$.

The algorithm to find the ground state then works as follows:

1. Start with a random set of tensors $A_1^{i_1}, \ldots, A_N^{i_N}$ or an initial guess if available.

2. Starting on the left boundary we sweep to the right and sequentially update the tensors by solving the eigenvalue problem described above at every site.

3. After reaching the right boundary we continue sweeping to the left again and update tensor by tensor until reaching the left boundary.

4. After each full sweep we check the stopping criterion (e.g. if the variance of the energy is below a certain threshold and the current wave function is sufficiently close to an eigenstate or the relative change in energy is below a certain tolerance or simply if the number of sweeps exceeds a certain maximum). If this is fulfilled we stop, otherwise we continue with steps 2. - 4.

The problem can even be further simplified by making use of the gauge conditions from Eqs. (3.3) and (3.4). Looking at the graphical representation of the gauge condition in Fig. 3.2 it is apparent that the matrix N_k is the identity, if we keep the tensors in mixed gauge: all the tensors to the left of site k in left canonical gauge and all the tensors to the right in right canonical gauge. Hence, the generalized eigenvalue problem can be turned into a conventional one[6] which can be solved efficiently [205, 206]. If we keep the tensors in every step in the proper mixed gauge to simplify the computation of the matrix N_k and reuse the partial contractions, the algorithm can be implemented with leading cost $\mathcal{O}(D^3)$ [168].

Moreover, it can also easily be extended to low-lying excitations [35]. After obtaining the ground state, $|\Psi_0\rangle$, with energy E_0, one can project the Hamiltonian on a subspace orthogonal to the ground space using the projector $P_0 = \mathbb{1} - |\Psi_0\rangle\langle\Psi_0|$ which results in

$$\overline{H} = P_0 H P_0 = H - E_0 |\Psi_0\rangle\langle\Psi_0|.$$

Assuming that all the energy eigenvalues of the low-lying states are strictly smaller than zero,[7] the first excited state, $|\Psi_1\rangle$, is now the ground state of $\overline{H}$ which can be found by applying the ground-state algorithm to the projected Hamiltonian. Subsequently, one can iterate this procedure to compute higher excited states. In general, given the states up to level l, we apply the projector $P_l = \mathbb{1} - \sum_{k=0}^{l} |\Psi_k\rangle\langle\Psi_k|$ to the Hamiltonian and obtain the $(l+1)$-th excited state by running the algorithm for the projected Hamiltonian

$$\overline{H} = P_l H P_l = H - \sum_{k=0}^{l} E_k |\Psi_k\rangle\langle\Psi_k|.$$

The leading cost of the algorithm for all the l levels using the projected Hamiltonian is $\mathcal{O}(l^2 D^3)$ which is the same as for finding the ground state up to a quadratic prefactor [35].

[6] Notice that besides simplifying the computation, this also improves the stability of the algorithm, as otherwise the matrix N_k can have a very large condition number leading to an amplification of numerical errors [168, 203].

[7] If this is not the case, we can always subtract a large enough constant from the Hamiltonian to ensure that.

3.2.2 Time evolution

The time-evolution algorithm we are using in our simulations is based on the one presented in Ref. [197]. The key idea here is to break the total evolution time in small intervals for which we can find an efficient (approximate) MPO representation for the time-evolution operator and to compute the evolution as sequential application of those operators to the initial MPS. In Sec. 3.1.2 we saw that applying a MPO to a MPS results again in a MPS, however, with a bond dimension given by the product of the bond dimension of the MPO and the initial MPS. Hence, if we compute the evolution as series of small time steps, the bond dimension of the resulting MPS would grow exponentially in the number of steps. To render the problem numerically feasible, we have to approximate the resulting MPS with one of smaller bond dimension. In the following we address these two questions.

Matrix product operator form for the time-evolution operator

Let us for the moment consider only time independent Hamiltonians, hence the time-evolution operator is simply $\mathcal{T} = \exp(-iHt)$. In general, it will not be possible to find an efficient MPO representation for $\mathcal{T}$, even if we have an efficient MPO representation for the Hamiltonian.[8] Dividing the time interval t in n intervals of size Δt we can compute the evolution as

$$|\Psi(t)\rangle = \Big(\exp(-iH\Delta t)\Big)^n |\Psi(t=0)\rangle.$$

For small Δt, we can find an (approximate) MPO representation for the operator $\exp(-iH\Delta t)$, as we are going to show in the following.

One obvious way to approximate $\exp(-iH\Delta t)$ is a simple Taylor expansion up to first order

$$\exp(-iH\Delta t) = \mathbb{1} - iH\Delta t + \mathcal{O}\Big((\Delta t)^2\Big).$$

Provided one has an efficient MPO representation for the Hamiltonian of the system, it is straightforward to find a MPO representation for this expression. Additionally, this way of approximating the time-evolution operator preserves all symmetries of the original Hamiltonian. However, it is nonunitary and one has to normalize the state after every time step. Furthermore, the bond dimension of the resulting MPO grows fast with the order of the Taylor expansion, thus preventing to go to higher orders in practice.

A more elaborate method for local, nearest-neighbor Hamiltonians, which easily allows for obtaining higher order approximations, was shown in Ref. [197]. To illustrate the method, let us assume that H is the sum of nearest-neighbor

[8] One can, however, always find a MPO representation with exponentially growing bond dimension in system size, as we discussed in Sec. 3.1.2.

terms $H = \sum_{i=1}^{N-1} h_{i,i+1}$, where $h_{i,i+1}$ acts on sites i and $i+1$. We can divide the Hamiltonian in two parts, one containing the two-body terms starting at even sites, and one containing the terms starting at odd sites, $H = H_{\text{odd}} + H_{\text{even}}$ with $H_{\text{odd}} = \sum_{i=1,3,\ldots}^{N-1} h_{i,i+1}$ and $H_{\text{even}} = \sum_{i=2,4,\ldots}^{N-1} h_{i,i+1}$. Using a first-order Suzuki-Trotter decomposition [207], we can approximate the time-evolution operator as

$$\exp(-iH\Delta t) = \exp(-iH_{\text{even}}\Delta t)\exp(-iH_{\text{odd}}\Delta t) + \mathcal{O}\left((\Delta t)^2\right) \tag{3.13}$$

Since $h_{i,i+1}$ has support on two sites only, all the two-body terms in H_{odd} (H_{even}) mutually commute. Thus, we can write

$$\mathcal{T}_{\text{odd}} = \exp\left(-iH_{\text{odd}}\Delta t\right) = \exp\left(-i\Delta t \sum_{i=1,3,\ldots}^{N-1} h_{i,i+1}\right) = \prod_{i=1,3,\ldots}^{N-1} \exp\left(-ih_{i,i+1}\Delta t\right)$$

and similarly for $\mathcal{T}_{\text{even}} = \exp\left(-iH_{\text{even}}\Delta t\right)$, without further approximation. The resulting operators consist of a product of local, nonoverlapping terms as illustrated in Fig. 3.8(a). This can be used to obtain a MPO form of the time-

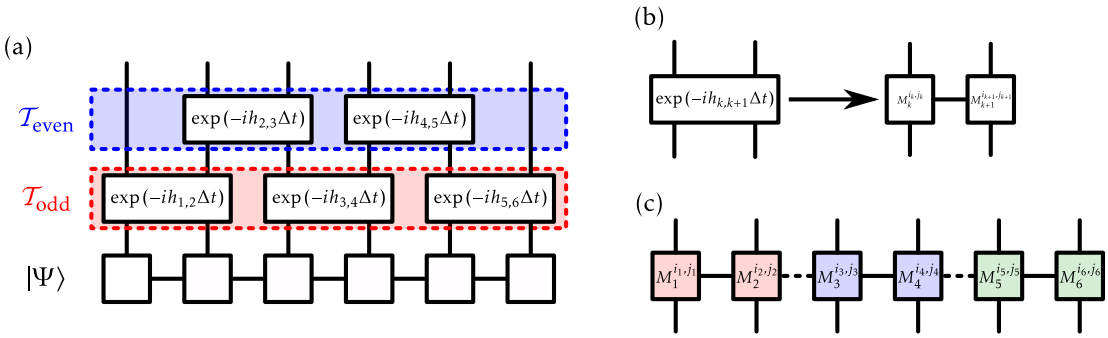

Figure 3.8: (a) Illustration of the decomposition in local terms starting on odd and even sites. (b) Splitting a local term in MPO form. (c) Resulting MPO for $\mathcal{T}_{\text{odd}}$, where the tensors having the same color represent the MPO decomposition of a single nearest-neighbor term. The dashed lines indicate bonds with bond dimension 1 between the MPO representations for different nearest neighbor terms.

evolution operator: the local terms with disjoint support appearing in $\mathcal{T}_{\text{odd}}$ ($\mathcal{T}_{\text{even}}$) can always be written as MPO with bond dimension at most d^2. Hence, after decomposing all the local terms appearing in $\mathcal{T}_{\text{odd}}$ ($\mathcal{T}_{\text{even}}$) we obtain a MPO form for the entire operator (see Fig. 3.8(b)-(c)).

The approach is not restricted to the nearest-neighbor case and can also be generalized to more complicated situations. However, for those cases it is in general necessary to divide the Hamiltonian in more than two parts to obtain sums of mutually commuting terms, thus resulting in a larger number of

different MPOs to approximate the evolution operator for a single step. The maximum bond dimension for each of those MPOs grows exponentially with the maximum range of the interactions present in the corresponding part of the Hamiltonian. Hence, for practical numerical simulations one is typically restricted to local, short-ranged interactions. Moreover, to minimize the error in the Suzuki-Trotter decomposition, one can use higher-order decomposition formulas [207]. The approximation may nevertheless introduce errors, as for example components in the wave function in the wrong symmetry sector. This can be (partially) corrected by projecting it back into the desired subspace after every few time steps.

From the considerations above, it is apparent that the method also applies to time-dependent Hamiltonians. Since we compute the time evolution as series of steps for small time intervals of length Δt, we can simply take the Hamiltonian constant on every interval [207] and proceed the same way as described above.

Approximating a matrix product state with one of smaller bond dimension

In the previous Section we demonstrated how the evolution operator can be represented as a MPO for a small time step. Hence, we could compute the evolution of a MPS by repeatedly applying this MPO. However, as we have seen in Sec. 3.1.2, the resulting MPS after applying a MPO has in general a bond dimension given by the product the bond dimension of the MPO and the initial MPS. Consequently, this approach would lead to an exponential growth of the bond dimension with the number of steps. To render the computation numerically feasible, the resulting MPS has to be approximated by one with smaller bond dimension. Here we show how this can be done using an algorithm similar to the one for the variational ground-state search.

Given a MPS $|\Psi\rangle$ with bond dimension D and tensors $B_1^{i_1},\ldots,B_N^{i_N}$, we want to find a MPS $|\Psi'\rangle$ with bond dimension $D' < D$ and tensors $A_1^{i_1},\ldots,A_N^{i_N}$ which maximizes the overlap with the original MPS or equivalently minimizing the norm distance [168]

$$\left\| |\Psi\rangle - |\Psi'\rangle \right\|_2^2 = \langle\Psi|\Psi\rangle - \langle\Psi|\Psi'\rangle - \langle\Psi'|\Psi\rangle + \langle\Psi'|\Psi'\rangle.$$

To find $|\Psi'\rangle$ we can use the same approach we took for finding a MPS approximation for the ground state: starting from a certain $|\Psi'\rangle$ we update the tensors sequentially using an alternating least squares scheme to maximize the overlap. The optimal tensor in every step is found by minimizing the norm distance

with respect to each component of the tensor $A_k^{i_k *}$

$$\frac{\partial}{\partial \vec{A}_k^\dagger} \left\| |\Psi\rangle - |\Psi'\rangle \right\|_2^2 = \frac{\partial}{\vec{A}_k^\dagger} \Big(\langle \Psi|\Psi\rangle - \langle \Psi|\Psi'\rangle - \langle \Psi'|\Psi\rangle + \langle \Psi'|\Psi'\rangle \Big) = 0.$$

where $\vec{A}_k^\dagger$ is the vectorization of the tensor components. Since $\langle \Psi|\Psi\rangle$ and $\langle \Psi|\Psi'\rangle$ do not depend on $A_k^{i_k *}$, the derivative vanishes. The other terms result, after proper reshaping, in a system of $D^2 d$ linear equations, $N_k \vec{A}_k = \vec{v}_k$, which can be seen by looking at the graphical representation of the equation above in Fig. 3.9. Again, we can use the gauge condition to simplify the expression and

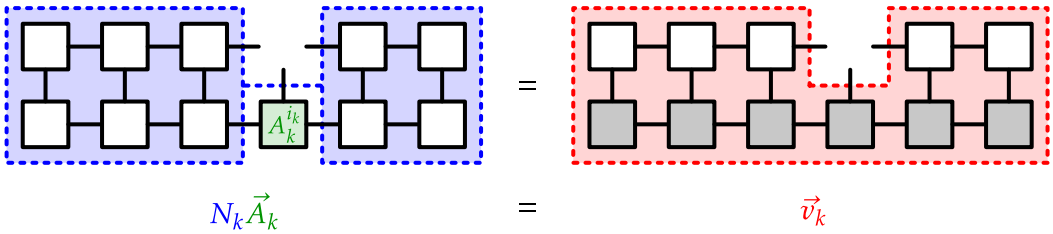

Figure 3.9: Linear equation system for updating a single site. The left part corresponds to $\partial/\partial \vec{A}_k^\dagger \langle \Psi'|\Psi'\rangle$, where the hole in the upper part is due to the derivative with respect to $\vec{A}_k^\dagger$. The matrix N_k is obtained by contracting the tensor network corresponding to $\langle \Psi'|\Psi'\rangle$ up to site k. The right part corresponds to $\partial/\partial \vec{A}_k^\dagger \langle \Psi'|\Psi\rangle$ where the hole arises again from the derivative with respect to $\vec{A}_k^\dagger$ and the darker tensors correspond to $|\Psi\rangle$. The vector $\vec{v}_k$ is obtained by contracting the network and vectorizing the result. The green box indicates the tensor $A_k^{i_k}$ which is determined after proper vectorization by solving $N_k \vec{A}_k = \vec{v}_k$.

ensure that the matrix N_k is the identity. Similarly to ground-state case, sweeping left and right and iteratively updating the tensors until the relative change of the norm distance is below a certain tolerance yields $|\Psi'\rangle$. The algorithm can again be implemented with leading computational cost $\mathcal{O}(D^3)$ [168].

The time evolution for an initially given MPS, $|\Psi(t=0)\rangle$, can now be computed as a sequence of applying the MPOs approximating $\exp(-iH\Delta t)$ and subsequently truncating the result after a certain number of steps to a MPS of smaller bond dimension D'. A crucial question is how large D' has to be to be able to find a good approximation. The answer is related to the evolution of the entanglement in the state. In a MPS with bond dimension D' the entanglement is upper bounded by $S \leq \log_2(D')$, as we have seen at the beginning of the Chapter. In situations far from equilibrium, the entanglement can grow linearly in time [208–210], hence, D' has to grow exponentially and only short time scales are available, although there exist improved algorithms for these situations [211]. As long as the system stays close to the ground state the method works well with moderate D' [182].

Switching to imaginary time $t \to -i\tau$, the time-evolution algorithm can also be used to obtain a MPS approximation for the ground state, $|\Psi_0\rangle$, which is formally given by [203]

$$|\Psi_0\rangle = \lim_{\tau\to\infty} \frac{\exp(-H\tau)|\Psi(\tau=0)\rangle}{\|\exp(-H\tau)|\Psi(\tau=0)\|}$$

with some initial state $|\Psi(\tau=0)\rangle$ having nonvanishing overlap with the ground state. Thus, in practice, if we evolve the initial state long enough in imaginary time, the result should be close to the ground state. Within the formalism presented above, this can be done by computing a large number of small time steps. While the numerical cost for computing a single of those steps is smaller than the one of the variational algorithm, this approach is typically less efficient then the variational one due to the large number of steps required. Nevertheless, it can be advantageous, as it allows for targeting a certain symmetry sector of the Hamiltonian by appropriately choosing an in initial state in the desired sector without having to implement these symmetries in the algorithm. In addition, it is less prone to get trapped in local minima which renders it favorable for computing ground states with TN in higher dimensions [212–214].

3.3 Application to lattice gauge models

The numerical techniques presented above have been highly successful for the study of strongly correlated quantum many-body systems, and with the accuracies that can be achieved in nowadays numerical calculations, they are considered as quasi exact for many one-dimensional problems [215]. In particular, TN methods do not suffer from the sign problem and hence are suited for both, bosonic and fermionic systems [213, 216, 217]. This also renders them to promising candidates for the numerical exploration of LGT, as they offer the possibility to access parameter regimes and questions which cannot be tackled with the conventional Monte Carlo approach.

In the context of LGT, they can be used to approximate the partition function in the Lagrangian formulation [25–34], however they are particularly suited for addressing the Hamiltonian framework. Our discussion of the numerical methods working in the Hamiltonian formulation in the previous Section shows that they enable access to the wave function at any stage of the algorithm. Hence, contrary to the MC approach, it is straightforward to compute all kinds of (local) observables. Moreover, as we discussed at the beginning of the Chapter, the MPS formalism also allows for easy access to the entanglement structure in the state. Thus, the TN approach to LGT also opens up new possibilities to characterize LGT problems. In recent years, there has been a variety of works demonstrating the suitability of MPS and more general TN

to describe the relevant states for gauge theories by computing spectral properties [35–38, 41, 42, 49, 53], thermal states [39, 40, 45, 46, 49, 50], phase diagrams at finite matter density [47, 52] and real-time evolution for Abelian as well as non-Abelian gauge models [37, 41, 43, 44, 51]. Some of these works even achieved precisions beyond the reach of MC calculations for the considered models in one spatial dimension. Besides these numerical results, there has been a steady progress in the more formal approach, in particular in the development of gauge invariant TN suitable for LGT problems [37, 55, 56, 59, 62, 63].

In addition, MPS and TN in general are a well suited tool to investigate experimentally relevant questions for quantum simulators which we discussed in Sec. 2.4. Spectral calculations with TN can help to explore the effects and limitations of truncating the gauge degrees of freedom to a finite dimension in a systematic manner. Moreover, the possibility to simulate real-time evolution allows for investigating ground-state preparation protocols, and the effect of noise therein, as within the TN framework it is straightforward to consider gauge-invariance-breaking noise terms in the Hamiltonian. Furthermore, numerical simulations with TN can also provide benchmarking data for quantum simulators that might help to test and validate future experimental realizations.

Throughout the rest of this thesis, we use the MPS methods discussed above to investigate both, questions related to certain 1+1 dimensional LGTs and the quantum simulation thereof.

Chapter 4

The Schwinger model: potential candidates for a future quantum simulator

In Sec. 2.4 we discussed the prospects and challenges of potential future quantum simulators for LGT. In this Chapter, we address some of these questions concerning the practical feasibility of such a simulation for the Schwinger model, which is presumably the simplest nontrivial gauge theory with dynamical fermions. Despite its simplicity, the lattice formulation shares some interesting features with more complicated gauge theories such as confinement, an anomalous U(1) current in the massless limit and a nonvanishing chiral condensate [143, 218]. Hence, it is an interesting candidate for the implementation in future quantum simulation experiments. The content of this Chapter has been published in Ref. [91] and is a modification thereof.

4.1 Introduction

In this Chapter, we address some of the issues affecting quantum simulation of LGT by studying two possible realizations of the Schwinger model that might be suitable for an implementation with ultracold atoms. We focus on proposals which have a built-in gauge symmetry, but where the gauge degrees of freedom are represented by a system with a Hilbert space of small dimension. For these models we numerically address three questions using MPS with OBC to reflect a possible experimental realization:

1. We investigate how the truncation of the gauge degrees of freedom to a finite-dimensional Hilbert space affects the nature of the ground state and reveal that even a small dimension allows quite accurate predictions for the ground-state energy.

2. We examine the resources needed for the adiabatic preparation of the ground state. We give evidence that the first part of the adiabatic evolution is crucial and, for the systems we study, with up to hundred sites,

the total time required for a successful preparation is practically independent of system size. Our results also show that the Hilbert space dimension of the gauge degrees of freedom hardly affects the success of the preparation procedure.

3. We analyze the effect of imperfect gauge symmetry by studying the adiabatic preparation in the presence of noninvariant noise terms, as those might occur in an experimental realization. We quantify the level of noise up to which the results for the ground-state energy are still reasonably close to the noiseless case.

The rest of the Chapter is organized as follows. In Sec. 4.2 we briefly review the Schwinger model and explain the two particular discrete versions studied here. Furthermore, we comment on the numerical methods we use. In Sec. 4.3 we present our results on how the finite-dimensional Hilbert space for the gauge degrees of freedom affects the ground state. Subsequently we examine one possible scenario for the adiabatic preparation of the ground state in Sec. 4.4 and study the effect of gauge invariance breaking noise during this procedure in Sec. 4.5. Finally we conclude in Sec. 4.6.

4.2 Models and methods

The model we are studying is the compact Hamiltonian lattice formulation of the Schwinger model with Kogut-Susskind staggered fermions from Sec. 2.3. We focus on the single-flavor case without chemical, and after making it dimensionless, the Hamiltonian from Eq. (2.35) for a system of N sites reads

$$W = \frac{2H}{ag^2} = -ix \sum_{n=1}^{N-1} \left(\psi_n^\dagger U_n \psi_{n+1} - \text{h.c.} \right) + \mu \sum_{n=1}^{N} (-1)^n \psi_n^\dagger \psi_n + \sum_{n=1}^{N-1} L_n^2, \tag{4.1}$$

where the adimensional parameters in units of the coupling, g, are given by $x = 1/(ag)^2$, $\mu = \sqrt{x}m/g$ with m the fermion mass. As we have seen, for the full model the link operators are given by $U_n = \exp\left(i\Lambda_n\right)$, with Λ_n and L_n fulfilling the commutation relation $[\Lambda_n, L_m] = i\delta_{nm}$, $\Lambda_n \in [0, 2\pi]$, and the Gauss Law is given in Eq. (2.36).

There are several proposals to quantum simulate the Schwinger model [77–80, 82, 85–87, 89, 149, 157]. Since the dimensions of quantum systems available for quantum simulation are finite, most proposals focus on models with finite-dimensional variables on the links that recover Hamiltonian (4.1) in the limit $d_{\text{link}} \to \infty$. One way is to simulate a quantum link model, in which the gauge variables are represented by finite-dimensional quantum spins [162–

164], another is to truncate the dimension of the link variables.[1] These approaches can lead to a Hamiltonian with a gauge symmetry which is different from the one of the Schwinger model.

Here we consider two particular models, one which has the same gauge symmetry as the Schwinger model despite the finite-dimensional links, and one which has a different gauge symmetry due to the finite dimension.

4.2.1 Truncated cQED model

The first model we examine corresponds to the proposal for the simulation of compact QED (cQED) from Ref. [80], using fermionic and bosonic atoms trapped in an optical superlattice. The fermions are sitting in the minima of one lattice forming the sites. The links are populated by an (even) number of particles $N_0 = a_n^\dagger a_n + b_n^\dagger b_n$, consisting of two bosonic species A and B, sitting between the fermions in the minima of another lattice (see Fig. 4.1). The operators a_n, b_n ($a_n^\dagger$, $b_n^\dagger$) are the annihilation (creation) operators for species A and B on link n, fulfilling the usual commutation relations. This model gives rise to a Hamiltonian of the form (4.1) with link operators

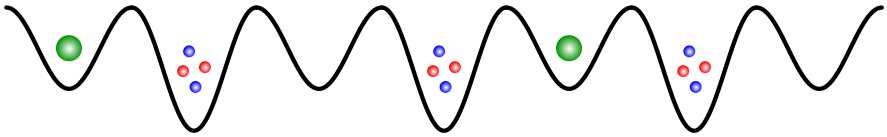

Figure 4.1: Illustration of the optical superlattice. The shallow wells correspond to the fermionic sites, which can either be occupied by a single fermion (indicated by a green circle) or empty. The deeper wells correspond to the gauge links which are populated by a fixed, even number of particles consisting of two bosonic species A and B (indicated by the red and blue circles).

$$U_n = i\frac{a_n^\dagger b_n}{\sqrt{l(l+1)}}, \qquad L_n = \frac{1}{2}(a_n^\dagger a_n - b_n^\dagger b_n), \tag{4.2}$$

where $l = N_0/2$, so that the link operators are angular momentum operators in the Schwinger representation. As $a_n^\dagger a_n + b_n^\dagger b_n$ is a constant of motion, the number of particles on a link, N_0, is conserved. The dimension of the Hilbert space for each link is given by $d_{\text{link}} = N_0 + 1$, and in the limit $N_0 \to \infty$ the link operators become pure phases that coincide with those from the Kogut-Susskind Hamiltonian. In this realization, the angular momentum conservation in the scattering between the fermions and bosonic species ensures Gauss law, which does not have to be imposed effectively via a penalty term.

[1] A similar truncation of the Hilbert space dimension for the gauge degrees of freedom is also used in many DMRG [219, 220] and TN simulations [37, 38, 41–44, 50–53, 55, 221] of LGT.

The Hamiltonian in this case is invariant under local transformations that affect the annihilation operator for one fermion on site n and its adjacent bosons as

$$\psi_n \to e^{i\alpha_n}\psi_n, \qquad b_{n-1} \to e^{i\alpha_n} b_{n-1}, \qquad a_n \to e^{-i\alpha_n} a_n, \qquad \alpha_n \in \mathbb{R},$$

while the operators acting on other sites and links are unchanged. The model has then the same U(1) symmetry as the untruncated Schwinger model and we will refer to it as *truncated cQED model*. The Hamiltonian of this model commutes with the Gauss law generators from Eq. (2.36)

$$G_n^{\text{cQED}} = L_n - L_{n-1} - \psi_n^\dagger \psi_n + \frac{1}{2}\left(\mathbb{1} - (-\mathbb{1})^n\right),$$

where the L_n-operators are given by Eq. (4.2).

4.2.2 $\mathbb{Z}_d$ model

Another possibility to represent the links with finite-dimensional objects is to substitute the infinite dimensional U(1) gauge operators in Eq. (4.1) by $\mathbb{Z}_d$ operators. This can be realized with the following link operators

$$U_n = \sum_{k=-J}^{J} |\varphi_n^{k+1}\rangle\langle\varphi_n^k|, \quad L_n = \sum_{k=-J}^{J} k|\varphi_n^k\rangle\langle\varphi_n^k|, \tag{4.3}$$

where one needs to identify $|\varphi_n^{J+1}\rangle$ with $|\varphi_n^{-J}\rangle$. Consequently the dimension of the Hilbert space of a link is given by $d_{\text{link}} = 2J + 1$. As shown in Ref. [222], these operators approach in the limit $d_{\text{link}} \to \infty$ the link operators of the Kogut-Susskind Hamiltonian.

The resulting Hamiltonian is invariant under local transformations of the fermions and adjacent links[2] as

$$\psi_n \to e^{i\alpha_n}\psi_n, \qquad |\varphi_{n-1}^k\rangle \to e^{-ik\alpha_n}|\varphi_{n-1}^k\rangle, \qquad |\varphi_n^k\rangle \to e^{ik\alpha_n}|\varphi_n^k\rangle,$$

with $\alpha_n = 2\pi q/d_{\text{link}}$, $q \in \mathbb{Z}$. Different from the truncated cQED case, here only discrete phase transformations leave the Hamiltonian invariant, hence we refer to the model as $\mathbb{Z}_d$ *model* in the following.[3] Correspondingly the Gauss law is

[2] For simplicity we show here the effect of the transformation on the basis states for the links and not the operators. One should also note that one has the freedom to add arbitrary constant phase factors to the transformation for the basis states.

[3] We call the model presented here $\mathbb{Z}_d$ model because of this discrete symmetry. However, one should note that it does not correspond to a $\mathbb{Z}_d$ LGT [223], as we use a different kinetic term for the gauge field in the Hamiltonian.

only fulfilled modulo d_{link} and the operators that commute with the Hamiltonian are actually

$$\mathcal{U}_n^{\mathbb{Z}_d} = e^{i\frac{2\pi}{d_{\text{link}}}\left(L_n - L_{n-1} - \psi_n^\dagger\psi_n + \frac{1}{2}(\mathbb{1}-(-\mathbb{1})^n)\right)}, \tag{4.4}$$

where the L_n-operators are given by Eq. (4.3).

In the following we restrict ourselves for both models to the massless case, $m = 0$, and the subspace of vanishing total charge, $\sum_n \left(\psi_n^\dagger\psi_n - \frac{1}{2}(\mathbb{1} - (-\mathbb{1})^n)\right) = 0$, for which analytical results are available [101]. No big qualitative changes are expected for the massive case.

4.2.3 Numerical approach

We study the model Hamiltonians using the standard MPS techniques to compute the ground state and simulate the time evolution introduced in Chapter 3. For convenience of the simulations, we use an equivalent spin formulation of each Hamiltonian [121], which can be obtained via a Jordan-Wigner transformation on the fermionic degrees of freedom (see App. A.1 for details).

In our simulations, we are interested in different aspects:

1. *Quantum simulation protocol*
   To analyze the performance of a possible quantum simulation protocol, we investigate the following questions:
   - First, we would like to determine the effect of using finite-dimensional Hilbert spaces for the gauge degrees of freedom. Thus, we compute the ground state for each of the models by variationally for a series of different truncations to study the effect in a systematic manner.
   - Second, we analyze the performance of a possible adiabatic preparation protocol for the interacting vacuum of the theory. We simulate the evolution and quantify the resources needed for the protocol.
   - Third, we investigate the effect of gauge-invariance-breaking noise on the performance of the adiabatic preparation scheme. To do so, we again simulate the time evolution, but this time in the presence of noise sources.

2. *Numerical errors*
   Potential errors in our numerical calculations may originate from two main sources.
   - As described in Sec. 3.2, both in the ground state and in the dynamical simulations, the bond dimension employed is limited. Nevertheless, this source of error is controlled by choosing a sufficiently large D.

- In order to compute the evolution numerically we use a second order Suzuki-Trotter decomposition to split the time-evolution operator in $\mathcal{T}_{\text{odd}}$ and $\mathcal{T}_{\text{even}}$ as shown in Sec. 3.2. This error can be controlled via the time step size used for the splitting (a more detailed analysis of our numerical errors for the results presented in the following Sections can be found in App. B.1).

4.3 Effect of the finite dimension

In order to analyze the effect of using finite-dimensional systems to represent the gauge degrees of freedom, we study the ground states of the truncated cQED and $\mathbb{Z}_d$ models for different (odd) values of d_{link} ranging from 3 to 9 and compare them to the case of the lattice Schwinger model.

In a lattice calculation, in which the goal is to extract the continuum limit, simulations need to be run at different values of the lattice spacing. Hence, we also explore the effect of the finite d_{link} for various lattice spacings, ga, and for several system sizes. As a figure of merit, we analyze the ground-state energy density, $\omega = E_0/2Nx$, and compare the values in the thermodynamic limit obtained in each case to those from finite-size extrapolations of the lattice Schwinger model. In the previous expression N is the number of fermionic sites in the chain, x is related to the lattice spacing as $x = 1/(ga)^2$ and E_0 denotes the ground-state energy of the dimensionless Hamiltonian.[4] To get the energy density in the thermodynamic limit, we first compute the ground-state energy, E_0, for each set of parameters (N, d_{link}, x) for various bond dimensions D, which allows us to extrapolate $D \to \infty$ and estimate our numerical errors. Subsequently, we extrapolate $N \to \infty$ for each combination of (x, d_{link}) which yields the values for ω in the thermodynamic limit (details about the extrapolation to the thermodynamic limit can be found in App. B.1).

In our simulations we explore system sizes such that N ranges from 50 to 200, and lattice spacings corresponding to values of $x \in [50, 100]$. Our results are shown in Fig. 4.2.[5] We observe that the truncated cQED model converges to the values of the Schwinger model with increasing value of d_{link}. By contrast, the $\mathbb{Z}_d$ model already yields very accurate results even for low values of d_{link} and the level of accuracy practically stays constant for larger d_{link}.

[4] The quantities ω, E_0, and x are frequently used in lattice calculations for the Schwinger model [35, 121, 141, 143, 224] and we adapt to this convention for better comparability

[5] Here we show the energy density as this quantity allows an extrapolation to the thermodynamic and to the continuum limit for the range of parameters studied. We observe that also other quantities like the chiral condensate approach the values of the Schwinger model with increasing Hilbert space dimension of the links. However, the extrapolation process for the condensate is a lot more delicate and it is not expected to yield very accurate results in the parameter regime we have explored, even for the full model [36].

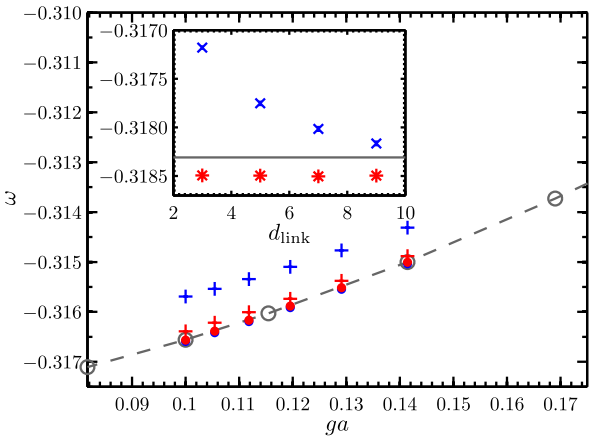

Figure 4.2: Thermodynamic limit for the energy density for various values of x. Crosses show the values for the truncated cQED model for $d_{\text{link}} = 3$ (blue) and $d_{\text{link}} = 9$ (red). Circles show the values for the $\mathbb{Z}_d$ model for $d_{\text{link}} = 3$ (blue) and $d_{\text{link}} = 9$ (red) which are almost identical. Values obtained for the Schwinger model are shown in gray. The inset shows the values obtained by extrapolating $x \to \infty$ for the continuum energy density for the truncated cQED model (blue ×'s) and the $\mathbb{Z}_d$ model (red asterisks). The horizontal gray line represents the value for the Schwinger model in the massless case, $-1/\pi$. In both cases the error bars from the extrapolation procedure are smaller than the markers.

In our range for x, we can also attempt a continuum limit extrapolation for each set of values (see inset in Fig. 4.2) [224, 225]. Here we observe that the truncated cQED model rapidly approaches the exact value for increasing d_{link}, whereas for the $\mathbb{Z}_d$ model the continuum extrapolation is already quite close to it for $d_{\text{link}} = 3$ and there is almost no change for larger d_{link}. This is consistent with our observations for the thermodynamic limit, where the results in the $\mathbb{Z}_d$ case are already very accurate for each lattice spacing, even for small d_{link}. However, one should take into account that the values of x used in this work are relatively small to extrapolate to the continuum [35], which is likely the source of larger systematic errors not taken into account here (a more detailed description of the extrapolation procedure and error estimation can be found in App. B.1). Hence, the level of error due to the finite-dimensional Hilbert spaces is expected to be already smaller than that of the extrapolation.

4.4 Adiabatic preparation of the ground state

Given a physical system which effectively implements one of these models, the nontrivial vacuum state could, in principle, be constructed using an adiabatic step [153, 154]. In this step one starts with an initial state, which is the ground

state of a simpler Hamiltonian and easy to prepare. Subsequently the interactions are slowly switched on to reach the desired model.

For both models considered here, a valid initial state could be the strong coupling ground state ($x = 0$) in the *physical* (i.e. Gauss law fulfilling) subspace from Eq. (2.37), which for the single-flavor case reads [121, 141, 143, 224]

$$|\Psi_{\text{sc}}\rangle = |\mathbf{1}\rangle|0\rangle|\mathbf{0}\rangle|0\rangle|\mathbf{1}\rangle|0\rangle|\mathbf{0}\rangle\dots\,.$$

The coupling strength can be tuned by changing x from 0 to x_{F}. Since the cQED ($\mathbb{Z}_d$) Hamiltonian commutes with G_n^{cQED} ($\mathcal{U}_n^{\mathbb{Z}_d}$) independently of the value of x, and our initial state is in the physical subspace, the Gauss law will be fulfilled at any time during the preparation procedure. Provided the change is slow enough, the adiabatic theorem ensures that the final state will be close to the ground state for x_{F}.

The resources required to successfully perform this preparation are dominated by the total time T needed for an evolution close enough to adiabaticity, which depends on the inverse gap of the Hamiltonian. As our model Hamiltonians are of the form of Eq. (4.1), it can be directly seen that the gap vanishes in the massless case for $x = 0$. For finite values of x, Fig. 4.3 reveals that the gap starts to grow with increasing x, and the growth in the region of small x is almost independent of system size N and Hilbert space dimension d_{link} for both models. Thus the change of the Hamiltonian at early times (or *while x is small*) needs to be very slow, whereas it is rather unimportant after reaching larger values of x.

To analyze the performance of a quantum simulation that runs this adiabatic preparation, we simulate a ramping of the parameter x from 0 to a value of $x_{\text{F}} = 100$ which corresponds to the smallest lattice spacing used in the previous Section. In our evolution simulations, we use a function $x(t) = x_{\text{F}} \times (t/T)^3$, which turns out to be flat enough at the beginning.

In order to probe the scaling of the required time with system size and other parameters, we deem an evolution successful if the overlap with the exact ground state is above a certain threshold. Since we are only interested in the overall scaling of the required resources, the value of the threshold can be chosen arbitrarily and in our simulations we set it to 0.99. We monitor the overlap between the evolved state and the exact ground state for various values of t, where the exact ground state is computed using the same methods as in the previous Section.[6] The results obtained by the preparation procedure described above can be seen in Fig. 4.4. We find that for the chosen parameters, we can obtain overlaps higher than 0.99 for both models around a total evolution time of $T = 60$ and the results still improve until $T = 80$, where we reached an overlap close to one and the error bars are already smaller than the

[6] To compute the ground state variationally, we use a significantly higher bond dimension of $D = 100$ than for the evolution to make sure we have a quasi-exact state.

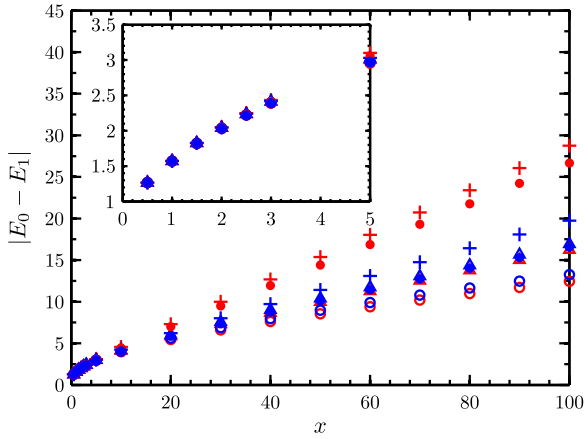

Figure 4.3: Gap between the ground state and the first excited state in the Gauss law fulfilling sector for the $\mathbb{Z}_d$ model and the truncated cQED model. Open symbols represent the values for the $\mathbb{Z}_d$ model for $N = 50$ (triangles) and $N = 100$ (circles). Values for the truncated cQED model are represented by the crosses ($N = 50$) and dots ($N = 100$). Red markers indicate $d_{\text{link}} = 3$; blue markers $d_{\text{link}} = 9$. The inset shows the region for small values of x in greater detail. All data points were computed with a bond dimension $D = 60$.

markers. The relative error, ε, in the energy with respect to the exact ground-state energy (see insets in Fig. 4.4) shows a similar behavior. Remarkably, for the range of parameters we have studied, the results are almost independent of the system size, N, and the Hilbert space dimension, d_{link}, as can be checked from Fig. 4.4, where data are shown for $N = 50$ and 100. This is in accordance with our observation that the gap does not depend on the system size and the Hilbert space dimension for small values of x (see Fig. 4.3).

A comment on the possible numerical errors is in order. The discussion in Sec. 3.2 showed that the employed splitting of the time-evolution operator can in principle induce components of the wave function in the wrong symmetry sector. As a consistency check for the numerics, we monitored whether the simulated state stays in the physical subspace with total charge equal 0, which is characterized by $\mathcal{U}_n^{\mathbb{Z}_d} = \mathbb{1}$ ($G_n^{\text{cQED}} = 0$) for the $\mathbb{Z}_d$ (truncated cQED) model. Therefore a violation results in a finite expectation value of the observable $P^{\mathbb{Z}_d} = \sum_n \left(\mathcal{U}_n^{\mathbb{Z}_d} - \mathbb{1}\right)^\dagger \left(\mathcal{U}_n^{\mathbb{Z}_d} - \mathbb{1}\right)$ ($P^{\text{cQED}} = \sum_n G_n^{\text{cQED}\dagger} G_n^{\text{cQED}}$) in the $\mathbb{Z}_d$ (truncated cQED) case that can be detected during the evolution. For all the data presented in this Section, we checked that the expectation values of P^ν during the evolution indeed stay down to zero up to machine accuracy, where $\nu = \text{cQED}, \mathbb{Z}_d$ labels the appropriate model.

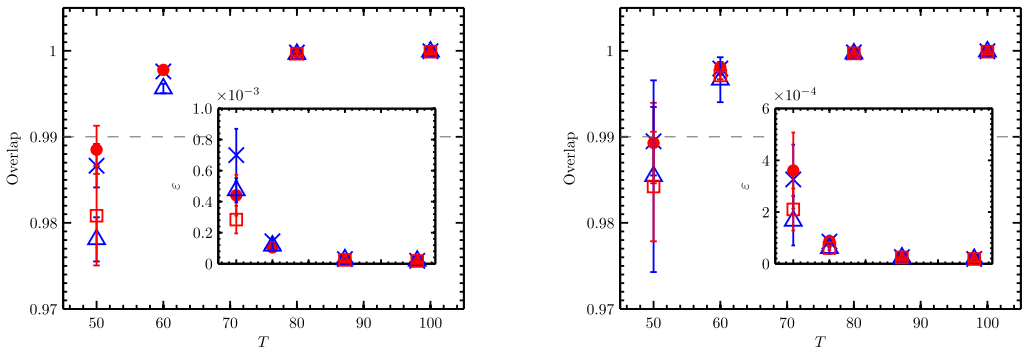

Figure 4.4: Final overlap with the variationally computed ground state at the end of the adiabatic preparation as a function of total evolution time for the truncated cQED model (left) and the $\mathbb{Z}_d$ model (right) with $D = 50$. The blue ×'s represent the data for $N = 50$, $d_{\text{link}} = 3$; blue triangles for $N = 100$, $d_{\text{link}} = 3$; red circles for $N = 50$, $d_{\text{link}} = 9$; and red squares for $N = 100$, $d_{\text{link}} = 9$. Error bars were obtained from the difference in results with bond dimension $D = 50$ and $D = 30$. The inset is showing the relative error of the energy with respect to the exact ground state.

4.5 Effect of broken gauge invariance

One crucial question for the quantum simulation of LGTs is whether the non-fundamental character of the gauge invariance will limit the power of the method. Even though it has been shown that it is possible to have models where the invariance is ensured at the level of interactions among the quantum systems [80, 81, 87, 89], external sources of noise that do not fulfill the gauge symmetry will likely be present in an experiment.

In order to study the effect of such nongauge symmetric contributions, we add a noise term to the Hamiltonian, which is given by $\sum_n \lambda x(t)(U_n + U_n^\dagger)$ for the $\mathbb{Z}_d$ case and by $\sum_n \lambda x(t)(a_n^\dagger b_n + b_n^\dagger a_n)$ for the truncated cQED case. This could represent some noise that occurs in the experimental setup implementing the interactions, and is thus proportional to their strengths, x. The parameter λ would then be the relative strength of the noise. We simulate the same adiabatic protocol of the previous Section, for a total time $T = 100$ that ensures success of the evolution as described earlier, under different levels of noise and for the same values of the other parameters $(N, d_{\text{link}}, x_{\text{F}})$ studied before. In addition to the overlap with the exact ground state, we quantify the violation of Gauss law per particle P^ν/N for each case. The results are shown in Fig. 4.5. Notice that due to the noise terms in the Hamiltonian, the violation of Gauss law in that case is of physical origin and not an effect of the numerics.

We observe that even small levels of noise ($\lambda = 5 \times 10^{-4}$) result in finite values of P^ν/N and a drastic reduction of the final overlap with the ground state.

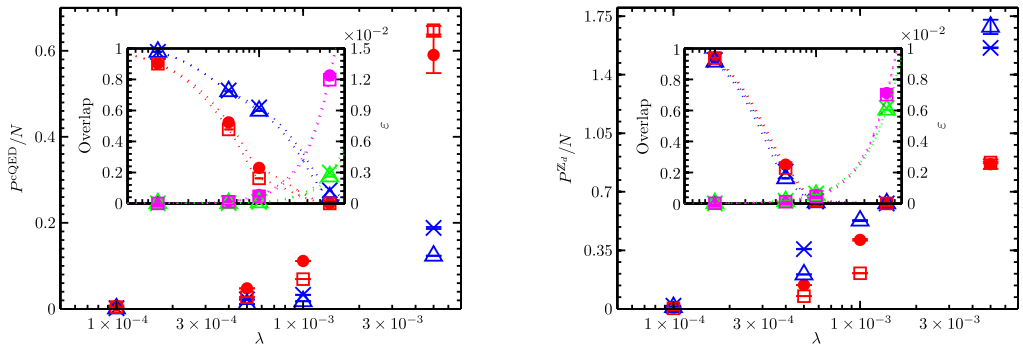

Figure 4.5: Penalty energy per site at the end of the noisy adiabatic preparation as a function of the noise strength for the truncated cQED model (left) and the $\mathbb{Z}_d$ model (right). The blue (green) ✕'s represent the values for $N = 50$, $d_{\mathrm{link}} = 3$; the blue (green) triangles the $N = 100$, $d_{\mathrm{link}} = 3$ case; the red (magenta) dots the $N = 50$, $d_{\mathrm{link}} = 5$ case; and the red (magenta) squares the $N = 100$, $d_{\mathrm{link}} = 5$ case. Error bars were computed the same way as in the noiseless case. The inset shows the overlap (blue and red markers) and the relative error in energy (green and magenta markers) with respect to the noise-free exact ground state. As a guide for the eye, the data points are connected.

Nevertheless the relative error in the energy stays below 2% for both models. Consequently, if the noise can be controlled relatively to the value of x, the predictions for some ground-state observables may still be quite accurate although the gauge invariance is broken.

Figure 4.5 also shows that the quantity P^{ν}/N does not show a strong dependence on the system size. To get an idea of how the violation of the Gauss law scales in the case of the noisy evolution, we compute the lowest order contribution to $\langle\Psi(t)|P^{\nu}|\Psi(t)\rangle$ using perturbation theory following Ref. [226]. For clarity we simply write P and suppress throughout the calculation the index labeling the model. Starting from the dimensionless Hamiltonian with the noise term

$$\widetilde{W}(t) = W(t) + \sum_n \lambda x(t)\left(\bar{U}_n + \bar{U}_n^{\dagger}\right),$$

where $\bar{U}_n$ refers to U_n for the $\mathbb{Z}_d$ model and to $a_n^{\dagger}b_n$ for the truncated cQED model, we can treat the noise term as perturbation to the Hamiltonian $W(t)$ small times t and small values of λ. The contributions to $\langle\Psi(t)|P|\Psi(t)\rangle$ are

given by subsequent commutators of P with the Hamiltonian

$$\begin{aligned}\langle\Psi(t)|P|\Psi(t)\rangle &= \langle\Psi_0|P|\Psi_0\rangle \\ &+ \frac{1}{i}\int_0^t \mathrm{d}t'\langle\Psi_0|[P,\widetilde{W}(t')]|\Psi_0\rangle \\ &+ \frac{1}{i^2}\int_0^t \mathrm{d}t'\int_0^{t'}\mathrm{d}t''\langle\Psi_0|\Big[[P,\widetilde{W}(t')],\widetilde{W}(t'')\Big]|\Psi_0\rangle \\ &+ \dots\end{aligned} \tag{4.5}$$

where $|\Psi_0\rangle$ is the initial state, in our case this is a product state fulfilling the Gauss law. As the unperturbed Hamiltonian commutes with $\mathcal{U}_n^{\mathbb{Z}_d}$ (G_n^{cQED}) in the $\mathbb{Z}_d$ (truncated cQED) case and $\bar{U}_n|\Psi_0\rangle$, $\bar{U}_n^\dagger|\Psi_0\rangle$ are still eigenstates of $\mathcal{U}_n^{\mathbb{Z}_d} - \mathbb{1}$ (G_n^{cQED}) which are orthogonal to $|\Psi_0\rangle$, it is immediately clear that the first contribution occurs at second order and the double commutator reduces to

$$\begin{aligned}\langle\Psi_0|\Big[[P,\widetilde{W}(t')]\,,\widetilde{W}(t'')\Big]|\Psi_0\rangle &= -\lambda^2 x(t')x(t'') \\ &\times\sum_{n,m,k}\Big(\langle\Psi_0|\bar{U}_m\Theta_n^\dagger\Theta_n\bar{U}_k^\dagger|\Psi_0\rangle + \langle\Psi_0|\bar{U}_m^\dagger\Theta_n^\dagger\Theta_n\bar{U}_k|\Psi_0\rangle \\ &\quad + \langle\Psi_0|\bar{U}_k\Theta_n^\dagger\Theta_n\bar{U}_m^\dagger|\Psi_0\rangle + \langle\Psi_0|\bar{U}_k^\dagger\Theta_n^\dagger\Theta_n\bar{U}_m|\Psi_0\rangle\Big) \\ &= -2\lambda^2 x(t')x(t'') \\ &\times\sum_n\Big(\langle\Psi_0|\bar{U}_n^\dagger\Theta_n^\dagger\Theta_n\bar{U}_n|\Psi_0\rangle + \langle\Psi_0|\bar{U}_n\Theta_n^\dagger\Theta_n\bar{U}_n^\dagger|\Psi_0\rangle\Big).\end{aligned}$$

Here we have introduced Θ_n which refers to $\mathcal{U}_n^{\mathbb{Z}_d} - \mathbb{1}$ (G_n^{cQED}) in the $\mathbb{Z}_d$ (truncated cQED) case, to keep the equations short.

In the second step we have used that $\bar{U}_m|\Psi_0\rangle$ and $\bar{U}_m^\dagger|\Psi_0\rangle$ are eigenstates of Θ_n, with nonzero eigenvalue iff $m = n$ and that $\langle\Psi_0|\bar{U}_k^\dagger\bar{U}_m|\Psi_0\rangle = c_m\delta_{k,m}$ ($\langle\Psi_0|\bar{U}_k\bar{U}_m^\dagger|\Psi_0\rangle = \bar{c}_m\delta_{k,m}$) with constants c_m, $\bar{c}_m$. Thus, there are only contributions if $n = k = m$ and we are left with a single sum. The two different matrix elements appearing in the sum are simply giving two constants, hence the sum can be estimated as cN with a constant c. Plugging this back into Eq. (4.5), we obtain

$$\langle\Psi(t)|P|\Psi(t)\rangle \approx 2\lambda^2 cN\int_0^t \mathrm{d}t'x(t')\int_0^{t'}\mathrm{d}t''x(t'').$$

Hence we see that $P^\nu \propto N, \lambda^2$ for fixed T, x_F independently from the ramping. For our choice of ramping, $x(t) = x_\mathrm{F}\times(t/T)^3$, the integrals can be easily solved yielding

$$\langle\Psi(t)|P|\Psi(t)\rangle \approx 2(\lambda x_\mathrm{F})^2\frac{t^8}{32T^6}cN. \tag{4.6}$$

Consequently, independent of the system size, P^{ν}/N is proportional to λ^2 for a fixed value of t, consistent with our data in Fig. 4.5.

In order to analyze the scaling with t and λ further, we plot P^{ν}/N as a function of time in Fig. 4.6 for the three smallest values of noise. The time interval is chosen as close as possible to the beginning of the evolution but late enough to ensure that the values for P^{ν}/N are above the machine accuracy. These plots reveal that P^{ν}/N indeed shows a power law behavior in t which is independent from N. Extracting the slope from the curves yields values between 7.5544 and 7.5589 for all cases presented in Fig. 4.6, which is in good agreement with our calculations. Additionally, we can investigate the scaling with λ. From Eq. (4.6) we obtain for the offset Δ between two curves with different noise levels λ_1 and λ_2

$$\Delta = \left|\log_{10}(\lambda_1^2) - \log_{10}(\lambda_2^2)\right| = 2 \times \left|\log_{10}(\lambda_1) - \log_{10}(\lambda_2)\right|.$$

For the values of λ used here (1×10^{-4}, 5×10^{-4} and 1×10^{-3}) this yields $\Delta_1 = 1.3979$ and $\Delta_2 = 0.6021$. The values extracted from our numerical data for both models with various N and d_{link} show a relative deviation of at most 10^{-4} from these predictions, which indicates again that there is almost no dependency on system size and Hilbert space dimension, in excellent agreement with our theoretical calculation.

4.6 Conclusion

There are several proposals for quantum simulation of the Schwinger model [77, 79, 80, 82, 85–87, 89, 149]. MPS techniques allow us here to address important questions that affect the feasibility of those and also for quantum simulation of more general LGTs. Our results give evidence that although the finite dimension of the physical systems that represent the gauge variables on the links may affect the ground state of the model, the results converge rapidly as this dimension is increased. In particular, for the truncated cQED model, we observed fast convergence to the exact ground state of the Schwinger model for d_{link} ranging from 3 to 9. For the $\mathbb{Z}_d$ model, the results with $d_{\text{link}} = 3$ are already extremely close to the ones of the full model. Our observations for the ground state are consistent with those recently reported in another study with TN for the Schwinger model using a different truncation for the gauge links [53].

In addition, our study of the adiabatic preparation protocol for the ground state starting from a simple product state suggests that the preparation is feasible and that the initial part of the evolution is crucial for its success. With a suitable choice of $x(t)$, we can obtain an overlap of more than 0.99 with the exact ground state for both models. Most remarkably, the required total time (for a given final value x_{F}) is practically insensitive to the system size and the

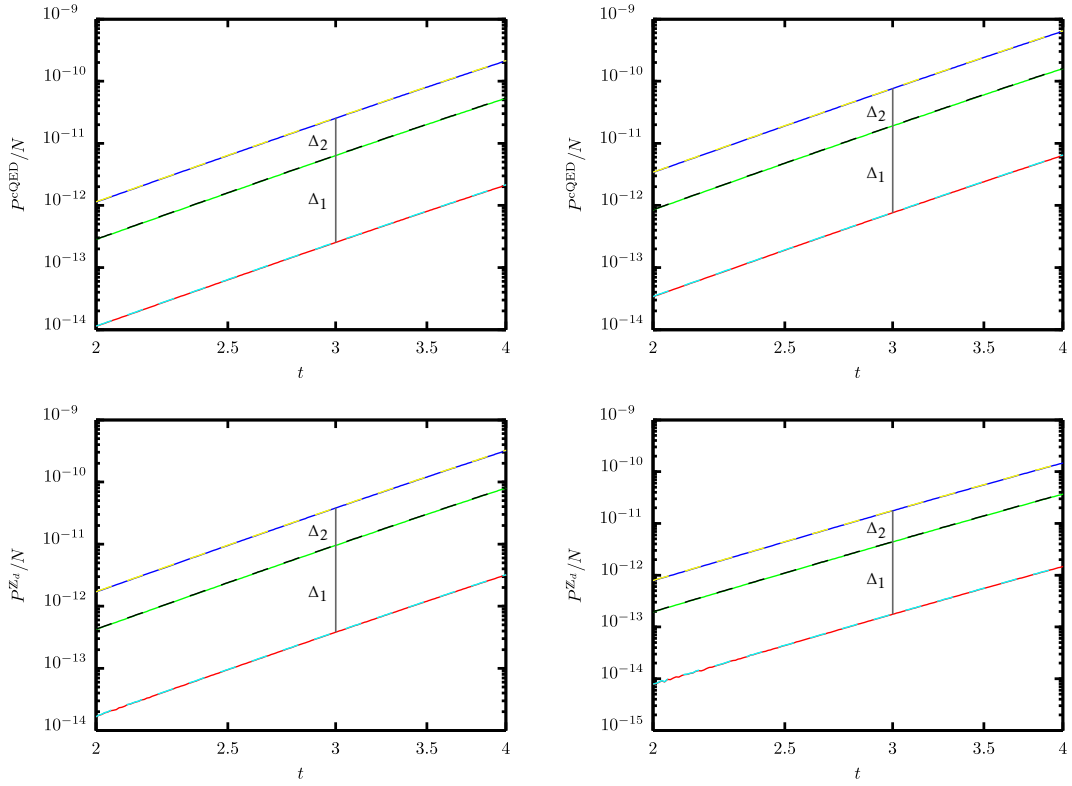

Figure 4.6: Penalty energy per site as a function of time for the cQED model (upper row) and the $\mathbb{Z}_d$ model (lower row) for $d_{\mathrm{link}} = 3$ (left column) and $d_{\mathrm{link}} = 5$ (right column) (both axes are on a logarithmic scale). The gray line indicates the point in time where we determined the offsets Δ_1 and Δ_2. The red ($N = 50$) and cyan ($N = 100$) lines show the values for $\lambda = 1 \times 10^{-4}$, the green ($N = 50$) and the black ($N = 100$) lines show the values for $\lambda = 5 \times 10^{-4}$ and the blue ($N = 50$) and yellow ($N = 100$) lines show the values for $\lambda = 1 \times 10^{-3}$.

physical dimension of the gauge variables, in accordance with the observed gap.

Moreover, our results for the procedure for adiabatic preparation of the ground state in the presence of noise give evidence that it is to some extent robust to noninvariant terms, as the energy can still be reliably determined up to a certain noise level. This is promising, as it demonstrates that even if the gauge invariance is broken, which could happen due to noise or at the fundamental level of interactions among the basic ingredients, the proposals do not immediately lose their predictive power. Furthermore, the scaling of our results is in good agreement with a perturbative calculation.

In our simulations, we proposed a polynomial ramp for x, slow enough to achieve the desired preparation. However, with the observation that the gap opens with increasing values of x and the results from the perturbative

calculation, one could think about designing an optimized ramp $x(t)$. Furthermore optimal control concepts could also be helpful to design optimized ramps [227]. On the one hand, this could allow shorter total evolution times while keeping the same level of overlap with the exact ground state in the noise-free case. On the other hand, one could possibly achieve a better scaling of the Gauss law violation with time in the presence of noninvariant terms and therefore improve the robustness of the preparation scheme proposed.

Chapter 5

The multiflavor Schwinger model at nonzero chemical potential

Quantum simulators for LGT, as the examples we studied in the previous Chapter, are in the long run arguably the most promising approach to overcome the limitations faced in MC simulations. However, despite nowadays unprecedented level of experimental control, the practical implementation is technically challenging. Although recently a first realization in a small system has been demonstrated [102], it will still take some time until a fully fledged quantum simulator being able to address interesting problems and system size is available. On the other hand, classical simulations are not yet exhausted with currently used methods. TN represent a tool that can take classical computations to regimes and problems beyond those amenable with conventional numerical approaches to LGT. One clear example is that of scenarios with a sign problem. In this Chapter we illustrate this potential using the multiflavor Schwinger model as a benchmark and explore the phase structure for the two-flavor case at finite chemical potential, a regime intractable with conventional MC methods. Moreover, we also study the position resolved chiral condensate in the different phases and address the question of spatial inhomogeneities in the ground state of the model. Regarding the simulations in this Chapter, we decide to proceed different to the previous one. There we used a formulation, where the link Hilbert spaces were truncated to a finite dimension. While this approach can be generalized to higher dimensions and more complicated gauge groups [60, 78, 80, 83, 84, 87, 88, 90, 93, 96, 98, 148, 160, 228], here we take advantage of the fact that for 1+1 dimensional systems with OBC the gauge degrees of freedom can be integrated out, as we showed in Sec. 2.3. The results presented in this Chapter have been published in Refs. [47–49] and the rest of the Chapter is a modification of Refs. [47, 48].

5.1 Introduction

The TN approach should provide a very general solution in regimes where MC simulations suffer from the sign problem. This is most apparent in the PEPS

construction for fermionic systems in 2 or higher dimensions [213, 216, 217]. Even for the one-dimensional case, we can already demonstrate this feature, a task that we tackle in this Chapter. A simple example is offered by the multiflavor Schwinger model at nonzero chemical potential. For the two-flavor case with equal masses for both flavors, on which we focus here, the model has an SU(2) isospin symmetry between the flavors and is in many aspects similar to QCD as it shows confinement, a nonvanishing chiral condensate and an anomalous U(1) current in the massless limit. The phase structure for two flavors of massless fermions was determined analytically in Refs. [229, 230], where it was found that at zero temperature the model supports an infinite number of phases characterized by the isospin number and separated by first-order phase transitions. Moreover, there is an ongoing discussion about spatial inhomogeneities in the ground state of the model. Similar to the large N_c limit of QCD at high density [231], the chiral condensate for the two-flavor case is predicted to have an oscillatory behavior, too [232].

Here, we numerically study these aspects with MPS using the Hamiltonian lattice formulation of the model. First, we analyze the phase structure and perform a full calculation in regimes where MC simulations would suffer from a sign problem. We go through the full extrapolation procedure to recover the continuum limit, to explicitly show the power of TN approaches for overcoming the sign problem. As a first necessary step, we reproduce the analytical prediction for massless fermions from Refs. [229, 230] with great precision. Furthermore, our calculation can be readily extended to the massive case, where no analytical computations are available. For the massive case we observe that the phase structure of the model changes significantly. Using the MPS approach, and considering the case of vanishing background field, we are able to map out accurately the phase diagram of the model in the mass - chemical potential plane for a fixed volume. Our results thus constitute an explicit demonstration that MPS allow reliable numerical simulations in a regime where the MC approach would suffer from the sign problem.

Second, taking advantage of the fact that the MPS approach to the Hamiltonian formulation also explicitly yields the ground-state wave function, we can also compute the spatially resolved chiral condensate within the phases and address the question of spatial inhomogeneities in the ground state for the massless case. We find that the condensate shows sinusoidal oscillations, consistent with analytical calculations for the fermion bilinears in the two-flavor case [232], and we quantify the dependence of their amplitude and their frequency on the isospin density.

The rest of the Chapter is organized as follows. In Sec. 5.2 we briefly introduce the formulation we are using and comment on the numerical methods we are applying. In Secs. 5.3 and 5.4 we present our results for the phase structure and the spatially resolved chiral condensate before concluding in Sec. 5.5.

5.2 Model and methods

We again adopt the compact lattice formulation with Kogut-Susskind staggered fermions from Sec. 2.3. The physical states, $|\Psi\rangle$, in the sector of vanishing external charge have to satisfy the Gauss law, $G_n|\Psi\rangle = 0\ \forall n$, where G_n are the generators for gauge transformations, given by Eq. (2.36). For OBC, this allows us to integrate out the gauge fields, as we showed in Sec. 2.3. Assuming zero electric field on the left boundary and applying a rescaling that makes it dimensionless [121], the Hamiltonian from Eq. (2.38) reads[1]

$$\begin{aligned} W = &- ix \sum_{n=0}^{N-2} \sum_{f=0}^{F-1} \left(\psi_{n,f}^\dagger \psi_{n+1,f} - \text{h.c.} \right) + \sum_{n=0}^{N-1} \sum_{f=0}^{F-1} \left(\mu_f (-1)^n + \nu_f \right) \psi_{n,f}^\dagger \psi_{n,f} \\ &+ \sum_{n=0}^{N-2} \left(\sum_{k=0}^{n} \left(\sum_{f=0}^{F-1} \psi_{k,f}^\dagger \psi_{k,f} - \frac{F}{2} (1 - (-1)^k) \right) \right)^2 , \end{aligned} \tag{5.1}$$

where the adimensional parameters of the problem in units of the coupling, g, are $x = 1/(ag)^2$, $\mu_f = 2\sqrt{x} m_f / g$ and $\nu_f = 2\sqrt{x}\kappa_f / g$. In the following, we will focus on the case of two flavors in the sector of vanishing total charge, for which the conventional MC approach in general suffers from the sign problem.[2]

To study the phase structure of the model, we use the MPS ansatz introduced in Chapter 3, and compute the ground state of the Hamiltonian variationally. In order to show that MPS allow for reliable calculations with proper continuum limit in the regime of the sign problem, we first reproduce the analytical predictions for the massless case from Refs. [229, 230], which studied the continuum model in a fixed volume. To compare to these results, we consider lattices of constant volume, $Lg = N/\sqrt{x}$. The isospin number on the lattice is defined to be $\Delta N = N_0 - N_1$, with $N_i = \sum_{n=0}^{N-1} \psi_{n,i}^\dagger \psi_{n,i}$. As we are going to show in the following Section, the Hamiltonian (5.1), up to a constant, only depends on the difference between the chemical potentials, $\nu_1 - \nu_0$, commonly called the isospin chemical potential in the literature. Thus we study ΔN in the ground state as a function of the difference between the chemical potentials. Following Refs. [229, 230], we define the rescaled isospin chemical potential $\mu_I / 2\pi = N(\nu_1 - \nu_0)/4\pi x$, and hereafter we fix $\nu_0 = 0$ and only vary ν_1. We are thus studying the model in a situation where MC suffers from the sign problem.

[1] Contrary to Sec. 2.3, we label the sites and flavors starting with a 0 instead of a 1, because this turns out to be favorable for the later spin formulation.

[2] It has been noticed that in the special case $\nu_0 + \nu_1 = 0$ and in certain restricted parameter regimes the sign problem can be circumvented for massless fermions [20, 21, 229]. However, here we adopt a general prescription, common for massless and massive cases, where this does not apply.

In order to be able to extrapolate to the continuum limit, we consider several lattice spacings corresponding to $x \in [9, 121]$. Moreover, to probe for possible finite volume effects, we explore several volumes, $Lg = 2, 6, 8$. As we have seen in Sec. 3.2, MPS calculations are subject to a truncation error due to the limited bond dimension reachable, bounded by the computational cost of treating too large matrices in the variational ansatz. To control this truncation error, we repeat the computation for each combination of $(Lg, x, \mu_I/2\pi)$ for several bond dimensions, $D \in [40, 220]$, and extrapolate to $D \to \infty$ (see App. B.2 for details on the extrapolation procedure). For the numerical simulations we again map Eq. (5.1) to a spin chain by a Jordan-Wigner transformation (details about the spin formulation are given in the App. A.1).

5.3 Phase structure

5.3.1 Exact dependence on the isospin number

Before turning to our numerical results, let us briefly discuss the dependence of the phase structure on the isospin number. A short calculation shows that the Hamiltonian from Eq. (5.1) conserves N_0 and N_1 as well as $N = N_0 + N_1$ in the sector of vanishing total charge, in which we work. Hence it is block diagonal and the blocks can be labeled with $(N, \Delta N = N_0 - N_1)$. Inside a block the chemical potential terms are proportional to the identity and the Hamiltonian can be written as

$$W = \nu_0 N_0 + \nu_1 N_1 + W_{\text{aux}},$$

where W_{aux} sums up all remaining terms that are independent of the chemical potential. The ground-state energy of this Hamiltonian is given by

$$E_{(N,\Delta N)}(\nu_0, \nu_1) = \nu_0 N_0 + \nu_1 N_1 + E_{\min}(W_{\text{aux}}|_{(N,\Delta N)}) \tag{5.2}$$

$$= \frac{N}{2}(\nu_0 + \nu_1) - \underbrace{\frac{\Delta N}{2}}_{p_{(N,\Delta N)}}(\nu_1 - \nu_0) + E_{\min}(W_{\text{aux}}|_{(N,\Delta N)}). \tag{5.3}$$

where $E_{\min}(W_{\text{aux}}|_{(N,\Delta N)})$ is a block dependent, i.e. isospin number dependent constant. From the equation above, one can immediately see that having a single value for $E_{(N,\Delta N)}(\nu_0, \nu_1)$ available inside each block is enough to determine this constant. Moreover, Eq. (5.3) reveals that for fixed N the energy inside each block only depends linearly on $\nu_1 - \nu_0$, up to a (chemical potential dependent) constant, with a slope proportional to ΔN (see Fig. 5.1).

A first-order (discontinuous) quantum phase transition, and hence a discontinuity in the isospin number, occurs, if it is energetically favorable to go from one block characterized by $(N, \Delta N)$ to a neighboring block characterized by

$(N, \Delta\overline{N} = \Delta N \pm 2)$. Thus, the value of ΔN exhibits discontinuous changes, by two units as the isopsin chemical potential is increased (see Fig. 5.1). Hence the phase transitions and consequently the discontinuities in ΔN correspond to the intersection points of the two linear functions describing the energy inside these blocks, as can be seen in Fig. 5.1.

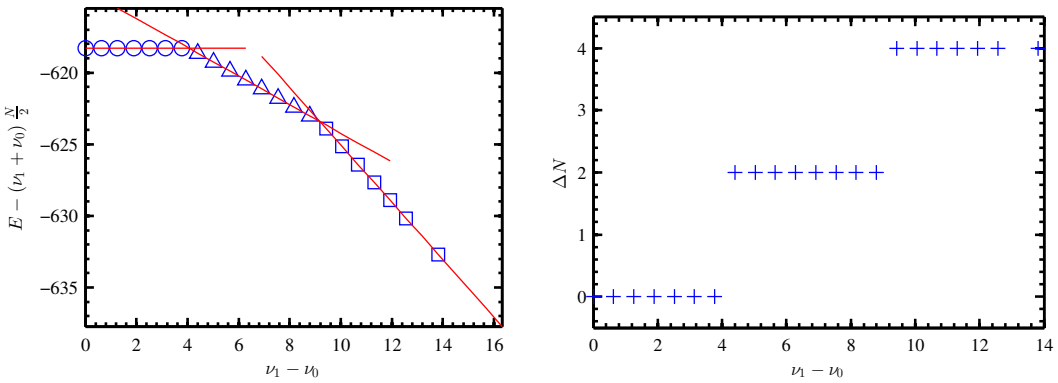

Figure 5.1: Ground state energy (left) and isospin number (right) and as a function of the chemical potential difference for $m/g = 0$, $Lg = 8$, $x = 16$, and $D = 160$. The different symbols in the left panel correspond to $\Delta N = 0$ (circles), $\Delta N = 2$ (triangles) and $\Delta N = 4$ (squares). The lines represent linear functions with slope $p_{(N,\Delta N)}$.

The intersection points can be computed analytically by solving the equation $E_{(N,\Delta N)}(\nu_0, \nu_1) = E_{(N,\Delta\overline{N})}(\nu_0, \nu_1)$. Plugging the explicit expressions from Eq. (5.3) into the relation, we obtain the following expression for the location of the discontinuities in the isospin number

$$(\nu_1 - \nu_0)|_{\text{jump}} = \frac{E_{\min}(W_{\text{aux}}|_{(N,\Delta\overline{N})}) - E_{\min}(W_{\text{aux}}|_{(N,\Delta N)})}{p_{(N,\Delta\overline{N})} - p_{(N,\Delta N)}} \tag{5.4}$$

$$= \frac{E_{(N,\Delta\overline{N})}(\bar{\nu}_0^*, \bar{\nu}_1^*) - \bar{\nu}_0^* N_0 - \bar{\nu}_1^* N_1 - E_{(N,\Delta N)}(\nu_0^*, \nu_1^*) + \nu_0^* N_0 + \nu_1^* N_1}{\overline{N}_0 - N_0}. \tag{5.5}$$

In the second line we have explicitly substituted p and used the observation that Eq. (5.2) allows us to determine $E_{\min}(W_{\text{aux}}|_{(N,\Delta N)})$ ($E_{\min}(W_{\text{aux}}|_{(N,\Delta\overline{N})})$) at arbitrary values ν_0^*, ν_1^* ($\bar{\nu}_0^*$, $\bar{\nu}_1^*$). In our simulations we can extract the isospin number as well as the ground-state energies, where the former can be determined exactly as the Hamiltonian conserves N_0 and N_1, which enables us to compute the location of the phase transitions using Eq. (5.5). The overall precision we can achieve for $(\nu_1 - \nu_0)|_{\text{jump}}$ only depends on the precision for the ground-state energies extracted from our simulations. Assuming a systematic

error of ΔE in the energies due to the truncation error in our simulations, one obtains for the error of the location of the phase transition

$$\begin{aligned}\Delta(\nu_1-\nu_0)|_{\text{jump}} =& \left|\frac{\partial(\nu_1-\nu_0)|_{\text{jump}}}{\partial E_{(N,\Delta\overline{N})}(\vec{\nu}_0^*,\vec{\nu}_1^*)}\Delta E_{(N,\Delta\overline{N})}(\vec{\nu}_0^*,\vec{\nu}_1^*)\right| \\ &+\left|\frac{\partial(\nu_1-\nu_0)|_{\text{jump}}}{\partial E_{(N,\Delta N)}(\nu_0^*,\nu_1^*)}\Delta E_{(N,\Delta N)}(\nu_0^*,\nu_1^*)\right| \\ =&\frac{1}{\left|p_{(N,\Delta\overline{N})}-p_{(N,\Delta N)}\right|}\left(\left|\Delta E_{(N,\Delta\overline{N})}(\vec{\nu}_0^*,\vec{\nu}_1^*)\right|+\left|\Delta E_{(N,\Delta N)}(\nu_0^*,\nu_1^*)\right|\right).\end{aligned} \tag{5.6}$$

5.3.2 Numerical results

Phase structure for the massless case

In order to determine the phase structure for the massless case, we repeat the calculation for several lattice spacings and select for every spacing a single data point inside of each of the phases, where we determine N_0 and N_1. To estimate the corresponding exact energy value and our numerical error for a given lattice spacing, we extrapolate our data in bond dimension, as described in App. B.2. Subsequently, we extract for every value of x the location of the phase transition and estimate the error using Eqs. (5.5) and (5.6), as described in the previous Section. In a final step, we extrapolate these values to the continuum limit corresponding to $1/\sqrt{x} = ag \to 0$ (see App. B.2 for details). The results for the phase structure after extrapolating to the continuum are shown in Fig. 5.2 and Tab. 5.1. For the first two transitions, our continuum estimates do not show any volume dependence, in agreement with Refs. [229, 230]. However, for transitions between phases with larger ΔN, we can see that for volume $Lg = 2$ there are deviations due to finite volume effects, which disappear for a larger volume, $Lg = 6$, for which we recover the analytical results in the entire parameter regime under study. We conclude that the transitions occur for $\mu_I/2\pi$ values which are odd multiples of 1/2, in agreement with the analytical results. The finite volume effects found in our MPS calculation for small Lg can be explained because the total fermion number coincides with the number of sites, $N_0 + N_1 = N$. Hence, the system size ultimately upper bounds N_i and larger values for ΔN at fixed volume would require larger system sizes and correspondingly larger values of x to reach the correct continuum limit.

Phase structure for the massive case

While the analytical calculation in Refs. [229, 230] is limited to the massless case, the MPS formalism can deal with (arbitrary) mass values. Repeating the

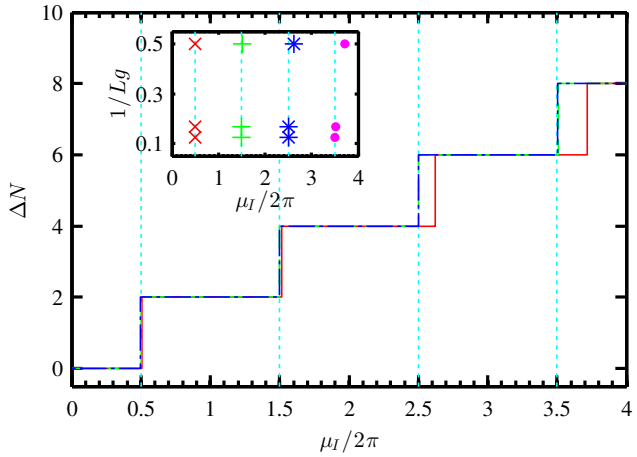

Figure 5.2: Inset: Continuum estimate of the location of the phase transition versus inverse volume for the first (red ×'s), second (green crosses), third (blue asterisks) and fourth (magenta dots) transition. Main plot: Continuum estimate for ΔN as a function of $\mu_I/2\pi$, for volumes 2 (red solid line), 6 (green dashed line) and 8 (blue dash-dotted line). The (dotted) vertical lines indicate the theoretical prediction for the phase transitions in the massless case.

Volume	1. transition	2. transition	3. transition	4. transition
$Lg = 2$	0.499960(88)	1.513345(47)	2.617208(11)	3.716041(12)
$Lg = 6$	0.499(21)	1.501(23)	2.504(22)	3.511(20)
$Lg = 8$	0.497(49)	1.501(60)	2.502(55)	3.505(51)

Table 5.1: Continuum estimates for the locations of the first four phase transitions for the massless case $m/g = 0$.

same calculations and extrapolation procedure for $m/g = 0.5$, we obtain the results shown in Fig. 5.3. Comparing Figs. 5.2 and 5.3, we observe that the new energy scale introduced by m/g leads to a change in the phase structure, as the locations of the first-order phase transitions are not equidistantly spaced anymore. The continuum estimates show a clear dependence on the volume, even for the first phase transition, and the size of the plateaus is no longer equal.

Computing the phase structure for several masses, we can map out the phase diagram for the model in the $(m/g, \mu_I/2\pi)$-plane for a fixed volume. Fig. 5.4 shows the results for volume $Lg = 8$. One can see that for larger masses the phase characterized by $\Delta N = 0$ survives up to noticeably larger values of $\mu_I/2\pi$ and the size of the region for the $\Delta N = 2$ phase shrinks for larger masses. The regions describing phases with larger values for ΔN are less affected and only slightly bend towards higher values of the chemical potential difference. Tabs. 5.2 - 5.4 reveal that also for a smaller volume of $Lg = 6$ the effect of the nonzero

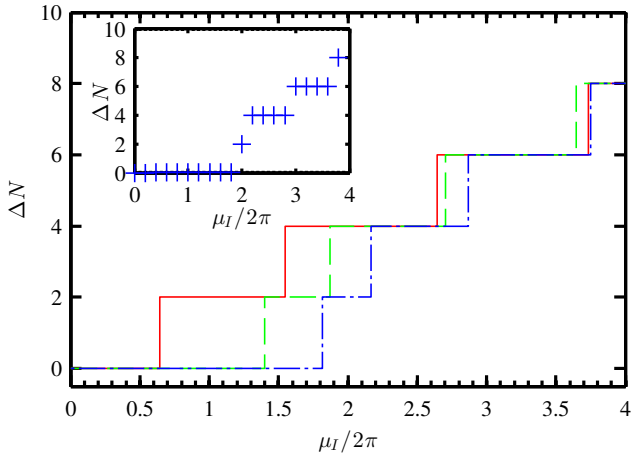

Figure 5.3: Inset: Isospin number as a function of $\mu_I/2\pi$ for $Lg = 8$, $x = 121$, $m/g = 0.5$ and $D = 220$. Main plot: Continuum estimate for ΔN as a function of $\mu_I/2\pi$, for volumes 2 (red solid line), 6 (green dashed line) and 8 (blue dash-dotted line).

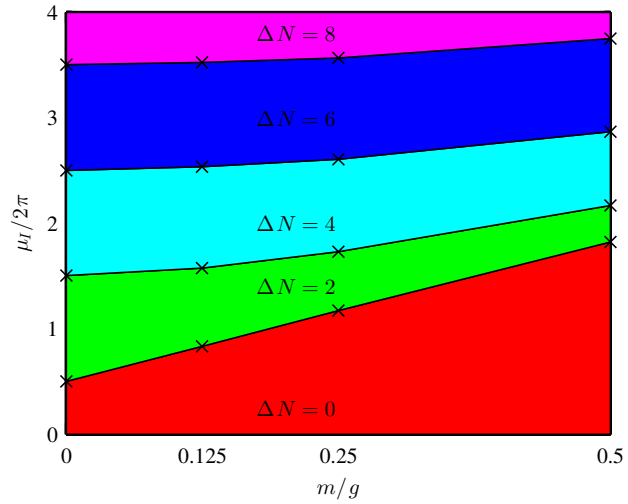

Figure 5.4: Phase diagram in the $(m/g,\ \mu_I/2\pi)$-plane for volume $Lg = 8$. The different colors indicate the regions for the different phases characterized by different values of ΔN. The black ×'s mark the data points obtained after the extrapolation procedure.

mass is similar. For increasing values of m/g the phase transitions are displaced to larger values of $\mu_I/2\pi$ and again the transition from the $\Delta N = 0$ phase to the $\Delta N = 2$ phase is most affected. For $Lg = 2$ we again observe the trend that the phase transitions shift to larger values of the isospin chemical potential with increasing mass, however, the effect is less pronounced compared to the larger

volumes as Tabs. 5.2 - 5.4 show.

Volume	1. transition	2. transition	3. transition	4. transition
$Lg = 2$	0.522620(86)	1.515910(40)	2.620237(14)	3.716558(20)
$Lg = 6$	0.711(19)	1.538(26)	2.519(23)	3.520(20)
$Lg = 8$	0.831(42)	1.575(65)	2.532(57)	3.523(52)

Table 5.2: Continuum estimates for the locations of the first four phase transitions for $m/g = 0.125$.

Volume	1. transition	2. transition	3. transition	4. transition
$Lg = 2$	0.554897(76)	1.522594(40)	2.624794(14)	3.720370(19)
$Lg = 6$	0.938(16)	1.617(26)	2.558(23)	3.546(20)
$Lg = 8$	1.165(39)	1.728(66)	2.606(57)	3.571(52)

Table 5.3: Continuum estimates for the locations of the first four phase transitions for $m/g = 0.25$.

Volume	1. transition	2. transition	3. transition	4. transition
$Lg = 2$	0.643234(66)	1.548542(35)	2.644094(11)	3.732926(20)
$Lg = 6$	1.402(12)	1.874(23)	2.703(22)	3.647(20)
$Lg = 8$	1.816(24)	2.168(53)	2.871(55)	3.752(49)

Table 5.4: Continuum estimates for the locations of the first four phase transitions for $m/g = 0.5$.

This behavior can be understood qualitatively as follows. Since the only mass dependent contribution to the energy is given by $E_{\min}(W_{\text{aux}}|_{(N,\Delta N)})$ (see Eqs. (5.2) and (5.3)), a nonvanishing mass leads to a shift, $\Delta E_{\min}$, in this quantity with respect to the massless case:

$$E_{\min}(W_{\text{aux}}|_{(N,\Delta N)}) = E_{\min}(W_{\text{aux}}|_{(N,\Delta N)})|_{m/g=0} + \Delta E_{\min}.$$

Equation (5.4) reveals that these energy shifts affect the locations of the phase transitions, as soon as they are distinct for every phase. Extracting $\Delta E_{\min}/N$ inside each phase for our smallest lattice spacing for several masses, we obtain the results shown in Fig. 5.5, which show that the values for the shifts are indeed different for each phase. In particular, we see that for the phase characterized by $\Delta N = 0$, the energy shift is a lot more pronounced than for the phase characterized by $\Delta N = 2$, thus explaining the significant displacement towards higher values of $\mu_I/2\pi$ for the location of the first phase transition with respect to the massless case. For phases with larger isospin number, the energy shifts

differ less, consistent with the observation that the locations of the phase transitions between these phases are less affected. Although for all three volumes studied we observe similar energy shifts, Fig. 5.3 as well as Tabs. 5.2 - 5.4 show that for $Lg = 2$ the locations of the phase transitions are less affected by a nonzero fermion mass. This is likely due to the finite volume effects arising from the fact that the total fermion number corresponds to the number of sites, as we have seen for the massless case.

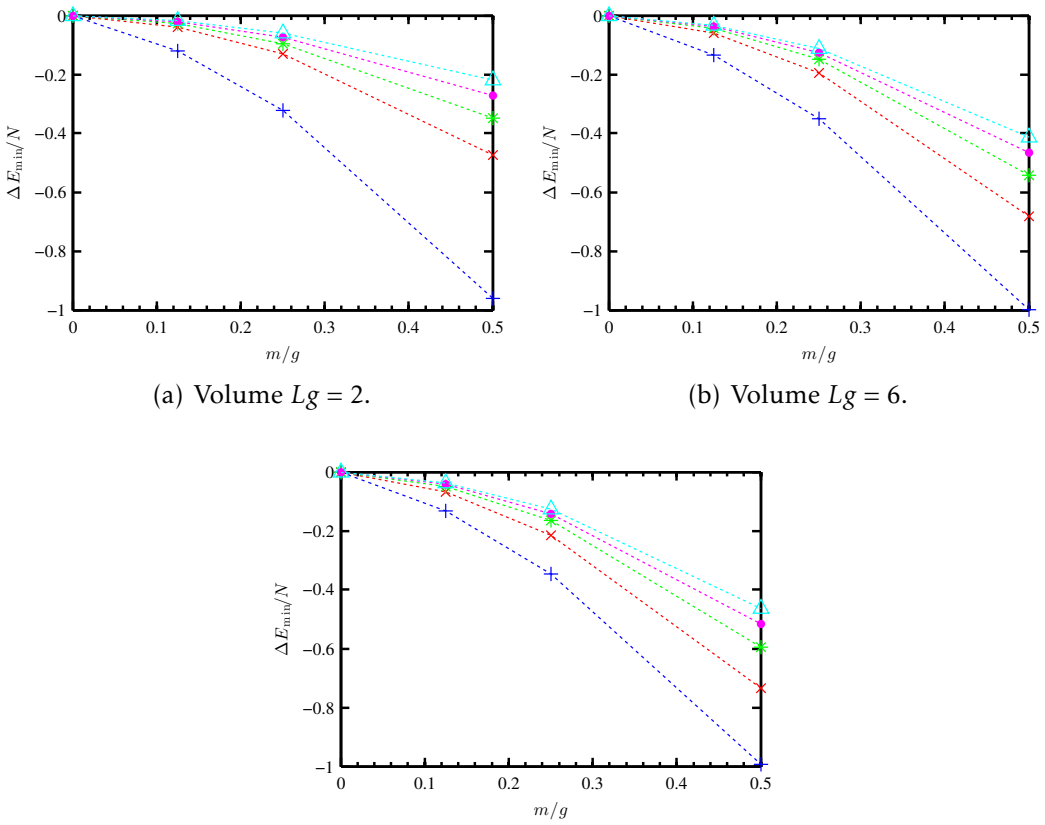

(a) Volume $Lg = 2$.

(b) Volume $Lg = 6$.

(c) Volume $Lg = 8$.

Figure 5.5: Energy shift per site $\Delta E_{\min}/N$ as a function of m/g for $x = 121$ and volumes $Lg = 2$ (a), $Lg = 6$ (b) and $Lg = 8$ (c). The different markers indicate the different phases characterized by the isospin number, blue crosses represent $\Delta N = 0$, red ×'s $\Delta N = 2$, green asterisks $\Delta N = 4$, magenta dots $\Delta N = 6$ and cyan triangles $\Delta N = 8$. As a guide for the eye the data points are connected with dotted lines.

5.4 Chiral condensate

A further advantage of the MPS method is that not only it is free from the sign problem, but at the end of the computation it also yields the ground-state wave function, hence giving easy access to any observables that can be expressed as a MPO. An interesting observable is the chiral condensate. For the single-flavor Schwinger model analytical computations show that the condensate at any finite density has the form of a standing wave [233–235], $\langle\bar{\psi}(y)\psi(y)\rangle = \langle\bar{\psi}\psi\rangle_0 \cos(2\kappa y)$, where ψ is a two component Dirac spinor, $\langle\bar{\psi}\psi\rangle_0$ the (spatially homogeneous) zero-density expectation value for the chiral condensate and κ is the chemical potential. A possible explanation for the oscillations, put forward in Ref. [236], linked the phenomenon to the breaking of translational invariance due to the introduction of a uniform background charge. For the multiflavor case, which was addressed in Ref. [232], it was also found that fermion bilinears show spatial inhomogeneities.

In order to address this question, we compute the spatially resolved condensate in the ground state. In our lattice formulation the condensate corresponds to $C(y = 2n/\sqrt{x}) = \sum_{f=0}^{1}(C_{n,f} + C_{n+1,f})$, $n = 0, 2, 4, \ldots$, where $C_{n,f} = \frac{\sqrt{x}}{N}(-1)^n \psi^\dagger_{n,f}\psi_{n,f}$. To account for the staggered formalism, the condensate is summed over each pair of even and odd neighboring sites.[3] We focus on the massless case, $m/g = 0$, at fixed volumes Lg ranging from 2 to 16. Different to the simulations for the phase structure, we use a very fine lattice spacing, corresponding to $x = 1024$, for which lattice effects are very small and do not extrapolate to the continuum limit. Moreover, we fix $D = 160$ for all the rest which is sufficiently large to control truncation errors well enough.

To assess the effect of the chemical potential (and hence different isospin number) on the condensate, we choose a point in every phase and compute the position dependent condensate, $\langle C(y)\rangle$, for each case. The results are shown in Fig. 5.6. For $\Delta N = 0$, the condensate is homogeneous, except close to the edges, what we interpret as small finite size effects. For $\Delta N > 0$, by contrast, we observe sinusoidal oscillations with an amplitude close to the condensate value at vanishing ΔN. At a fixed volume, the frequency of the oscillations increases with the isospin number, ΔN, and we observe $\Delta N/2$ oscillation periods inside our system.

Our data suggest that the oscillations for $\Delta N > 0$ are of the form $\langle C(y)\rangle = A\cos(\omega y + \theta) + B$ and thus we fit it to this function to extract the amplitude A, frequency ω, phase shift θ and offset B. Determining these parameters for several system sizes and several phases, we obtain the results shown in Figs. 5.7 and 5.8, where the error bars correspond to 1σ confidence intervals for the fit

[3] For convenience in the visualization, we also sum both flavors for each site. However, we observe the same behavior for each individual flavor.

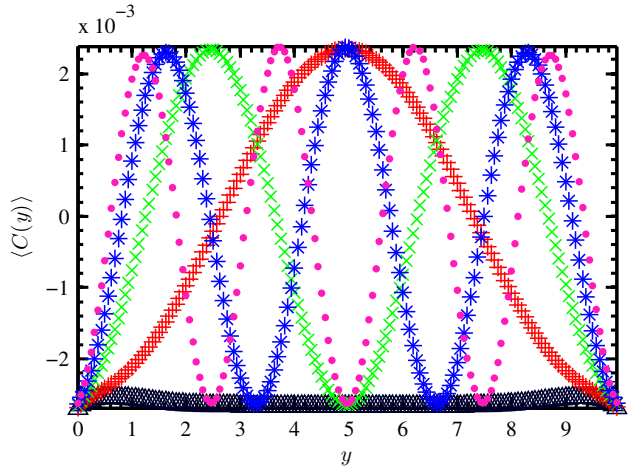

Figure 5.6: Expectation value of the chiral condensate as a function of position for $Lg = 10$. The different curves correspond to different phases characterized by different ΔN, black triangles represent $\Delta N = 0$, red crosses $\Delta N = 2$, green ×'s $\Delta N = 4$, blue asterisks $\Delta N = 6$ and magenta dots $\Delta N = 8$.

parameters.[4] The frequency, depicted in Fig. 5.7(a), shows a clear dependence on the isospin density, $\Delta N/Lg$. For $Lg > 2$ we see a linear decrease with increasing volume for each phase, as inside every phase we always have $\Delta N/2$ oscillation periods, independently of volume. The deviations for volume 2 are likely due to remaining lattice effects, which become increasingly important for small volumes and large ΔN, as observed in the previous Sections. As Fig. 5.7(b) reveals, the amplitudes of the oscillations are close to the expectation value of the condensate in the $\Delta N = 0$ phase, $\langle C \rangle_0$. We observe that for $\Delta N > 2$, the values obtained for A deviate less from $\langle C \rangle_0$ than those for $\Delta N = 2$ and that there is hardly any change with volume, except for the smallest volume $Lg = 2$.

The phase shift, θ, depicted in Fig. 5.8(a), shows a similar behavior. While for $\Delta N > 2$ the data approaches zero for increasing volume, there is no clear trend towards zero for $\Delta N = 2$. Finally, the offset, B, converges to zero for large volumes, with the smallest values found for $\Delta N = 2$. For $\Delta N > 2$ there is hardly any difference between the offset for different phases anymore.

[4] Notice that we have not performed a continuum extrapolation, different to our simulations for the phase structure, but the results presented correspond to a fixed (albeit very small) lattice spacing.

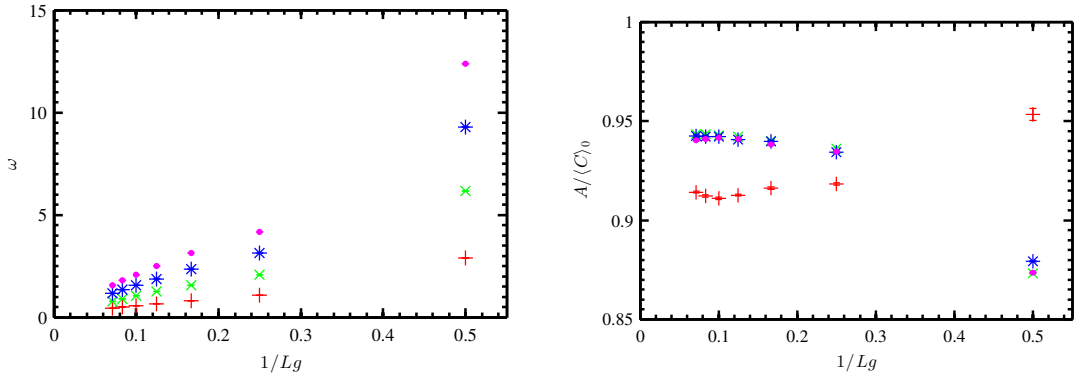

(a) Frequency (b) Amplitude

Figure 5.7: Frequency ω (left) and amplitude A in units of the zero density expectation value (right) as a function of inverse volume for different phases, where the red crosses represent $\Delta N = 2$, the green ×'s $\Delta N = 4$, the blue asterisks $\Delta N = 6$ and the magenta dots $\Delta N = 8$.

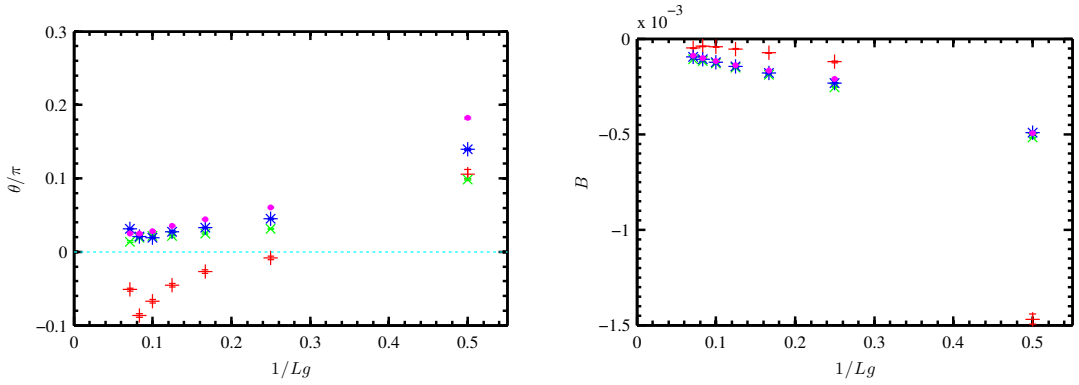

(a) Phase shift (b) Offset

Figure 5.8: Phase shift θ (left) and offset B (right) as a function of inverse volume for the different phases, where the red crosses represent $\Delta N = 2$, the green ×'s $\Delta N = 4$, the blue asterisks $\Delta N = 6$ and the magenta dots $\Delta N = 8$.

5.5 Conclusion

This Chapter illustrates a successful lattice calculation with TN in a regime, where the conventional MC approach suffers from the sign problem. Our results for the phase structure for the massless case in a sufficiently large volume agree with great precision with the analytical calculations from Refs. [229, 230], and we recover the predicted locations of the phase transitions after extrapolating to the continuum limit. Furthermore, our calculations can be immediately extended to the massive case, where no analytical results are available. In this case, the observed phase structure is significantly different, and the locations of the phase transitions are no longer independent of Lg. We can map out the phase diagram of the model at a fixed volume in the $(m/g, \mu_I/2\pi)$-plane, and we see that the transition from $\Delta N = 0$ to $\Delta N = 2$ is significantly shifted towards higher values of the chemical potential at the expense of the phase characterized by $\Delta N = 2$. Phases with larger values of ΔN are apparently less affected and only slightly shifted towards higher values of $\mu_I/2\pi$ for increasing mass.

Regarding the spatial structure of the ground state, our results for the condensate show a standing wave structure similar to the theoretically predicted behavior for the single-flavor case [233–235] and consistent with analytical calculations for the multiflavor case [232]. We fitted the results to an oscillatory function and analyzed the behavior of the various parameters in terms of isospin number and volume. For a fixed volume, we find that the frequency of the oscillations increases when the isospin number, which characterizes the phase, increases. Inside a phase with a given isospin number ΔN, we see $\Delta N/2$ oscillation periods of the condensate over the spatial extension of the system. Consequently, the frequency shows a linear decrease with the isospin density, $\Delta N/Lg$, except for the smallest volumes considered, which presumably suffer from enhanced lattice effects. The amplitudes of the oscillations are approximately given by the expectation value of the homogeneous condensate at vanishing isospin number, independently of volume. The observed offsets show a clear tendency towards zero for increasing volume, whereas for the phase shifts this tendency is less clearly visible. For phases characterized by $\Delta N > 2$ we observe that the shift is getting closer to zero, however for $\Delta N = 2$ there is no clear trend recognizable.

In our study, we focused on zero background field and temperature, with nonvanishing chemical potential, in order to explore a regime that suffers from the sign problem in conventional MC calculations. Notice, however, that the model also exhibits interesting features in other parameter regimes. In particular, in the absence of chemical potential and background field, it has been shown to have a second order phase transition for zero fermion mass at $T_c = 0$ [10, 237]. It might also show a transition, similar to the single flavor case, at nonvanishing background field, as has been argued in Ref. [238]. Adding a

background field as well as a generalization to nonzero temperature [40, 46, 50] is straightforward, hence these regimes are also amenable to tensor network studies.

Although we studied the two-flavor case, the MPS approach can be easily extended to an arbitrary number of flavors as shown in the App. A.1. Furthermore, with the MPS approach it is to some extent feasible to simulate real-time evolution [37], thus making it possible to address also dynamical aspects of the model. Moreover, our results can serve as a test bench for other methods trying to overcome the sign problem.

Chapter 6

Non-Abelian string breaking phenomena with matrix product states

In the previous Chapters we demonstrated the suitability of MPS for exploring Abelian gauge models and questions related the quantum simulation thereof. However, TN and in particular MPS are not limited to the Abelian case and are also adequate for studying non-Abelian gauge models. To illustrate that, we investigate the phenomenon of string breaking in a non-Abelian SU(2) LGT, where the gauge degrees of freedom are truncated to a finite dimension. In the spirit of a potential future quantum simulator, we consider systems of finite size and with a finite lattice spacing. The results presented here have been published in Ref. [43] and the rest of the Chapter is a slight modification thereof.

6.1 Introduction

The phenomenon of string breaking, as a consequence of confinement, is one of the most fundamental aspects of the Standard Model. While a comprehensive understanding in many cases, such as QCD, is still lacking, a lot of insight has been gained thanks to LGT [239–244]. Such studies are typically restricted to static properties or consider partly nondynamical scenarios, as for example the ground state in the presence of static external charges, whereas the TN approach does not suffer from such limitations.

In this Chapter, we consider dynamical aspects of the string breaking phenomenon for a non-Abelian LGT with dynamical charges in one spatial dimension. The Hamiltonian we simulate realizes an exact SU(2) gauge symmetry using a finite-dimensional representation for the bosonic degrees of freedom [57, 96]. This model is hence a suitable candidate for the design of an atomic quantum simulator of SU(2) LGT. The finite dimension of the link Hilbert spaces allows the simulation of the model via direct application of MPS techniques,

which we employ here in order to numerically explore the statical and dynamical aspects of the string breaking phenomenon.

Even if these scenarios can be realized in a future quantum simulator, measuring the string breaking phenomenon in an experiment is not trivial, especially for the dynamical case. In order to detect and characterize the breaking of the string, we propose three different observables. They can be monitored during the MPS simulation, and should in principle also be accessible in an experiment, so that our results will be measurable in a potential future quantum simulator.

More specifically we study three different scenarios.

1. *Ground state in the presence of static external charges*
   First, we consider the static aspects of string breaking by determining the ground state of the system, which includes fully dynamical fermions, in the presence of two additional external static charges. This calculation relates closely to the ones traditionally accessible by lattice MC methods. We show that we can reliably determine if the string is present, and therefore identify the regions where we expect string breaking to occur. These calculations additionally demonstrate the suitability of the proposed observables for the detection of string breaking in dynamical scenarios.

2. *Dynamics in the presence of static external charges*
   In the second place, we investigate the dynamics of string breaking by introducing the external static charges on top of the interacting vacuum and evolving the state in real time. When the string breaks, we can explicitly observe the screening of the charges via the creation of dynamical particles.

3. *Real-time dynamics with fully dynamical charges*
   Finally, we analyze how the picture changes when the charges added to the vacuum are themselves dynamical, a scenario which is closer to more realistic out-of-equilibrium situations. Also in this case we can recognize the string breaking if the fermion mass is small enough.

The rest of the Chapter is organized as follows. In Sec. 6.2 we briefly review the model and our numerical methods. In Sec. 6.3 we present our results for the static calculations. Section 6.4 contains the results for the real-time dynamics of string breaking with two static external charges. In Sec. 6.5 we present the results for the real-time dynamics of string breaking when a pair of dynamical charges is added to the interacting vacuum. To conclude, we summarize our findings in Sec. 6.6.

6.2 Model and methods

6.2.1 Truncated theory

The model we consider is the Hamiltonian formulation of a 1+1 dimensional SU(2) LGT with dynamical fermions, in which the gauge symmetry is exactly realized with finite-dimensional link variables [96, 245]. It can be understood as a truncation of the complete SU(2) gauge theory presented in Sec. 2.3. For convenience, we work in units of lattice spacing $a = 1$ and use an equivalent formulation of Eq. (2.39) which is related to the original one by a phase transformation on the fermion fields [144] and given by

$$H = \varepsilon \sum_{n=1}^{N-1} \left(\psi_n^\dagger U_n \psi_{n+1} + \text{h.c.} \right) + m \sum_{n=1}^{N} (-1)^n \psi_n^\dagger \psi_n + \frac{g^2}{2} \sum_{n=1}^{N-1} \mathbf{J}_n^2. \tag{6.1}$$

As we have seen previously, the physical states, $|\Psi\rangle$, have to be eigenstates of Gauss Law from Eq. (2.40), i.e. $G_n^a|\Psi\rangle = q_n^a|\Psi\rangle$ for all sites, n, where a nonzero value for q_n^a indicates a nonvanishing static external charge.

Starting from the strong-coupling state in Eq. (2.41), the application of the gauge invariant string operator

$$S_{nl} = \psi_n^\dagger U_n \dots U_{n+l-1} \psi_{n+l} \tag{6.2}$$

or its adjoint, $S_{nl}^\dagger$, for odd l,[1] generates a particle-antiparticle pair at sites n and $n+l$, connected by a flux tube of length l. Such configurations will have an excess of energy of $2m$ due to the particle-antiparticle pair, plus a flux energy proportional to the string length, l. Consequently, from a certain length on, it will be energetically favorable to reduce the flux energy by creating extra particle-antiparticle pairs, leading to configurations with a broken string.

As we discussed in detail in Sec. 2.3, for the complete SU(2) model the flux on a link is not bounded, and the dimension of the Hilbert space for each link is infinite. It is nevertheless possible to consider a theory truncated in a gauge invariant manner, where the maximum flux a link can carry is limited and the Hilbert spaces of the links are finite dimensional. Following the method in Ref. [57], each matrix element $(U_n)_{ll'}$ can be decomposed as a sum over all irreducible representations, which may be separated to summands that are gauge invariant themselves. Here we consider the model corresponding to the simplest nontrivial truncation of the full theory, meaning that only the trivial and the fundamental representation are kept, resulting in dimension 5 for the links. This would be the simplest nontrivial physical model for a quantum simulator following the proposals from Refs. [57, 80, 81].

[1] As we are working with a staggered formulation the odd (even) sites correspond to antiparticles (particles), consequently l has to be odd to create a string between an antiparticle and a particle.

6.2.2 Numerical approach

The string breaking phenomenon can be studied statically or dynamically. Here, we employ simulations of time evolution where the evolution operator is approximated via a first order Taylor expansion. This allows us to access both, the static and the dynamic scenarios, by respectively using imaginary or real time as explained in Sec 3.2. Additionally, the Taylor expansion preserves the symmetries of the Hamiltonian, such as gauge invariance. Then it is possible to explore a specific sector of the external charge distribution without explicitly implementing symmetries in the tensors.

The numerical simulations have three main sources of error, each of them controllable by a suitable choice of parameters. The first one is due to the approximation of the evolution operator via a Taylor series. This error can be controlled by choosing the time step suitably small. Another source of error is due to the limited bond dimension. By obtaining results with different bond dimensions, the size of this truncation error can also be estimated and controlled. As we are working with finite systems, a third source of error arises from finite-size effects which can be avoided by using sufficiently large systems.

Although TN and in particular MPS can be formulated in terms of fermionic degrees of freedom, we again choose to translate the fermionic degrees of freedom in Hamiltonian (6.1) to spins via a Jordan-Wigner transformation for our numerical simulations (details about the procedure and the relevant operators in spin formulation can be found in App. A.2) and in the following we work with the spin formulation.

6.2.3 Detection of string breaking

Detecting the presence or absence of the flux string during the evolution requires observables that are suitable for the dynamical case. The Wilson loop and more general correlation functions, widely used in lattice calculations to determine the static potential, are typically evaluated in the limit of large Euclidean time and therefore not suitable for our setup [112, 240, 243]. Instead, to detect strings and string breaking in the dynamical setup, we propose three different observables.

1. *Spin and flux configuration*
   In the first place, the spatially resolved spin and flux configurations in the system allow us to visualize the change with respect to the initial configuration (see e.g. Fig. 6.3).

2. *Local color imbalance*
   A second observable is the local imbalance between the different colors of fermions, also spatially resolved. A string operator from Eq. (6.2)

changes the fermionic content of the sites at its end-points, such that, on the strong-coupling vacuum, it will produce a superposition of states having a single red or a single green fermion at the beginning or at the end of the string. This can be detected by the operator $Q_n^{a\,2} = \frac{1}{4}(n_{r,n} - n_{g,n})^2$, where $n_{r,n}$ and $n_{g,n}$ are the occupation numbers for the two fermionic species[2] on site n.[3]

3. *Statistics of string lengths*
   A third observable can be proposed that looks only at the flux content of the links. Applying a string of length l, starting at site n, on the strong-coupling vacuum produces a state in which links between sites n and $n+l$ carry nonvanishing flux, whereas outside the region there is no flux. We can construct projectors P_{nl} on this kind of configurations. However, we are not interested in a single string but rather in the statistics of string lengths in a (time-dependent) state $|\Psi(t)\rangle$. Thus, we bin all strings of a certain length together and normalize by the number of possible strings of length l:

$$P_l = \frac{\sum_{n=1}^{N-l} \langle \Psi(t)|P_{nl}|\Psi(t)\rangle}{N-l}.$$

   In this way we can obtain histograms for the distribution of the string lengths in the state at a given time t.

As we show in the next Section, these three observables allow us to reliably determine whether our system still contains the initially imposed string or the string is broken. Taking advantage of the fact that in our MPS simulations we have access to wave function at all times, we can monitor their values throughout the entire evolution.

6.3 Ground state with static external charges

The usual way of probing for string breaking in lattice MC studies is the analysis of the static quark-antiquark potential. Using the MPS method, we can also determine the energy of an extra pair of external charges as a function of their

[2] In Sec. Sec. 2.3 we referred to the different color components of the spinor as $\pm 1/2$ to make the z-component of the angular momentum related to them explicit. Since for the considerations in this Chapter the explicit values of the different z-components are not important, we instead refer to them as r and g ("red" and "green") for illustrative purposes.

[3] One should note that the index a in $Q_n^{a\,2}$ is not summed. This might look puzzling at first, as it seems that we are using a non color-neutral object as observable. However, a little calculation shows (see App. A.2) that $Q_n^{a\,2}$ is identical for all a. Therefore summing the group index would only yield an additional factor of 3 which we are not taking into account.

distance by simply computing the ground state in a sector, where two external static charges are placed at the desired separation.

In particular, we choose two static external charges $q^y = \pm 1/2$, located in the central region of the system (to minimize finite-size effects) at a distance l. Gauge invariance requires that there is a flux tube connecting them. In the strong-coupling vacuum the charge at each site is zero, as well as the left and right electric field on each link. Consequently, we can prepare a state with the desired external charge distribution by applying the (noninvariant) operator $U_n \dots U_{n+l-1}$ on the strong-coupling ground state. This operator only acts on links from n to $n+l-1$, on which it creates a finite electric field. Hence the Gauss Law at the beginning and the end of the string yields a nonzero value corresponding to a state with $q^y_n = \pm 1/2$ and $q^y_{n+l} = \mp 1/2$. Subsequently we evolve this state in imaginary time to determine the ground state of the Hamiltonian for a chosen set of parameters, (ε, m, g).

In Fig. 6.1 we compare the ground-state energy E for $\varepsilon = 3.0$, $g = 1.0$ and various masses, where we subtracted the energy of the interacting vacuum without external charges E_{vac}. For $m = 3.0$ and $m = 5.0$ we observe three regions as functions of the string length. For short strings the energy grows linearly with the string length, indicating the stretching flux tube between the charges, namely the presence of the string in the ground state. From a certain length l_c on, the ground-state energy does not depend on l. This is the signature for string breaking, as after reaching the threshold for creating particle-antiparticle pairs, reducing the flux is energetically favorable, the string breaks and the energy is independent of the initial string length. Finally we observe a third region, when the string length is already close to the system size, and finite-size effects become noticeable. In our plots we clearly see that the values of l_c, where one transitions from the string region to the breaking region, are independent of the system size. For $m = 10.0$ the mass is large enough that one does not leave the linear scaling region, even if we create the longest string that fits in our system. Hence, we do not expect string breaking to occur in a system of this size.

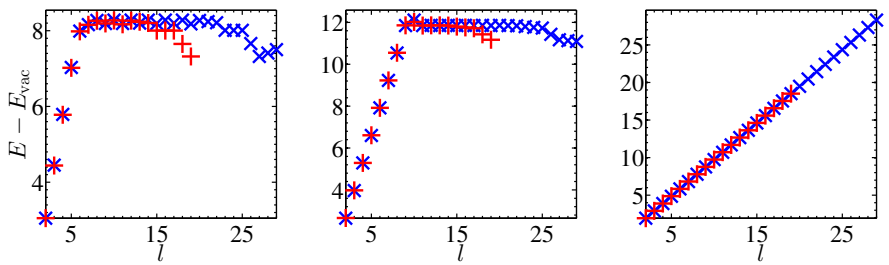

Figure 6.1: Ground-state energy for $N = 22$ (red crosses) and $N = 30$ (blue ×'s) as a function of the initial separation of the external charges for $m = 3.0$ (left panel), $m = 5.0$ (central panel) and $m = 10.0$ (right panel).

The difficulty of numerically detecting string breaking with MC techniques has been traced back to the mixing of two-meson states being hard to capture by Wilson loops [240, 241, 246]. With our method we can explicitly see this mixing happening, as illustrated by Fig. 6.2. The figure shows the energy as a function of imaginary time for several cases in the breaking region. At the beginning of the imaginary-time evolution, we observe the energy going down until it reaches a metastable plateau, corresponding to the interacting string state, evidenced by the spin and flux configurations at that point, shown in the left inset panels. For later times there is then again a significant decrease in energy corresponding to the breaking of the string. This can also be seen in the spin and flux configuration (right inset panels of Fig. 6.2), where the region of high flux between the static charges is going away after the decrease in energy, and only a peak in the flux around the external charges remains.

We illustrate the breaking and the nonbreaking scenario with two masses, $m = 3.0$ and 10.0, for which we monitor the spin, flux and charge square configurations throughout the whole imaginary-time evolution. Moreover, to probe for possible finite-size effects, we use different system sizes of $N = 22$ and 30. The results for these cases are shown in Fig. 6.3. The flux configuration is giving an indication that the particle-antiparticle pairs created during the breaking process are clustering around the heavy external charges and screen the electric flux. Furthermore Fig. 6.3 reveals that there is essentially no difference between both system sizes, thus showing that finite-size effects for this particular case are negligible.

In Fig. 6.4 we plot the charge squared $Q_n^{a\,2}$ and the histograms P_l for the initial configuration and for the final ground state respectively. Since the interacting vacuum in the sector without external charges of the theory also contains string configurations with a certain probability distribution, we subtract this configuration in order to better visualize the difference. As one can see, in the breaking case two peaks around the external charges form in the charge square configuration, thus verifying that the particles created during the breaking process indeed cluster around the external charges and screen the flux. By contrast, in the nonbreaking case the charge square configuration only changes slightly. The histograms for the string lengths show a similar picture. In the nonbreaking case the clear initial peak at $l = 11$ is preserved, whereas for $m = 3.0$ it vanishes and peaks emerge around smaller string length.

For all the results presented in this Section we used a time step $\Delta t = 1.0 \times 10^{-3}$ and a bond dimension $D = 100$, parameters which turn out to be sufficient to avoid noticeable numerical errors (see App. B.3 for a more detailed error analysis).

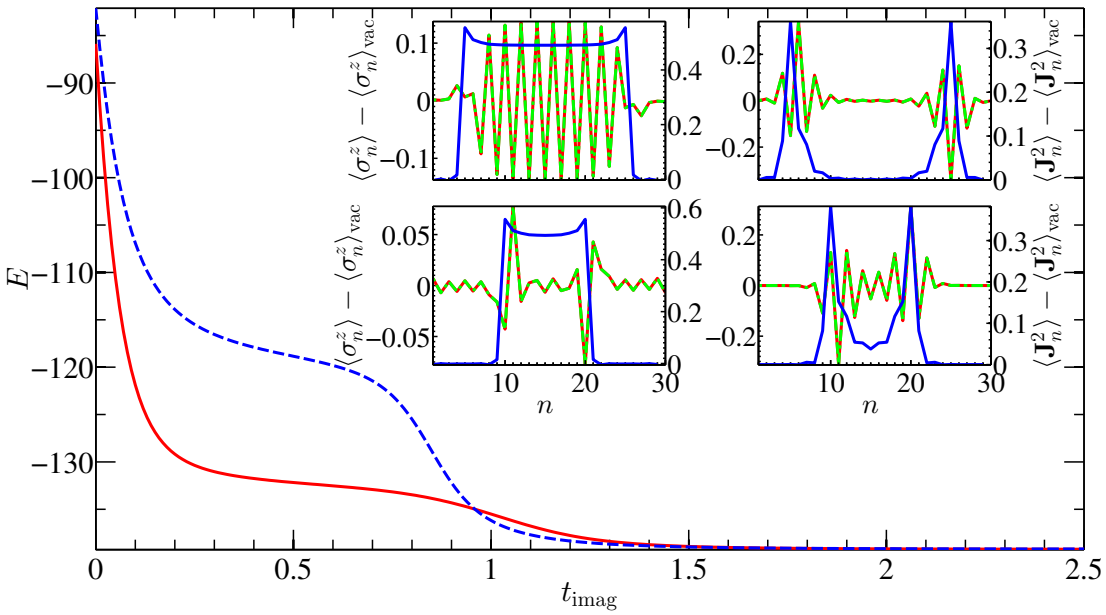

Figure 6.2: Energy as function of imaginary time for $N = 30$, $m = 3.0$, $l = 11$ (red solid line) and $l = 21$ (blue dashed line). The insets show the difference of expectation values for $\sigma^z_{r,n}$ (red lines, left y-axes), $\sigma^z_{g,n}$ (green lines, left y-axes), and $\mathbf{J}^2_n$ (blue lines, right y-axes) with respect to the interacting vacuum, shortly before and after the drop in energy (left upper panel: $l = 21$, $t = 0.75$, right upper panel: $l = 21$, $t = 1.25$; left lower panel: $l = 11$, $t = 0.5$, right lower panel: $l = 11$, $t = 1.25$).

6.4 Real-time evolution with static external charges

From Fig. 6.1 we can identify the parameter regions in which we expect string breaking to occur. To study the real-time dynamics of the string breaking we select two distinct situations. We choose $l = 11$, which is deeply in the breaking region for $m = 3.0$ but still far enough from the point where finite-size effects are noticeable, and for which we do not expect any string breaking with $m = 10.0$. For all the following real-time cases we set $\varepsilon = 3.0$ and $g = 1.0$, as in the imaginary-time setup.

MPS methods give us access not only to the static properties, but also to the real-time dynamics of the system. We may then investigate how the string breaking process manifests dynamically when the static charges are introduced in the interacting vacuum. To this end, we first compute a MPS approximation to the interacting vacuum of the theory using the variational energy minimization discussed in Sec. 3.2. Starting from this state, we apply again the non gauge invariant operator $U_n \dots U_{n+l-1}$, which effectively creates two static exter-

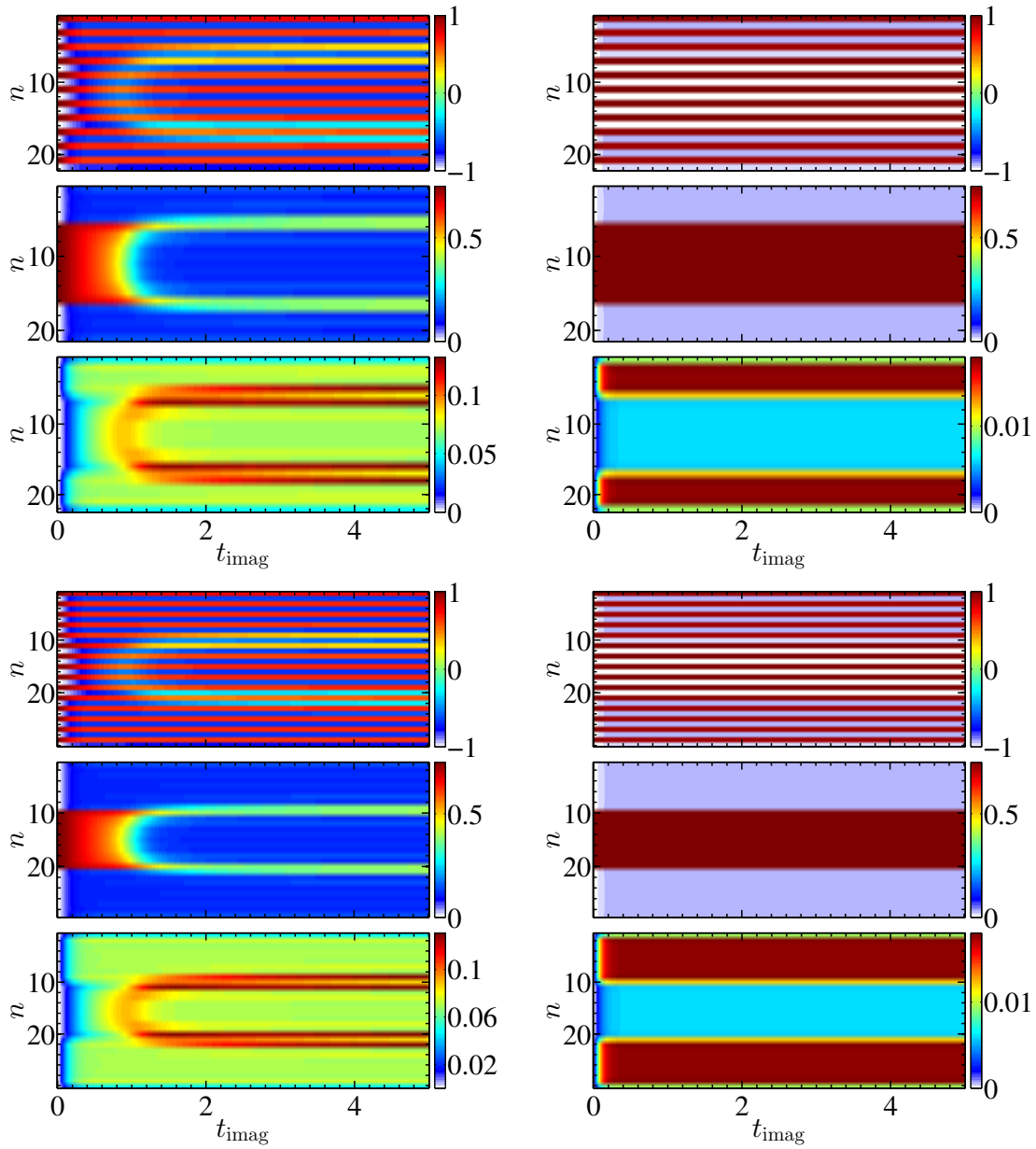

Figure 6.3: Imaginary-time evolution of a string with length $l = 11$ between two external static charges, in a system of size $N = 22$ (upper three rows) and $N = 30$ (lower three rows), for dynamical fermion masses $m = 3.0$ (left column) and 10.0 (right column). Shown are the site resolved expectation values for $\sigma^z_{r,n}$, $\sigma^z_{g,n}$ (first and fourth row), $\mathbf{J}^2_n$ (second and fifth row) and $Q^{a\,2}_n$ (third and sixth row) as a function of imaginary time.

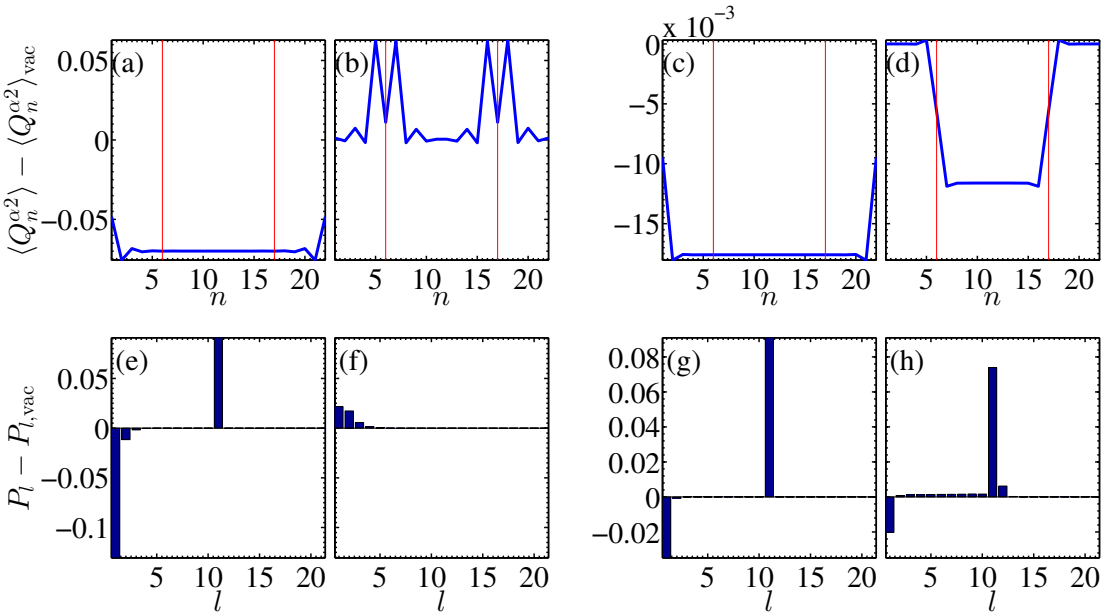

Figure 6.4: Charge square configuration (upper panels) and histograms of string lengths (lower panels) at the beginning and the end of the evolution for a system of size $N = 22$ and $l = 11$, the vertical lines in the upper panels indicate the position of the external charges. Panel (a) and (e) show the data for $m = 3.0$ at the beginning, panel (b) and (f) for $m = 3.0$ at the end, panel (c) and (g) for $m = 10.0$ at the beginning and panel (d) and (h) for $m = 10.0$ at the end of the evolution.

nal charges $q^y = \pm 1/2$ separated by a distance $l = 11$, in a gauge invariant manner, thus starting the connecting flux tube. Subsequently we evolve this state in real time with $\Delta t = 1.0 \times 10^{-4}$, $D = 100$ and determine the time-dependent spin, flux and charge square configurations along the chain, as shown in Fig. 6.5. As in the imaginary-time case, one can see that a system size $N = 22$ is sufficient to avoid finite-size effects. In order to better appreciate the dynamics, we show the details of the three proposed observables at fixed times in the evolution, $t = 0$, 0.25, 0.5 and 2, for each mass in Figs. 6.6 and 6.7, where we again subtracted the interacting vacuum configuration to visualize the difference to the ground state without external charges.

For $m = 3.0$ the plots in Fig. 6.6 reveal that between $t = 0$ and $t = 0.25$ particle-antiparticle pairs are created inside the string region, leading to a significant increase in $Q_n^{a\,2}$ there. This is accompanied with a considerable decrease of the initial peak in the string length histogram around $l = 11$ and a change in the spin and flux configurations. This growth is continuing up to $t = 0.5$ where there has been a large amount of particles created in the string region and the peak in the histogram at $l = 11$ is already gone. At later times, $t = 2.0$, these particles are clustering around the region of the external charges

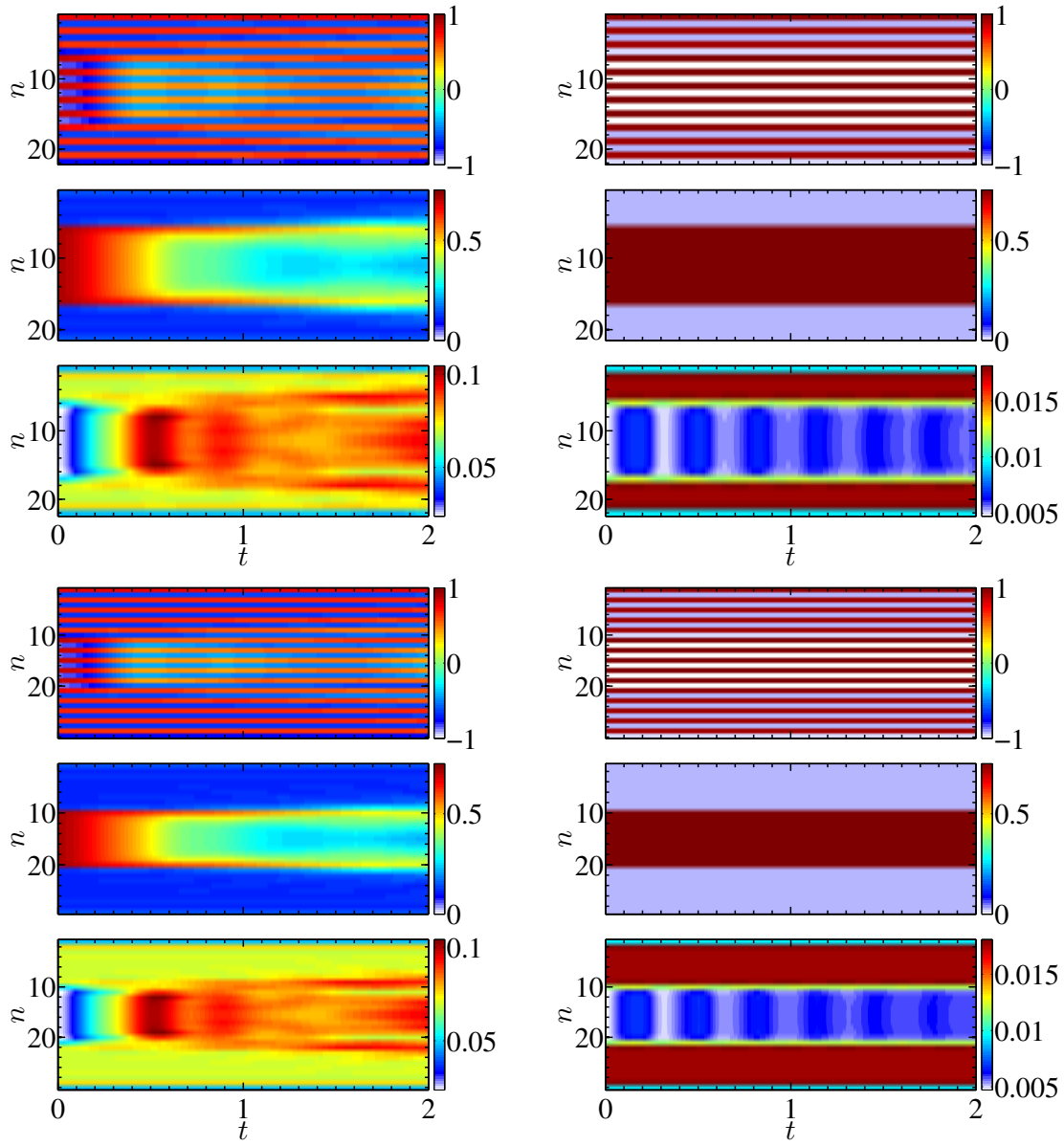

Figure 6.5: Real-time evolution of a string with length $l = 11$ between two external static charges, in a system of size $N = 22$ (upper three rows) and $N = 30$ (lower three rows), for dynamical fermion masses $m = 3.0$ (left column) and 10.0 (right column). Shown are the site resolved expectation values for $\sigma^z_{r,n}$, $\sigma^z_{g,n}$ (first and fourth row), $\mathbf{J}^2_n$ (second and fifth row) and $Q^{a\,2}_n$ (third and sixth row) as a function of time.

and, as the flux configuration reveals, the external charges are screened, leading to a reduction of flux in the center region of the original string. For $m = 10.0$ the picture is significantly different, as there is essentially no change during

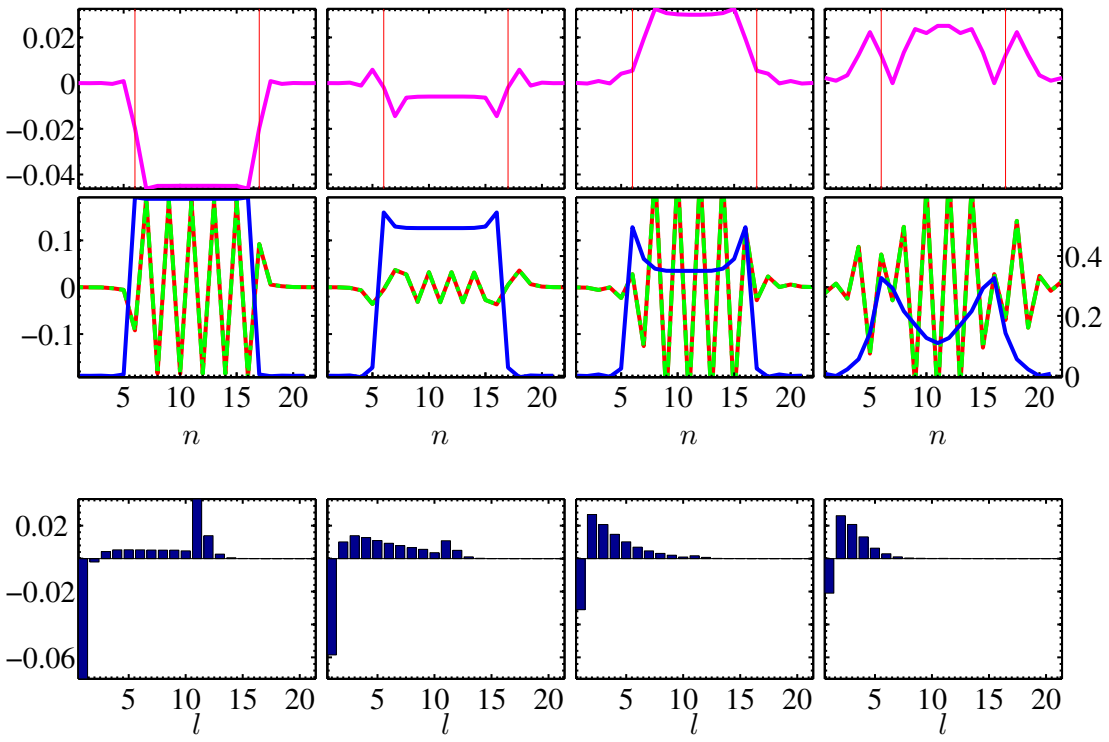

Figure 6.6: Real-time snapshots for a system with external static charges at a distance $l = 11$, dynamical fermion mass $m = 3.0$ and size $N = 22$. The upper row shows the charge square configuration, $\langle Q_n^{a\,2}\rangle - \langle Q_n^{a\,2}\rangle_{\text{vac}}$, the central row the spin, $\langle \sigma^z_{r/g,n}\rangle - \langle \sigma^z_{r/g,n}\rangle_{\text{vac}}$ (red and green lines, left y-axes), and flux configuration, $\langle \mathbf{J}_n^2\rangle - \langle \mathbf{J}_n^2\rangle_{\text{vac}}$ (blue lines, right y-axes), and the lower row the histograms for the string lengths, $P_l - P_{l,\text{vac}}$. The vertical red lines in the upper row indicate the position of the external charges. Each column corresponds to a time instant, $t = 0$, 0.25, 0.5 and 2.0.

the evolution in neither the charge, spin and flux configurations nor the string length histograms, which show a single dominant peak at $l = 11$ at all times, therefore indicating that the initial string is preserved during the evolution. The minor changes over time present in Fig. 6.7 result from the fact that the starting state of the evolution is not an eigenstate of the Hamiltonian, and consequently it is not perfectly steady.

6.5 Real-time evolution with dynamical charges

The scenarios with external static charges allow us to isolate and study the string breaking phenomenon. Contrary to the MC approach, MPS techniques make it also possible to study a more realistic scenario, in which the charges added to the vacuum are themselves dynamical. This enables additional con-

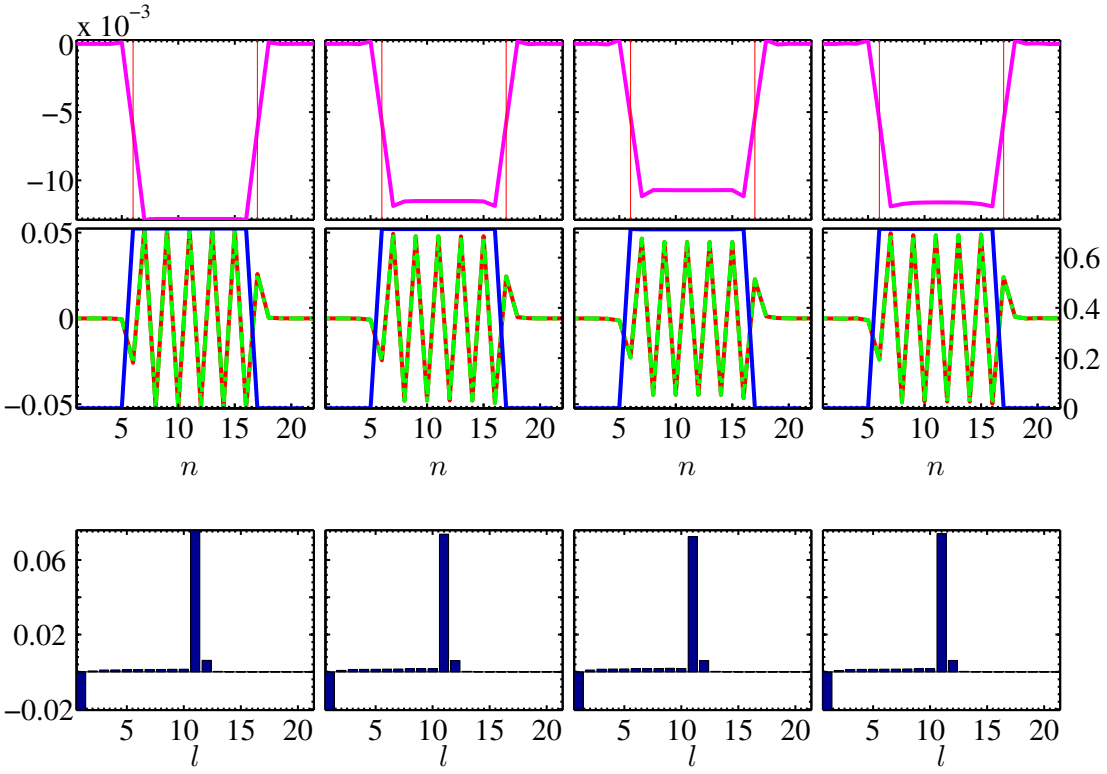

Figure 6.7: Real-time snapshots for a system with external static charges at a distance $l = 11$, dynamical fermion mass $m = 10.0$ and size $N = 22$. The upper row shows the charge square configuration, $\langle Q_n^{a\,2}\rangle - \langle Q_n^{a\,2}\rangle_{\text{vac}}$, the central row the spin, $\langle \sigma^z_{r/g,n}\rangle - \langle \sigma^z_{r/g,n}\rangle_{\text{vac}}$ (red and green lines, left y-axes), and flux configuration, $\langle \mathbf{J}_n^2\rangle - \langle \mathbf{J}_n^2\rangle_{\text{vac}}$ (blue lines, right y-axes), and the lower row the histograms for the string lengths, $P_l - P_{l,\text{vac}}$. The vertical red lines in the upper row indicate the position of the external charges. Each column corresponds to a time instant, $t = 0$, 0.25, 0.5 and 2.0.

figurations, in which the charges can move, to also play a role in the evolution, so that the string breaking phenomenon may be displayed differently.

Using the same MPS techniques, we can also explore this setup. Thus we repeat the simulations described in Sec. 6.4 but applying the gauge invariant string operator from Eq. (6.2) on the interacting vacuum to construct our initial state. This again results in a state with a string between two charges. Different to the systems studied earlier, the charges are not external, but they are now created on a site and are fully dynamical. Again, we study the time evolution of the spin, flux and charge square configurations for different fermion masses and system sizes, as shown in Fig. 6.8, where we use $\Delta t = 1.0 \times 10^{-4}$ and $D = 100$ as in the previous Section. We compare the case $m = 10.0$, in which the string does not break (see also Fig. 6.11), with $m = 3.0$. In the latter case,

which exhibited clear breaking for static external charges, the fully dynamical situation shows differences (compare Figs. 6.6 and 6.10). To better identify the features of string breaking, we look at an even smaller fermion mass, $m = 1.0$, shown in Fig. 6.9.

In all cases we see a clear initial peak in the charge square configuration at the beginning and at the end of the string. For $m = 1.0$ and 3.0 new charges emerge especially in the string region and these peaks are quickly decaying. Also the flux in the string region is decaying while two small peaks are preserved roughly around the start and end point of the original string. The histograms for the distribution of string lengths show a similar picture: at the beginning of the evolution there is a clear peak at around $l = 11$ which is gone at around $t = 0.25$. In the $m = 1.0$ case the initial peak at $l = 11$ is less dominant as in the $m = 3.0$ case, due to the fact that in this case the interaction strength ε is more important, leading to a state less close to a strong-coupling string. For later times one sees that in both cases smaller string lengths are dominating in the system, therefore indicating that the string is broken. By contrast, in the case of $m = 10.0$ the dominant peak at $l = 11$ is preserved during the entire evolution. Although the magnitude decreases, one can see from the flux and charge square configurations that there is not a lot of change, which indicates that the original string is still present. The slight changes have the same origin as in the previous cases. As we are not starting with an eigenstate of the Hamiltonian but rather do a local quench, the state is not perfectly steady. Furthermore in this case the charges are fully dynamical, what leads to richer dynamics.

6.6 Conclusion

The scenarios analyzed in this Chapter correspond to potentially realizable quantum simulators of SU(2) lattice gauge models. Using MPS and simulating real-time dynamics, it is possible to predict how the string breaking phenomenon can be observed in such a context. Moreover, we proposed different observables, notably the charge square, the flux configuration and the statistics of string lengths, to detect and characterize string breaking in statical and dynamical scenarios which should also be accessible in an experimental setup.

We calculated the ground state in the sector with two static external charges. This allows us to clearly pick up the static signature of string breaking, and to identify parameter regions where we expect string breaking to occur. Furthermore our calculation shows that the string state is metastable during the imaginary-time evolution, until configurations with a broken string mix in and reduce the energy, as expected. We also showed that the particle-antiparticle pairs resulting from the breaking string cluster around the external charges and subsequently screen the electric field. This can be detected with the spin

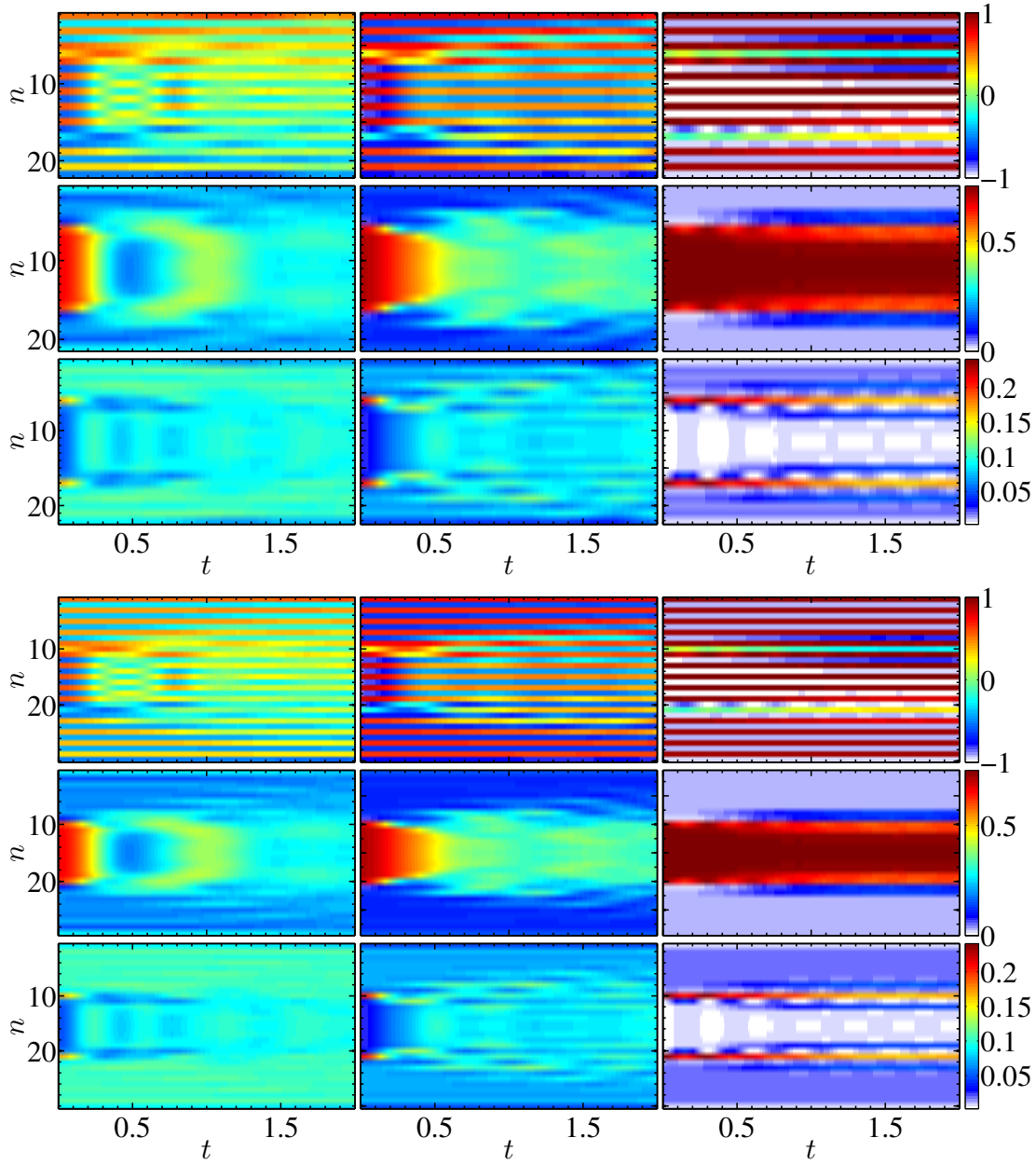

Figure 6.8: Real-time evolution of a string with length $l = 11$ between fully dynamical fermions, in a system of size $N = 22$ (upper three rows) and $N = 30$ (lower three rows), for dynamical fermion masses $m = 1.0$ (left column), $m = 3.0$ (central column) and 10.0 (right column). Shown are the site resolved expectation values for $\sigma^z_{r,n}$, $\sigma^z_{g,n}$ (first and fourth row), $\mathbf{J}^2_n$ (second and fifth row) and $Q^{a\,2}_n$ (third and sixth row) as a function of time.

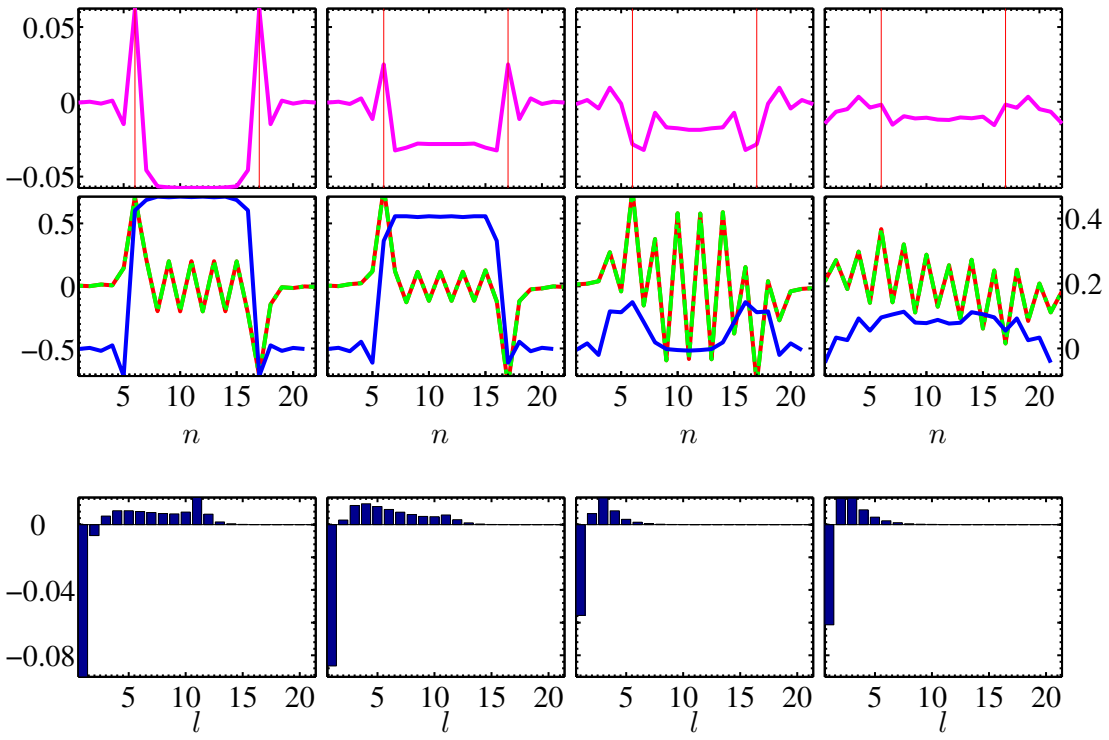

Figure 6.9: Real-time snapshots from the evolution of a string with length $l = 11$ between fully dynamical fermions, for $m = 1.0$ and system size $N = 22$. The upper row shows the charge square configuration, $\langle Q_n^{a\,2}\rangle - \langle Q_n^{a\,2}\rangle_{\text{vac}}$, the central row the spin, $\langle \sigma^z_{r/g,n}\rangle - \langle \sigma^z_{r/g,n}\rangle_{\text{vac}}$ (red and green lines, left y-axes), and flux configuration, $\langle \mathbf{J}_n^2\rangle - \langle \mathbf{J}_n^2\rangle_{\text{vac}}$ (blue lines, right y-axes), and the lower row the histograms for the string lengths, $P_l - P_{l,\text{vac}}$. The vertical red lines in the upper row indicate the initial position of the charges added to the vacuum. Each column corresponds to a time instant, $t = 0$, 0.125, 0.5 and 1.5.

and flux configuration as well as in the charge square and the distribution of string lengths in the system.

Neither quantum simulations nor our MPS computations are restricted to the static case, and using real-time simulations, we also explored the dynamics of string breaking in a setup with two static external charges. With the observables proposed before, the breaking and nonbreaking cases are clearly distinguishable. We can explicitly see that, in case the string is breaking, dynamical fermions are created that cluster around the external charges and screen them, therefore reducing the flux in the system. In principle, this could also be directly observed in a future quantum simulator by measuring the observables we analyzed in our simulations.

Finally, we also simulated the time evolution of a string between fully dynamical fermions. We also identify situations in which the string breaks in

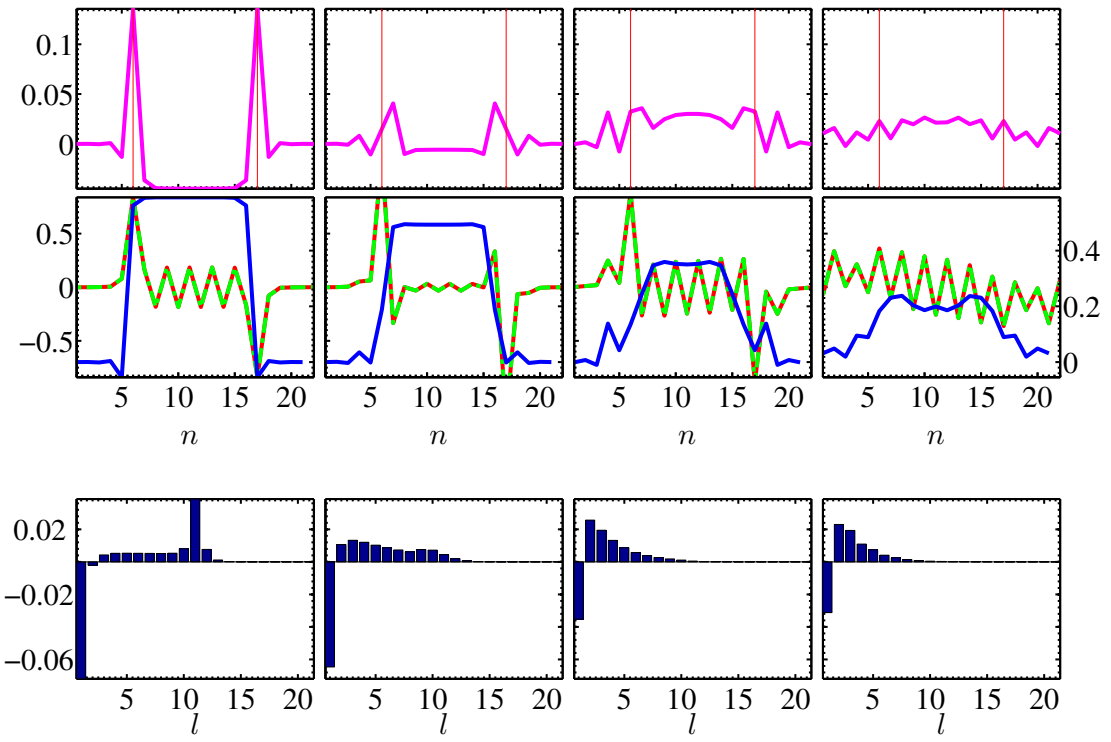

Figure 6.10: Real-time snapshots from the evolution of a string with length $l = 11$ between fully dynamical fermions, for $m = 3.0$ and system size $N = 22$. The upper row shows the charge square configuration, $\langle Q_n^{a\,2}\rangle - \langle Q_n^{a\,2}\rangle_{\text{vac}}$, the central row the spin, $\langle \sigma^z_{r/g,n}\rangle - \langle \sigma^z_{r/g,n}\rangle_{\text{vac}}$ (red and green lines, left y-axes), and flux configuration, $\langle \mathbf{J}_n^2\rangle - \langle \mathbf{J}_n^2\rangle_{\text{vac}}$ (blue lines, right y-axes), and the lower row the histograms for the string lengths, $P_l - P_{l,\text{vac}}$. The vertical red lines in the upper row indicate the initial position of the charges added to the vacuum. Each column corresponds to a time instant, $t = 0$, 0.25, 0.5 and 2.0.

this case. In particular, the decay of charges and the reduction of the flux in the middle of the string region indicate string breaking. Due to the fact that the initially created particle-antiparticle pair is now dynamical, we do not observe the clustering of the dynamically created charges, but rather a distribution along the system.

The study described here is focused on the particular case of SU(2) truncated to the smallest set of irreducible representations, however, the truncation method used from Ref. [57] works for arbitrary finite or compact Lie groups and is not limited to the case of one spatial dimension. Therefore also other gauge groups could be studied.

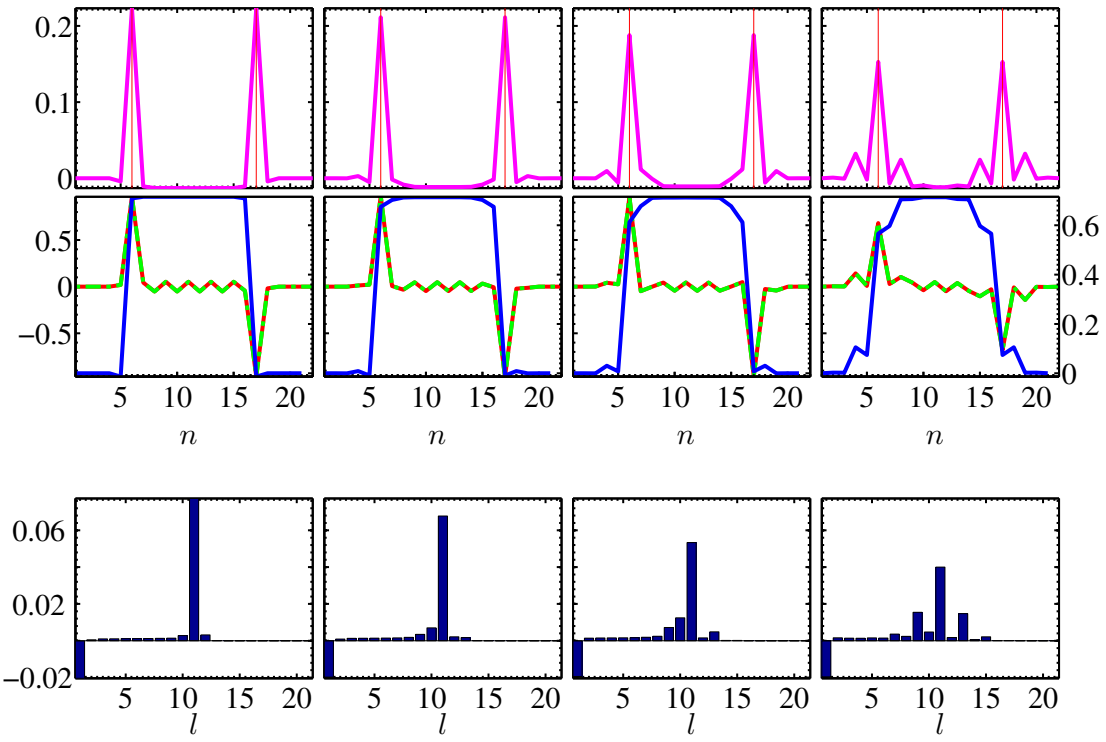

Figure 6.11: Real-time snapshots from the evolution of a string with length $l = 11$ between fully dynamical fermions, for $m = 10.0$ and system size $N = 22$. The upper row shows the charge square configuration, $\langle Q_n^{a\,2}\rangle - \langle Q_n^{a\,2}\rangle_{\text{vac}}$, the central row the spin, $\langle \sigma^z_{r/g,n}\rangle - \langle \sigma^z_{r/g,n}\rangle_{\text{vac}}$ (red and green lines, left y-axes), and flux configuration, $\langle \mathbf{J}_n^2\rangle - \langle \mathbf{J}_n^2\rangle_{\text{vac}}$ (blue lines, right y-axes), and the lower row the histograms for the string lengths, $P_l - P_{l,\text{vac}}$. The vertical red lines in the upper row indicate the initial position of the charges added to the vacuum. Each column corresponds to a time instant, $t = 0$, 0.25, 0.5 and 2.0.

Chapter 7

Efficient basis formulation for 1+1 dimensional SU(2) lattice gauge theories

In Chapter 2 we reviewed how the gauge degrees of freedom in the Schwinger model can be integrated out, resulting in a formulation for the physical subspace of the theory. In general, for two space-time dimensions the gauge degrees of freedom are not truly independent, and, in principle, it should be possible to proceed similarly also for the non-Abelian case. In this Chapter we show a concrete formulation that realizes this for the lattice version of a non-Abelian SU(2) gauge theory and develop a basis for the physical subspace of the model. Our formulation, which is completely general and can be used with any numerical or analytical method, is especially suited for TN. Moreover, it enables to restrict calculations to a sector of the physical subspace, in which the color-electric flux implied by the fermionic content is upper bounded by an arbitrary finite value, thus effectively truncating gauge degrees of freedom of the model. Combining this possibility with the MPS approach, we study the low-lying spectrum and the scaling exponents of the vector mass gap for a family of truncated SU(2) models. Moreover, recent developments in the context of the holographic principle have suggested a deep connection between entanglement and emergent geometry [247, 248], and have rekindled the interest in understanding the peculiarities of entanglement in gauge theories [249–253]. Being especially well-suited to compute entanglement entropies, TN allow us to study how the truncation of the flux alters the entanglement of the vacuum in the approach to the continuum. The truncation effects we investigate might also affect future quantum simulators and our MPS approach enables us to explore them systematically. The results shown in this Chapter have been published in Ref. [254] and the rest of the Chapter is a modification of this reference.

7.1 Introduction

The local symmetry in gauge theories is ensured by introducing additional degrees of freedom in form of a gauge field, as we have seen in Chapter 2. However, this also leads to redundant degrees of freedom in the theory. As the physical observables are strictly gauge invariant, the only relevant subspace is the one spanned by the gauge invariant states, which is in general much smaller than the full Hilbert space of the model given by the tensor product of the individual Hilbert spaces for the fermionic sites and the gauge links. Due to the absence of transversal directions for the special case of 1+1 dimensions, the gauge fields are not genuinely independent degrees of freedom, but it is possible to remove them by integrating the Gauss law. This long known fact, to the best of our knowledge, has only been explicitly exploited in practice for the Abelian case of the Schwinger model [141, 218, 255].

Although this renders 1+1 dimensional gauge theories seemingly simple, nevertheless, they often cannot be solved analytically, in particular in the non-perturbative regime. Despite the encouraging prospects due to quantum simulation and classical simulations with TN, there are also some limitations. In particular, as we have seen in Chapters 2 and 3, the link Hilbert spaces are infinite dimensional for continuous gauge symmetries and thus, unless they can be integrated out, typically have to be truncated to a finite dimension to allow for a TN approach or a potential implementation in a quantum simulator. Previous works therefore resorted to the truncation methods from Refs. [57, 245] to achieve a finite dimension while simultaneously preserving gauge invariance. A different type of finite dimensional gauge models explored in that context are quantum link models [162–164], where the gauge degrees of freedom are replaced by discrete spins. However, these truncated models do not necessarily correspond to the continuum theory in the limit of vanishing lattice spacing, or might not have a continuum limit at all [256].

Here, we address these questions for a 1+1 dimensional SU(2) lattice gauge theory. In a first step, we show how, starting from a color-neutral basis developed in Ref. [144], the gauge degrees of freedom can be integrated out on a lattice with OBC. The resulting basis efficiently describes the physical subspace and can in principle be used with any analytical or numerical method. The corresponding, abelianized, Hamiltonian is nonlocal, similar to the one recently realized in trapped ions for the Schwinger model [102]. Hence it might have potential applications for the design of future quantum simulators. Moreover, our formulation allows for truncating the color-electric flux at an arbitrary value. These truncated models can be efficiently addressed with TN. In principle, since the maximum flux on a finite lattice with OBC is upper bounded, it is possible to treat the model exactly. In practice, to solve the model with MPS, we cut the number of color-flux sectors and compute the low-lying spectrum for this family of truncated SU(2) gauge models. Due to

the vastly reduced number of basis states in our formulation, we are able to explore much larger values for the maximum color-electric flux than achieved in previous TN studies of the model [43, 52], and we can investigate truncation effects in a systematic manner. In particular, here we explore such effects in the closing of the mass gaps as we approach criticality, and in the entanglement entropy of the ground state.

The rest of the Chapter is organized as follows: In Sec. 7.2 we introduce the model we are studying. After a brief review of the color-neutral basis developed in Ref. [144], we present our new formulation for systems with OBC where the gauge field is integrated out in Sec. 7.3. Furthermore, we explain how this formulation readily allows for a truncation of the link Hilbert spaces in a gauge invariant manner to a finite dimension. In Sec. 7.4 we briefly review the MPS methods we are applying and present our results for the low-lying spectrum and the entanglement properties of the ground state while approaching the continuum limit in Secs. 7.5 and 7.6 . Finally, we conclude in Sec. 7.7.

7.2 Model

The model we are studying is a 1+1 dimensional SU(2) lattice gauge theory which we have introduced in Sec. 2.3. As we have seen there, a suitable basis for addressing the Hamiltonian is given by $|n_1^{-\frac{1}{2}}, n_1^{\frac{1}{2}}\rangle \otimes |j_1 \ell_1 \ell_1'\rangle \otimes |n_2^{-\frac{1}{2}}, n_2^{\frac{1}{2}}\rangle \otimes \dots$ where n_k^ℓ is the fermionic occupation number for color ℓ on site k.

For the following spectral calculations it is convenient to use a dimensionless formulation of Hamiltonian (2.39), $W = xV + W_0$, where

$$V = \sum_{k=1}^{N-1} \sum_{l,l'=-1/2}^{1/2} \left(\psi_{l,k}^\dagger (U_k)_{ll'} \psi_{l',k+1} + \text{h.c.} \right), \tag{7.1}$$

$$W_0 = \mu \sum_{k=1}^{N} \sum_{l=-1/2}^{1/2} (-1)^k \psi_{l,k}^\dagger \psi_{l,k} + \sum_{k=1}^{N-1} \mathbf{J}_k^2, \tag{7.2}$$

and we have again applied a phase transformation on the fermion fields as in the previous Chapter [144]. The adimensional parameters of the problem in units of the coupling, g, are $x = 1/(ag)^2$ and $\mu = 2\sqrt{x}m/g$.

The basis we considered in Sec. 2.3 contains all the information about the color degrees of freedom and, in particular, states which are not color singlets. However, the physical states consist of color-neutral superpositions of basis states satisfying the Gauss law. As we show in the next Section, a suitable choice of basis ensures the color-singlet character, and restricts calculations to the physically relevant subspace of these color-neutral superpositions with a significant reduction of the superfluous degrees of freedom.

7.3 Integrating out the gauge field

7.3.1 Color-neutral basis

A first step towards a physical basis was made by Hamer in the context of a strong-coupling expansion of the model [144]. Here we briefly review the basis formulation developed there. As shown in Refs. [142, 144], the physically relevant states can be generated by applying the operator V from Eq. (7.1) repeatedly to a certain color-neutral initial state having the desired quantum numbers. This operator has no uncontracted color indices, thus, it can locally only generate or annihilate excitations consisting of color-neutral superpositions of quark-antiquark (antiquark-quark) pairs connected by a color-flux string, as it is illustrated in Fig. 7.1(a)-(b). The resulting superposition has a well defined value of $\mathbf{J}_k^2$ on the links and fermionic occupation number $n_k = n_k^{-\frac{1}{2}} + n_k^{\frac{1}{2}}$. In particular, applying V to such a color-singlet characterized by n_k, n_{k+1} and j_k results in general again in a superposition of different color-singlets with n'_k, n'_{k+1} and j'_k. In Ref. [144] all possible transitions were worked out and the matrix elements of the operator V for each of those vertices are shown in Fig. 7.1(c).

Looking at Eq. (7.2), one can easily see that the states generated in that manner are eigenstates of the mass term, as it only depends on the total occupation number, and of the color-electric energy, as it only depends on j_k. Thus, W_0 acts identically on all those states. Consequently, instead of working in the basis containing the full color information, we can restrict ourselves to a basis formed by those color-singlet states, characterized by the fermionic occupation number of each site and by the color-electric flux j carried by a link

$$|\Psi\rangle = |\mathbf{n}\rangle \otimes |j\rangle \otimes |\mathbf{n}\rangle \otimes |j\rangle \ldots .$$

Here $\mathbf{n} \in \{0, 1, 2\}$, as we are not distinguishing between fermions of different colors anymore. Gauss law in this color-singlet basis simply reduces to the fact that the electric flux j_{k+1} can only differ from the one on the previous link by one quantum, if the site is occupied by a single fermion:

$$j_{k+1} = \begin{cases} j_k & \text{if } n_{k+1} = 0, 2 \\ j_k \pm \frac{1}{2} & \text{if } n_{k+1} = 1. \end{cases} \tag{7.3}$$

In addition to reducing the degrees of freedom significantly compared to the full basis, the color-singlet basis also offers the possibility to trivially truncate the color-electric flux at a certain value of $j_{\max}$ in a gauge invariant manner. Taking into account only states with $j \leq j_{\max}$ results in a truncated model with Hilbert spaces of dimension $d_{\text{link}} = 2j_{\max} + 1$ for the gauge links. Compared to the full basis, where for $j_{\max} = 1/2,\ 1,\ 3/2,\ 2$ one would have link Hilbert

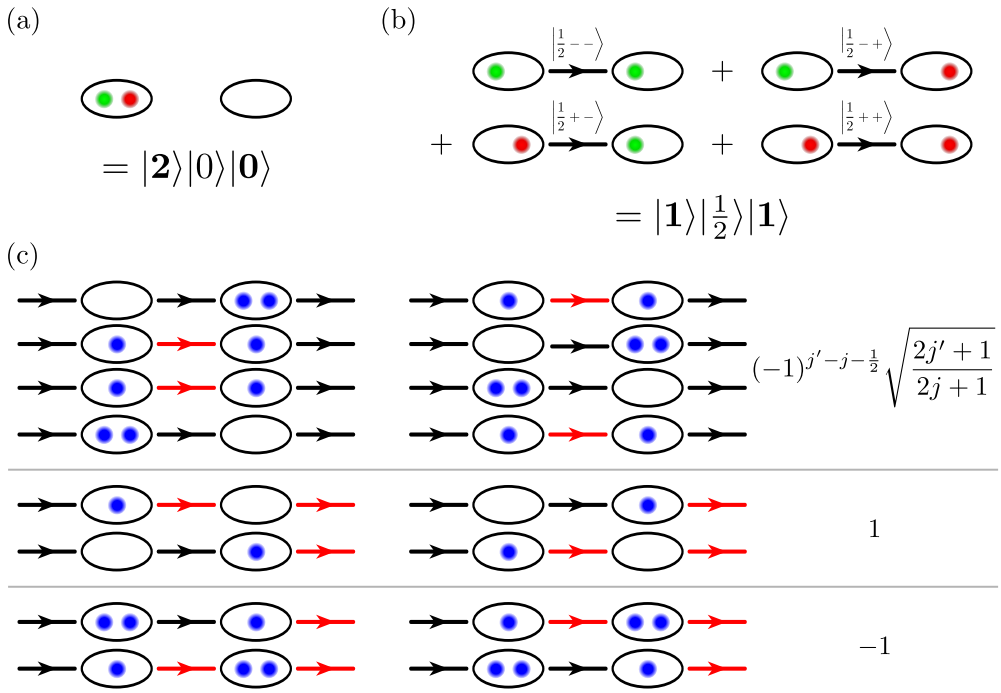

Figure 7.1: (a) Strong coupling configuration with an odd site filled with two fermions, one of every color, and its neighboring empty even site. (b) Resulting color-neutral superposition of four states after applying the operator V. Each of the four states has a single fermion per site and a color-electric flux of $j = 1/2$ on the intermediate link, with a different combination of z-components. The corresponding state in the color-neutral basis for those two cases are written below. (c) Transitions induced by the operator V in the color-neutral basis. The left block represents the possible gauge invariant starting configurations $|\Psi_i\rangle$, the right block the final states $|\Psi_f\rangle$ after application of the operator V. The arrows show the gauge links, where the black arrows indicate a color-electric flux of j and the red arrows a value of $j' = j \pm 1/2$. The sites are represented by ovals, where the small blue dots indicate the number of fermions sitting on the site. The numbers to the right show the matrix element $\langle\Psi_f|V|\Psi_i\rangle$.

spaces of dimension 5, 14, 30, 55, one only has to deal with spaces of dimension $d_{\text{link}} = 2, 3, 4, 5$.

7.3.2 Removing the gauge fields

The color-singlet basis reviewed in the previous paragraph still contains redundant information which can be (partially) removed. While the discussion above still applies to both, open and periodic boundary conditions, we restrict ourselves from now on to OBC.

Realizing that due to Eq. (7.3) the flux j_{k+1} only depends on j_k and n_{k+1},

one can reconstruct the color-electric flux at every link from the value j_0 at the left boundary by recursive application of the Gauss law. However, for the case of a site occupied by a single fermion the SU(2) non-Abelian Gauss law allows a change of the color-electric flux by $\pm 1/2$. To deal with this ambiguity, we use two states $|1_+\rangle$, $|1_-\rangle$ to describe the singly occupied site, which encode if the electric flux is increasing ($|1_+\rangle$) or decreasing ($|1_-\rangle$) with respect to the link to the left. As a result, the basis for a single fermionic site is again four dimensional and consists of the set of states $\{|0\rangle, |1_-\rangle, |1_+\rangle, |2\rangle\}$. The expense of increasing the basis for the fermionic sites by one allows us to integrate out the gauge links from the Hamiltonian, as the j_k can now be reconstructed solely from the fermionic content via

$$\hat{j}_k = j_0 + \sum_{p=1}^{k} \frac{1}{2}\Big(|1_+\rangle\langle 1_+|_p - |1_-\rangle\langle 1_-|_p\Big), \tag{7.4}$$

where j_0 is the color-flux value at the left boundary. Hence, a suitable basis for a system with N sites is given by

$$|\Psi\rangle = |\alpha_1\rangle \otimes |\alpha_2\rangle \otimes \cdots \otimes |\alpha_N\rangle \tag{7.5}$$

with $|\alpha_k\rangle \in \{|0\rangle, |1_-\rangle, |1_+\rangle, |2\rangle\}$. Similar to the (Abelian) Schwinger model, in this basis the configuration of the sites uniquely determines the content of the gauge links, thus effectively *abelianizing* the model.[1] Additionally, one can immediately see that this construction leads to long-range interactions in Hamer's color-electric energy term. Moreover, as some of the matrix elements for the hopping term in Fig. 7.1(c) also depend on the color-electric flux, the hopping term becomes nonlocal, too (the Hamiltonian in this basis is shown in detail in the App. C.2).

It is instructive to study the dimension of the physical subspace compared to the tensor product Hilbert space. Without further constraint, our basis still contains unphysical states implying negative values of j_k,[2] e.g. $|\Psi\rangle = |1_-\rangle...$ implies a value of $j_1 = -1/2$. For vanishing background field, $j_0 = 0$, the case on which we focus on in our numerical calculations, physical basis states are characterized by a simple condition: the number $l_{k,-}$ of sites with $|1_-\rangle$ up to a site k can never exceed the corresponding number $l_{k,+}$ of sites with $|1_+\rangle$, $l_{k,+} \geq l_{k,-}$ $\forall k = 1, \ldots, N$. The dimension of the physically relevant subspace fulfilling this condition is given by $d_{N,\text{phys}} = 4^N(1 - \sum_{k=1}^{N} C_k/4^k)$, where $C_k = (2k)!/(k+1)!k!$ is the Catalan number (for details see App. C.1). In Fig. 7.2 we show a comparison between the scaling of our basis and the color-neutral basis from Ref. [144] which has dimension $d_{N,\text{Hamer}} = 3^N(2j_{\max}+1)^{N-1}$. As the figure

[1] In principle one could also treat arbitrary gauge groups SU(N_c) with $N_c \geq 2$ in a similar fashion after obtaining the matrix elements for the vertices.

[2] Notice that for physical states the values of j_k represent the total angular momentum corresponding to the quantum rigid rotor on that link and, thus, are positive.

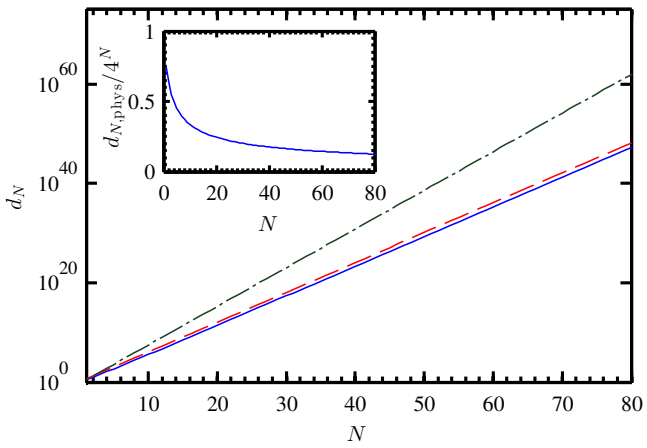

Figure 7.2: Dimension of the physical subspace $d_{N,\mathrm{phys}}$ (blue solid line), the total number of basis states 4^N in our formulation (red dashed line) and the dimension of the basis from Ref. [144], $3^N(2j_{\max}+1)^{N-1}$, for the simplest nontrivial truncation $j_{\max} = 1/2$ (green dash-dotted line) as a function of system size. Inset: Fraction of the physical subspace with respect to the total number of states in our basis.

reveals, for systems with OBC our basis offers a vast improvement over the one from Ref. [144] already for the case of the simplest nontrivial truncation $j_{\max} = 1/2$. Even though the fraction of physical states in our basis, $d_{N,\mathrm{phys}}/4^N$, quickly decreases with system size, the total number of states is still exponentially smaller. Compared to formulations for the physical subspace for the U(1) case with dynamical fermions [56, 141], we observe that the number of basis states in our formulation is exactly the square.

Notice that our reduced basis formulation is completely general and contains the entire information about the physical subspace. Hence, it lends itself to any analytical or numerical method.

7.3.3 Relation between our basis and the tensor product basis

The states in our basis formulation and the ones in the full basis are related by a simply isometry. Here we explicitly show this transformation, which sequentially reconstructs the color flux on each link from the fermion content, and prepares a suitable combination of states in the full basis such that the state is a color singlet.

The corresponding iometric map is given by

$$\mathcal{M}_{\text{loc}} = \sum_{j=0,\frac{1}{2},\ldots}^{j_{\max}} \sum_{\alpha} \sum_{\ell,\ell'=-j}^{j} \sum_{s=-|q_\alpha|}^{|q_\alpha|} \frac{C_{s\ \ell'\ \ell'+s}^{|q_\alpha|\ j\ \ j+q_\alpha}}{\sqrt{2(j+q_\alpha)+1}} |j\ell\ell'; n_\alpha s; j+q_\alpha, \ell'+s\rangle\langle j\ell; \alpha|. \quad (7.6)$$

where $C_{\ell_1\ \ell_2\ M}^{j_1\ j_2\ J} = \langle J, M | j_1, \ell_1; j_2, \ell_2\rangle$ are again the usual Clebsch-Gordan coefficients for coupling two angular momenta j_1, j_2 with z-components ℓ_1, ℓ_2 to a total angular momentum J with z-component M. The numbers n_α and q_α are the respective eigenvalues of the operators

$$\hat{n} = |1_-\rangle\langle 1_-| + |1_+\rangle\langle 1_+| + 2\,|2\rangle\langle 2|, \quad (7.7)$$

$$\hat{q} = \frac{1}{2}\Big(|1_+\rangle\langle 1_+| - |1_-\rangle\langle 1_-|\Big). \quad (7.8)$$

when applied to the state $|\alpha\rangle$. The states $|n_\alpha s\rangle$ correspond to a relabeling of the full basis $|n^{-\frac{1}{2}}, n^{\frac{1}{2}}\rangle$, where, different to the previous Sections, we use the total occupation number and the z-component of the related angular momentum, $n_\alpha = n^{-\frac{1}{2}} + n^{\frac{1}{2}}$, $s = (n^{-\frac{1}{2}} - n^{\frac{1}{2}})/2$, to make the dependence explicit. The effect of the map is to introduce extra degrees of freedom, ℓ' for the incoming link and j, ℓ on the outgoing link, by simultaneously respecting the proper SU(2) composition rules, which is ensured by the Clebsch-Gordan coefficients (see Fig. 7.3(a)). Notice that for empty or doubly occupied sites $q_\alpha = 0$ and the Clebsch-Gordan coefficients are trivial. In the case of singly occupied sites $|q_\alpha| = 1/2$ and the spin-1/2 of the single fermion couples to the angular momentum of the previous link to ensure a color-neutral superposition. The prefactors $1/\sqrt{2(j+q_\alpha)+1}$ ensure proper normalization of the resulting state and have to be chosen such that $\mathcal{M}_{\text{loc}}^\dagger \mathcal{M}_{\text{loc}}$ is the projector on the physical subspace as we are going to show in the following. A straightforward calculation yields

$$\mathcal{M}_{\text{loc}}^\dagger \mathcal{M}_{\text{loc}} = \sum_{j,\alpha,\ell} \frac{1}{2(j+q_\alpha)+1} \left(\sum_{\ell',s} C_{s\ \ell'\ \ell'+s}^{|q_\alpha|\ j\ \ j+q_\alpha\ 2} \right) |j\ell;\alpha\rangle\langle j\ell;\alpha|. \quad (7.9)$$

The sum inside the bracket over the squares of the Clebsch-Gordan coefficients can be simplified as follows:

$$\begin{aligned}
\sum_{\ell'=-j}^{j} \sum_{s=-|q_\alpha|}^{|q_\alpha|} \left(C_{s\ \ell'\ \ell'+s}^{|q_\alpha|\ j\ \ j+q_\alpha} \right)^2 &= \sum_{\ell'=-j}^{j} \sum_{s=-|q_\alpha|}^{|q_\alpha|} \sum_{t=-(j+q_\alpha)}^{j+q_\alpha} \left(C_{s\ \ell'\ t}^{|q_\alpha|\ j\ \ j+q_\alpha} \right)^2 \\
&= \sum_{t=-(j+q_\alpha)}^{j+q_\alpha} \left(\sum_{\ell'=-j}^{j} \sum_{s=-1/2}^{1/2} \left(C_{s\ \ell'\ t}^{|q_\alpha|\ j\ \ j+q_\alpha} \right)^2 \right) \\
&= \sum_{t=-(j+q_\alpha)}^{j+q_\alpha} 1 = 2\,(j+q_\alpha)+1,
\end{aligned}$$

where in the first line, we have used that the Clebsch-Gordan coefficients vanish, if the resulting z-component differs from the sum of the individual z-components and hence we can sum over t. To arrive at the last line we have used the orthogonality relations. Thus, we see that Eq. (7.9) is the identity on the physical subspace and $\mathcal{M}_{\text{loc}}$ is indeed an isometry.

Considering a system with N sites, we can recover the full state after fixing the link on the left boundary, $|j_0 \ell_0\rangle$, via a sequential application of $\mathcal{M}_{\text{loc}}$, $\mathcal{M} = \mathcal{M}_{\text{loc}}^{(1)} \mathcal{M}_{\text{loc}}^{(2)} \dots \mathcal{M}_{\text{loc}}^{(N)}$. As sketched in Fig. 7.3(b), the sequential application of the map corresponds to a quantum circuit of depth N [257]. In all our calculations,

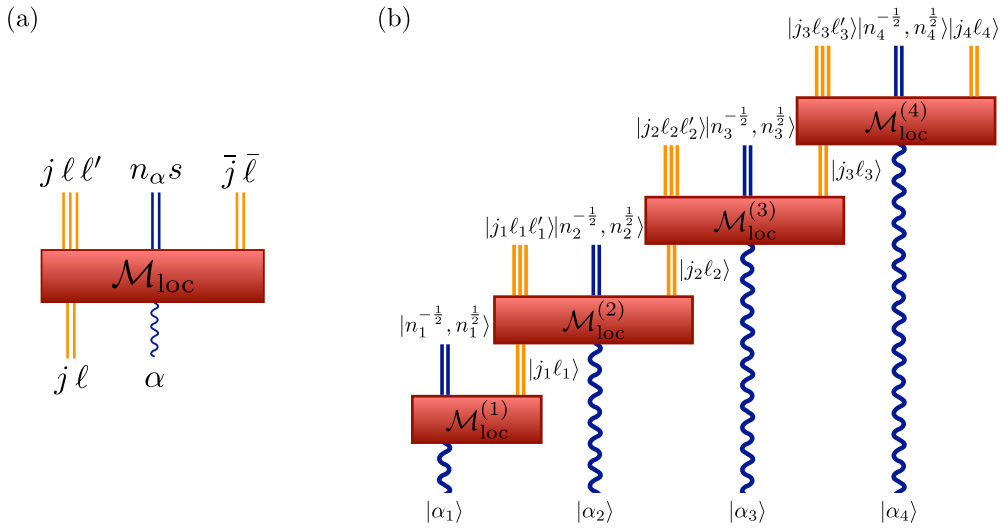

Figure 7.3: (a) Schematic representation of $\mathcal{M}_{\text{loc}}$ that locally maps the reduced basis to the full one. Different line styles are used to indicate the different spaces where $\bar{j} = j + q_\alpha$ and $\bar{\ell} = \ell' + s$. (b) Mapping a MPS in the reduced basis to the full one by applying $\mathcal{M} = \mathcal{M}_{\text{loc}}^{(1)} \mathcal{M}_{\text{loc}}^{(2)} \dots \mathcal{M}_{\text{loc}}^{(N)}$.

we work in the sector $j_0 = 0$, hence the left electric field necessarily has to vanish and the input left link is $|00\rangle$ (thus not explicitly shown in Fig. 7.3(b)).

7.4 Numerical approach

While the formulation derived in Sec. 7.2 can in principle be approached with any numerical method, it is well suited for MPS. In order to demonstrate that, we compute the ground state and the vector state of the theory at vanishing background field, $j_0 = 0$, in the sector of vanishing total charge, $j_N = 0$. Moreover, the MPS approach also allows us to access the entanglement entropy, and we can also study the scaling of the von Neumann entanglement entropy in the ground state while approaching the continuum limit.

For our numerical simulations we use the MPS ansatz with OBC presented in Chapter 3. Using the methods from Sec. 3.2, we variationally compute MPS approximations for the ground state and the vector state. In the continuum, the vector candidate is the lowest lying zero-momentum mesonic excitation of the ground state with charge conjugation quantum number -1 and parity -1. On the finite lattices with OBC we are working with, however, charge conjugation as well as the momentum are no longer good quantum numbers due to the broken translational invariance. Nonetheless, the remnants of these symmetries allow us to properly identify the vector state (see App. C.3 for details).

In addition, to be able to address the problem with MPS, it is advantageous to express the Hamiltonian as a MPO. This can be done exactly with the bond dimension of the MPO representation growing linearly with the maximum color-electric flux, $j_{\max}$, present in the system (for details see App. C.2). In the sector $j_0 = 0 = j_N$, on which we focus in our calculations, $j_{\max}$ is upper bounded by $N/2 \times 1/2$ for a system with N sites. Hence, it is possible to work efficiently with the exact MPO representation of the Hamiltonian, since the leading cost only grows polynomially in the system size. Nevertheless, for the ground state and the low-lying excitations, which we are interested in, the contribution of states having a high color flux is very small, and it is possible to truncate $j_{\max}$ to smaller values. With our basis formulation we can easily reach maximum values for the color-electric flux far beyond those amenable in previous numerical studies with TN [43, 52] and systematically study the effect of the truncation, thus controlling the error introduced by it. Additionally, this also allows us to explore the effects of truncating the gauge degrees of freedom to a finite dimension as might be necessary for a potential future quantum simulator [57, 80, 81, 84, 86, 87, 96].

In our calculations, we target the physical states in the low-energy sector of the Hamiltonian with specific properties. In particular, we are interested in the ground state and the vector state in the sector of vanishing total charge. To ensure the right sector in our calculations, we choose to add penalty terms to the Hamiltonian.[3] In order to remove the unphysical states we use the following penalty which has a nonvanishing contribution at sites with negative value of j_k:

$$P_1 = \lambda_1 \sum_{k=1}^{N} \Theta\left(-j_0 - \sum_{l=1}^{k} \hat{q}_l\right),$$

where $\Theta(x)$ is the Heavyside step function. The constant λ_1 has to be chosen large enough to shift states with a negative value for j high enough in the spectrum such that they do not mix into the low-energy sector we are interested

[3] Notice that some of these properties could also be implemented as symmetries directly on the level of the tensors [37, 56].

in. Moreover, since we are focusing on the vector meson states, we avoid any baryon states by restricting the total fermion number to the number of sites in the system which is achieved by the penalty term

$$P_2 = \lambda_2 \left(\sum_{k=1}^{N} \hat{n}_k - N \right)^2 .$$

Again, λ_2 again has to be chosen large enough to shift the states high enough in the spectrum to prevent them from mixing with the low-lying ones we are interested in. In addition, to ensure that we are in the sector of vanishing total charge $j_0 = 0 = j_N$, we add another energy penalty of the form

$$P_3 = \lambda_3 \left(\sum_{k=1}^{N} \hat{q}_k \right)^2 ,$$

where λ_3 is again a constant that has to be chosen large enough to penalize unwanted states sufficiently. For our calculations presented in the following, we checked the expectation values for all three penalties and found that they are negligible for $\lambda_i = 1000$, $i = 1, 2, 3$.

7.5 Low-lying spectrum

We compute the ground state and the vector state of the model for a range of masses, $m/g \in [0.1, 1.6]$, using the basis we developed in the previous Sections. To probe for truncation effects, we explore a family of models with maximum color-electric flux $j_{\max} = 1/2, 1, 3/2, 2$. Moreover, we consider for each combination of $(m/g, j_{\max})$ several system sizes $N \in [100, 200]$ with lattice spacings corresponding to $x \in [50, 150]$ to be able to extrapolate to the continuum. Compared to a conventional lattice calculation, we have an additional source of error due to the limited bond dimension that can be reached in the numerical simulations. To control this error, we repeat the calculation for each combination of parameters $(m/g, j_{\max}, x, N)$ for several bond dimensions $D \in [50, 200]$. To estimate the exact ground-state energy values, $E_0(N, x)$, and vector mass gap values, $\Delta_{\text{vec}}(N, x) = E_1(N, x) - E_0(N, x)$, we first extrapolate our data to the limit $1/D \to 0$, as illustrated in Fig. 7.4(a)-(b) (details about the extrapolation procedure are given in App. B.4). Subsequently, we can proceed in a standard manner and estimate the continuum values by first extrapolating to the thermodynamic limit and then to the limit of vanishing lattice spacing.

Figure 7.4(c)-(d) shows examples for the extrapolation to the thermodynamic limit for $j_{\max} = 2$. Even for this case with the largest color-electric flux, for which we expect the error due to the finite bond dimension to be most pronounced, the error bars resulting from the extrapolation in D are small and

we can obtain precise estimates for the ground-state energy density and vector mass gap in the thermodynamic limit.

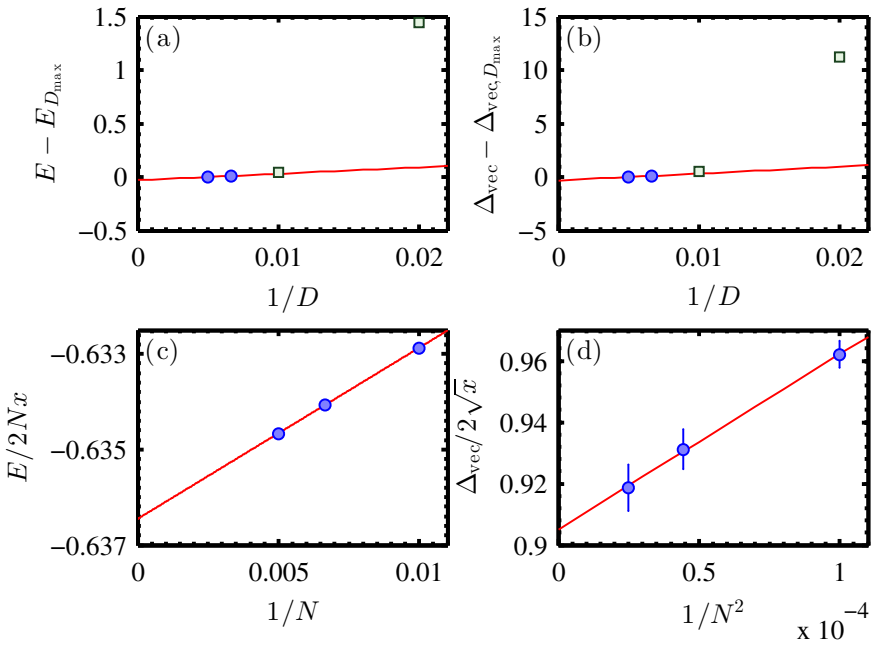

Figure 7.4: Upper row: Extrapolation in bond dimension for the ground-state energy (a) and the vector mass gap (b) for $m/g = 0.3$, $j_{\max} = 2$, $N = 150$, and $x = 150$. The central value is determined with a linear fit through the largest two bond dimensions represented by the blue dots. Lower row: Extrapolation to the thermodynamic limit for the ground-state energy density (c) and the vector mass gap (d) for $j_{\max} = 2$, and $x = 150$.

In the final step, we extrapolate the data obtained in the previous step to the continuum limit, $ag = 1/\sqrt{x} \to 0$, by fitting a polynomial in ag. To estimate our systematic error, we compare different fits up to quadratic order using different ranges of ag (details about the error estimation procedure are given in App. B.4). For the ground state, we observe that in general lattice effects are well under control, independently of the truncation, and we can reliably extrapolate to the continuum limit, as can be seen in Fig. 7.5. The values obtained for the ground-state energy density, shown in Fig. 7.6, deviate at most at the percentage level from the result for the continuum theory, even for the simplest nontrivial truncation $j_{\max} = 1/2$. For larger $j_{\max}$ our data are closer to the analytic solution for the untruncated lattice Hamiltonian in the limit $ag = 1/\sqrt{x} \to 0$, especially for smaller masses. In particular, the data obtained for the largest two values of $j_{\max}$ show hardly any difference. The dip around $m/g = 0.35$ for $j_{\max} = 3/2, 2$ is due to the fact that for for $m/g < 0.4$ our estimates for the ground-state energy are lower than the exact results, whereas for $m/g \geq$

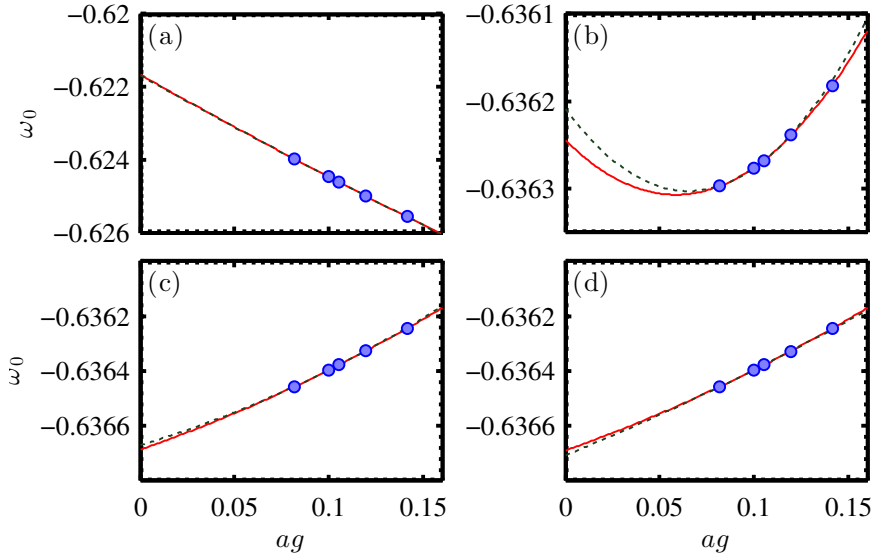

Figure 7.5: Continuum extrapolation for the ground-state energy density for $m/g = 0.3$ and $j_{\max} = 1/2$ (a), $j_{\max} = 1$ (b), $j_{\max} = 3/2$ (c) and $j_{\max} = 2$ (d). The red line shows the quadratic fit through all data points used to extract the central value. The dashed green line shows a quadratic fit omitting the largest lattice spacing to estimate the systematic error of the central value.

0.4 we obtain values slightly above the analytical prediction. For $j_{\max} = 1/2, 1$ the values are consistently larger than the exact continuum solution, hence, in these cases there is no dip. Notice that here we extrapolated the results for each fixed value of $j_{\max}$ to the continuum limit. Nevertheless, the only case for which we know that the theory has a continuum limit is the full SU(2) lattice model in the absence of a truncation.

Looking at the continuum extrapolation for the vector mass gaps, we observe a noticeably different behavior. While the ground-state energy densities do not show any significantly different behavior for small $j_{\max}$, the vector mass gaps do, as Fig. 7.7 reveals. In particular, for $j_{\max} = 1/2$ our data suggests that higher than quadratic order corrections in ag are still relevant which results in large $\chi^2_{\text{d.o.f.}}$ in our fits. With the range of lattice spacings available, we do not seem to control lattice effects well enough to give a reliable error estimate for that case. For $j_{\max} = 1$ our data is reasonably well described with a quadratic function in ag ($\chi^2_{\text{d.o.f.}}$ around 1), nevertheless the error of the continuum estimate is still large. In contrast, for $j_{\max} = 3/2$ and 2 quadratic corrections in ag are irrelevant and our data is well described by a linear fit in the range of lattice spacings we study (for details see App. B.4). The final results obtained after the extrapolation for various masses and truncations are shown in Fig. 7.8. As the figure reveals, there is a considerable difference between the values obtained

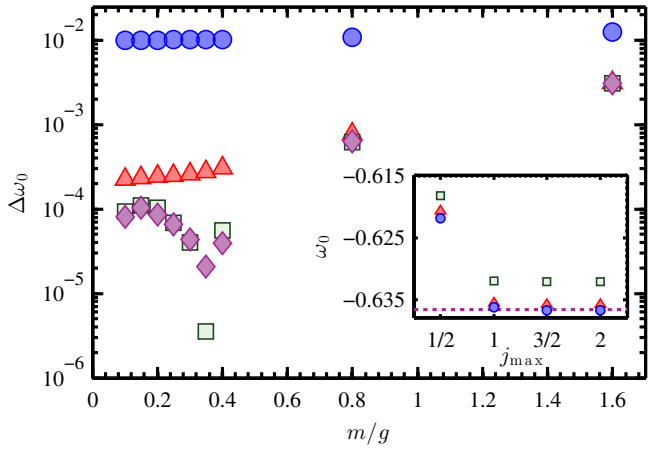

Figure 7.6: Relative deviation of the ground-state energy density with respect to the continuum solution of the full theory $-2/\pi$, $\Delta\omega_0$, as a function of m/g. The markers indicate different values for $j_{\max}$, where blue circles represent $j_{\max} = 1/2$, red triangles $j_{\max} = 1$, green squares $j_{\max} = 3/2$ and magenta diamonds $j_{\max} = 2$. Inset: Ground state energy density as a function of $j_{\max}$ for $m/g = 0.1$ (blue circles), $m/g = 0.8$ (red triangles) and $m/g = 1.6$ (green squares). The horizontal dashed line indicates the analytic solution for the ground-state energy, $-2/\pi$, for the full lattice Hamiltonian without truncation in the limit $ag = 1/\sqrt{x} \to 0$ [144]. The error bars are smaller than the markers.

for $j_{\max} = 1/2, 1, 3/2$. Only for values of $j_{\max} \geq 3/2$ our data agrees well with the numerical results obtained by a strong-coupling expansion in Ref. [144]. In particular, for the largest mass, $m/g = 1.6$ the data for $j_{\max} = 3/2, 2$ and from Ref. [144] are already close to the nonrelativistic limit, $m/g \to \infty$, for which the vector mass gap is given by $\Delta_{\text{vec}} = 2m/g$. On the contrary, the values obtained for $j_{\max} = 1/2, 1$ severely differ from the nonrelativistic prediction.

The fact we do not recover the continuum limit for the full theory for $j_{\max} = 1/2, 1$ might be due to several reasons. On the one hand, the truncation to a small value of $j_{\max}$ might lead to enhanced lattice effects. While the extrapolations to the bulk limit are in general unproblematic for all truncations we study, for the continuum extrapolations we observe that higher than linear order corrections are relevant for small $j_{\max}$, whereas this is not the case for $j_{\max} = 3/2, 2$. This could indicate that one would need smaller lattice spacings for truncations to a small color-electric flux, to control lattice effects properly. On the other hand, this might be a hint that the continuum limit for small $j_{\max}$ does not exist, similar to quantum link models [164, 256]. These different types of truncated gauge models, in which the gauge links are replaced by spins, are known to approach the continuum limit by dimensional reduction of an extra dimension.

Contrary to the Abelian Schwinger model, in the SU(2) case the chiral sym-

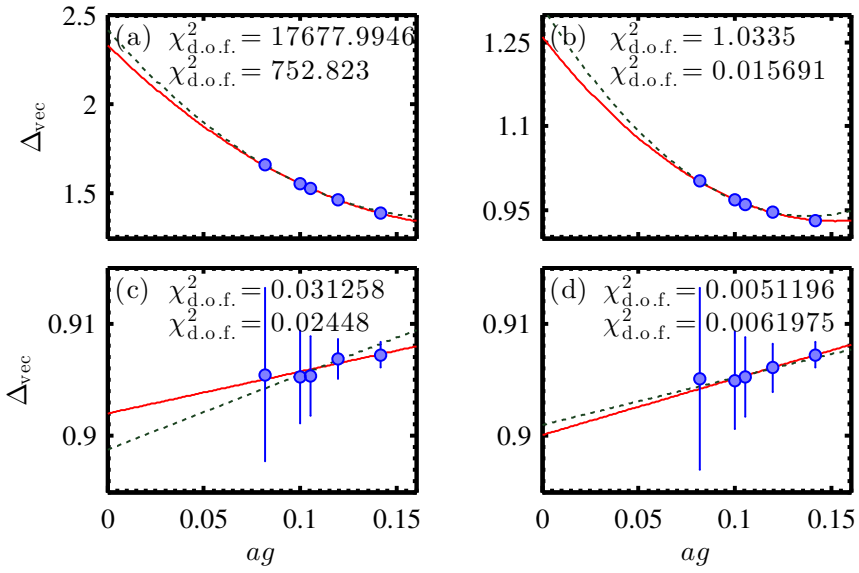

Figure 7.7: Continuum extrapolation for the vector mass gap for $m/g = 0.3$ and $j_{\max} = 1/2$ (a), $j_{\max} = 1$ (b), $j_{\max} = 3/2$ (c) and $j_{\max} = 2$ (d). The red line shows the fit used to extract the central value. The dashed green line shows the same fit omitting the largest lattice spacing to estimate the systematic error. The values indicate the $\chi^2_{\text{d.o.f.}}$ of the two fits, where the upper one corresponds to the red solid line and the lower one to the green dashed line. Notice the different scales of the y-axis between panels (a), (b) and (c), (d) showing that systematic errors are much larger for $j_{\max} = 1/2$ and 1.

metry is restored in the limit $m/g \to 0$ and hence the vector mass gap goes to zero and the theory becomes critical. From our data we can extract the critical exponent for the vector mass gap, too. In order to obtain the critical exponent, we fit our data to a power law $\gamma(m/g)^\nu$ in the region of small masses $m/g \leq 0.4$, for which the model is still far away from the nonrelativistic limit. The final results obtained for the critical exponents are shown in Tab. 7.1. For $j_{\max} = 3/2$, 2

$j_{\max}$	ν
1	$0.781(93)_{\text{stat}}(65)_{\text{sys}}$
3/2	$0.700(29)_{\text{stat}}(11)_{\text{sys}}$
2	$0.700(29)_{\text{stat}}(12)_{\text{sys}}$

Table 7.1: Critical exponent for various values of $j_{\max}$, the first error is the fitting error with respect to a 1σ confidence interval, the second one the systematic error (for more details see App. B.4).

our estimates for the critical exponents essentially agree, within error bars, with 2/3, obtained for the large N_c limit of the model [258]. The central value

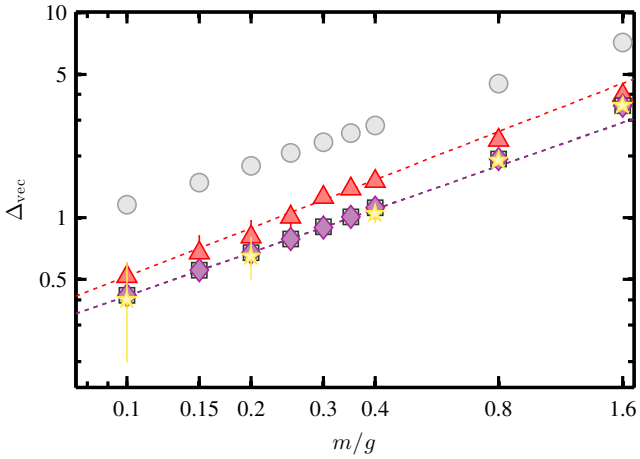

Figure 7.8: Vector state mass gap as a function of m/g for $j_{\max} = 1$ (red triangles), $j_{\max} = 3/2$ (green squares) and $j_{\max} = 2$ (magenta diamonds) on double logarithmic scale. The yellow stars represent the numerical values obtained from the strong-coupling expansion [144]. The dotted lines represent the best fit of the form $\gamma(m/g)^{\nu}$ to the data obtained on the interval $[0.1; (m/g)_{\max}]$ with $0.25 \leq (m/g)_{\max} \leq 0.4$. For completeness, we also show the data for $j_{\max} = 1/2$ (light gray circles), although in this case our lattice spacings do not allow for a reliable estimate.

for $j_{\max} = 1$ is not so close to 2/3, nevertheless, within the relatively large error bars it is still compatible. In the case of the simplest nontrivial truncation, $j_{\max} = 1/2$, a fit to our data yields 0.639 for the critical exponent. However, due to the large lattice effects in the vector mass gaps, the value is not reliable and we cannot confidently estimate the uncertainty, which we expect to be large, too.

These observations also have important implications for a potential future quantum simulator. Our data show that the ground-state energy densities obtained from our family of truncated models already give a good estimate for the one of the full model in the continuum, even with the simplest nontrivial truncation. In contrast, the vector state is much more sensitive to truncation effects. Although with our data it is not possible to fully rule out that for small $j_{\max}$ one suffers from enhanced lattice effects, they might indicate that the model does not have a proper continuum limit in those cases.

7.6 Entanglement entropy

7.6.1 Entanglement entropy in lattice gauge theories

There is a renewed interest in understanding the structure of entanglement in the gauge invariant scenario, motivated in part by a deep connection between entanglement and space-time geometry that has been suggested in the context of the gauge/gravity duality [247, 248]. However, the definition of entanglement entropy for the vacuum of a LGT entails some subtleties since the gauge constraints do not respect the locality of a chosen bipartition [249–253].

Recently it has been shown that the gauge symmetry acts as a superselection rule and the RDM for a subsystem can be written as a direct sum of terms supported on sectors corresponding to different flux configuration of the boundary links [250–252]. Specifically for the 1+1 dimensional case, we can decompose the RDM for the leftmost L sites and links as $\rho = \oplus_j \hat{\rho}_j$, where j labels the flux on the (outgoing) L-th link (see Fig. 7.9). Hence, the von Neumann entropy

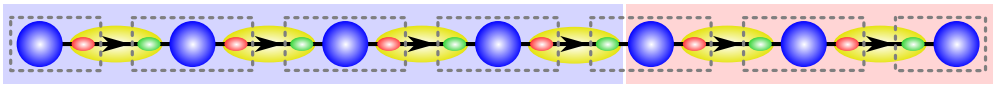

Figure 7.9: Illustration of a bipartition in the first L sites and links (light blue shaded area) and the rest (light red shaded area). The fermionic sites are indicated by blue circles, the black lines with the yellow ovals represent the gauge links connecting two sites, where the arrows show the orientation. The red (green) ovals correspond to the left (right) electric field on a link. The gray dashed squares indicate the gauge constraints.

can be written as

$$S(\rho) = -\mathrm{tr}\Big(\rho \log_2(\rho)\Big) = -\sum_j p_j \log_2(p_j) + \sum_j p_j S(\rho_j).$$

Here ρ_j is the (normalized) RDM corresponding to sector j and $p_j = \mathrm{tr}(\hat{\rho}_j)$. For non-Abelian theories, the second term can be further simplified. For a given sector, j, the Gauss law fixes the sum of the charge and the incoming flux in the last vertex (see Fig. 7.9). As a consequence, ρ_j has a block diagonal structure $\rho_j = \bar{\rho}_j \otimes \mathbb{1}_j$, where $\mathbb{1}_j$ is the identity on on the subspace corresponding to j for the combined incoming flux plus vertex charge. Specifically for SU(2), the identity for the sector j is $2j+1$ dimensional which finally yields

$$S(\rho) = -\sum_j p_j \log_2(p_j) + \sum_j p_j \log_2(2j+1) + \sum_j p_j S(\bar{\rho}_j), \tag{7.10}$$

Looking at Eq. (7.10), we can identify three contributions to the entanglement entropy. The last part, $S_{\mathrm{dist}} := \sum_j p_j S(\bar{\rho}_j)$, represents the physical entropy

which can be distilled from the system by means of local operations and classical communication (LOCC). The first two terms, $S_{\text{class}} := -\sum_j p_j \log_2 p_j$ and $S_{\text{rep}} := \sum_j p_j \log_2(2j+1)$, which we respectively call the classical and the representation part, have their origin in the Gauss law, implying that the physical subspace is not a direct product of the Hilbert spaces for the links and the sites. They cannot be extracted with LOCC and appear due to the embedding of the physical subspace in the larger space spanned by the basis states discussed in Sec. 7.2 supporting a tensor product structure [250–252].

Our reduced gauge invariant formulation, together with TN techniques, allow us not only to determine the mass spectrum of the theory, but also to compute the different contributions to the entanglement entropy of the corresponding ground state and to analyze the behavior of this quantity as we approach the continuum limit, as well as to tell to what extent these features are sensitive to a truncation in the gauge degrees of freedom. Looking at a state in the full basis, we can compute the RDM for the L leftmost sites in the sector j by simply applying a local projector $\Pi_j^{(L)}$ on link L projecting it onto flux j. In our reduced formulation the gauge degrees of freedom are integrated out, but the value of j can be read out from the fermionic content, and the RDM $\tilde{\rho}$ for the corresponding state in our basis is still block diagonal. Thus we can write

$$S(\tilde{\rho}) = -\sum_j \tilde{p}_j \log_2(\tilde{p}_j) + \sum_j \tilde{p}_j S(\tilde{\rho}_j),$$

where $\tilde{p}_j = \text{tr}(\tilde{\rho}_j)$. Similarly to the full basis, we can obtain $\tilde{\rho}_j$ by applying the corresponding projector $\tilde{\Pi}_j$. In our formulation the model is effectively abelianized, hence, compared to the full basis, the last term cannot be further simplified and does not give rise to a representation contribution. Since the quantum circuit which takes a state from our basis to the full one does not change j, the weights for the different sectors of the reduced density matrices are equal in both bases, $p_j = \tilde{p}_j$. Moreover, one can prove that $S(\bar{\rho}_j) = S(\tilde{\rho}_j)$, the distillable entropy is also equal in both bases (see App. C.4 for the formal argument). Thus, we can directly compute the different contributions S_{dist}, S_{class} and S_{rep} and therefore the total entropy in the full basis from our formulation. Notice, however, that the calculation in the reduced basis is much more efficient, because of the smaller physical dimensions we need to manipulate.

In 1+1 dimensions, a massive relativistic quantum field theory corresponds to a spin model off criticality in the scaling limit, for which the correlation length in lattice units, $\hat{\xi}$, is large. For such a system the entanglement entropy for the RDM describing half of the system is given by $S \propto (c/6)\log_2(\hat{\xi})$ [259], where the parameter c is the central charge of the underlying conformal field theory describing the system at the critical point. Taking the continuum limit of the lattice formulation, $ag = 1/\sqrt{x} \to 0$, corresponds to approaching the limit of diverging correlation length in lattice units [112]. Consequently, for the full

theory without truncation, we expect the entropy for the RDM for half of the system to be logarithmically UV divergent as

$$S = -\frac{c}{6}\log_2(ag) + c_2 \times ag + c_3 + \mathcal{O}\left((ag)^2\right), \tag{7.11}$$

where c_2, c_3 are constants and we take into account finite lattice corrections as in Ref. [41]. If the color flux is truncated at a finite value $j_{\max}$, both S_{class} and S_{rep} are upper bounded by a finite quantity for any value of the lattice spacing. Therefore, the logarithmic divergence can only originate from the physical entropy. Considering our results from the previous Sections, we observe convergence for small values of $j_{\max}$ at all lattice spacings we use, consistent with similar studies in the Schwinger model [53], thus indicating that contributions with large j are negligible. Consequently, we also expect the logarithmic divergence for the full model to be caused only by S_{dist}, although when taking the continuum limit and going to increasingly small lattice spacings, we may need larger $j_{\max}$ to observe the saturation of S_{class} and S_{rep}.

7.6.2 Numerical results

With our numerical data, we can check if the entropy in the ground state for our family of truncated models diverges, too. To this end, we look at the different contributions to the entanglement entropy for a cut along the center of the system in the same range of values for $(j_{\max}, m/g, x, N, D)$ as in the previous Sections and study the scaling of S for $ag = 1/\sqrt{x} \to 0$. In general, we observe that none of the different contributions to the entropy shows strong finite size effects for bipartitions that are far away from the boundaries (see Fig. 7.10(a) for an example). Nevertheless, we may expect an oscillating contribution to the entropy that becomes smaller as the system size increases [260, 261]. To minimize these effects, we average over the values obtained for 4 bipartitions around the center to estimate the different entropy contributions for the half-chain. As Figs. 7.10(b)-(c) indicate, these averaged values are essentially converged in bond dimension and their dependence on the system size is negligible. Hence, we simply take the values obtained for $D = 200$ as central value for every combination of $(j_{\max}, m/g, x, N)$ and estimate our error as the difference with respect to the value obtained for $D = 150$. Additionally, we take into account a systematic error due to the finite precision in our simulations (see App. B.4 for details). To compensate for residual finite size effects, we take the weighted average for every $(j_{\max}, m/g, x)$ for the largest two system sizes available. In a final step, we extrapolate the total entropies, obtained from the sum of the different contributions, to the limit $ag = 1/\sqrt{x} \to 0$ by fitting our data to Eq. (7.11). Figure 7.10(d) shows an example for the continuum extrapolation. We clearly observe a curvature in the data, thus indicating that the logarithmic term contributes and the entropy is indeed UV divergent. The final results for

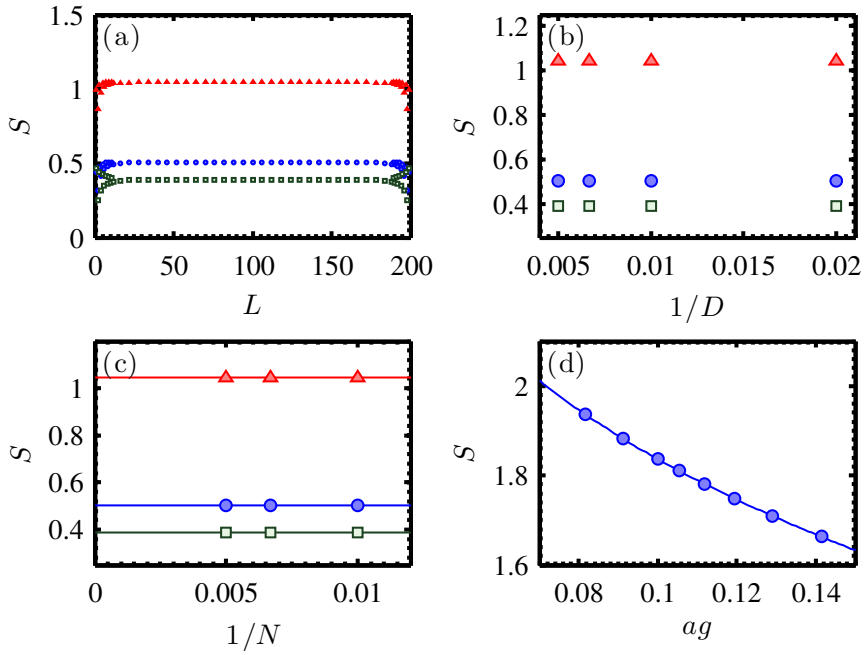

Figure 7.10: (a) The different contributions to the entanglement entropy, S_{dist} (blue circles), S_{class} (red triangles) and S_{rep} (green squares) for the RDM of the leftmost L sites for $N = 200$, $D = 200$, $m/g = 0.8$ and $j_{\max} = 2$. (b) Entropy contributions averaged over 4 bipartitions close to the center as a function of bond dimension. (c) Averaged entropy contributions for $D = 200$, $m/g = 0.8$ and $j_{\max} = 2$ as a function of system size. (d) Continuum extrapolation for the total entropy. In panels (b)-(d) the error bars of the data points are smaller than the markers.

c for different truncations as a function of the bare fermion mass are shown in Fig. 7.11. Notice that for the full theory, i.e., without a $j_{\max}$ truncation, we expect a central charge $c = 2$, corresponding to the two Dirac fermions that constitute the independent degrees of freedom of the theory. We see that our numerical results for $j_{\max} = 3/2, 2$ follow Eq. (7.11) well ($\chi^2_{\text{d.o.f.}} \ll 1$ in all our fits), and the values for c are close to the one for the full theory (see Fig. 7.11). Again, there is hardly any difference between the data for $j_{\max} = 3/2$ and $j_{\max} = 2$. For the smallest two truncations $j_{\max} = 1/2, 1$, instead, the picture is significantly different. In these cases our data is not very well compatible with a logarithmic divergence for $m/g \geq 0.2$ (resulting in $\chi^2_{\text{d.o.f.}} \gg 1$ in our fits). In the region of small m/g, for which our data follows Eq. (7.11) reasonably well, the central charges we obtain differ noticeably from 2. Hence, although the ground-state energy densities are rather insensitive to the truncation, the entanglement entropies of the same states show another sign that we do not recover the proper continuum limit for a small $j_{\max}$ truncation.

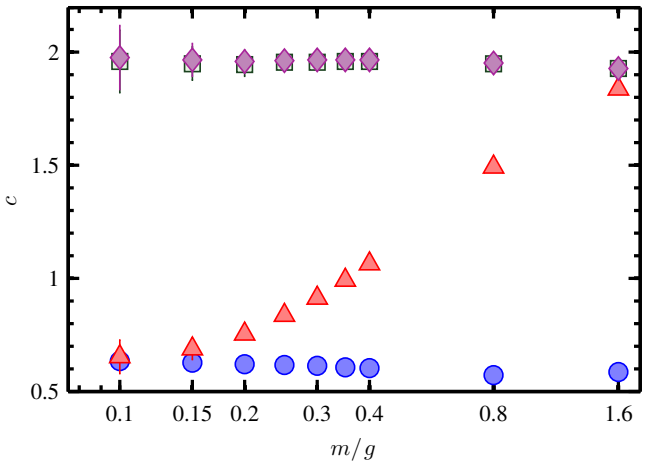

Figure 7.11: Central charges extracted from the scaling of the entanglement entropy as a function of m/g for $j_{\max} = 1/2$ (blue circles), $j_{\max} = 1$ (red triangles), $j_{\max} = 3/2$ (green squares), and $j_{\max} = 2$ (magenta diamonds).

7.7 Conclusion

In this Chapter, we introduced an efficient physical basis for a 1+1 dimensional SU(2) lattice gauge theory on a finite lattice with OBC. Building on a color-neutral basis used for the strong-coupling expansion of the model [142, 144], we showed how to remove the gauge degrees of freedom. Moreover, our formulation allows us to truncate the maximum color-electric flux at a finite value $j_{\max}$ in a gauge invariant manner, yielding a family of SU(2) gauge models with finite dimensional Hilbert spaces, that coincide with a SU(2) lattice gauge theory in the limit $j_{\max} \to \infty$. While general methods exist to truncate arbitrary gauge models with discrete finite or continuous compact Lie groups to a finite dimension [57], the truncation achieved for this particular case is a lot more efficient.

The basis we developed is completely general and can in principle be used with any numerical technique. Here we combined the use of MPS with an efficient truncation for the color-electric flux to explore different limits. Due to the reduced number of degrees of freedom, we are able to reach values for $j_{\max}$ far beyond those ones reached in previous numerical work with TN [43, 52]. To systematically study truncation effects, we computed the ground-state energy density, the entanglement entropy in the ground state, the vector mass gap and its critical exponent for a family of truncated SU(2) models with a maximum color-electric flux of $j_{\max} = 1/2, 1, 3/2, 2$.

In general, our findings for the ground state in the SU(2) case are consistent with those recently reported for the Schwinger model with truncated gauge links [53]. There it was observed that truncating the maximum electric field

to a modest value yields a ground state close to the one of the full model in a wide range of bare fermion masses and lattice spacings. In our calculations we also see that the continuum estimates for the ground-state energy density are rather insensitive to the truncation. Even for the simplest nontrivial truncation, the deviation between the values obtained from our family of truncated model with respect to the continuum result of the full theory is only at the percentage level. Moreover, the results converge quickly with increasing $j_{\max}$ such that between results for $j_{\max} = 3/2$ and 2 we observe hardly any difference. This is also encouraging for future quantum simulators for which it might be necessary to truncate the gauge degrees of freedom to allow for an experimental realization.

However, truncating the model has also observable effects. The vector mass gap is a lot more sensitive to a truncation of the maximum color-electric flux. For the simplest nontrivial truncation, $j_{\max} = 1/2$, we cannot control lattice effects in the extrapolations well and reliably estimate the errors. The final value obtained for the mass gap in this case differs significantly from previous numerical results. For $j_{\max} = 1$ lattice effects are becoming smaller, thus allowing for a reliable error estimate. Nevertheless, they are still pronounced and again the continuum estimate for the vector mass gap is not compliant with previous numerical results within error bars. On the contrary, for $j_{\max} = 3/2, 2$ the continuum extrapolations are unproblematic and we obtain precise values for the vector mass gap which agree with the ones from Ref. [144]. Although our data for $j_{\max} = 1/2, 1$ do not allow us to rule out with certainty that for finer lattices the results would approach the continuum result of the full model, the pronounced lattice effects in those cases might indicate that the continuum limit for these truncated models does not exist, as it is the case for quantum link models [256]. Our findings for the critical exponents for the vector mass gap are essentially in agreement with a calculation in the large N_c limit [258].

Looking at the scaling of the bipartite entanglement entropy in the ground state towards the continuum limit, we observe similar effects as for the vector mass gap. The central charges for the two simplest nontrivial truncations differ noticeably from the expected value of 2 for two Dirac fermions and, in particular, for large bare fermion masses our data do not follow the expected logarithmic UV divergence well. On the contrary, for $j_{\max} = 3/2, 2$ our numerical values show a clear indication of a logarithmic divergence and we find values close to 2 throughout our entire regime of bare fermion masses we study. Thus, although the ground-state energy densities extracted for $j_{\max} = 1/2, 1$ are close to the values for the continuum model, this is giving a further indication that for these truncations we do not recover the continuum theory in the limit of vanishing lattice spacing.

Finally, regarding the applicability of MPS and more general TN for LGT calculations, it is also possible to target other masses in the theory, such as scalar mass gap or baryon masses, which can be computed in a similar fashion with

the basis we have developed. Moreover, our formulation is not restricted to static problems and can be used to compute time evolution, hence also giving access to dynamical properties.

Chapter 8

Summary and outlook

In this thesis, we have numerically investigated several 1+1 dimensional lattice gauge models using a particular kind of one-dimensional TN, the MPS. Our studies are focused around two specific models, the (Abelian) Schwinger model, or quantum electrodynamics in 1+1 dimensions, and a (non-Abelian) SU(2) LGT. We have used these studies as a testbench for different aspects of quantum and classical simulations of LGT.

On the one hand we we have shown that MPS are an adequate tool to explore the feasibility of quantum simulations proposals and to investigate the limitations arising from the necessary approximations to allow for an experimental implementation. To this end, we have examined two proposals for quantum simulating the Schwinger model for the single-flavor case, where the gauge degrees of freedom are truncated to a finite dimension. Using variational methods based on TN, we have shown that the ground-state energy density is relatively insensitive to the truncation of the gauge degrees of freedom and the results converge rapidly with increasing dimension for the link Hilbert spaces. Moreover, taking advantage of the fact that TN enable the simulation of real-time dynamics, we have also explored a possible adiabatic preparation protocol for the interacting vacuum of theory starting from the strong coupling ground state. In the parameter regime under consideration, our simulations show that the initial part of the evolution is crucial for the success of the preparation, as the energy gap is small in this region. Furthermore, our results give evidence that this protocol is to some extent robust to gauge-invariance-breaking noise. Although the overlap with the exact wave function for the noise-free case decays fast with increasing noise level, local quantities, such as the ground-state energy of the model, can still be estimated with a small error in the presence of noninvariant terms.

The MPS approach is not limited to the Abelian case, and we have also studied a suitable candidate for the implementation of a quantum simulator for a SU(2) lattice gauge theory. Simulating the evolution in imaginary and real time, we have investigated static as well as the dynamical properties of string breaking in this system. Our simulations in imaginary time allow us to determine the static potential between two heavy external charges, similar to the

conventional Monte Carlo approach, and to identify the parameter regions for which string breaking occurs. Moreover, exploiting again that MPS give access to all kinds of local observables, we can clearly locate the signatures of the string breaking process in the site resolved flux and charge square configuration as well in as in the statistics of string lengths, which are in principle also accessible in an experimental realization. Using real-time simulations, we can also access the dynamical aspects of string breaking. In a first setup, we have studied the dynamics of a string between two heavy external charges. With the observables proposed before, we can clearly distinguish between the non-breaking and the breaking case and observe the creation of dynamical fermions which over time start clustering around the external charges in the latter. In a second setup, we have investigated the dynamics of a string between two fully dynamical charges placed inside the system. Also for this case we can identify the breaking case and the associated creation of dynamical particles which are spreading through the system due to the absence of external charges. In particular, the real-time scenarios we have analyzed should be directly realizable in a quantum simulation experiment.

On the other hand, we have demonstrated precise lattice calculations using classical simulations with MPS, also in regimes which are intractable with the conventional MC approach. First, we have analyzed the phase structure for the two-flavor Schwinger model in the presence of a (isospin) chemical potential at a fixed physical volume, a regime where the conventional MC approach suffers from the sign problem. For sufficiently large volumes, our results for the massless case after extrapolating to the continuum limit are in agreement with the analytical predictions from Refs. [229, 230]. The MPS formalism also readily extends to the massive case, for which no analytical predictions are available, and we observe that the location of the phase transitions becomes volume dependent. Using the MPS approach, we are able to map out the phase diagram of the model in the mass – chemical potential plane, thus explicitly giving an example of TN overcoming the sign problem in a LGT calculation. Furthermore, using the fact variational methods based on TN yield the wave function at the end of the computation, we have also computed the spatially resolved chiral condensate within the different phases. Our study for the condensate in the massless case reveals spatial oscillations, similar to those predicted for the single-flavor case [233–235] and compliant with analytical predictions for the spatial dependence of fermion bilinear in the multiflavor case [232]. The amplitude of the observed oscillations is essentially given by the homogeneous condensate for vanishing isospin number, independently of the volume, whereas the oscillation frequency inside each phase shows a linear decrease with volume.

Furthermore, we have developed a formulation for the physical subspace of a SU(2) LGT, similar to the one which we employed in our simulations for the two-flavor Schwinger model. Our formulation is completely general and,

thus, suitable for any numerical or analytical method. In addition, with our formulation it is straightforward to truncate the color flux in a gauge invariant manner at arbitrary values. Combining MPS methods with the possibility to efficiently truncate the color-electric flux, we have studied the low-lying spectrum, the scaling exponents for the vector mass and the scaling of the bipartite entanglement in the ground state towards the continuum limit for a family of truncated models. Due to the great reduction of degrees of freedom in our formulation, we can reach much larger values for the maximum color-electric flux then previous studies with TN, thus allowing us to explore truncation effects in a systematic manner. Comparable to the Schwinger case, we observe that the ground-state energy density is relatively insensitive to the truncation and close to the value for the full theory in the continuum, even for the simplest nontrivial truncation. In contrast, the vector mass gaps and the scaling of the bipartite entanglement in the ground state are much more sensitive to the truncation, but the results converge again quickly with increasing value for the maximum color flux. In addition, the formulation we have developed is similar to the one already realized experimentally for the single-flavor Schwinger model in a small system of trapped ions [102]. Hence, it might also have potential applications for the design of future quantum simulators and possibly allow for simpler realizations due to reduced number of basis states compared to other truncation methods.

In our numerical studies we have focused on the case of zero temperature. However, the TN approach to LGT also allows for simulating thermal states as has been demonstrated in Refs. [40, 45, 46]. Moreover, our results are promising for a TN approach to higher-dimensional gauge models. For the same reasons MPS with small bond dimension provide a good ansatz for the one-dimensional case, we expect that the low-lying spectrum for the two-dimensional case can be efficiently described by PEPS [172]. Extending the success of MPS simulations to higher dimensions is not an immediate task, as the computational cost for PEPS simulations is much higher, thus making them much harder to handle numerically. However, in recent years there has been remarkable progress in both, the theoretical and the computational techniques for PEPS: on the one hand gauge invariant formulations suitable for LGT simulations have been developed [58, 59, 62], on the other hand there has been a steady improvement in the numerical algorithms [214, 262–266] for PEPS. Hence, TN simulations of higher-dimensional LGTs models are coming into reach [221].

The findings from our studies have also import implications for potential future quantum simulators for gauge theories. Our results give evidence that even if the gauge degrees of freedom have to be truncated to a small, finite dimension to allow for an experimental realization, one could obtain good estimates for ground-state energy with such a simulator. Although other quantities are more sensitive to the truncation, we observe in general a fast conver-

gence with increasing values for the maximum (color) electric flux allowed on the links. Moreover, our numerical results can also serve as benchmarking data that could help to test and validate future quantum simulation experiments.

Appendix A

Spin formulation

In general, MPS and TN can describe fermionic degrees of freedom with essentially no additional cost in the numerical algorithms [213, 216, 217]. For our simulations it is nevertheless convenient to map the models to a spin chain via a Jordan-Wigner transformation, as for the one-dimensional case this mapping preserves the locality properties of the original Hamiltonian. Here we show how to obtain the spin formulation for the lattice Hamiltonians we explored in the main text.

A.1 Spin formulation for the Schwinger model

The spin formulation can be obtained via the Jordan-Wigner transformation [121]

$$\psi_k = \prod_{l<k}(i\sigma_l^z)\sigma_k^-, \qquad \psi_k^\dagger = \prod_{l<k}(-i\sigma_l^z)\sigma_k^+,$$

where in case of multiple fermion flavors we choose to order the fermions inside each site according to their flavor such that $\psi_{k,f} = \psi_{kF+f}$. In the formula above σ_j^z and $\sigma_j^\pm$ are the usual Pauli matrices acting on spin j. Applying this transformation the Hamiltonian from Eq. (4.1) for the single-flavor case we obtain

$$W = -x\sum_{n=1}^{N-1}(\sigma_n^+ U_n \sigma_{n+1}^- + \text{h.c.}) + \frac{\mu}{2}\sum_{n=1}^{N}(-1)^n(\mathbb{1}+\sigma_n^z) + \sum_{n=1}^{N-1}L_n^2.$$

For the multiflavor case with chemical potential, we integrated out the gauge field which for vanishing background field and external charges corresponds to replacing $L_n = \sum_{k=0}^{n}\left(\sum_{f=0}^{F-1}\psi_{k,f}^\dagger\psi_{k,f} - \frac{F}{2}(1-(-1)^k)\right)$. The resulting spin for-

mulation for Eq. (5.1) after the transformation then reads

$$\begin{aligned} W = &- x \sum_{p=0}^{NF-1} \left(\sigma_p^+ (i\sigma_{p+1}^z) \dots (i\sigma_{p+F-1}^z) \sigma_{p+F}^- + \text{h.c.} \right) \\ &+ \sum_{n=0}^{N-1} \sum_{f=0}^{F-1} \left(\mu_f (-1)^n + \nu_f \right) \frac{1+\sigma_{nF+f}^z}{2} \\ &+ \sum_{n=0}^{N-2} \left(\frac{F}{2} \sum_{k=0}^{n} (-1)^k + \frac{1}{2} \sum_{k=0}^{n} \sum_{f=0}^{F-1} \sigma_{kF+f}^z \right)^2 . \end{aligned} \tag{A.1}$$

Hence, in this case a system with N sites and F flavors of fermions results in a spin chain of length NF after the transformation. Notice that the nonlocal term has already been present in the original Hamiltonian and did not arise due to the Jordan-Wigner transformation.

In both cases, we are targeting the sector with vanishing total charge. In principle this could be ensured by implementing this constraint directly at the level of the tensors in the MPS simulations. Here we choose a simpler method and enforce it in our variational calculations by adding a penalty term $P = \lambda \left(\sum_{n=0}^{N-1} Q_n \right)^2$ to the Hamiltonian. The staggered charge, Q_n, in spin formulation is given by

$$Q_n = \sum_{f=0}^{F-1} \frac{1}{2} \left(\sigma_{nF+f}^z + (-1)^n \right).$$

The spin Hamiltonian including the penalty term for vanishing total charge can be implemented efficiently as MPO for both, the single and the multiflavor case, despite the long-range interactions for the latter.

For our calculations presented in Chapter 5, we chose $\lambda = 1000$ and checked the expectation value of P, where we found that it is negligible for all our simulations.

A.2 Spin formulation for the SU(2) lattice gauge theory

For the SU(2) case we use the particular transformation from Ref. [267] and make the different colors explicit:

$$\psi_{r,n} = i \left[\prod_{l<n} \left(i\sigma_r^z \otimes i\sigma_g^z \right)_l \right] (\sigma_r^- \otimes \mathbb{1})_n, \quad \psi_{g,n} = - \left[\prod_{l<n} \left(i\sigma_r^z \otimes i\sigma_g^z \right)_l \right] \left(\sigma_r^z \otimes \sigma_g^- \right)_n . \tag{A.2}$$

The σ-matrices are the usual Pauli matrices, where the subscript indicates on which color on site n they are acting. This labeling is convenient for practical purposes and completely equivalent to ordering the fermions as $\psi_{r,1}$, $\psi_{g,1}$, $\psi_{r,2}$, $\psi_{g,2}\ldots$ and doing a usual Jordan-Wigner transformation on a single fermionic field $\tilde{\psi}_n$ which is related to original ones as $\tilde{\psi}_1 = \psi_{r,1}$, $\tilde{\psi}_2 = \psi_{g,1}$, $\tilde{\psi}_3 = \psi_{r,2}$, ...

Using the transformation from Eq. (A.2), the Hamiltonian can be expressed in spin language as follows:

$$\begin{aligned} H =& \varepsilon \sum_n \Big[\left(\sigma_r^+ \otimes \sigma_g^z\right)_n (U_n)_{-\frac{1}{2},-\frac{1}{2}} \left(\sigma_r^- \otimes \mathbb{1}_g\right)_{n+1} + \text{h.c.} \\ &+ \left(i\sigma_r^+ \otimes \sigma_g^z\right)_n (U_n)_{-\frac{1}{2},\frac{1}{2}} \left(\sigma_r^z \otimes \sigma_g^-\right)_{n+1} + \text{h.c.} \\ &- \left(\mathbb{1}_r \otimes i\sigma_g^+\right)_n (U_n)_{\frac{1}{2},-\frac{1}{2}} \left(\sigma_r^- \otimes \mathbb{1}_g\right)_{n+1} + \text{h.c.} \\ &+ \left(\mathbb{1}_r \otimes \sigma_g^+\right)_n (U_n)_{\frac{1}{2},\frac{1}{2}} \left(\sigma_r^z \otimes \sigma_g^-\right)_{n+1} + \text{h.c.} \Big] \\ &+ \frac{m}{2} \sum_n (-1)^n \Big[\left(\left(\sigma_r^z \otimes \mathbb{1}_g\right)_n + 1 \right) + \left(\left(\mathbb{1}_r \otimes \sigma_g^z\right)_n + 1 \right) \Big] + \frac{g^2}{2} \sum_n \mathbf{J}_n^2. \end{aligned}$$

The charge operators $Q_n^a = \frac{1}{2}\psi_n^\dagger \sigma^a \psi_n$ can then be expressed in spin language as

$$\begin{aligned} Q_n^x &= \frac{1}{2}\Big[\left(-i\sigma_r^+ \otimes \sigma_g^-\right)_n + \left(i\sigma_r^- \otimes \sigma_g^+\right)_n \Big], \\ Q_n^y &= -\frac{1}{2}\Big[\left(\sigma_r^+ \otimes \sigma_g^-\right)_n + \left(\sigma_r^- \otimes \sigma_g^+\right)_n \Big], \\ Q_n^z &= \frac{1}{4}\Big[\left(\sigma_r^z \otimes \mathbb{1}_g\right)_n - \left(\mathbb{1}_r \otimes \sigma_g^z\right)_n \Big]. \end{aligned}$$

A simple calculation yields for the charge square components

$$Q_n^{a\,2} = \frac{1}{8}\Big[1 - \left(\sigma_r^z \otimes \sigma_g^z\right)_n \Big] \qquad a = x, y, z.$$

Appendix B

Analysis of the numerical errors

In this Appendix we provide details about the extrapolation procedures and the estimation of the numerical errors we used to obtain the results presented in Chapters 4 - 7.

B.1 Quantum simulation of the Schwinger model

For the ground-state calculations presented in Chapter 4, we run the variational ground-state search, which we reviewed in Sec. 3.2, for different system sizes, N, lattice spacings, x, and several (odd) physical dimensions of the link variables $d_{\text{link}} = 3, 5, 7, 9$. For each combination of (N, d_{link}, x) we increase the bond dimension until the ground-state energy converges up to a predefined relative accuracy. For the truncated cQED case we find $D = 100$ together with a relative accuracy 10^{-6} to be sufficient for all the studied parameters, while for the $\mathbb{Z}_d$ model we go up to $D = 200$ and a relative accuracy of 10^{-12}. Our final energy value is extrapolated linearly in $1/D$ using the two largest computed bond dimensions and the error is estimated as the difference to the largest D result.

To obtain the ground-state energy density in the thermodynamic limit for a fixed lattice spacing (see Fig. 4.2), we perform a finite-size extrapolation for each pair (x, d_{link}) using the same functional form as in Refs. [35, 141]

$$\frac{E_0}{2Nx} \approx \omega + \frac{c_1}{N} + \mathcal{O}\left(\frac{1}{N^2}\right).$$

The continuum estimates for the ground state energy density are again obtained following Refs. [35, 141], and we extrapolate our data from the previous step for each d_{link} by fitting it to a quadratic function in $1/\sqrt{x} = ga$. The results from this extrapolation are expected to be only of limited precision, since the lattice spacings used in Chapter 4 correspond to $x \in [50, 100]$ and are still far away from the continuum, which constitutes a source of error much more important than that of the particular fit.

In our time-evolution simulations we have an additional source of error due to the second order time dependent Suzuki-Trotter approximation [207] of the

time-evolution operator. For the results presented in Sec. 4.4 and 4.5 we have tried different time steps and a value of $\Delta t = 0.001$ turns out to be sufficiently small, so that the errors are much below the observed effects. The large error bars in Fig. 4.5 for small T are due to the limited bond dimension. In these cases the evolution is not close enough to adiabaticity and one ends up in a superposition state which differs from the ground state and cannot be well approximated by a MPS with our values of $D = 30, 50$. As one can see, for larger total evolution times, for which one stays close to ground state throughout the entire evolution, this effect vanishes and the simulations converge with a small D.

B.2 The multiflavor Schwinger model at nonzero chemical potential

Our discussion of the multiflavor Schwinger model in Chapter 5 shows that the precision that can be obtained for the phase transition locations crucially depends on the precision of the ground-state energies (see Eq. (5.6)). To get precise estimates for the exact energy, we extrapolate our numerical data to the limit $D \to \infty$. To do so, we repeat the calculation for each data point for a given combination of volume Lg, lattice spacing x and chemical potential difference $\mu_I/2\pi$ for several bond dimensions until the energy approximately scales linearly in $1/D$. For the data presented in the Chapter 5, we find that for $x \in [9, 36]$ a maximum bond dimension of $D = 160$ is enough to enter the linear scaling region, whereas for larger values of x we have to increase the bond dimension up to 220. Once we enter this regime, we take the last three data points to extrapolate linearly (see Fig. B.1 for an example). As an estimate for the exact energy we take the mean value of our data point computed with the largest bond dimension, $E_{D_{\max}}$, and $E_{D=\infty}$ obtained by our extrapolation. The error is estimated as $\Delta E = \frac{1}{2}(E_{D_{\max}} - E_{D=\infty})$. Subsequently, we plug these estimates for the exact energies in Eqs. (5.5) and (5.6) to obtain the location of the phase transition and the corresponding systematic error for a fixed combination of (Lg, x).

In a final step we can now extrapolate the extracted locations for the phase transitions to the continuum. We proceed analogously to the single-flavor case and fit a second order polynomial in $1/\sqrt{x}$ and take the intersection point with the y-axis as estimate for the continuum value (see Fig. B.2 for an example). As an error estimate for the continuum value, we take the fitting error where we use a 1σ confidence interval. The final results for the location of the phase transitions obtained after the full extrapolation procedure are shown in Chapter 5 in Tabs. 5.1 - 5.4.

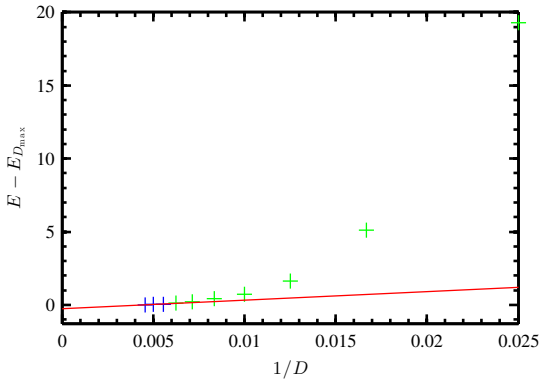

Figure B.1: Extrapolation in bond dimension for $m/g = 0$, $\mu_I/2\pi = 0.8$, $x = 121$ and $Lg = 8$. The blue data points are the ones used for the extrapolation to the limit $D \to \infty$ and the red line shows the linear fit through the blue data points.

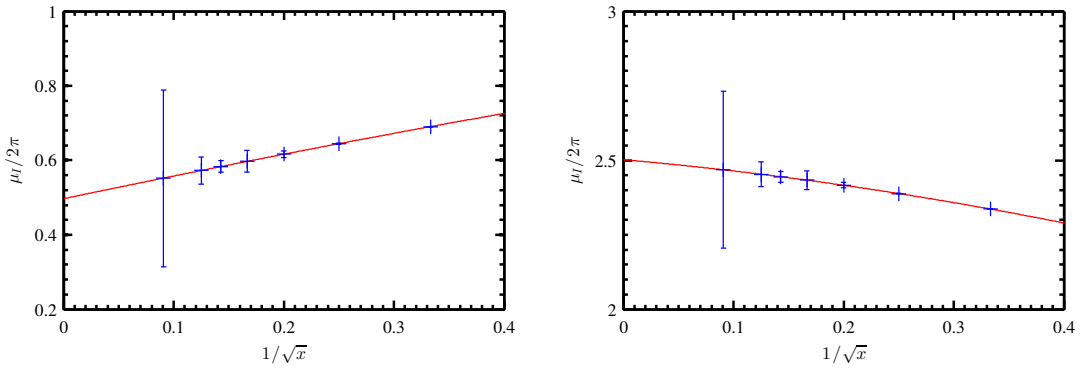

Figure B.2: Extrapolation of the phase transition points to the continuum for $Lg = 8$ in the massless case for the first (left) and the third (right) phase transition. The red line represents a second order polynomial fit in $1/\sqrt{x}$ and the continuum limit is estimated by taking the value of the fit function at $1/\sqrt{x} = 0$.

B.3 Non-Abelian string breaking phenomena with matrix product states

In this Appendix we analyze the numerical errors of the results presented in Chapter 6. In the main text we have already presented data for different system sizes, thus showing that $N = 22$ is enough to avoid noticeable finite-size effects for the considered range of parameters. Here we focus on the influence of the time-step size and the bond dimension on our results.

B.3.1 Ground state with static external charges

In Fig. B.3 we show how the spin and the flux configuration changes for a system of size $N = 22$, if a larger bond dimension or a smaller time step is used. As the figure shows, there is no significant improvement with larger bond dimension. Reducing the time step by a factor of two to $\Delta t = 0.5 \times 10^{-3}$ leads to a slightly different spin and flux configuration on the order of 10^{-2} for $m = 3.0$. However, these changes are predominantly at an early stage of the evolution and the difference in the final configuration is much smaller. For $m = 10.0$ the picture is qualitatively similar, at a very early stage there are small differences which are roughly one order of magnitude less than in the $m = 3.0$ case. All in all, the variations for reduced time step and larger bond dimension are rather small compared to the data for $\Delta t = 1.0 \times 10^{-3}$, $D = 100$ presented in Fig. 6.3, hence justifying our choice of time step and bond dimension.

B.3.2 Real-time evolution with static external charges

Also for the real-time evolution case with static external charges, we analyze our error analogous to the imaginary-time case. The difference in results for a smaller time step $\Delta t = 0.5 \times 10^{-4}$ and larger bond dimension $D = 130$ is presented in Fig. B.4. A reduction of the time step shows an effect rather similar to the imaginary-time scenario and leads to variations on the order of 10^{-3} for $m = 3.0$ and 10^{-4} for $m = 10.0$. For $m = 3.0$, the differences compared to results with enlarged bond dimension are more pronounced than in the imaginary-time case, whereas for $m = 10.0$ there is essentially no change up to machine accuracy. Overall, we see the same picture as in the imaginary-time setup: our choice of time step and bond dimension controls the error well enough to avoid considerable influences on the effects observed in Fig. 6.5.

B.3.3 Real-time evolution with dynamical charges

For the real-time evolution with dynamical charges the same error estimation as in the previous cases yields the results in Fig. B.5. A reduction of the time step from $\Delta t = 1.0 \times 10^{-4}$ to 0.5×10^{-4} leads to variations in the spin and flux configuration on the order of 10^{-2}. Contrary to the scenarios with static charges, the difference is more pronounced for a large fermion mass $m = 10.0$, whereas for smaller fermion masses there is less deviation. For the bond dimension, however, we see again the same effect as in the static setups that the variations are more pronounced if the mass is smaller, whereas there is almost no difference for larger mass. Nevertheless, also for this case the absolute changes in the spin and flux configuration are rather small compared to the data presented in Fig. 6.8, thereby showing that the errors due to our choice of time step and bond dimension are negligible.

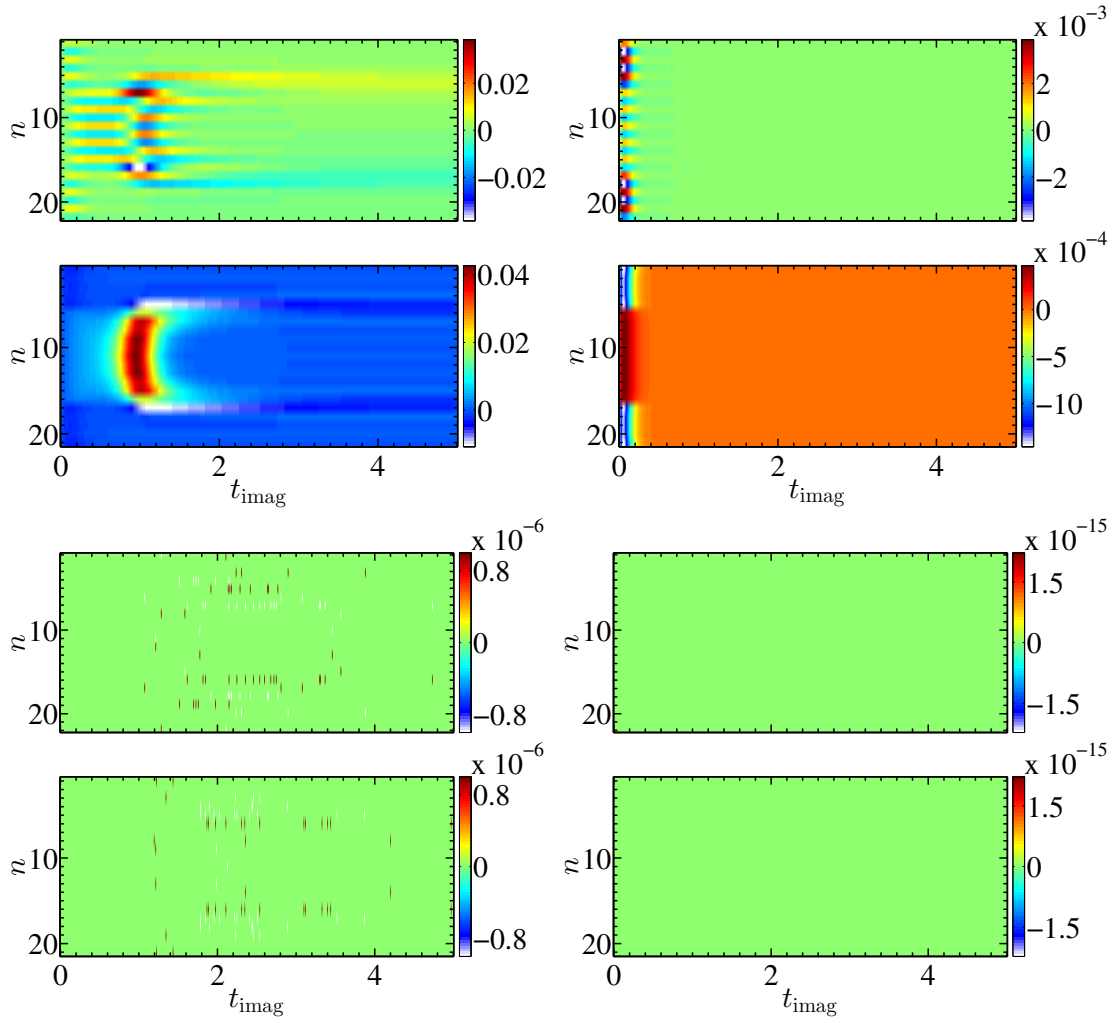

Figure B.3: Difference in the site resolved expectation values for the spin (first and third row) and the flux (second and fourth row) for a system of size $N = 22$ and dynamical fermion mass $m = 3.0$ (left column) and 10.0 (right column). The upper two rows show the difference between results computed with a time step $\Delta t = 1.0 \times 10^{-3}$ and 0.5×10^{-3} for $D = 100$, the lower two rows the difference between results computed with $D = 100$ and 130 for $\Delta t = 1.0 \times 10^{-3}$.

B.4 Efficient basis formulation for 1+1 dimensional SU(2) lattice gauge theories

Here we give more details on the extrapolation procedure for our data and the analysis of our numerical errors we used to obtain the results presented in Chapter 7.

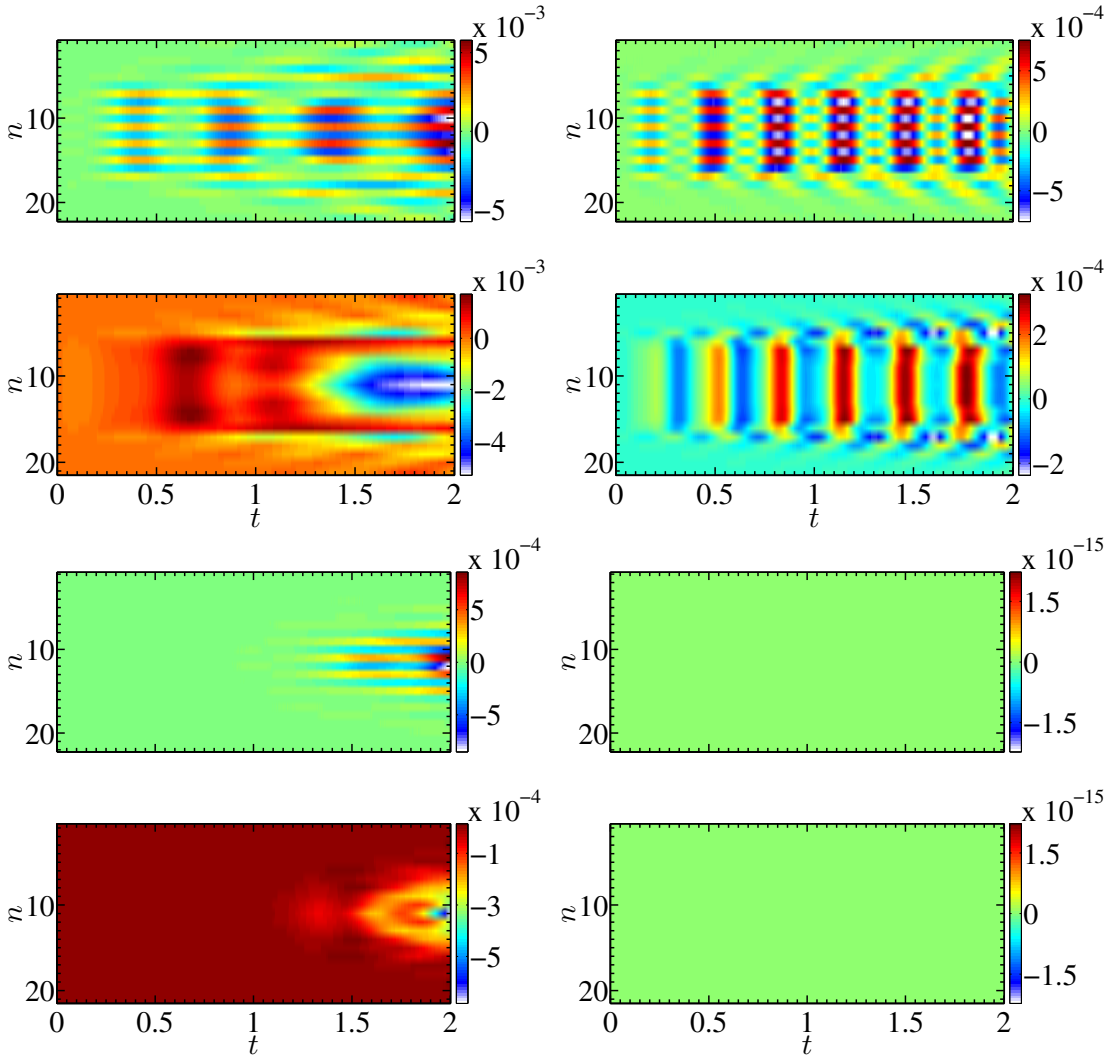

Figure B.4: Difference in the site resolved expectation values for the spin (first and third row) and the flux (second and fourth row) for a system of size $N = 22$ and dynamical fermion mass $m = 3.0$ (left column) and 10.0 (right column). The upper two rows show the difference between results computed with a time step $\Delta t = 1.0 \times 10^{-4}$ and 0.5×10^{-4} for $D = 100$, the lower two rows the difference between results computed with $D = 100$ and 130 for $\Delta t = 1.0 \times 10^{-4}$.

B.4.1 Ground state energy and vector state mass gap

In a first step, we estimate the exact values for the ground-state energy and the vector mass gap by extrapolating for each combination of $(j_{\max}, m/g, x, N)$ to the limit $D \to \infty$, analogous to the multiflavor Schwinger case. As the examples in Fig. 7.4(a)-(b) in the main text show, we plot our data versus $1/D$ and fit a line through the two data points with the largest bond dimension.

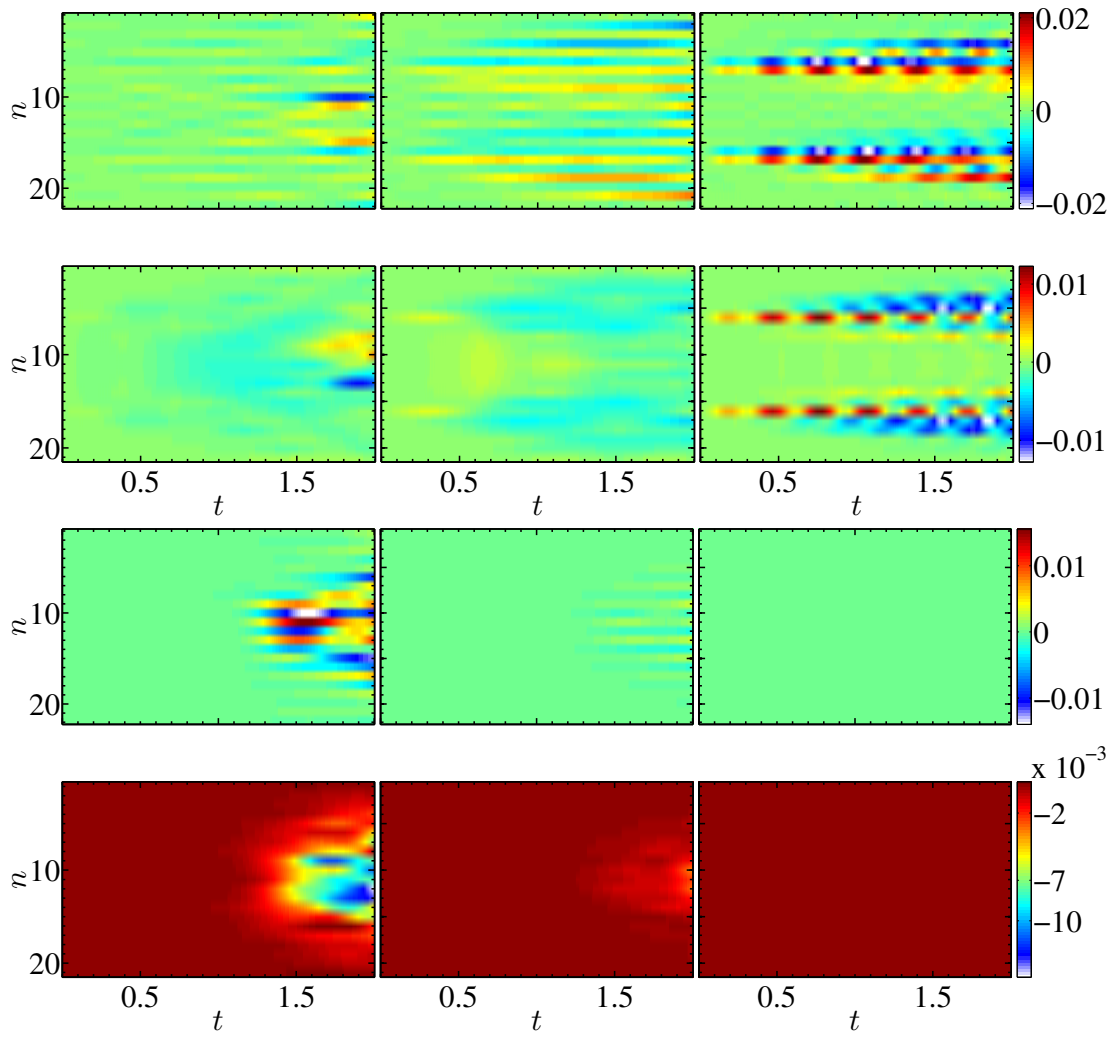

Figure B.5: Difference of the site resolved expectation values for the spin (first and third row) and the flux (second and fourth row) for a system of size $N = 22$ and dynamical fermion mass $m = 1.0$ (left column), 3.0 (central column) and 10.0 (right column). The upper two rows show the difference between results computed with a time step $\Delta t = 1.0 \times 10^{-4}$ and 0.5×10^{-4} for $D = 100$, the lower two rows the difference between results computed with $D = 100$ and 130 for $\Delta t = 1.0 \times 10^{-4}$.

As an estimate for the exact energy value (vector mass gap), we take the mean value of our data point computed with maximum bond dimension $E_{0,D_{\max}}(N,x)$ ($\Delta_{\mathrm{vec},D_{\max}}(N,x)$) and the extrapolated value corresponding to infinite bond dimension, $E_{0,D_\infty}(N,x)$ ($\Delta_{\mathrm{vec},D_\infty}(N,x)$). We estimate the error of the central value in a standard manner by taking half of the difference between these two values $\delta E_{\mathrm{fit}} = (E_{0,D_{\max}}(N,x) - E_{0,D_\infty}(N,x))/2$. Additionally to the extrapolation error, the central value obtained also has a systematic error due to the convergence

tolerance of $\varepsilon = 10^{-6}$ set in the simulations, $\delta E_{\text{sys}} = \varepsilon E_{0,D_\infty}(N,x)$. Taking into account this error, too, the final error for the ground-state energy (vector mass gap) is given by $\delta E_{\text{tot}} = \sqrt{(\delta E_{\text{fit}})^2 + \left(\delta E_{\text{sys}}\right)^2}$.

With the estimates for the exact ground-state energies and the vector mass gaps, we extrapolate to the thermodynamic limit for each combination of ($j_{\max}$, m/g, x), where we use the asymptotic behavior up to linear order [35, 141]

$$\frac{E_0}{2Nx} \approx \omega_0 + \frac{c_1}{N} + \mathcal{O}\left(\frac{1}{N^2}\right),$$
$$\frac{\Delta_{\text{vec}}}{2\sqrt{x}} \approx \omega_1 + \frac{c_2}{N^2} + \mathcal{O}\left(\frac{1}{N^3}\right),$$

and propagate our errors from the previous extrapolation in D. As an estimate for the error we take the fitting error with a 1σ confidence interval.

In a final step, we extrapolate to the continuum limit $ag = 1/\sqrt{x} \to 0$ by fitting a polynomial in $1/\sqrt{x}$ up to second order. In general, we take the value obtained by the lowest order statistically significant fit which achieves $\chi^2_{\text{d.o.f.}} < 1$ as central value. Statistically significant means that the errors for the fit coefficients are smaller than the actual value of the coefficient. In addition to the statistical error of the fit, we estimate the systematic error as the difference between our central value and the next statistically significant fit of the next highest order and/or omitting the largest lattice spacing. For the ground-state energy density the central value is for all cases determined by a quadratic fit. As an estimate for the systematic error we take the difference with respect to the value obtained by a quadratic fit omitting the largest lattice spacing, meaning in the region $x \in [70, 150]$.

Regarding the vector mass gap we observe largely enhanced lattice effects for small values of $j_{\max}$. In particular, for $j_{\max} = 1/2$ quadratic fits have high values for $\chi^2_{\text{d.o.f.}}$ (see Fig. 7.7). However, as we only have 5 different lattice spacings we cannot take higher order corrections into account. Thus, we again determine the central value with a quadratic fit taking into account all lattice spacings and again estimate the systematic error as the difference with respect to the value obtained by a quadratic fit omitting the largest lattice spacing. Consequently, in this case the error might be heavily underestimated as we are neglecting higher order corrections. For $j_{\max} = 1$, we find that for all $m/g \geq 0.3$ quadratic corrections are sufficient and proceed the same way for estimating the central value and its systematic error as for $j_{\max} = 1/2$. For $m/g = 0.25$, we estimate the central value via a linear fit taking into account the lattice spacings corresponding to $x \in [90, 150]$. The systematic error in this case is estimated as the difference with respect to a quadratic fit in the region $x \in [70, 150]$. For smaller masses $m/g \leq 0.2$ we find that both, linear and quadratic fits are statistically significant. Hence, we estimate our central value with a linear fit through all available lattice spacings, and, the systematic error as the

difference with respect to a quadratic fit in the same region. For the largest two truncations, $j_{\max} = 3/2, 2$, the quadratic correction loses significance and thus we estimate our central value for those cases with a linear fit. The systematic error is then determined as difference with respect to a linear fit discarding the largest lattice spacing, corresponding to $x = 50$. The final results obtained for the ground-state energy densities and the vector mass gaps following the procedure described above are listed in Tabs. B.1 and B.2.

	Ground-state energy density			
m/g	$j_{\max} = 1/2$	$j_{\max} = 1$	$j_{\max} = 3/2$	$j_{\max} = 2$
0.10	−0.621933(20)	−0.636285(28)	−0.636758(31)	−0.636740(84)
0.15	−0.621878(17)	−0.636275(36)	−0.636782(53)	−0.636773(24)
0.20	−0.621815(18)	−0.636258(56)	−0.636771(28)	−0.636745(33)
0.25	−0.621743(25)	−0.636255(45)	−0.636721(18)	−0.636716(22)
0.30	−0.621668(28)	−0.636239(45)	−0.636679(20)	−0.636684(39)
0.35	−0.621582(31)	−0.636210(40)	−0.636625(17)	−0.636650(22)
0.40	−0.621499(47)	−0.636170(19)	−0.636538(50)	−0.636562(25)
0.80	−0.62070(11)	−0.63548(10)	−0.63570(11)	−0.63569(13)
1.60	−0.61823(40)	−0.63200(63)	−0.63205(65)	−0.63205(65)

Table B.1: Ground-state energy densities obtained for various values for m/g and $j_{\max}$. The errors represent the sum in quadrature of the fitting uncertainty with a 1σ confidence interval and the systematic error.

	Vector mass gap			
m/g	$j_{\max} = 1/2$	$j_{\max} = 1$	$j_{\max} = 3/2$	$j_{\max} = 2$
0.10	1.154(43)	0.521(81)	0.418(20)	0.418(20)
0.15	1.489(46)	0.67(14)	0.557(15)	0.555(15)
0.20	1.788(63)	0.81(16)	0.678(12)	0.675(13)
0.25	2.067(74)	1.01(13)	0.790(10)	0.788(10)
0.30	2.329(85)	1.260(57)	0.9020(85)	0.9001(84)
0.35	2.576(97)	1.389(58)	1.0108(71)	1.0100(79)
0.40	2.82(10)	1.508(59)	1.1180(56)	1.1168(76)
0.80	4.51(11)	2.391(88)	1.9329(28)	1.9322(28)
1.60	7.14(17)	3.954(97)	3.5196(11)	3.5191(10)

Table B.2: Vector mass gaps obtained for various values for m/g and $j_{\max}$. The errors represent the sum in quadrature of the fitting uncertainty with a 1σ confidence interval and the systematic error.

B.4.2 Critical exponents for the vector mass gap

The values for the critical exponents for the vector mass gaps (see Tab. 7.1) are estimated in a similar fashion. Our data for $j_{\max} = 3/2, 2$, which are close to the ones from Ref. [144], reveal that for our largest fermion mass $m/g = 1.6$ we are already relatively close to the nonrelativistic limit. Hence, we restrict ourselves to data for small fermion mass to estimate the critical exponent. For each value of $j_{\max}$, we fit our data to a power law, $\gamma(m/g)^{\nu}$, for every interval $[0.1, (m/g)_{\max}]$ with $0.25 \leq (m/g)_{\max} \leq 0.4$. The central value is then determined from the fit with the smallest $\chi^2_{\text{d.o.f.}}$. To estimate our systematic error we take the difference between our central value and the fit giving the most outlying value. The statistical error is again given by 1σ error bar for the fitting error.

B.4.3 Entanglement entropy in the ground state

To study the scaling of the entropy towards the continuum limit and obtain an estimate for the central charges, we proceed as described in Sec. 7.6. First, to minimize finite size effects, we average each of the different contributions to the entropy for $D = 200$ and every combination of $(j_{\max}, m/g, x, N)$ for 4 bipartitions close to the center. To estimate our systematic error, we take the difference with respect to the values obtained with $D = 150$. Additionally, our data has another systematic error due to the finite precision in our simulations which has to be added on top. For the entropies we cannot give the same precise estimates for this systematic error as for the energies. To get nevertheless a rough idea of the order of magnitude, we compare results with convergence tolerance $\varepsilon = 10^{-6}$ and $\varepsilon = 10^{-10}$. Figure B.6 reveals that even for the largest value of $j_{\max}$, where we expect the largest differences between these results, it is around 10^{-5}. Hence, we simply assume a systematic error of 10^{-5} due to the finite precision of our simulations in all cases.

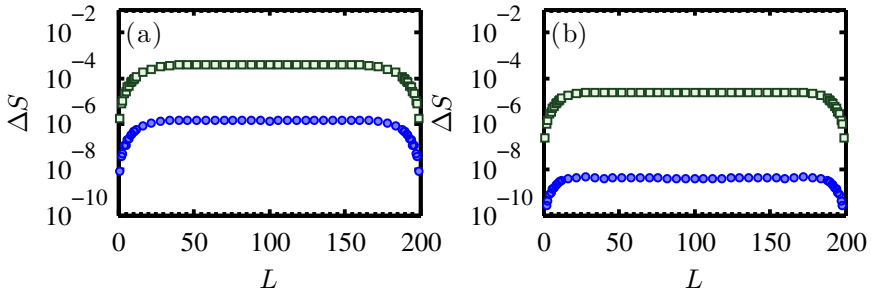

Figure B.6: Difference in the total entropy for the RDM for the leftmost L sites between simulation results obtained with $\varepsilon = 10^{-10}$ and $\varepsilon = 10^{-6}$. The panels show the results for $N = 200$, $x = 50$, $m/g = 0.1$ (a) and $m/g = 0.3$ (b). The blue dots indicate $j_{\max} = 1/2$, the green squares $j_{\max} = 2$.

Appendix C

Technical details for the efficient basis formulation for 1+1 dimensional SU(2) lattice gauge theories

C.1 Dimension of the physical subspace

Here we compute the dimension of the physical subspace contained in the basis developed in Chapter 7. For all the following we focus on a system with N sites and the case of vanishing background field, $j_0 = 0$.

As shown in Sec. 7.3, an arbitrary basis state can be expressed as $|\Psi\rangle = \otimes_{k=1}^{N} |\alpha_k\rangle$, $|\alpha_k\rangle \in \{|0\rangle, |1_-\rangle, |1_+\rangle, |2\rangle\}$. To calculate the dimension of the physical subspace, it is convenient to represent the 4^N basis states as directed paths from the root r to one of the leaves in a perfect quaternary tree of depth N. The vertices at level k are labeled with the color-electric flux j_k at link k, implied by the fermionic states sitting at the edges along the path from the root to the vertex due to Eq. (7.4) (cf. Fig. C.1). Unphysical states now correspond to directed paths from the root to one of the leaves that contain at least one vertex labeled by a negative number. Looking at a path starting from the root along vertices with nonnegative labels to the vertex v at level $k-1$, a vertex v' with negative label in level k can arise if and only if:

i) v is labeled by a 0,

ii) from v the path is continued along the edge corresponding to $|1_-\rangle$ thus ending up in a vertex v' labeled by $-1/2$.

Hence, the first vertex v' with negative label along a path corresponding to an unphysical state is always one carrying a $-1/2$. Moreover, all paths containing v' necessarily correspond to unphysical states. The number of paths containing v' is simply the number of paths through the perfect quaternary subtree of depths $N-k$ rooted by v', 4^{N-k}. Consequently, the number of unphysical states

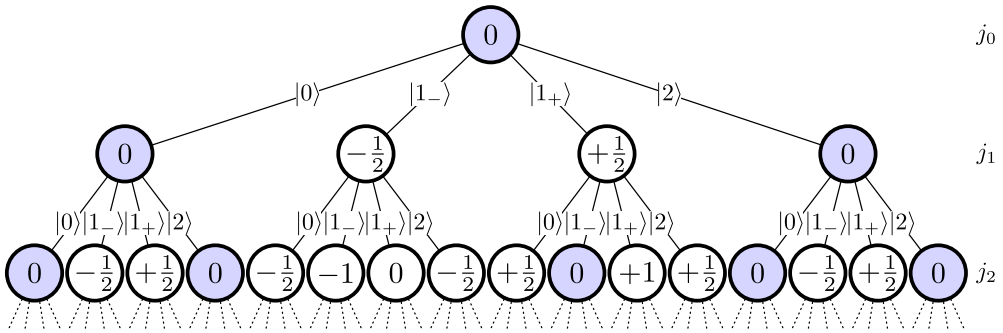

Figure C.1: The first three levels of the quaternary perfect tree representing the basis states. The vertices represent the color-electric flux indicated by the fermionic states on the edges along the path to each vertex using Eq. (7.4). The circles in light blue color correspond those vertices, for which one encounters for the first time a negative value, if the path leading to the vertex is continued along the edge carrying $|1_-\rangle$.

is given by $\sum_{k=1}^{N} \bar{t}_k 4^{N-k} = \sum_{k=0}^{N-1} \bar{t}_{k+1} 4^{N-(k+1)}$. Here $\bar{t}_k$ is the number of vertices carrying label $-1/2$ at level k, for which the path starting from r did not yet pass any other vertex with negative label. Due to observations i) and ii) $\bar{t}_k$ is equivalent to the number of paths t_{k-1} starting from r to a vertex at level $k-1$ with label 0 that did not yet pass any vertex with negative label. As we are going to show in the following, t_{k-1} is exactly given by the Catalan number $C_k = (2k)!/(k+1)!k!$. As a result, the number of unphysical states is $\sum_{k=0}^{N-1} t_k 4^{N-(k+1)} = \sum_{k=0}^{N-1} C_{k+1} 4^{N-(k+1)} = \sum_{k=1}^{N} C_k 4^{N-k}$.

To compute the number of paths starting from the root to a vertex at level k with label 0 that did not yet pass any vertex with negative label we use to following observations:

1. As explained in Sec. 7.3, the number of edges $l_{k,-}$ passed with $|1_-\rangle$ at any level $k' < k$ must not exceed the ones with $|1_+\rangle$, $l_{k,+}$, to avoid encountering any negative vertices along the path.

2. Looking at a path from the root with $j_0 = 0$, to any vertex labeled by 0 at level k, we immediately see that the condition $l_{k,+} = l_{k,-}$ has to be fulfilled in order to compensate for the flux changes induced by $|1_-\rangle$ and $|1_+\rangle$. In particular, this implies that $2l_{k,+} \leq k$ or equivalently $l_{k,+} \leq \llcorner k/2 \lrcorner$. The other $k - 2l_{k,+}$ edges along the path have to carry $|0\rangle$ or $|2\rangle$, as those states do not lead to a flux change while going from one layer to the other.

The number of paths of length $2l_{k,+}$ which contain at any point at least as many $|1_-\rangle$ as $|1_+\rangle$ is exactly the number of Dyck paths and given by the Catalan number $C_{l_{k,+}}$ [268]. Hence, the number of path fulfilling the conditions 1 and 2 at

level k is given by

$$t_k = \sum_{l_{k,+}=0}^{\lfloor k/2 \rfloor} C_{l_{k,+}} \binom{k}{2l_{k,+}} 2^{k-2l_{k,+}} = C_{k+1},$$

where the factor $\binom{k}{2l_{k,+}}$ takes into account the number of ways that the $2l_{k,+}$ symbols $|1_+\rangle$ and $|1_-\rangle$ can be distributed among the k levels and $2^{k-2l_{k,+}}$ the possible ways of filling the remaining edges with $|0\rangle$ and $|2\rangle$. In the last step we have used an identity for the Catalan numbers.

Thus, the dimension of the physical subspace is given by

$$d_{N,\text{phys}} = 4^N \left(1 - \sum_{k=1}^{N} \frac{C_k}{4^k}\right). \tag{C.1}$$

C.2 Hamiltonian in the new basis

In this Appendix we show how the terms of the Hamiltonian given in Eqs. (7.1) and (7.2) can be formulated in the basis presented in Sec. 7.3. As explained in the main text, the mass term is straightforward as even in the original formulation it only depends on the fermionic occupation number. The color-electric energy term can also readily be formulated in the new basis using Eq. (7.4). Hence, W_0 is given by

$$W_0 = \mu \sum_{k=1}^{N} (-1)^k \hat{n}_k + \sum_{k=1}^{N-1} \left(j_0 + \sum_{l=1}^{k} \hat{q}_l\right)\left(j_0 + \sum_{l=1}^{k} \hat{q}_l + 1\right), \tag{C.2}$$

with the single site operators $\hat{n}_k$, $\hat{q}_k$ that are given in Eq. (7.7) and Eq. (7.8) in the main text. From Eq. (C.2) one can see explicitly that integrating out the gauge field leads to nonlocal interactions in the color-electric energy term.

The hopping term can be obtained by translating the possible hopping processes shown in Fig. 7.1(c) in the new basis. The possible hopping processes in the new basis are listed in Tab. C.1. As the table reveals, the matrix elements for certain transitions depend on the color-electric flux, too, thus also leading to long-range interactions in the hopping term. The hopping term V can then be expressed in the new basis by defining the operators $O_{i,k}$

$$O_{1,k} = |0\rangle\langle 1_-|_k, \qquad O_{2,k} = |0\rangle\langle 1_+|_k,$$
$$O_{3,k} = |1_-\rangle\langle 2|_k, \qquad O_{4,k} = |1_+\rangle\langle 2|_k,$$

Initial state		Final state	Matrix element
$\|0\rangle\otimes\|2\rangle$	$\rightarrow$	$\|1_-\rangle\otimes\|1_+\rangle$	$(-1)^{j_k-j_{k-1}-1/2}\sqrt{\frac{2j_k+1}{2j_{k-1}+1}}$
$\|0\rangle\otimes\|2\rangle$	$\rightarrow$	$\|1_+\rangle\otimes\|1_-\rangle$	
$\|1_-\rangle\otimes\|1_+\rangle$	$\rightarrow$	$\|0\rangle\otimes\|2\rangle$	
$\|1_+\rangle\otimes\|1_-\rangle$	$\rightarrow$	$\|0\rangle\otimes\|2\rangle$	
$\|1_-\rangle\otimes\|1_+\rangle$	$\rightarrow$	$\|2\rangle\otimes\|0\rangle$	
$\|1_+\rangle\otimes\|1_-\rangle$	$\rightarrow$	$\|2\rangle\otimes\|0\rangle$	
$\|2\rangle\otimes\|0\rangle$	$\rightarrow$	$\|1_-\rangle\otimes\|1_+\rangle$	
$\|2\rangle\otimes\|0\rangle$	$\rightarrow$	$\|1_+\rangle\otimes\|1_-\rangle$	
$\|1_-\rangle\otimes\|0\rangle$	$\rightarrow$	$\|0\rangle\otimes\|1_-\rangle$	$+1$
$\|1_+\rangle\otimes\|0\rangle$	$\rightarrow$	$\|0\rangle\otimes\|1_+\rangle$	
$\|0\rangle\otimes\|1_-\rangle$	$\rightarrow$	$\|1_-\rangle\otimes\|0\rangle$	
$\|0\rangle\otimes\|1_+\rangle$	$\rightarrow$	$\|1_+\rangle\otimes\|0\rangle$	
$\|2\rangle\otimes\|1_-\rangle$	$\rightarrow$	$\|1_-\rangle\otimes\|2\rangle$	-1.
$\|2\rangle\otimes\|1_+\rangle$	$\rightarrow$	$\|1_+\rangle\otimes\|2\rangle$	
$\|1_-\rangle\otimes\|2\rangle$	$\rightarrow$	$\|2\rangle\otimes\|1_-\rangle$	
$\|1_+\rangle\otimes\|2\rangle$	$\rightarrow$	$\|2\rangle\otimes\|1_+\rangle$	

Table C.1: Gauge invariant transitions induced by the hopping term from Fig. 7.1(c) expressed in the new basis. The value on the right hand side shows the corresponding matrix elements for the hopping operator

and translating the possible transitions in from Tab. C.1 in operator form

$$V = \sum_{k=1}^{N}\Big(c^-_{k-1}O^\dagger_{1,k}O_{4,k+1} + c^+_{k-1}O^\dagger_{2,k}O_{3,k+1} + c^-_{k-1}O^\dagger_{3,k}O_{2,k+1} + c^+_{k-1}O^\dagger_{4,k}O_{1,k+1} + O^\dagger_{1,k}O_{1,k+1} + O^\dagger_{2,k}O_{2,k+1} - O^\dagger_{3,k}O_{3,k+1} - O^\dagger_{4,k}O_{4,k+1} + \text{h.c.}\Big), \tag{C.3}$$

where the h.c. refers to the hermitian conjugates of all terms appearing in the formula above. The color flux dependent constants $c^\pm_k$ are given by

$$c^+_k = \sqrt{\frac{2j_k+2}{2j_k+1}}, \qquad c^-_k = -\sqrt{\frac{2j_k}{2j_k+1}},$$

and are nothing but the matrix elements shown in the transition table. In order to compute these constants, the value for j_k has to be reconstructed from the fermionic occupation number via Eq. (7.4).

C.3 Distinguishing vector and scalar states

Due to the fact that we are working with finite lattices with OBC the symmetries which enable to distinguish between the different meson states are no longer preserved. Nevertheless, following the ideas from Ref. [35], the remnants make it possible to separate the different type of states. However, in the basis formulation presented in Sec. 7.3 it is not straightforward to write down a pseudo-momentum operator as it was done in the reference. Thus, to identify the zero-momentum excitations of the ground state we use a simpler approach. On a lattice with periodic boundary conditions, the zero-momentum states correspond exactly to the translational invariant states. For our finite lattice this should still be approximately fulfilled as long as the system size is large enough. Due to the staggered formulation a translational invariant state should be invariant under a cyclic shift by two lattice sites. To assign a pseudo-momentum to our states, we thus compute the expectation value of the operator $C^{(2)}$, where $C^{(k)}$ describes a cyclic shift by k lattice sites to the right. Moreover, to probe for the charge conjugation number, we proceed again similar to Ref. [35], and apply a cyclic shift followed by exchanging the two states $|0\rangle \leftrightarrow |2\rangle$, $\sum_{k=1}^{N} (|0\rangle\langle 2|_k + |2\rangle\langle 0|_k)\, C^{(1)}$. While this lattice analog of charge conjugation is not a good quantum number in the case of OBC, the phase of this operator allows for distinguishing between vector candidates (charge conjugation number -1) and scalar candidates (charge conjugation number $+1$). For states with charge conjugation number $+1$ we observe phases close to 0, whereas for states with charge conjugation number -1 the observed phase is close to π. Together with the dispersion obtained from the pseudo-momentum operator this allows us to identify the different states as shown in Fig. C.2. Above the ground state, we observe a vector candidate with $\langle C^{(2)} \rangle \approx 1$. Subsequently we discover the momentum excitations of the vector state which are characterized by decreasing $\langle C^{(2)} \rangle$ before we finally obtain a scalar candidate with $\langle C^{(2)} \rangle \approx 1$ again.

C.4 Entanglement entropy in the full basis and our formulation

In this Appendix we discuss the relation between the different contributions to the von Neumann entropy in our reduced basis formulation and the full basis. As we have seen in Sec. 7.3, one can recover the full basis state from the reduced one by means of an isometry which can be written as a sequence of N local isometries, and thus corresponds to a quantum circuit of depth equal to the system size, N. Here, we formally argue why the weights of different sectors, p_j, are the same in both bases, and show the explicit relation between the entanglement entropies computed in each basis.

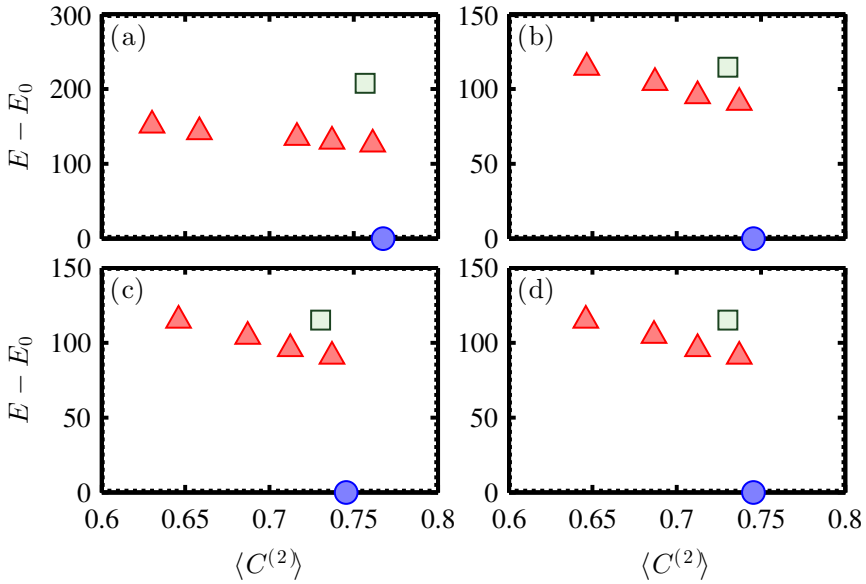

Figure C.2: Dispersion relation for $m/g = 1.6$, $N = 50$, $x = 150$, $D = 50$, $j_{\max} = 1/2$ (a), $j_{\max} = 1$ (b), $j_{\max} = 3/2$ (c) and $j_{\max} = 2$ (d). The blue dot indicates the ground state, the red triangles the vector states and the green square the scalar candidate.

C.4.1 Classical part of the entropy

Here we show that the weights of sectors with a particular value of j on a certain link, p_j, are identical in both, the full basis and our formulation. For all the following, we assume a system of N sites in a physical state $|\tilde{\Psi}\rangle$ in the reduced basis, corresponding, in the full one, to $|\Psi\rangle = \mathcal{M}|\tilde{\Psi}\rangle$. We will consider the bipartition of the system obtained by cutting at the L-th gauge link.

In the full basis, the RDM for the leftmost L sites has block diagonal structure thanks to the gauge constraints, and we can write

$$\begin{aligned} \rho_j &= \Pi_j \mathrm{tr}_{L+1,\dots,N}(|\Psi\rangle\langle\Psi|)\Pi_j = \mathrm{tr}_{L+1,\dots,N}(\Pi_j|\Psi\rangle\langle\Psi|\Pi_j) \\ &= \mathrm{tr}_{L+1,\dots,N}\left(\Pi_j \mathcal{M}|\tilde{\Psi}\rangle\langle\tilde{\Psi}|\mathcal{M}^\dagger \Pi_j\right) \end{aligned} \tag{C.4}$$

where Π_j is the projector on total flux j for the L-th link. In the full basis, this projector acts locally on the link and thus can be written $\Pi_j = \mathbb{1}_{\mathrm{in}} \otimes \Pi_j^{(L)} \otimes \mathbb{1}$, where the left factor is the identity on the inner part, i.e. the part where ρ is defined (see Fig. C.3(a)).

The corresponding projection in our basis formulation is given by

$$\tilde{\Pi}_j = \sum_{q_{\alpha_1}+\dots+q_{\alpha_L}=j} |\alpha_1 \dots \alpha_N\rangle\langle\alpha_1 \dots \alpha_N|,$$

where $\sum_{q_{\alpha_1}+\ldots+q_{\alpha_L}=j}$ takes into account all basis states, for which the sum of the eigenvalues q_{α_k}, $k = 1,\ldots,L$, for the single site operators from Eq. (7.8) is equal to j. The corresponding RDM thus reads

$$\tilde{\rho}_j = \tilde{\Pi}_j \mathrm{tr}_{L+1,\ldots,N}(|\tilde{\Psi}\rangle\langle\tilde{\Psi}|)\tilde{\Pi}_j = \mathrm{tr}_{L+1,\ldots,N}(\tilde{\Pi}_j|\tilde{\Psi}\rangle\langle\tilde{\Psi}|\tilde{\Pi}_j)$$

It turns out, as we will show next, that the action of the projector Π_j on a certain value of the flux link *commutes* with the isometry that changes the basis, namely, $\Pi_j\mathcal{M}|\tilde{\Psi}\rangle = \mathcal{M}\tilde{\Pi}_j|\tilde{\Psi}\rangle$. This implies the following

$$\begin{aligned} p_j &= \mathrm{tr}(\rho_j) = \mathrm{tr}\left(\Pi_j\mathcal{M}|\tilde{\Psi}\rangle\langle\tilde{\Psi}|\mathcal{M}^\dagger\Pi_j\right) \\ &= \mathrm{tr}\left(\mathcal{M}\tilde{\Pi}_j|\tilde{\Psi}\rangle\langle\tilde{\Psi}|\tilde{\Pi}_j\mathcal{M}^\dagger\right) = \mathrm{tr}\left(\tilde{\Pi}_j|\tilde{\Psi}\rangle\langle\tilde{\Psi}|\tilde{\Pi}_j\right) = \tilde{p}_j. \end{aligned}$$

To proof the statement $\Pi_j\mathcal{M}|\tilde{\Psi}\rangle = \mathcal{M}\tilde{\Pi}_j|\tilde{\Psi}\rangle$, we proceed as sketched in Fig. C.3. The individual steps are justified as follows:

- (a)=(b): In the full basis, the projector onto a flux value of j for link L is the identity everywhere, except for the local basis of the link, where it acts as $\Pi_j^{(L)} = \sum_{\ell,\ell'=-j}^{j}|j\,\ell\,\ell'\rangle\langle j\,\ell\,\ell'|$. Looking at Eq. (7.6) it is clear that its action on $\mathcal{M}_{\mathrm{loc}}$ just fixes the value of j, and thus

  $$(\Pi_j^{(L)} \otimes \mathbb{1}_{n_\alpha s, j\ell})\mathcal{M}_{\mathrm{loc}}^{(L)} = \mathcal{M}_{\mathrm{loc}}^{(L)}(\Pi_j^{\prime(L)} \otimes \mathbb{1}_\alpha),$$

  where $\Pi_j^{\prime(L)}$ acts to the same effect on the link variables before the isometry, as $\Pi_j^{\prime(L)} = \sum_{\ell=-j}^{j}|j\,\ell\rangle\langle j\,\ell|$.

- (b)=(c): The second step is guaranteed by gauge invariance, in particular by the form of $\mathcal{M}_{\mathrm{loc}}$ in Eq. (7.6). It is immediate to see that $(\mathbb{1}\otimes\Pi_j^{\prime(L)})\mathcal{M}_{\mathrm{loc}}^{(L-1)} = \mathcal{M}_{\mathrm{loc}}^{(L-1)}\Pi_j^{*(L-1,L)}$, where the projector $\Pi_j^{*(L-1,L)}$ acts on the degrees of freedom j,ℓ of the $(L-1)$-th link and the *decorated* fermion occupation number, α, of the L-th vertex, as

  $$\Pi_j^{*(L-1,L)} = \sum_{j'}\sum_{\alpha}\sum_{\ell=-j'}^{j'}\delta_{j'+q_\alpha,j}|j'\,\ell;\,\alpha\rangle\langle j'\,\ell;\,\alpha|.$$

- (c)=(d): The third equivalence can be formally expressed as

  $$(\mathbb{1}\otimes\Pi_j^{*(L-1,L)})(\mathcal{M}_{\mathrm{loc}}^{(L-1)}\otimes\mathbb{1}_\alpha^{(L)}) = \left(\mathcal{M}_{\mathrm{loc}}^{(L-1)}\otimes\mathbb{1}_\alpha^{(L)}\right)\Pi_j^{*(L-2,L-1,L)},$$

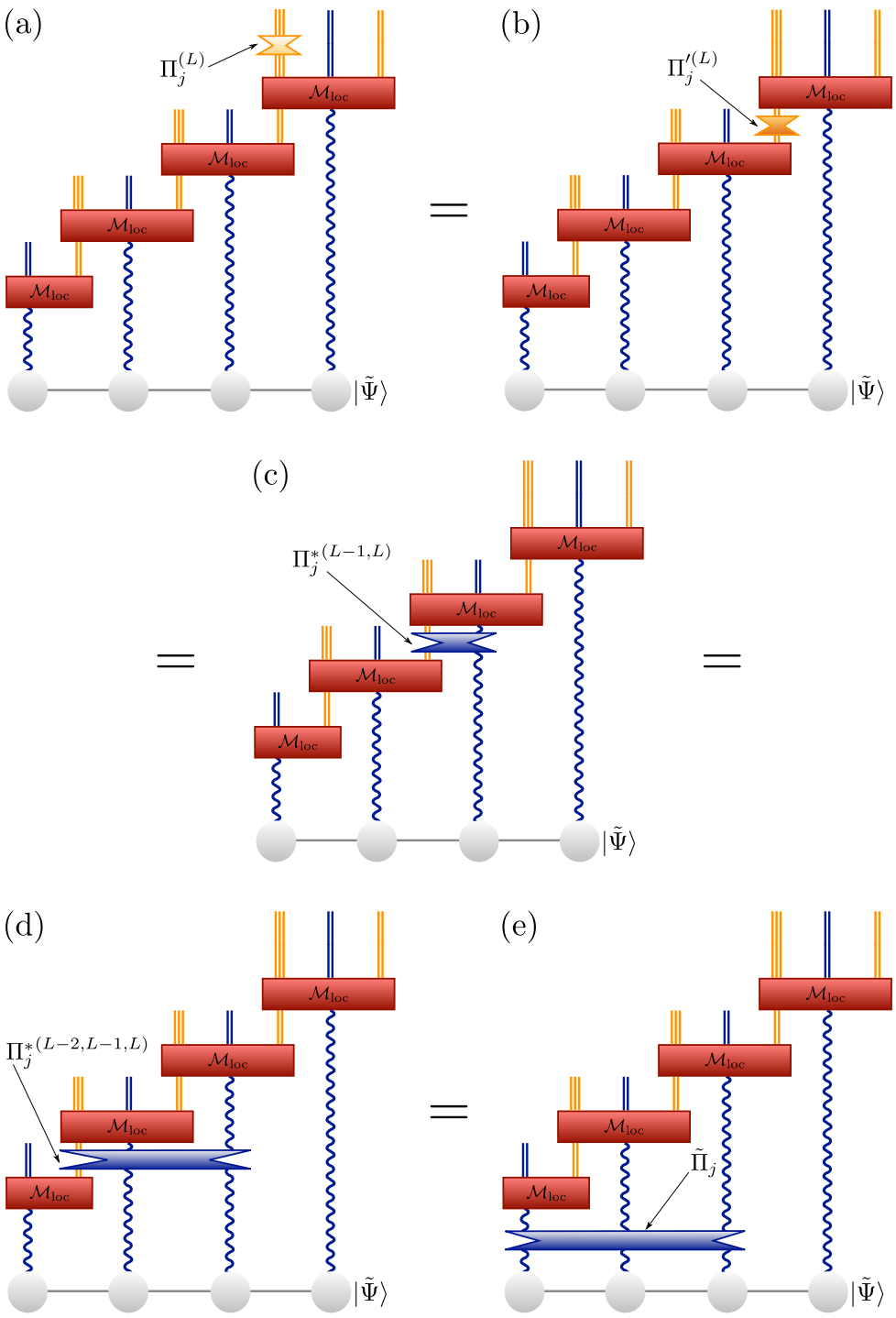

Figure C.3: (a) The action of a projector onto a given sector of flux, j, for an intermediate link on the full basis. For physical states, it can be pulled through the basis changing isometries (b)-(d), and expressed in the reduced basis as a projector onto the corresponding sum of q_{α_k} values for the vertices to the left of the target link (e).

with

$$\Pi_j^{*(L-2,L-1,L)} = \sum_{j'\alpha\alpha'} \sum_{\ell=-j'}^{j'} \delta_{j'+q_\alpha+q_{\alpha'},j} |j'\ell;\alpha;\alpha'\rangle\langle j'\ell;\alpha;\alpha'|.$$

On the left-hand side, the only effect of the projector for a sector $\bar{j}$ which acts on $\mathcal{M}_{\text{loc}} \otimes \mathbb{1}_\alpha^{(L)}$ is to restrict the sum over j in Eq. (7.6) to values such that $j + q_\alpha + q'_\alpha = \bar{j}$, which is precisely the effect of the projector on the right-hand side.

- (d)=(e): Iterating the step above we can pull the projector through very $\mathcal{M}_{\text{loc}}$ block, until the edge of the chain, where the input j is fixed to 0 and can be ignored.

C.4.2 Distillable part of the entropy

Let us assume that for a physical state, in the reduced basis, the unnormalized RDM for the L leftmost sites for the sector with (outgoing) flux j has spectrum λ_σ, i.e.

$$\tilde{\rho}_j = \sum_\sigma \lambda_\sigma |\sigma\rangle\langle\sigma|, \qquad \tilde{p}_j = \text{tr}(\tilde{\rho}_j) = \sum_\sigma \lambda_\sigma,$$

with the eigenvectors $|\sigma\rangle$ supported on the reduced basis for the L leftmost sites.

We can use the relations discussed above to relate the density operators in the full and reduced basis. The RDM in the full basis, given by Eq. (C.4), can be computed from the RDM for $L+1$ sites in the reduced basis, as sketched in Fig. C.4(a), since the isometries acting to the right of the projector cancel out in the trace. Thus, the RDM in the full basis is obtained by first applying the isometry $\mathcal{M}_{L+1} = \mathcal{M}_{\text{loc}}^{(L+1)} \mathcal{M}_{\text{loc}}^{(L)} \cdots \mathcal{M}_{\text{loc}}^{(1)}$ to the RDM for $L+1$ sites in the reduced basis, $\tilde{\rho}_{L+1}$, then projecting onto the sector j, and finally tracing out the $(L+1)$-th site and the gauge degrees of freedom introduced by $\mathcal{M}_{\text{loc}}^{(L)}$ and $\mathcal{M}_{\text{loc}}^{(L+1)}$. Following the above discussion, the projector can be pushed through the local isometries (see Fig. C.4(b)) so that $\mathcal{M}_{\text{loc}}^{(L+1)}$ cancels and we finally obtain $\rho_j = \text{tr}_{(j\ell)_L}(\mathcal{M}_{\text{loc}}^{(L)} B^{(j)} \mathcal{M}_{\text{loc}}^{(L)\dagger})$ where $B^{(j)} := \mathcal{M}_{L-1} \tilde{\rho}_j \mathcal{M}_{L-1}^\dagger$. Since $B^{(j)}$ is simply an isometric transformation of $\tilde{\rho}_j$, it has the same spectrum. We can write,

$$B^{(j)} = \sum_{k_{\text{in}}\ell\alpha, k'_{\text{in}}\ell'\alpha'} B_{k_{\text{in}}\ell\alpha, k'_{\text{in}}\ell'\alpha'} |k_{\text{in}}; j - q_\alpha, \ell; \alpha\rangle\langle k'_{\text{in}}; j - q_{\alpha'}, \ell'; \alpha'|,$$

where we make the degrees of freedom of the $(L-1)$-th link and the L-th vertex explicit, and represent all the others for the inner part with global indices k_{in}, k'_{in}. Then

$$B_{k_{\text{in}}\ell\alpha,k'_{\text{in}}\ell'\alpha'} = \sum_{\sigma} \lambda_\sigma \mathcal{U}_{k_{\text{in}}\ell\alpha,\sigma} \mathcal{U}^{\dagger}_{\sigma,k'_{\text{in}}\ell'\alpha'},$$

where $\mathcal{U}_{k_{\text{in}}\ell\alpha,\sigma} = \langle k_{\text{in}}; j-q_\alpha, \ell; \alpha | \mathcal{M}_{L-1} | \sigma \rangle$.

Applying the local isometry $\mathcal{M}^{(L)}_{\text{loc}}$ and tracing out the L-th link, we get

$$\rho_j = \frac{1}{2j+1} \sum_{k_{\text{in}}\ell\alpha,k'_{\text{in}}\ell'\alpha'} B_{k_{\text{in}}\ell\alpha,k'_{\text{in}}\ell'\alpha'} \sum_{s=-|q_\alpha|}^{|q_\alpha|} \sum_{s'=-|q_{\alpha'}|}^{|q_{\alpha'}|} \sum_{r=-j}^{j} C_{s\ r-s\ r}^{|q_\alpha|\ j-q_\alpha\ j} C_{s'\ r-s'\ r}^{|q_{\alpha'}|\ j-q_{\alpha'}\ j} \times$$
$$|k_{\text{in}}; j-q_\alpha, \ell, r-s; n_\alpha\, s\rangle\langle k'_{\text{in}}; j-q_{\alpha'}, \ell', r-s'; n_{\alpha'}\, s'|.$$

We observe that defining

$$|v(k_{\text{in}}; jr; \alpha\ell)\rangle = \sum_{s=-|q_\alpha|}^{|q_\alpha|} C_{s\ r-s\ r}^{|q_\alpha|\ j-q_\alpha\ j} |k_{\text{in}}; j-q_\alpha, \ell, r-s; n_\alpha\, s\rangle,$$

we obtain a set of orthogonal vectors (with respect to all the labels), corresponding to changing the basis of the $(L-1)$-th link and the L-th vertex to a basis of total angular momentum. As a result, if we use the unitary $\mathcal{U}_{k_{\text{in}}\ell\alpha,\sigma}$ to express the internal degrees of freedom in the diagonal basis,

$$|w(\sigma; jr)\rangle = \sum_{k_{\text{in}}\ell q} \mathcal{U}^{*}_{k_{\text{in}}\ell\alpha,\sigma} |v(k_{\text{in}}; jr; \alpha\ell)\rangle,$$

the resulting vectors are also orthogonal, and

$$\rho_j = \frac{1}{2j+1} \sum_{\sigma} \sum_{r=-j}^{j} \lambda_\sigma |w(\sigma; jr)\rangle\langle w(\sigma; jr)|. \tag{C.5}$$

Thus ρ_j consists of $2j+1$ blocks, with identical spectrum $\{\lambda_\sigma/(2j+1)\}$. Consequently, the entropy is given by

$$\begin{aligned} S(\rho_j) &= -\sum_{r=-j}^{j} \sum_{\sigma} \frac{\lambda_\sigma}{2j+1} \log_2 \frac{\lambda_\sigma}{2j+1} \\ &= -\sum_{\sigma} \lambda_\sigma \log_2 \frac{\lambda_\sigma}{2j+1} \\ &= \tilde{p}_j \log_2(2j+1) - \sum_{\sigma} \lambda_\sigma \log_2 \lambda_\sigma \\ &= \tilde{p}_j \log_2(2j+1) + S(\tilde{\rho}_j). \end{aligned}$$

Putting this result together with the fact that each j sector has the same weight in the reduced and the full representations, $p_j = \tilde{p}_j$, we have found that the relation between the entropies is

$$\begin{aligned} S(\rho) &= -\sum_j p_j \log_2(p_j) + \sum_j p_j S(\rho_j) \\ &= -\sum_j p_j \log_2(p_j) + \sum_j p_j (\log_2(2j+1) + S(\tilde{\rho}_j)) \\ &= \sum_j p_j \log_2(2j+1) + S(\tilde{\rho}). \end{aligned} \tag{C.6}$$

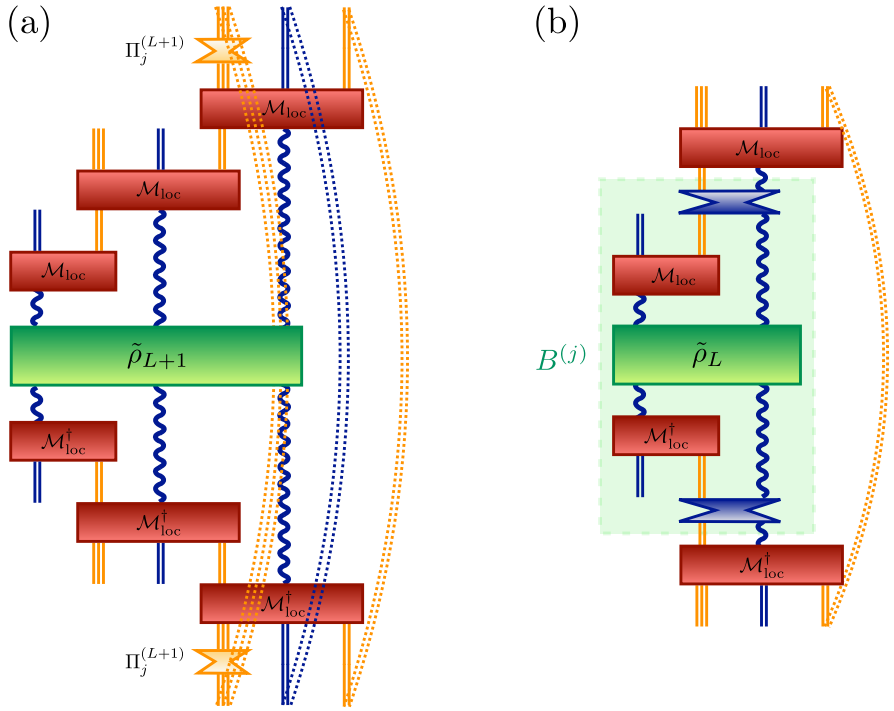

Figure C.4: RDM corresponding to a fixed flux sector, j, computed in the full basis. (a) ρ_L^j in the full basis. After pushing the projectors through as explained in the text and using that $\mathcal{M}_{\text{loc}}^{(L+1)}$ is an isometry one obtains the equivalent form depicted in (b).

Bibliography

[1] G. Aad et al., "Observation of a new particle in the search for the Standard Model Higgs boson with the ATLAS detector at the LHC", Phys. Lett. B **716**, 1–29 (2012).

[2] S. Chatrchyan et al., "Observation of a new boson at a mass of 125 GeV with the CMS experiment at the LHC", Phys. Lett. B **716**, 30–61 (2012).

[3] H. Weyl, "Elektron und gravitation. I", Z. Phys. **56**, 330–352 (1929).

[4] C. N. Yang and R. L. Mills, "Conservation of Isotopic Spin and Isotopic Gauge Invariance", Phys. Rev. **96**, 191–195 (1954).

[5] D. J. Gross and F. Wilczek, "Ultraviolet Behavior of Non-Abelian Gauge Theories", Phys. Rev. Lett. **30**, 1343–1346 (1973).

[6] H. D. Politzer, "Reliable Perturbative Results for Strong Interactions?", Phys. Rev. Lett. **30**, 1346–1349 (1973).

[7] J. A. Carlson, A. Jaffe, and A. Wiles, *The millennium prize problems* (American Mathematical Soc., 2006).

[8] K. G. Wilson, "Confinement of quarks", Phys. Rev. D **10**, 2445–2459 (1974).

[9] J. Kogut and L. Susskind, "Hamiltonian formulation of Wilson's lattice gauge theories", Phys. Rev. D **11**, 395–408 (1975).

[10] S. Dürr, "The phase transition in the multiflavour Schwinger model", arXiv:hep-th/0009094 (2000).

[11] K. Fukushima and T. Hatsuda, "The phase diagram of dense QCD", Rep. Prog. Phys. **74**, 014001 (2011).

[12] M. Troyer and U.-J. Wiese, "Computational Complexity and Fundamental Limitations to Fermionic Quantum Monte Carlo Simulations", Phys. Rev. Lett. **94**, 170201 (2005).

[13] M. Cristoforetti, F. Di Renzo, and L. Scorzato, "New approach to the sign problem in quantum field theories: High density QCD on a Lefschetz thimble", Phys. Rev. D **86**, 074506 (2012).

[14] M. Cristoforetti, F. Di Renzo, A. Mukherjee, and L. Scorzato, "Monte Carlo simulations on the Lefschetz thimble: Taming the sign problem", Phys. Rev. D **88**, 051501 (2013).

[15] D. Sexty, "New algorithms for finite density QCD", PoS(LATTICE 2014)016 (2014).

[16] L. Scorzato, "The Lefschetz thimble and the sign problem", PoS(LATTICE 2015)016 (2015).

[17] C. Gattringer and K. Langfeld, "Approaches to the sign problem in lattice field theory", Int. J. Mod. Phys. A **31**, 1643007 (2016).

[18] K. Langfeld, "Density of states", PoS(LATTICE 2016)010 (2016).

[19] C. Gattringer, "New developments for dual methods in lattice field theory at non-zero density", PoS(LATTICE 2013)002 (2013).

[20] C. Gattringer, T. Kloiber, and V. Sazonov, "Solving the sign problems of the massless lattice Schwinger model with a dual formulation", Nucl. Phys. B **897**, 732–748 (2015).

[21] D. Göschl, "Dual simulation of the massless lattice Schwinger model with topological term and non-zero chemical potential", arXiv:1709.04280 (2017).

[22] C. Gattringer, D. Göschl, and C. Marchis, "Kramers-Wannier duality and worldline representation for the SU(2) principal chiral model", arXiv:1709.04691 (2017).

[23] A. Ammon, T. Hartung, K. Jansen, H. Leövey, and J. Volmer, "New polynomially exact integration rules on U(N) and SU(N)", PoS(LATTICE 2016)334 (2016).

[24] A. Ammon, T. Hartung, K. Jansen, H. Leövey, and J. Volmer, "Overcoming the sign problem in one-dimensional QCD by new integration rules with polynomial exactness", Phys. Rev. D **94**, 114508 (2016).

[25] J. Unmuth-Yockey, Y. Meurice, J. Osborn, and H. Zou, "Tensor renormalization group study of the 2d O(3) model", PoS(LATTICE 2014)325 (2014).

[26] Y. Shimizu and Y. Kuramashi, "Grassmann tensor renormalization group approach to one-flavor lattice Schwinger model", Phys. Rev. D **90**, 014508 (2014).

[27] Y. Shimizu and Y. Kuramashi, "Critical behavior of the lattice Schwinger model with a topological term at $\theta = \pi$ using the Grassmann tensor renormalization group", Phys. Rev. D **90**, 074503 (2014).

[28] H. Kawauchi and S. Takeda, "Tensor renormalization group analysis of CP(N-1) model in two dimensions", PoS(LATTICE 2015)284 (2015).

[29] S. Takeda and Y. Yoshimura, "Grassmann tensor renormalization group for the one-flavor lattice Gross–Neveu model with finite chemical potential", Prog. Theor. Exp. Phys. **2015**, 043B01 (2015).

[30] H. Kawauchi and S. Takeda, "Tensor renormalization group analysis of CP(N-1) model", Phys. Rev. D **93**, 114503 (2016).

[31] Y. Meurice, A. Denbleyker, Y. Liu, T. Xiang, Z. Xie, J.-F. Yu, J. Unmuth-Yockey, and H. Zou, "Comparing Tensor Renormalization Group and Monte Carlo calculations for spin and gauge models", PoS(LATTICE 2013)329 (2013).

[32] A. Denbleyker, Y. Liu, Y. Meurice, M. P. Qin, T. Xiang, Z. Y. Xie, J. F. Yu, and H. Zou, "Controlling sign problems in spin models using tensor renormalization", Phys. Rev. D **89**, 016008 (2014).

[33] Y. Meurice, L.-P. Yang, J. Unmuth-Yockey, Y. Liu, J. Osborn, Z. Y. Xie, and H. Zou, "Approaching conformality with the Tensor Renormalization Group method", PoS(LATTICE 2015)285 (2015).

[34] H. Kawauchi and S. Takeda, "Phase structure analysis of CP(N-1) model using Tensor renormalization group", PoS(LATTICE 2016)322 (2016).

[35] M. C. Bañuls, K. Cichy, K. Jansen, and J. I. Cirac, "The mass spectrum of the Schwinger model with Matrix Product States", J. High Energy Phys. **2013**, 158 (2013).

[36] M. C. Bañuls, K. Cichy, J. I. Cirac, K. Jansen, and H. Saito, "Matrix Product States for Lattice Field Theories", PoS(LATTICE 2013)332 (2013).

[37] B. Buyens, J. Haegeman, K. Van Acoleyen, H. Verschelde, and F. Verstraete, "Matrix Product States for Gauge Field Theories", Phys. Rev. Lett. **113**, 091601 (2014).

[38] B. Buyens, J. Haegeman, K. Van Acoleyen, and F. Verstraete, "Matrix product states for Hamiltonian lattice gauge theories", PoS(LATTICE 2014)308 (2014).

[39] H. Saito, M. C. Bañuls, K. Cichy, J. I. Cirac, and K. Jansen, "The temperature dependence of the chiral condensate in the Schwinger model with Matrix Product States", PoS(LATTICE 2014)302 (2014).

[40] M. C. Bañuls, K. Cichy, J. I. Cirac, K. Jansen, and H. Saito, "Thermal evolution of the Schwinger model with Matrix Product Operators", Phys. Rev. D **92**, 034519 (2015).

[41] B. Buyens, J. Haegeman, H. Verschelde, F. Verstraete, and K. Van Acoleyen, "Confinement and String Breaking for QED_2 in the Hamiltonian Picture", Phys. Rev. X **6**, 041040 (2016).

[42] B. Buyens, J. Haegeman, F. Verstraete, and K. Van Acoleyen, "Tensor networks for gauge field theories", PoS(LATTICE 2015)280 (2015).

[43] S. Kühn, E. Zohar, J. Cirac, and M. C. Bañuls, "Non-Abelian string breaking phenomena with matrix product states", English, J. High Energy Phys. **2015**, 130 (2015).

[44] T. Pichler, M. Dalmonte, E. Rico, P. Zoller, and S. Montangero, "Real-Time Dynamics in U(1) Lattice Gauge Theories with Tensor Networks", Phys. Rev. X **6**, 011023 (2016).

[45] H. Saito, M. C. Bañuls, K. Cichy, J. I. Cirac, and K. Jansen, "Thermal evolution of the one-flavour Schwinger model using Matrix Product States", PoS(LATTICE 2015)283 (2015).

[46] M. C. Bañuls, K. Cichy, K. Jansen, and H. Saito, "Chiral condensate in the Schwinger model with matrix product operators", Phys. Rev. D **93**, 094512 (2016).

[47] M. C. Bañuls, K. Cichy, J. I. Cirac, K. Jansen, and S. Kühn, "Density Induced Phase Transitions in the Schwinger Model: A Study with Matrix Product States", Phys. Rev. Lett. **118**, 071601 (2017).

[48] M. C. Bañuls, K. Cichy, J. I. Cirac, K. Jansen, S. Kühn, and H. Saito, "The multi-flavor Schwinger model with chemical potential - Overcoming the sign problem with Matrix Product States", PoS(LATTICE 2016)316 (2016).

[49] M. C. Bañuls, K. Cichy, J. I. Cirac, K. Jansen, S. Kühn, and H. Saito, "Towards overcoming the Monte Carlo sign problem with tensor networks", EPJ Web Conf. **137**, 04001 (2017).

[50] B. Buyens, F. Verstraete, and K. Van Acoleyen, "Hamiltonian simulation of the Schwinger model at finite temperature", Phys. Rev. D **94**, 085018 (2016).

[51] B. Buyens, J. Haegeman, F. Hebenstreit, F. Verstraete, and K. Van Acoleyen, "Real-time simulation of the Schwinger effect with Matrix Product States", arXiv:1612.00739 (2016).

[52] P. Silvi, E. Rico, M. Dalmonte, F. Tschirsich, and S. Montangero, "Finite-density phase diagram of a (1+1)-d non-abelian lattice gauge theory with tensor networks", Quantum **1**, 9 (2017).

[53] B. Buyens, S. Montangero, J. Haegeman, F. Verstraete, and K. Van Acoleyen, "Finite-representation approximation of lattice gauge theories at the continuum limit with tensor networks", Phys. Rev. D **95**, 094509 (2017).

[54] L. Tagliacozzo and G. Vidal, "Entanglement renormalization and gauge symmetry", Phys. Rev. B **83**, 115127 (2011).

[55] E. Rico, T. Pichler, M. Dalmonte, P. Zoller, and S. Montangero, "Tensor Networks for Lattice Gauge Theories and Atomic Quantum Simulation", Phys. Rev. Lett. **112**, 201601 (2014).

[56] P. Silvi, E. Rico, T. Calarco, and S. Montangero, "Lattice gauge tensor networks", New J. Phys. **16**, 103015 (2014).

[57] E. Zohar and M. Burrello, "Formulation of lattice gauge theories for quantum simulations", Phys. Rev. D **91**, 054506 (2015).

[58] E. Zohar and M. Burrello, "Building projected entangled pair states with a local gauge symmetry", New J. Phys. **18**, 043008 (2016).

[59] E. Zohar, M. Burrello, T. B. Wahl, and J. I. Cirac, "Fermionic projected entangled pair states and local gauge theories", Ann. Phys. (Amsterdam) **363**, 385–439 (2015).

[60] L. Tagliacozzo, A. Celi, A. Zamora, and M. Lewenstein, "Optical Abelian lattice gauge theories", Ann. Phys. **330**, 160–191 (2013).

[61] L. Tagliacozzo, A. Celi, and M. Lewenstein, "Tensor Networks for Lattice Gauge Theories with Continuous Groups", Phys. Rev. X **4**, 041024 (2014).

[62] E. Zohar, T. B. Wahl, M. Burrello, and J. I. Cirac, "Projected Entangled Pair States with non-Abelian gauge symmetries: An SU(2) study", Ann. Phys. **374**, 84–137 (2016).

[63] I. Kull, A. Molnar, E. Zohar, and J. I. Cirac, "Classification of Matrix Product States with a Local (Gauge) Symmetry", arXiv:1708.00362 (2017).

[64] R. P. Feynman, "Simulating physics with computers", Int. J. Theor. Phys. **21**, 467–488 (1982).

[65] M. Greiner, O. Mandel, T. Esslinger, T. W. Hänsch, and I. Bloch, "Quantum phase transition from a superfluid to a Mott insulator in a gas of ultracold atoms", Nature **415**, 39 (2002).

[66] E. Jané, G. Vidal, W. Dür, P. Zoller, and J. I. Cirac, "Simulation of quantum dynamics with quantum optical systems", Quantum Information & Computation **3**, 15–37 (2003).

[67] H. Bernien, S. Schwartz, A. Keesling, H. Levine, A. Omran, H. Pichler, S. Choi, A. S. Zibrov, M. Endres, M. Greiner, V. Vuletić, and M. D. Lukin, "Probing many-body dynamics on a 51-atom quantum simulator", arXiv:1707.04344 (2017).

[68] A. Mazurenko, C. S. Chiu, G. Ji, M. F. Parsons, M. Kanász-Nagy, R. Schmidt, F. Grusdt, E. Demler, D. Greif, and M. Greiner, "A cold-atom Fermi-Hubbard antiferromagnet", Nature **545**, 462 (2017).

[69] J. I. Cirac and P. Zoller, "Quantum Computations with Cold Trapped Ions", Phys. Rev. Lett. **74**, 4091–4094 (1995).

[70] D. Porras and J. I. Cirac, "Quantum Manipulation of Trapped Ions in Two Dimensional Coulomb Crystals", Phys. Rev. Lett. **96**, 250501 (2006).

[71] F. Schmidt-Kaler, H. Häffner, M. Riebe, S. Gulde, G. P. T. Lancaster, T. Deuschle, C. Becher, C. F. Roos, J. Eschner, and R. Blatt, "Realization of the Cirac-Zoller controlled-NOT quantum gate", Nature **422**, 408 (2003).

[72] H. Weimer, M. Müller, I. Lesanovsky, P. Zoller, and H. P. Büchler, "A Rydberg quantum simulator", Nat. Phys. **6**, 382 (2010).

[73] A. A. Houck, H. E. Türeci, and J. Koch, "On-chip quantum simulation with superconducting scircuits", Nat. Phys. **8**, 292 (2012).

[74] X.-s. Ma, B. Dakic, W. Naylor, A. Zeilinger, and P. Walther, "Quantum simulation of the wavefunction to probe frustrated Heisenberg spin systems", Nat. Phys. **7**, 399 (2011).

[75] L. M. K. Vandersypen, M. Steffen, G. Breyta, C. S. Yannoni, M. H. Sherwood, and I. L. Chuang, "Experimental realization of Shor's quantum factoring algorithm using nuclear magnetic resonance", Nature **414**, 883 (2001).

[76] S. Trotzky, Y.-A. Chen, A. Flesch, I. P. McCulloch, U. Schollwöck, J. Eisert, and I. Bloch, "Probing the relaxation towards equilibrium in an isolated strongly correlated one-dimensional Bose gas", Nat. Phys. **8**, 325–330 (2012).

[77] E. Kapit and E. Mueller, "Optical-lattice Hamiltonians for relativistic quantum electrodynamics", Phys. Rev. A **83**, 033625 (2011).

[78] E. Zohar, J. I. Cirac, and B. Reznik, "Simulating Compact Quantum Electrodynamics with Ultracold Atoms: Probing Confinement and Nonperturbative Effects", Phys. Rev. Lett. **109**, 125302 (2012).

[79] D. Banerjee, M. Dalmonte, M. Müller, E. Rico, P. Stebler, U.-J. Wiese, and P. Zoller, "Atomic Quantum Simulation of Dynamical Gauge Fields Coupled to Fermionic Matter: From String Breaking to Evolution after a Quench", Phys. Rev. Lett. **109**, 175302 (2012).

[80] E. Zohar, J. I. Cirac, and B. Reznik, "Quantum simulations of gauge theories with ultracold atoms: Local gauge invariance from angular-momentum conservation", Phys. Rev. A **88**, 023617 (2013).

[81] E. Zohar, J. I. Cirac, and B. Reznik, "Cold-Atom Quantum Simulator for SU(2) Yang-Mills Lattice Gauge Theory", Phys. Rev. Lett. **110**, 125304 (2013).

[82] E. Zohar, J. I. Cirac, and B. Reznik, "Simulating (2+1)-Dimensional Lattice QED with Dynamical Matter Using Ultracold Atoms", Phys. Rev. Lett. **110**, 055302 (2013).

[83] U.-J. Wiese, "Ultracold quantum gases and lattice systems: quantum simulation of lattice gauge theories", Ann. Phys. (Amsterdam) **525**, 777–796 (2013).

[84] L. Tagliacozzo, A. Celi, P. Orland, M. W. Mitchell, and M. Lewenstein, "Simulation of non-Abelian gauge theories with optical lattices", Nat. Commun. **4**, 2615 (2013).

[85] P. Hauke, D. Marcos, M. Dalmonte, and P. Zoller, "Quantum Simulation of a Lattice Schwinger Model in a Chain of Trapped Ions", Phys. Rev. X **3**, 041018 (2013).

[86] M. Bögli, "Quantum Simulation of Non-Abelian Lattice Gauge Theories", PoS(LATTICE 2013)331 (2013).

[87] D. Banerjee, M. Bögli, M. Dalmonte, E. Rico, P. Stebler, U.-J. Wiese, and P. Zoller, "Atomic Quantum Simulation of U(N) and SU(N) Non-Abelian Lattice Gauge Theories", Phys. Rev. Lett. **110**, 125303 (2013).

[88] U.-J. Wiese, "Towards quantum simulating QCD", Nucl. Phys. A **931**, 246–256 (2014).

[89] K. Stannigel, P. Hauke, D. Marcos, M. Hafezi, S. Diehl, M. Dalmonte, and P. Zoller, "Constrained Dynamics via the Zeno Effect in Quantum Simulation: Implementing Non-Abelian Lattice Gauge Theories with Cold Atoms", Phys. Rev. Lett. **112**, 120406 (2014).

[90] D. Marcos, P. Widmer, E. Rico, M. Hafezi, P. Rabl, U.-J. Wiese, and P. Zoller, "Two-dimensional lattice gauge theories with superconducting quantum circuits", Ann. Phys. **351**, 634–654 (2014).

[91] S. Kühn, J. I. Cirac, and M.-C. Bañuls, "Quantum simulation of the Schwinger model: A study of feasibility", Phys. Rev. A **90**, 042305 (2014).

[92] S. Notarnicola, E. Ercolessi, P. Facchi, G. Marmo, S. Pascazio, and F. V. Pepe, "Discrete Abelian gauge theories for quantum simulations of QED", J. Phys. A: Math. Theor. **48**, 30FT01 (2015).

[93] A. Mezzacapo, E. Rico, C. Sabín, I. L. Egusquiza, L. Lamata, and E. Solano, "Non-Abelian SU(2) Lattice Gauge Theories in Superconducting Circuits", Phys. Rev. Lett. **115**, 240502 (2015).

[94] C. Laflamme, W. Evans, M. Dalmonte, U. Gerber, H. Mejía-Díaz, W. Bietenholz, U.-J. Wiese, and P. Zoller, "Proposal for the Quantum Simulation of the CP(2) Model on Optical Lattices", PoS(LATTICE 2015)311 (2015).

[95] C. Laflamme, W. Evans, M. Dalmonte, U. Gerber, H. Mejía-Díaz, W. Bietenholz, U.-J. Wiese, and P. Zoller, "CP(N-1) quantum field theories with alkaline-earth atoms in optical lattices", Ann. Phys. **370**, 117–127 (2016).

[96] E. Zohar, J. I. Cirac, and B. Reznik, "Quantum simulations of lattice gauge theories using ultracold atoms in optical lattices", Rep. Prog. Phys. **79**, 014401 (2016).

[97] E. Zohar, A. Farace, B. Reznik, and J. I. Cirac, "Digital lattice gauge theories", Phys. Rev. A **95**, 023604 (2017).

[98] E. Zohar, A. Farace, B. Reznik, and J. I. Cirac, "Digital Quantum Simulation of $\mathbb{Z}_2$ Lattice Gauge Theories with Dynamical Fermionic Matter", Phys. Rev. Lett. **118**, 070501 (2017).

[99] D. Yang, G. S. Giri, M. Johanning, C. Wunderlich, P. Zoller, and P. Hauke, "Analog quantum simulation of (1+1)-dimensional lattice QED with trapped ions", Phys. Rev. A **94**, 052321 (2016).

[100] D. González-Cuadra, E. Zohar, and J. I. Cirac, "Quantum simulation of the Abelian-Higgs lattice gauge theory with ultracold atoms", New J. Phys. **19**, 063038 (2017).

[101] J. Schwinger, "Gauge Invariance and Mass. II", Phys. Rev. **128**, 2425–2429 (1962).

[102] E. A. Martinez, C. A. Muschik, P. Schindler, D. Nigg, A. Erhard, M. Heyl, P. Hauke, M. Dalmonte, T. Monz, P. Zoller, and R. Blatt, "Real-time dynamics of lattice gauge theories with a few-qubit quantum computer", Nature **534**, 516–519 (2016).

[103] W. Greiner and J. Reinhardt, *Field Quantization* (Springer Berlin Heidelberg, 1996).

[104] M. E. Peskin and D. V. Schroeder, *An introduction to quantum field theory*, 6. print. (Perseus Books, Reading, Mass. [u.a.], 1999), XXII, 842 S.

[105] M. Creutz, *Quarks, Gluons, and Lattices*, Cambridge monographs on mathematical physics (Cambridge University Press, 1983).

[106] I. Montvay and G. Münster, *Quantum fields on a lattice*, 1. publ., Cambridge monographs on mathematical physics (Cambridge Univ. Press, Cambridge, 1994), XIII, 491 S.

[107] L. H. Ryder, *Quantum field theory* (Cambridge university press, 1996).

[108] R. Jackiw, "Introduction to the Yang-Mills quantum theory", Rev. Mod. Phys. **52**, 661–673 (1980).

[109] N. K. Falck and A. C. Hirshfeld, "The QCD Hamiltonian and nonlinear quantum mechanics", Ann. Phys. **144**, 34–57 (1982).

[110] K. Haller, "Yang-Mills theory and quantum chromodynamics in the temporal gauge", Phys. Rev. D **36**, 1839–1845 (1987).

[111] P. Hoodbhoy, "Quantum chromodynamics for static sources in the $A^0 = 0$ gauge and Schrödinger representation-Quantum fluctuations about the classical limit", Phys. Rev. D **28**, 965–972 (1983).

[112] H. J. Rothe, *Lattice gauge theories: an introduction* (World Scientific Lecture Notes in Physics, 2006).

[113] D. B. Kaplan, "Chiral Symmetry and Lattice Fermions", arXiv:0912.2560 (2009).

[114] L. Susskind, "Lattice fermions", Phys. Rev. D **16**, 3031–3039 (1977).

[115] J. B. Kogut, "The lattice gauge theory approach to quantum chromodynamics", Rev. Mod. Phys. **55**, 775–836 (1983).

[116] H. Nielsen and M. Ninomiya, "A no-go theorem for regularizing chiral fermions", Phys. Lett. B **105**, 219–223 (1981).

[117] H. Nielsen and M. Ninomiya, "Absence of neutrinos on a lattice: (I). Proof by homotopy theory", Nucl. Phys. B **185**, 20–40 (1981).

[118] H. Nielsen and M. Ninomiya, "Absence of neutrinos on a lattice: (II). Intuitive topological proof", Nucl. Phys. B **193**, 173–194 (1981).

[119] H. B. Nielsen and M. Ninomiya, "Erratum: Absence of neutrinos on a lattice", Nucl. Phys. B **195**, 541–542 (1982).

[120] R. Frezzotti, P. A. Grassi, S. Sint, and P. Weisz, "Lattice QCD with a chirally twisted mass term", J. High Energy Phys. **2001**, 058 (2001).

[121] T. Banks, L. Susskind, and J. Kogut, "Strong-coupling calculations of lattice gauge theories: (1 + 1)-dimensional exercises", Phys. Rev. D **13**, 1043–1053 (1976).

[122] T. Banks, S. Raby, L. Susskind, J. Kogut, D. R. T. Jones, P. N. Scharbach, and D. K. Sinclair, "Strong-coupling calculations of the hadron spectrum of quantum chromodynamics", Phys. Rev. D **15**, 1111–1127 (1977).

[123] P. H. Ginsparg and K. G. Wilson, "A remnant of chiral symmetry on the lattice", Phys. Rev. D **25**, 2649–2657 (1982).

[124] M. Lüscher, "Exact chiral symmetry on the lattice and the Ginsparg-Wilson relation", Phys. Lett. B **428**, 342–345 (1998).

[125] J. H. Weber, "Properties of minimally doubled fermions", PhD thesis (Johannes Gutenberg-Universität in Mainz, 2015).

[126] L. H. Karsten, "Lattice fermions in euclidean space-time", Phys. Lett. B **104**, 315–319 (1981).

[127] F. Wilczek, "Lattice Fermions", Phys. Rev. Lett. **59**, 2397–2400 (1987).

[128] M. Creutz, "Four-dimensional graphene and chiral fermions", J. High Energy Phys. **2008**, 017 (2008).

[129] A. Boriçi, "Creutz fermions on an orthogonal lattice", Phys. Rev. D **78**, 074504 (2008).

[130] H. R. Quinn and M. Weinstein, "New Formulation for the Lattice-Fermion Derivative: Locality and Chirality without Spectrum Doubling", Phys. Rev. Lett. **57**, 2617–2620 (1986).

[131] W. Bietenholz and U.-J. Wiese, "Perfect lattice actions for quarks and gluons", Nucl. Phys. B **464**, 319–350 (1996).

[132] W. Bietenholz, R. Browerb, S. Chandrasekharan, and U.-J. Wiese, "Perfect lattice actions for staggered fermions", Nucl. Phys. B **495**, 285–305 (1997).

[133] D. B. Kaplan, "A method for simulating chiral fermions on the lattice", Phys. Lett. B **288**, 342–347 (1992).

[134] Y. Shamir, "Chiral fermions from lattice boundaries", Nucl. Phys. B **406**, 90–106 (1993).

[135] V. Furman and Y. Shamir, "Axial symmetries in lattice QCD with Kaplan fermions", Nucl. Phys. B **439**, 54–78 (1995).

[136] L. Polyakov, *Gauge Fields and Strings*, Contemporary concepts in physics (Taylor & Francis, 1987).

[137] X.-Q. Luo, S.-H. Guo, H. Kröger, and D. Schütte, "Improved lattice gauge field Hamiltonian", Phys. Rev. D **59**, 034503 (1999).

[138] J. Carlsson, J. McIntosh, B. McKellar, and L. Hollenberg, "Improved Hamiltonian lattice gauge theory", Nucl. Phys. Proc. Suppl. **106**, 853–855 (2002).

[139] J. B. Kogut, "An introduction to lattice gauge theory and spin systems", Rev. Mod. Phys. **51**, 659–713 (1979).

[140] R. Gupta, "Introduction to Lattice QCD", arXiv:hep-lat/9807028 (1998).

[141] C. J. Hamer, Z. Weihong, and J. Oitmaa, "Series expansions for the massive Schwinger model in Hamiltonian lattice theory", Phys. Rev. D **56**, 55–67 (1997).

[142] C. Hamer, "Lattice model calculations for SU(2) Yang-Mills theory in 1 + 1 dimensions", Nucl. Phys. B **121**, 159–175 (1977).

[143] C. Hamer, J. Kogut, D. Crewther, and M. Mazzolini, "The massive Schwinger model on a lattice: Background field, chiral symmetry and the string tension", Nucl. Phys. B **208**, 413–438 (1982).

[144] C. Hamer, "SU(2) Yang-Mills theory in (1 + 1) dimensions: A finite-lattice approach", Nucl. Phys. B **195**, 503–521 (1982).

[145] F. Hebenstreit, J. Berges, and D. Gelfand, "Simulating fermion production in 1+1 dimensional QED", Phys. Rev. D **87**, 105006 (2013).

[146] F. Hebenstreit, J. Berges, and D. Gelfand, "Real-Time Dynamics of String Breaking", Phys. Rev. Lett. **111**, 201601 (2013).

[147] F. Hebenstreit and J. Berges, "Connecting real-time properties of the massless Schwinger model to the massive case", Phys. Rev. D **90**, 045034 (2014).

[148] G. K. Brennen, G. Pupillo, E. Rico, T. M. Stace, and D. Vodola, "Loops and Strings in a Superconducting Lattice Gauge Simulator", Phys. Rev. Lett. **117**, 240504 (2016).

[149] V. Kasper, F. Hebenstreit, F. Jendrzejewski, M. K. Oberthaler, and J. Berges, "Implementing quantum electrodynamics with ultracold atomic systems", New J. Phys. **19**, 023030 (2017).

[150] J. I. Cirac, P. Maraner, and J. K. Pachos, "Cold Atom Simulation of Interacting Relativistic Quantum Field Theories", Phys. Rev. Lett. **105**, 190403 (2010).

[151] S. P. Jordan, K. S. M. Lee, and J. Preskill, "Quantum Algorithms for Quantum Field Theories", Science **336**, 1130–1133 (2012).

[152] I. Buluta and F. Nori, "Quantum Simulators", Science **326**, 108–111 (2009).

[153] J. I. Cirac and P. Zoller, "Goals and opportunities in quantum simulation", Nat. Phys. **8**, 264 (2012).

[154] I. M. Georgescu, S. Ashhab, and F. Nori, "Quantum simulation", Rev. Mod. Phys. **86**, 153–185 (2014).

[155] T. H. Johnson, S. R. Clark, and D. Jaksch, "What is a quantum simulator?", EPJ Quantum Technol. **1**, 10 (2014).

[156] S. Lloyd, "Universal Quantum Simulators", Science **273**, 1073–1078 (1996).

[157] E. Zohar and B. Reznik, "Confinement and Lattice Quantum--Electrodynamic Electric Flux Tubes Simulated with Ultracold Atoms", Phys. Rev. Lett. **107**, 275301 (2011).

[158] K. Kasamatsu, I. Ichinose, and T. Matsui, "Atomic Quantum Simulation of the Lattice Gauge-Higgs Model: Higgs Couplings and Emergence of Exact Local Gauge Symmetry", Phys. Rev. Lett. **111**, 115303 (2013).

[159] A. Kosior and K. Sacha, "Simulation of non-Abelian lattice gauge fields with a single-component gas", Europhys. Lett. **107**, 26006 (2014).

[160] Y. Kuno, S. Sakane, K. Kasamatsu, I. Ichinose, and T. Matsui, "Atomic quantum simulation of a three-dimensional U(1) gauge-Higgs model", Phys. Rev. A **94**, 063641 (2016).

[161] C. Muschik, M. Heyl, E. Martinez, T. Monz, P. Schindler, B. Vogell, M. Dalmonte, P. Hauke, R. Blatt, and P. Zoller, "U(1) Wilson lattice gauge theories in digital quantum simulators", New J. Phys., in press (2017).

[162] D. Horn, "Finite matrix models with continuous local gauge invariance", Phys. Lett. B **100**, 149–151 (1981).

[163] P. Orland and D. Rohrlich, "Lattice gauge magnets: Local isospin from spin", Nucl. Phys. B **338**, 647–672 (1990).

[164] S. Chandrasekharan and U.-J. Wiese, "Quantum link models: A discrete approach to gauge theories", Nucl. Phys. B **492**, 455–471 (1997).

[165] J. Richter and J. Schulenburg, "The spin-1/2 J1–J2 Heisenberg antiferromagnet on the square lattice:Exact diagonalization for N=40 spins", Eur. Phys. J. B **73**, 117–124 (2010).

[166] A. M. Läuchli, J. Sudan, and R. Moessner, "The S=1/2 Kagome Heisenberg Antiferromagnet Revisited", arXiv:1611.06990 (2016).

[167] D. Perez-Garcia, F. Verstraete, M. M. Wolf, and J. I. Cirac, "Matrix product state representations", Quantum Inf. Comput. **7**, 401–430 (2007).

[168] U. Schollwöck, "The density-matrix renormalization group in the age of matrix product states", Ann. Phys. **326**, January 2011 Special Issue, 96–192 (2011).

[169] G. Vidal, "Efficient Classical Simulation of Slightly Entangled Quantum Computations", Phys. Rev. Lett. **91**, 147902 (2003).

[170] M. Fannes, B. Nachtergaele, and R. F. Werner, "Finitely correlated states on quantum spin chains", Commun. Math. Phys. **144**, 443–490 (1992).

[171] F. Verstraete, D. Porras, and J. I. Cirac, "Density Matrix Renormalization Group and Periodic Boundary Conditions: A Quantum Information Perspective", Phys. Rev. Lett. **93**, 227205 (2004).

[172] F. Verstraete and J. I. Cirac, "Renormalization algorithms for Quantum-Many Body Systems in two and higher dimensions", arXiv:cond-mat/0407066 (2004).

[173] I. Affleck, T. Kennedy, E. H. Lieb, and H. Tasaki, "Rigorous results on valence-bond ground states in antiferromagnets", Phys. Rev. Lett. **59**, 799–802 (1987).

[174] J. Haegeman, J. I. Cirac, T. J. Osborne, H. Verschelde, and F. Verstraete, "Applying the Variational Principle to (1 + 1)-Dimensional Quantum Field Theories", Phys. Rev. Lett. **105**, 251601 (2010).

[175] J. I. Cirac and G. Sierra, "Infinite matrix product states, conformal field theory, and the Haldane-Shastry model", Phys. Rev. B **81**, 104431 (2010).

[176] J. Eisert, M. Cramer, and M. B. Plenio, "Colloquium: Area laws for the entanglement entropy", Rev. Mod. Phys. **82**, 277–306 (2010).

[177] D. N. Page, "Average entropy of a subsystem", Phys. Rev. Lett. **71**, 1291–1294 (1993).

[178] S. K. Foong and S. Kanno, "Proof of Page's conjecture on the average entropy of a subsystem", Phys. Rev. Lett. **72**, 1148–1151 (1994).

[179] S. Sen, "Average Entropy of a Quantum Subsystem", Phys. Rev. Lett. **77**, 1–3 (1996).

[180] M. B. Hastings, "An area law for one-dimensional quantum systems", J. Stat. Mech. **2007**, P08024 (2007).

[181] F. Verstraete and J. I. Cirac, "Matrix product states represent ground states faithfully", Phys. Rev. B **73**, 094423 (2006).

[182] N. Schuch, M. M. Wolf, F. Verstraete, and J. I. Cirac, "Entropy Scaling and Simulability by Matrix Product States", Phys. Rev. Lett. **100**, 030504 (2008).

[183] Y. Ge and J. Eisert, "Area laws and efficient descriptions of quantum many-body states", New J. Phys. **18**, 083026 (2016).

[184] P. Calabrese and J. Cardy, "Entanglement entropy and conformal field theory", J. Phys. A **42**, 504005 (2009).

[185] Y.-Y. Shi, L.-M. Duan, and G. Vidal, "Classical simulation of quantum many-body systems with a tree tensor network", Phys. Rev. A **74**, 022320 (2006).

[186] G. Vidal, "Class of Quantum Many-Body States That Can Be Efficiently Simulated", Phys. Rev. Lett. **101**, 110501 (2008).

[187] L. Tagliacozzo, G. Evenbly, and G. Vidal, "Simulation of two-dimensional quantum systems using a tree tensor network that exploits the entropic area law", Phys. Rev. B **80**, 235127 (2009).

[188] G. Evenbly and G. Vidal, "Class of Highly Entangled Many-Body States that can be Efficiently Simulated", Phys. Rev. Lett. **112**, 240502 (2014).

[189] J. Haegeman, T. J. Osborne, H. Verschelde, and F. Verstraete, "Entanglement Renormalization for Quantum Fields in Real Space", Phys. Rev. Lett. **110**, 100402 (2013).

[190] F. Verstraete, J. J. García-Ripoll, and J. I. Cirac, "Matrix Product Density Operators: Simulation of Finite-Temperature and Dissipative Systems", Phys. Rev. Lett. **93**, 207204 (2004).

[191] M. Zwolak and G. Vidal, "Mixed-State Dynamics in One-Dimensional Quantum Lattice Systems: A Time-Dependent Superoperator Renormalization Algorithm", Phys. Rev. Lett. **93**, 207205 (2004).

[192] I. P. McCulloch, "From density-matrix renormalization group to matrix product states", J. Stat. Mech. **2007**, P10014 (2007).

[193] B. Pirvu, V. Murg, J. I. Cirac, and F. Verstraete, "Matrix product operator representations", New J. Phys. **12**, 025012 (2010).

[194] G. M. Crosswhite and D. Bacon, "Finite automata for caching in matrix product algorithms", Phys. Rev. A **78**, 012356 (2008).

[195] N. Schuch and J. I. Cirac, "Matrix product state and mean-field solutions for one-dimensional systems can be found efficiently", Phys. Rev. A **82**, 012314 (2010).

[196] Z. Landau, U. Vazirani, and T. Vidick, "A polynomial time algorithm for the ground state of one-dimensional gapped local Hamiltonians", Nat. Phys. **11**, 566 (2015).

[197] G. Vidal, "Efficient Simulation of One-Dimensional Quantum Many-Body Systems", Phys. Rev. Lett. **93**, 040502 (2004).

[198] F. Verstraete, V. Murg, and J. Cirac, "Matrix product states, projected entangled pair states, and variational renormalization group methods for quantum spin systems", Adv. Phys. **57**, 143–224 (2008).

[199] J. J. García-Ripoll, "Time evolution of Matrix Product States", New J. Phys. **8**, 305 (2006).

[200] J. Haegeman, J. I. Cirac, T. J. Osborne, I. Pižorn, H. Verschelde, and F. Verstraete, "Time-Dependent Variational Principle for Quantum Lattices", Phys. Rev. Lett. **107**, 070601 (2011).

[201] S. R. White, "Density matrix formulation for quantum renormalization groups", Phys. Rev. Lett. **69**, 2863–2866 (1992).

[202] S. Östlund and S. Rommer, "Thermodynamic Limit of Density Matrix Renormalization", Phys. Rev. Lett. **75**, 3537–3540 (1995).

[203] R. Orús, "A practical introduction to tensor networks: Matrix product states and projected entangled pair states", Ann. Phys. **349**, 117–158 (2014).

[204] J. C. Bridgeman and C. T. Chubb, "Hand-waving and interpretive dance: an introductory course on tensor networks", J. Phys. A: Math. Theor. **50**, 223001 (2017).

[205] A. Stathopoulos and J. R. McCombs, "PRIMME: Preconditioned Iterative Multimethod Eigensolver – Methods and Software Description", ACM Trans. Math. Softw. **37**, 21:1–21:30 (2010).

[206] L. Wu, E. Romero, and A. Stathopoulos, "PRIMME_SVDS: A High--Performance Preconditioned SVD Solver for Accurate Large-Scale Computations", arXiv:1607.01404 (2016).

[207] M. Suzuki, "General Decomposition Theory of Ordered Exponentials", Proc. Jpn. Acad., Ser. B: Phys. Biol. Sci. **69**, 161–166 (1993).

[208] P. Calabrese and J. Cardy, "Evolution of entanglement entropy in one-dimensional systems", J. Stat. Mech. **2005**, P04010 (2005).

[209] N. Schuch, M. M. Wolf, K. G. H. Vollbrecht, and J. I. Cirac, "On entropy growth and the hardness of simulating time evolution", New J. Phys. **10**, 033032 (2008).

[210] H. Kim and D. A. Huse, "Ballistic Spreading of Entanglement in a Diffusive Nonintegrable System", Phys. Rev. Lett. **111**, 127205 (2013).

[211] M. C. Bañuls, M. B. Hastings, F. Verstraete, and J. I. Cirac, "Matrix Product States for Dynamical Simulation of Infinite Chains", Phys. Rev. Lett. **102**, 240603 (2009).

[212] J. Jordan, R. Orús, G. Vidal, F. Verstraete, and J. I. Cirac, "Classical Simulation of Infinite-Size Quantum Lattice Systems in Two Spatial Dimensions", Phys. Rev. Lett. **101**, 250602 (2008).

[213] P. Corboz, R. Orús, B. Bauer, and G. Vidal, "Simulation of strongly correlated fermions in two spatial dimensions with fermionic projected entangled-pair states", Phys. Rev. B **81**, 165104 (2010).

[214] H. N. Phien, J. A. Bengua, H. D. Tuan, P. Corboz, and R. Orús, "Infinite projected entangled pair states algorithm improved: Fast full update and gauge fixing", Phys. Rev. B **92**, 035142 (2015).

[215] A. E. Feiguin, "The Density Matrix Renormalization Group", in *Strongly correlated systems: numerical methods*, edited by A. Avella and F. Mancini (Springer Berlin Heidelberg, Berlin, Heidelberg, 2013) Chap. 2, pp. 31–65.

[216] C. V. Kraus, N. Schuch, F. Verstraete, and J. I. Cirac, "Fermionic projected entangled pair states", Phys. Rev. A **81**, 052338 (2010).

[217] C. Pineda, T. Barthel, and J. Eisert, "Unitary circuits for strongly correlated fermions", Phys. Rev. A **81**, 050303 (2010).

[218] K. Melnikov and M. Weinstein, "Lattice Schwinger model: Confinement, anomalies, chiral fermions, and all that", Phys. Rev. D **62**, 094504 (2000).

[219] T. M. R. Byrnes, P. Sriganesh, R. J. Bursill, and C. J. Hamer, "Density matrix renormalization group approach to the massive Schwinger model", Phys. Rev. D **66**, 013002 (2002).

[220] T. Sugihara, "Density matrix renormalization group in a two-dimensional $\lambda\phi^4$ hamiltonian lattice model", J. High Energy Phys. **2004**, 007 (2004).

[221] K. Zapp and R. Orús, "Tensor network simulation of QED on infinite lattices: Learning from (1+1) d, and prospects for (2+1) d", Phys. Rev. D **95**, 114508 (2017).

[222] A. De La Torre and J. Iguain, "Angle states in quantum mechanics", Am. J. Phys. **66**, 1115 (1998).

[223] D. Horn, M. Weinstein, and S. Yankielowicz, "Hamiltonian approach to $Z(N)$ lattice gauge theories", Phys. Rev. D **19**, 3715–3731 (1979).

[224] D. Crewther and C. Hamer, "Eigenvalues for the massive Schwinger model from a finite-lattice Hamiltonian approach", Nucl. Phys. B **170**, 353–368 (1980).

[225] S. Dürr and C. Hoelbling, "Scaling tests with dynamical overlap and rooted staggered fermions", Phys. Rev. D **71**, 054501 (2005).

[226] J. D. Franson and M. M. Donegan, "Perturbation theory for quantum-mechanical observables", Phys. Rev. A **65**, 052107 (2002).

[227] I. Walmsley and H. Rabitz, "Quantum physics under control", Phys. Today **56(8)**, 43 (2003).

[228] M. Dalmonte and S. Montangero, "Lattice gauge theory simulations in the quantum information era", Contemp. Phys. **57**, 388–412 (2016).

[229] R. Narayanan, "Two flavor massless Schwinger model on a torus at a finite chemical potential", Phys. Rev. D **86**, 125008 (2012).

[230] R. Lohmayer and R. Narayanan, "Phase structure of two-dimensional QED at zero temperature with flavor-dependent chemical potentials and the role of multidimensional theta functions", Phys. Rev. D **88**, 105030 (2013).

[231] D. V. Deryagin, D. YU. Grigoriev, and V. A. Rubakov, "Standing wave ground state in high density, zero temperature QCD at large N_c", Int. J. Mod. Phys. A **7**, 659–681 (1992).

[232] H. R. Christiansen and F. A. Schaposnik, "Multiflavor correlation functions in non-Abelian gauge theories at finite fermion density in two dimensions", Phys. Rev. D **55**, 4920–4930 (1997).

[233] W. Fischler, J. Kogut, and L. Susskind, "Quark confinement in unusual environments", Phys. Rev. D **19**, 1188–1197 (1979).

[234] Y.-C. Kao and Y.-W. Lee, "Inhomogeneous chiral condensate in the Schwinger model at finite density", Phys. Rev. D **50**, 1165–1166 (1994).

[235] H. R. Christiansen and F. A. Schaposnik, "Fermion condensates of massless two-dimensional QED at finite density in nontrivial topological sectors", Phys. Rev. D **53**, 3260–3265 (1996).

[236] M. A. Metlitski, "Is the Schwinger model at finite density a crystal?", Phys. Rev. D **75**, 045004 (2007).

[237] A. Smilga and J. J. M. Verbaarschot, "Scalar susceptibility in QCD and the multiflavor Schwinger model", Phys. Rev. D **54**, 1087–1093 (1996).

[238] Y. Hosotani and R. Rodriguez, "Bosonized massive N-flavour Schwinger model", J. Phys. A **31**, 9925 (1998).

[239] G. S. Bali and K. Schilling, "Static quark-antiquark potential: Scaling behavior and finite-size effects in SU(3) lattice gauge theory", Phys. Rev. D **46**, 2636–2646 (1992).

[240] O. Philipsen and H. Wittig, "String Breaking in Non-Abelian Gauge Theories with Fundamental Matter Fields", Phys. Rev. Lett. **81**, 4056–4059 (1998).

[241] F. Knechtli and R. Sommer, "String breaking in SU(2) gauge theory with scalar matter fields", Phys. Lett. B **440**, 345–352 (1998).

[242] M. Chernodub, E.-M. Ilgenfritz, and A. Schiller, "String breaking and monopoles: a case study in the 3D Abelian Higgs model", Phys. Lett. B **547**, 269–277 (2002).

[243] G. S. Bali, H. Neff, T. Düssel, T. Lippert, and K. Schilling, "Observation of string breaking in QCD", Phys. Rev. D **71**, 114513 (2005).

[244] M. Pepe and U.-J. Wiese, "From Decay to Complete Breaking: Pulling the Strings in $SU(2)$ Yang-Mills Theory", Phys. Rev. Lett. **102**, 191601 (2009).

[245] A. Milsted, "Matrix product states and the non-Abelian rotor model", Phys. Rev. D **93**, 085012 (2016).

[246] C. Michael, "Hadronic forces from the lattice", Nucl. Phys. B **26**, 417–419 (1992).

[247] S. Ryu and T. Takayanagi, "Holographic Derivation of Entanglement Entropy from the anti-de Sitter Space/Conformal Field Theory Correspondence", Phys. Rev. Lett. **96**, 181602 (2006).

[248] M. Van Raamsdonk, "Building up spacetime with quantum entanglement", Gen. Relativ. Gravit. **42**, 2323–2329 (2010).

[249] H. Casini, M. Huerta, and J. A. Rosabal, "Remarks on entanglement entropy for gauge fields", Phys. Rev. D **89**, 085012 (2014).

[250] S. Ghosh, R. M. Soni, and S. P. Trivedi, "On the entanglement entropy for gauge theories", J. High Energy Phys. **2015**, 69 (2015).

[251] R. M. Soni and S. P. Trivedi, "Aspects of entanglement entropy for gauge theories", J. High Energy Phys. **2016**, 136 (2016).

[252] K. Van Acoleyen, N. Bultinck, J. Haegeman, M. Marien, V. B. Scholz, and F. Verstraete, "Entanglement of Distillation for Lattice Gauge Theories", Phys. Rev. Lett. **117**, 131602 (2016).

[253] S. Aoki, N. Iizuka, K. Tamaoka, and T. Yokoya, "Entanglement Entropy for 2D Gauge Theories with Matters", Phys. Rev. D **96**, 045020 (2017).

[254] M. C. Bañuls, K. Cichy, J. I. Cirac, K. Jansen, and S. Kühn, "Efficient basis formulation for 1+1 dimensional SU(2) lattice gauge theory: Spectral calculations with matrix product states", arXiv:1707.06434 (2017).

[255] S. Coleman, "More about the massive Schwinger model", Ann. Phys. (N.Y.) **101**, 239 (1976).

[256] R. Brower, S. Chandrasekharan, and U.-J. Wiese, "QCD as a quantum link model", Phys. Rev. D **60**, 094502 (1999).

[257] M. A. Nielsen and I. L. Chuang, "Quantum Computation and Quantum Information (Cambridge Series on Information and the Natural Sciences)", (2004).

[258] P. J. Steinhardt, "Baryons and baryonium in QCD2", Nucl. Phys. B **176**, 100–112 (1980).

[259] P. Calabrese and J. Cardy, "Entanglement entropy and quantum field theory", J. Stat. Mech. **2004**, P06002 (2004).

[260] N. Laflorencie, E. S. Sørensen, M.-S. Chang, and I. Affleck, "Boundary Effects in the Critical Scaling of Entanglement Entropy in 1D Systems", Phys. Rev. Lett. **96**, 100603 (2006).

[261] P. Calabrese, M. Campostrini, F. Essler, and B. Nienhuis, "Parity Effects in the Scaling of Block Entanglement in Gapless Spin Chains", Phys. Rev. Lett. **104**, 095701 (2010).

[262] M. Lubasch, J. I. Cirac, and M.-C. Bañuls, "Algorithms for finite projected entangled pair states", Phys. Rev. B **90**, 064425 (2014).

[263] M. Lubasch, J. I. Cirac, and M.-C. Bañuls, "Unifying projected entangled pair state contractions", New J. Phys. **16**, 033014 (2014).

[264] P. Corboz, "Variational optimization with infinite projected entangled-pair states", Phys. Rev. B **94**, 035133 (2016).

[265] L. Vanderstraeten, J. Haegeman, P. Corboz, and F. Verstraete, "Gradient methods for variational optimization of projected entangled-pair states", Phys. Rev. B **94**, 155123 (2016).

[266] W.-Y. Liu, S.-J. Dong, Y.-J. Han, G.-C. Guo, and L. He, "Gradient optimization of finite projected entangled pair states", Phys. Rev. B **95**, 195154 (2017).

[267] P. J. Steinhardt, "SU(2)-flavor Schwinger model on the lattice", Phys. Rev. D **16**, 1782–1790 (1977).

[268] E. Deutsch, "Dyck path enumeration", Discrete Mathematics **204**, 167–202 (1999).

List of Acronyms

cQED compact quantum electrodynamics. 53, 54, 56–64, 133, 180, 181

DMRG density matrix renormalization group. 41, 53

LGT lattice gauge theory. 1–3, 7, 12, 26, 28–31, 48, 49, 51, 54, 60, 63, 67, 83, 85, 117, 122, 125–127

LOCC local operations and classical communication. 118

MC Monte Carlo. 2–4, 28, 67–69, 80, 84, 87, 89, 94, 126

MPO matrix product operator. 40–42, 44–47, 77, 110, 130, 178, 179

MPS matrix product states. 3–5, 31–33, 35–41, 44, 46–49, 51, 55, 63, 68–70, 72, 77, 81, 83, 84, 86, 87, 90, 94–96, 98, 101–103, 109, 110, 121, 122, 125–127, 129, 130, 134, 178

OBC open boundary conditions. 26, 28, 38, 51, 67, 69, 102, 103, 105, 107, 110, 121, 147

PEPS projected entangled pair states. 38, 67, 127

QCD quantum chromodynamics. 1, 2, 68

QED quantum electrodynamics. 3, 25, 53

RDM reduced density matrix. 34, 117–120, 142, 148, 149, 151, 153, 187, 188

TN tensor network. 2, 3, 5, 10, 13, 16, 24, 28, 30, 31, 39, 42, 48, 49, 53, 63, 67, 68, 80, 83, 110, 122, 125–127, 129, 179

List of Figures

List of Tables

Acknowledgements

The last five years would not have been possible without the help and friendship of many people whom I would like to thank here.

First of all, I would like to thank my supervisor Ignacio Cirac for giving me the opportunity to do a PhD in his group. His deep understanding of physics combined with his creativity to approach new problems has been extremely inspiring, and I would like to thank him for the guidance during my PhD. Second, I am greatly indebted to my co-supervisor Mari Carmen Bañuls for introducing me to MPS and, in particular, for guiding me through the numerical methods used in MPS simulations and providing parts of her codes. The countless discussions with her about theoretical questions as well as about practical coding issues have been invaluable during me entire PhD and I am deeply grateful for that.

I also would like to express my gratitude to all my other collaborators over the years: Krzysztof Cichy for helping me with the data analysis and explaining many aspects of LGT to me, Karl Jansen for many discussions about lattice gauge models and inviting me to DESY Zeuthen, Hana Saito for discussions about the Schwinger model and Erez Zohar for answering innumerable questions about the Kogut-Susskind lattice formulation. I profited a lot from their great knowledge about (lattice) gauge theories and it was a pleasure to work with them on our joint projects.

A big thank you also goes to Michael Lubasch and Ahmed Omran for introducing me to the MPQ music scene, and, to Gemma de las Cuevas, Henrik Dreyer, Alessandro Farace, Thomas Gantner, Nils Haag, Clément Lafargue, Leo Molinaro, Olivier Morin, Christian Schweizer, Jordi Tura i Brugués for many jam sessions and having fun playing music together.

I also would like to thank the entire theory group for providing such a relaxed and yet stimulating working atmosphere, many cakes and cookies and a lot of help in bureaucratic issues as well as with practical problems regarding software, LaTeX and a lot of other things. In particular, I would like to thank my former and present office mates Anika Pflanzer and Benedikt Herwerth for the numerous coffee breaks, Thorsten Wahl for discussing many theoretical questions about MPS and Julian Roos for a lot of conversations not only about physics. I also would like to thank Yue Chang and Tao Shi for some of the most memorable moments during my time at MPQ. Moreover, I am indebted to Andrea Kluth for all her support with administrative matters throughout the years.

This thesis would not have been possible without my parents and my grandparents. I would like to thank them for all their support throughout my entire PhD and for providing a safe haven during the time writing this thesis.

Finally, I would like to thank Theresa Zach for her love, support and patience especially during the time finishing my PhD.